Effective Utilization of Distributed and Renewable Energy Resources to Stabilize and Enhance Smart Power Grids Performance

by

Mohammadreza Fakhari Moghaddam Arani

A thesis submitted in partial fulfillment of the requirements for the degree of

Doctor of Philosophy

in

Energy Systems

Department of Electrical and Computer Engineering
University of Alberta

Abstract

Clean and renewable energy resources such as wind power and photovoltaics, along with advanced environmentally-friendly loads like electric vehicles, will be significant components of future grids. These resources are rapidly increasing, but they have an inherent tendency to degrade system performance due to their intermittent generation, complicated system dynamics, and distributed nature with an increasing penetration level. This research focuses mainly on studying and analyzing voltage and frequency dynamics in grids with these resources contributing to frequency and/or voltage stabilization. The following presents the highlights of the contributions of the research.

The use of wind generators for frequency regulation is becoming an essential objective in power grids. However, the conventional control applied to wind turbines and their generators does not allow them to participate in frequency regulation. A major part of this study is focused on forcing wind generation to mimic conventional generators in frequency regulation, with minimal possible modifications in their structure and controller being applied. The system stability and sensitivity of the proposed control were measured, and various implementation methods were compared using the linear control systems theory. The proposed solutions consider practical system constraints, including generator fatigue. Moreover, wind generators will be required to remain connected to power systems during grid faults in high penetration of this source. In this work, the behavior of one of the most common types of wind generators is studied and enhanced during faults.

In some offshore wind plants, connecting power-electronic-interfaced generation to long transmission lines with very high-impedances can be challenging. A conventional voltage source converter (VSC) is incapable of injecting its maximum theoretical active power in such grids. Benefiting from a comprehensive analytical model, a detailed analysis of the VSC dynamics is presented and showed how the assumptions which are usually made for designing VSC regulators in conventional grids are not valid in grids with high impedances. Two solutions which enabled the VSC to operate at its maximum theoretical active power by making minimal modifications in the widely accepted control method are proposed and compared.

The studies on asymmetrical distributed single-phase sources and loads such as photovoltaics and electric vehicles show that a central controller may result in delays and that a distributed control may lead to asymmetry. Both of these controllers may destabilize the system. In the presence of such loads/generations, the classic assumption of the decoupling between frequency and voltage stability is not valid. In this research, both linear and nonlinear control system theories were used and practical solutions suggested. This study shows the disadvantages of independent utilization of wind generators and electric vehicles for frequency regulation and come up with a coordinated control method in which these two sources compensate for each other weakness. Linear control theory has provided proper tools to consider the practical constraints of each resource and assure the effectiveness of the method.

In summary, this thesis shows that neglecting the impact of emerging power system components on system stability will lead to large and complicated problems in the near

future. The research work then evolved to develop new mechanisms to mitigate the adverse impacts of the new components on system stability, thereby contributing to the creation of a sustainable future.

Preface

This thesis is an original work by Mohammadreza Fakhari Moghaddam Arani. As detailed in the following, some chapters of this thesis have been published or accepted for publication as scholarly articles in which Professor Yasser Abdel-Rady I. Mohamed was the supervisory author and has contributed to concepts formation and the manuscript composition.

Chapter 3 of this thesis has been published as

> M. F. M. Arani and Y. A.-R. I. Mohamed, "Analysis and Impacts of Implementing Droop Control in DFIGs on Microgrid/Weak-Grid Stability," *IEEE Transactions on Power Systems*, vol. 30, no. 1, pp. 385-396, January 2015.
>
> M. F. M. Arani and Y. A.-R. I. Mohamed, "Dynamic Droop Control for Wind Turbines Participating in Primary Frequency Regulation in Microgrids" *IEEE Transactions on Smart Grid*, in press.

Chapter 4 of this thesis has been published as

> M. F. M. Arani and Y. A.-R. I. Mohamed, "Analysis and Mitigation of Undesirable Impacts of Implementing Frequency Support Controllers in Wind Power Generation," *IEEE Transactions on Energy Conversion*, vol. 31, no. 1, pp. 174-186, March 2016.
>
> M. F. M. Arani and Y. A.-R. I. Mohamed, "Analysis and Damping of Mechanical Resonance of Wind Power Generators Contributing to Frequency Regulation," *IEEE Transactions on Power Systems*, vol. 32, no. 4, pp. 3195-3204, July 2017.

Chapter 5 of this thesis has been published as M. F. M. Arani and Y. A.-R. I. Mohamed, "Assessment and Enhancement of a Full-Scale PMSG-Based Wind Power Generator Performance Under Faults," *IEEE Transactions on Energy Conversion*, vol. 31, no. 2, pp. 728-739, June 2016.

Chapter 6 of this thesis has been published as

M. F. M. Arani, Y. A.-R. I. Mohamed and E. El-Saadany, "Analysis and Mitigation of the Impacts of Asymmetrical Virtual Inertia," *IEEE Transactions on Power Systems*, vol. 29, no. 6, pp. 2862-2874, November 2014.

M. F. M. Arani and Y. A.-R. I. Mohamed, "Cooperative Control of Wind Power Generator and Electric Vehicles for Microgrid Primary Frequency Regulation" *IEEE Transactions on Smart Grid*, in press.

Chapter 7 of this thesis has been published as M. F. M. Arani and Y. A.-R. I. Mohamed, "Analysis and Performance Enhancement of Vector-Controlled VSC in HVDC Links Connected to Very Weak Grids," *IEEE Transactions on Power Systems*, vol. 32, no. 1, pp. 684-693, January 2017.

Acknowledgements

First and foremost, I would like to express my sincere gratitude to my advisor, Professor Yasser Mohamed, for the continuous support of my Ph.D. study and research, and for his patience, motivation, enthusiasm, and immense knowledge. He gave me the academic freedom to explore my fields of interests while his deep knowledge and continual involvement prevented me from being distracted. The joy and enthusiasm he has for his research was contagious and motivational for me.

Besides my advisor, I would like to thank the rest of my thesis committee: Professor Hao Liang, and Professor Sahar Pirooz Azad, for their insightful comments. I would like to extend special thanks to Professor Mohammad Shahidehpour and Professor Qing Zhao for the time and effort they invested in reviewing this dissertation.

I also need to thank Alberta Innovates Technology Future for its generous support which allowed me to remain focused on my research.

As well, I would like to thank my friends in our research group at the University of Alberta who contributed so wonderfully to my learning experience. I also wish to thank all of my dear friends who have enriched my life beyond my studies.

Last but not the least, my deep gratitude goes out to all of the members of my family, for the wonderful support, they have provided me, especially my parents.

Dedication

To my dear parents.

Table of Contents

List of Figures

List of Tables

List of Symbols

Chapters 2, 3, 4, and 5

A	State matrix
A_1	Derivative of wind input power in respect to pitch angle
a_2	Coefficient describing A_2
A_2	Derivative of wind input power in respect to turbine rotating speed
A_3	Derivative of wind input power in respect to wind speed
A_f	State matrix during fault
A_{pf}	State matrix pre-fault
A_r	Effective area covered by the turbine blades
ave	Subscript denotes the average value
B	Subscript denotes the base value
$B_{1,pf}$	Input matrix pre- and post-fault
$B_{2,pf}$	Input matrix during fault
C	Dc-link Capacitance
C_{dc}	Dc-link Capacitance
C_p	Efficiency coefficient
D	Damping Factor
D_v	Active Damping Gain
EffDr	Subscript denotes efficiency-droop method
f_{dc}	Dc-link voltage control bandwidth
g	Subscript denotes the wind generator
$H_1(s)$	Input-output transfer function of wind generator responds to frequency regulating command
$H_2(s)$	Input-output transfer function of wind generator responds to wind speed change
H_{DFIG}	Inertia constant of the generator
i_q	q-axis currents
K_f	Deloading factor

K_{ic}	Integral gain of PI current regulator
K_{OPT}	Optimal wind power gain
K_p	Governor speed droop gain
K_{pc}	Proportional gain of PI current regulator
K_{pi}	Pitch-angle controller integral Gain
K_{pp}	Pitch-angle controller proportional Gain
K_s	Shaft stiffness
K_{vf}	Deloading factor in respect to wind speed
K_{V2G}	Electric vehicle droop gain
K_{wf}	Deloading factor in respect to turbine speed
max	subscript denotes maximum value
M_{diesel}	Diesel inertia constant
m_{eff}	Effective droop gain
min	Subscript denotes minimum value
m_p	Droop gain
M_{vi}	Virtual Inertia Gain
opt	Subscript denotes the optimal value
P	Active power
P	pole-pair number
P_{ad}	Active damping needed power
P_{comp}	Compensated power
$P_{deloaded}$	Deloaded power
P_{drp}	Droop needed power
P_e	Electrical output power
P_{gen}	Generator electric output power
P_{grid}	GSC output active power
P_L	Load Demand
P_m	Mechanical input power
P_{nom}	Nominal power

$PoDr$	Subscript denotes power-droop method
P_{reg}	Frequency regulating needed Power
P_{vi}	Power needed for virtual inertia
P_{V2G}	Vehicle power injected to the grid
Q_{grid}	GSC output reactive power
R	the blade radius
ref	subscript denotes the reference value
s	Laplace operator
s	Subscript denotes the shaft
S_{conv}	Converter rating
ss	Subscript denotes steady-state value
t	Subscript denotes the wind turbine
T	Torque
t^*	Restoration time
T_{CH}	Turbine time constant
T_G	Governor time constant
$TrDr$	Subscript denotes torque-droop method
V_{nom}	Nominal value of the dc-link voltage
V_{ref}	Dc-link reference voltage
v_w	Wind speed
β	Pitch angle of the turbine blades
β_{cmd}	Desired pitch-angle
θ	Shaft angle
λ	Tip speed ratio
λ_{del}	Deloaded tip speed ratio
λ_m	Electromagnetic flux constant
ξ_{ad}	Active damping damping factor
ξ_n	Damping factor of the second-order filter
τ	Droop time constant

τ_{ad}	Active damping time constant
τ_i	Current controller time constant
τ_m	Droop time constant
τ_p	Pitch angle controller time-constant
τ_{vi}	Virtual inertia time constant
ϕ	Artificial state realizing the dynamics of the controllers
ω	Rotating speed
ω_{ad}	Active damping natural Frequency
ω_m	System frequency
ω_n	Second-order filter Cut-off frequency
ω_r	Rotational speed of the turbine
-	Superscripts describe the injection
+	Superscripts describe the absorption
*	Superscript refers to the nominal value
Δ	Denoting the small signal perturbation of a variable
$\lvert\Delta f_{max}\rvert$	Maximum frequency deviation
Δt_{max}	Occurrence time of the maximum frequency deviation
0	Subscript denotes the initial value

Chapter 6

a, b, c	Phase a, b, c portion
a, b, c	Subscript denotes different phases
ab, bc, ca	Subscript denotes different phases-to-phase
A_w	State matrix of wind generator
B_{wf}	Input matrix of wind generator responding to frequency regulation command
B_{wv}	Input matrix of wind generator responding to wind speed changes
C_w	Output matrix of wind generator

D_{wf}	Feedforward matrix of wind generator responding to frequency regulation command
D_{wv}	Feedforward matrix of wind generator responding to wind speed changes
f_{hpf}	HPF cutoff frequency
f_{lpf}	LPF cutoff frequency
$H_{ev}(s)$	Input-output transfer function of electric vehicle aggregator
H_{wf}	Input-output transfer function of wind generator responds to frequency regulating command
H_{wv}	Input-output transfer function of wind generator responds to wind speed change
i	Current
I	Current Magnitude
I	Identity Matrix
K_{ev}	Electric Vehicle Droop Factor
K_{ii}	Single-phase converter Resonant controller gain
K_{pi}	Single-phase converter Resonant controller gain
M_{ev}	Virtual Inertia gain
$m_{p,phev}$	PHEVs accumulated droop gain
$m_{p,wind}$	Wind generator droop gain
P_f	Power needed for frequency regulation
P_L	Load Demand
P_w	Active power output of the wind generator
Q	Reactive Power
v_w	Wind speed
V	Voltage magnitude
v	Voltage
x_w	Doubly-mass wind generator and its controller states
τ_c	Frequency regulation time constant
τ_d	Time delay
τ_{ev}	Time constant of electric vehicle

φ	Phase shift of Current
Δ	Denoting the small signal perturbation of a variable
0	subscript denotes the initial value

Chapter 7

a	Compensation factor
A_p	State matrix of active power regulating VSC
A_v	State matrix of dc-voltage regulating VSC
B_{1p}	Input matrix of active power regulating VSC, desired PCC voltage magnitude as input
B_{1v}	Input matrix of dc-voltage regulating VSC, desired PCC voltage magnitude as input
B_{2p}	Input matrix of active power regulating VSC, desired active power as input
B_{2v}	Input matrix of dc-voltage regulating VSC, desired dc-link voltage as input
B_{3p}	Input matrix of active power regulating VSC, grid voltage magnitude as input
B_{3v}	Input matrix of dc-voltage regulating VSC, grid voltage magnitude as input
B_{4p}	Input matrix of active power regulating VSC, dc link voltage as input
B_{4v}	Input matrix of dc-voltage regulating VSC, external power as input
C_f	Capacitance connected to the PCC
L	Grid Inductance
L'	Grid Inductance estimation
L_f	Ac-filter inductance
P_{ext}	External power
R	Grid Resistance
R_f	Ac-filter resistance
u	Input signal
V	Voltage magnitude

v_g	Grid Voltage
v_s	PCC voltage
x_p	States of active power-regulating VSC
x_v	States of dc link-regulating VSC
Z_f	Passive inductive filter
Z_g	Grid line impedance
θ	Grid angle
ρ	Synchronization angle
Δ	Denoting the small signal perturbation of a variable
0	subscript denotes the initial value

List of Abbreviations

AVR	Automatic voltage regulator
DFIG	Doubly fed induction generator
DG	Distributed generation
GSC	Grid side converter
HPF	High-pass filter
HVDC	High voltage direct current
LCC	Line-commutated converters
LFC	Load frequency control
LPF	Low-pass filter
LVRT	Low voltage ride thorough
PCC	Point of common coupling
PHEV	Plug-in hybrid electric vehicle
PLL	Phase-locked loop
PMSG	Permanent magnet synchronous generator
ROCOF	Rate of change of frequency
ROCOP	Rate of change of power
ROCOT	Rate of change of torque
RRL	Ramp-rate limiter
SCR	Short circuit ratio
SOC	State of charge
VSC	Voltage source converter
V2G	Vehicle to grid
WSC	Wind generator side converter

Chapter 1
Introduction

1.1 Preface

New clean and renewable energy resources, such as wind and photovoltaic, and advanced environment-friendly loads such as electric vehicles and interactive loads, are going to be significant parts of close-future grids. Spain experienced an instantaneous wind penetration of almost 60% in 2011 [1] and 42% of total electricity energy of Denmark in 2015 is extracted from the wind [2]. In 2016, China alone has installed more than 23 GW new wind generation capacity and Germany has reached 50 GW cumulated capacity [3]. The Netherland plans to completely phase out the vehicles with diesel engines by 2025 [4], and a Europe Union initiative is intended to mandate every new or refurbished house in Europe to be equipped with an electric vehicle recharging point [5]. Electric vehicles constituted almost 24% share of Norwegian market in 2016 [6].

In Canada, the liberal federal government has promised to spend $5 billion over the next five years on developing a green infrastructure [7]. Alberta has more than 1400 MW installed wind capacity and, there are proposed projects totaling 7000 MW in the queue in November 2016 [8], whereas wind-based generation is going to be 20% of the total power generation capacity in Canada by 2025 [9]. Some provinces offer up to $14000 incentive rebate on buying a hybrid electric vehicle [10]. More than five hundred and fifty public charging stations have already been built in British Columbia [11], and electric vehicles sales have increased 70% year-over-year since 2011 in Vancouver [12]. These resources expose power systems to new threats and opportunities.

Microgrid is among the most important opportunities [13]. It is a part of a power system which can operate in both grid-connected and islanded modes. India has targeted to achieve deployment of 10000 renewable energy based microgrid projects across the country in five years [14]. Government of New York State is offering $40 million in awards to the communities that build their own microgrids [15]. While the economic and environmental

benefits of using smart microgrids are very promising for governments and industry, their stability is still a major concern. Due to these concerns, the penetration of wind generators in remote communities of Canada has been limited to 30% [16]. To remove this barrier wind generator are needed to incorporate in frequency and voltage stabilization [17, 18]. Even in large power systems with high penetrations of wind energy, renewable generators are expected to contribute to power system stabilization [19] and they are the firsts to be accused, though falsely, for any undesired event, as it happened in South Australia blackout in 2016 [20, 21].

Offshore wind is another challenge. It is described as abundant, stronger, and blow more consistently than land-based wind resources [22]. It comes as no surprise that offshore wind generators growth is very promising. In UK, their capacity is increased from 0.4 GW in 2007 to 4.5 GW in 2014 [23]. Europe has a cumulative total of 12631 MW of offshore wind which is projected to grow to a total installed capacity of 24.6 GW by 2020 [24]. However, Ontario Government has imposed a moratorium on its wind farm projects since 2011 due to lack of sufficient research [25]. US Department of Energy has mentioned grid integration as one of the main challenges of this type of generation which needs further study and investigation [22]. Even in Germany that offshore generation is relatively well-developed, the grid bottleneck has prevented 4100 GWh of wind electricity to be transported in 2015, according to the German Federal Grid Agency. A European wind power pioneer has described storage technologies and better grid integration as the solutions – wind energy's "*golden bullets*" [26].

In such a situation, some researchers are seeking to use electric vehicles to improve the power system performance, although there are still suspicions about the adverse impacts of electric vehicles charging on power systems [27]. Battery Second Use (B2U) strategies, in which a single battery first serves an automotive application, then once deemed appropriate is redeployed into power system improvement, has been implemented in the campus of University of California – San Diego (UCSD) for both demand charge management and frequency regulation [28]. Utilizing batteries of vehicles when they are in parking mode has gained lots of attention too. National Renewable Energy Laboratory (NREL) worked with

Department of Defense and U.S. Army Corp of Engineers to develop a microgrid that integrates photovoltaic, plug-in electric vehicles, and a renewable energy management unit at Fort Carson [29]. In May 2016, Nissan and Enel confirmed their plans to launch a major vehicle-to-grid (V2G) trial, installing and connecting one hundred units, in the UK [30].

Smart grid is the solution that industry and academia are suggesting to deal with these threats and opportunities. While many different definitions are proposed for smart grids, all of these definitions agree that they are future evolutions of power systems [31, 32, 33, 34]. ABB Multinational Corporation predicts these grids will include both transmission and distribution systems and will focus on integration of renewable generation, reliability and efficiency of grids. This description adds the inclusion of new technologies such as large scale integration of electric vehicles as one of the main features of smart grids [33]. US Department of Energy also acknowledges "*accommodation of all generation and storage options*" as one of the principal characteristics of these grids [34].

Motivated by the aforementioned challenges, the proposed research project aims at developing new control algorithms for wind turbines with short-term energy storages to enhance the ability of wind turbines to contribute to frequency and voltage stabilization under the presence of practical machine and converter constraints; studying and analyzing voltage source converter (VSC)-interfaced offshore wind generation connected to long lines with high impedances; and developing coordinated control algorithms to enable effective contribution of distributed asymmetrical resources to frequency stabilization. Using the linear control theory, the impact of the proposed controllers on the system stability and the sensitivity of the proposed control methods to different system parameters will be characterized. Different implementation methods will be compared and assessed and solutions will be proposed wherever they are needed.

This research, first of all, shows that neglecting the impact of emerging power system components on the system stability leads to complicated problems, particularly under the expected high penetration level of these devices. Then, the research work evolves to develop

new mechanisms to mitigate adverse impacts on system stability. The proposed solutions consider the practical system and device constraints to provide practical methods.

1.2 Research Motivations

The detailed literature survey shows that there are serious problems facing effective utilization of wind and Plug-in Hybrid Electric Vehicles (PHEVs) resources to support the integrated system frequency and voltage dynamics. Key drawbacks that motivate the proposed research are:

1) Lack of detailed analysis of the impact of different droop control methods on the dynamic performance of wind power generators, and system frequency dynamics.

2) Lack of detailed assessment and mitigation of the adverse impacts of implementing frequency support controllers in wind power generators considering the generator's practical limits.

3) Lack of the thorough analysis of the performance of Permanent Magnet Synchronous Generator based wind generators during Low Voltage Ride Through.

4) Lack of proper analysis and performance enhancement of vector-controlled Voltage Source Converters connected to very weak grids.

5) Lack of control algorithms for coordinating the control efforts of distributed resources (e.g. electric vehicles) participating in system support functions.

1.3 Research Objectives

To address the aforementioned difficulties, the following objectives are identified for this research work:

1) Modeling and analysis of the impact of droop control in wind power generators. The models are used for comparative analysis and sensitivity studies of the impact of the proposed and present methods on the transient and steady-state behaviors of the frequency dynamics. The analysis provides a systematic approach to coordinate wind-droop with other energy sources available in a typical microgrid system.

Furthermore, it facilitates examining stand-alone operation of wind generation in a microgrid with real wind speed pattern.

2) Developing a detailed small-signal model for a systematic analysis of the impact of frequency regulation implementation on the mechanical tensions of generators in conventional types of wind turbines. Fatigue and mechanical resonance in frequency regulating wind generator are studied. The impact of different frequency regulation methods and effectiveness of the present and new compensation methods are also investigated.

3) Providing a small-signal-based model for a PMSG-based wind generator to analyze the fault ride-through dynamics by considering the double-mass mechanical dynamics and typical LVRT characteristics. The successful operation of a PMSG-based wind power generator under LVRT is investigated. Moreover, the impact of the LVRT control on the generator tear and wear is studied. Possible solutions for enhancement of PMSG-based wind generator performance with LVRT is studied and compared.

4) Analysis and control of distributed electric vehicles for frequency support. In this context, the single-phase distributed nature of electric vehicles is considered. Further, studying and comparing the present frequency regulation methods for system with deficient physical inertia is considered. Both centralized and distributed control strategies are investigated and a new hybrid method is proposed.

5) A proposal for a coordinated frequency regulation method that utilizes PHEVs and a wind generator considering their practical constraints. The virtual inertia and droop as tools for the coordinated frequency regulation is studied and compared. The impacts of two frequency regulating coordination structures, centralized and distributed, for wind generation and PHEVs are thoroughly investigated and compared.

6) A thorough analysis of the dynamics of a VSC with either active power or dc-voltage regulating controllers, and connected to a very weak grid, and the impacts

of the controller parameters on the overall system stability. A detailed analysis of conventional vector control is provided. A new method is developed to stabilize the performance of a vector-controlled VSC and maximize its power injection/absorption capability in a very weak grid condition. The robustness of the proposed method and a comparison with a retuned conventional vector controller is investigated.

1.4 Thesis Outline

This reminder of this thesis is structured as follows.

Chapter 2 presents the state-of-the-art and a critical literature survey on utilization of wind generators and electric vehicles for weak grids performance enhancement.

Chapter 3 presents a thorough investigation of droop control method to incorporate wind generation in autonomous frequency/power regulation in isolated microgrids, and in weak power grids with reduced inertia. Droop control is implemented on both torque and power by some simple modifications in the conventional wind power controller. Small-signal modeling and eigen-values analyses are employed to distinguish the differences among both methods and gauge their impacts on frequency stability. Sensitivity studies, with respect to the presence of turbine- and inverter-based generators in microgrids; and impacts of pitch-angle controller, wind speed variation and isolated mode operation with only wind generators, are conducted. The chapter also proposes a new solution which allows the droop gain to be tuned regardless of the variable wind speed. Thorough analyses are employed to demonstrate the method's effectiveness. The role of the proposed method in the both transient and steady-state frequency control is investigated and discussed.

Chapter 4 provides a systematic analysis of the impact of frequency regulation implementation on the mechanical tensions of generators in conventional types of wind turbines. It is shown that the contribution of wind generators to the frequency regulation dynamics can result in fatigue or even instability. The impact of different frequency regulation methods and effectiveness of the present compensation methods are also investigated. It is discussed why damping the natural resonance of a wind generator in such a

situation needs to be analyzed at the system level, in contrast to conventional mechanical resonance studies, which occur at the generator level.

Chapter 5 investigates the impacts of the LVRT control on the stability of wind power generator and the risk of resonance in its mechanical drive, successful operation during faults, and fatigue in a full-scale PMSG-based wind power generation system. An analytical model considering the double-mass nature of the turbine/generator and typical LVRT requirements is developed, validated, and used to characterize the dynamic performance of the wind generation system under LVRT control and practical generator characteristics. The model can also be effectively used to tune and optimize the control parameters in the generator system. To enhance the operation and reduce the fatigue under LVRT control, different solutions are proposed and compared.

Chapter 6 investigates different methods of utilizing PHEVs in frequency/power regulation while considering their single-phase nature. Not only droop and virtual inertia but also centralized and distributed controls are compared. Advantages and disadvantages of these methods are investigated and a new method based on a combination of both centralized and distributed control is proposed. A small-signal analysis is also employed to investigate which frequency regulation method, droop or virtual inertia is more suitable for cooperative control among a wind generator and PHEVs in a typical microgrid system. The centralized and distributed control structures are examined as two possible coordination methods to ensure that not only the wind generator and PHEVs constraints are not violated but also the communication system imperfections are considered.

Chapter 7 proposes solutions for VSC connected to very weak grids with high impedances that not only remain faithful to vector control, but are also simple and straightforward and maximize power injection/absorption and ensure robustness. The small-signal analysis is employed to study the dynamics of a grid-connected VSC under weak and very weak grid condition, and evaluate the performance of the proposed methods and their impacts on different aspects of VSC performance, such as voltage regulation, desired active power/dc voltage tracking, and system frequency measurement.

Chapter 8 presents the thesis summary, contributions, and directions for future work.

The thesis structure is visualized in Figure 1-1.

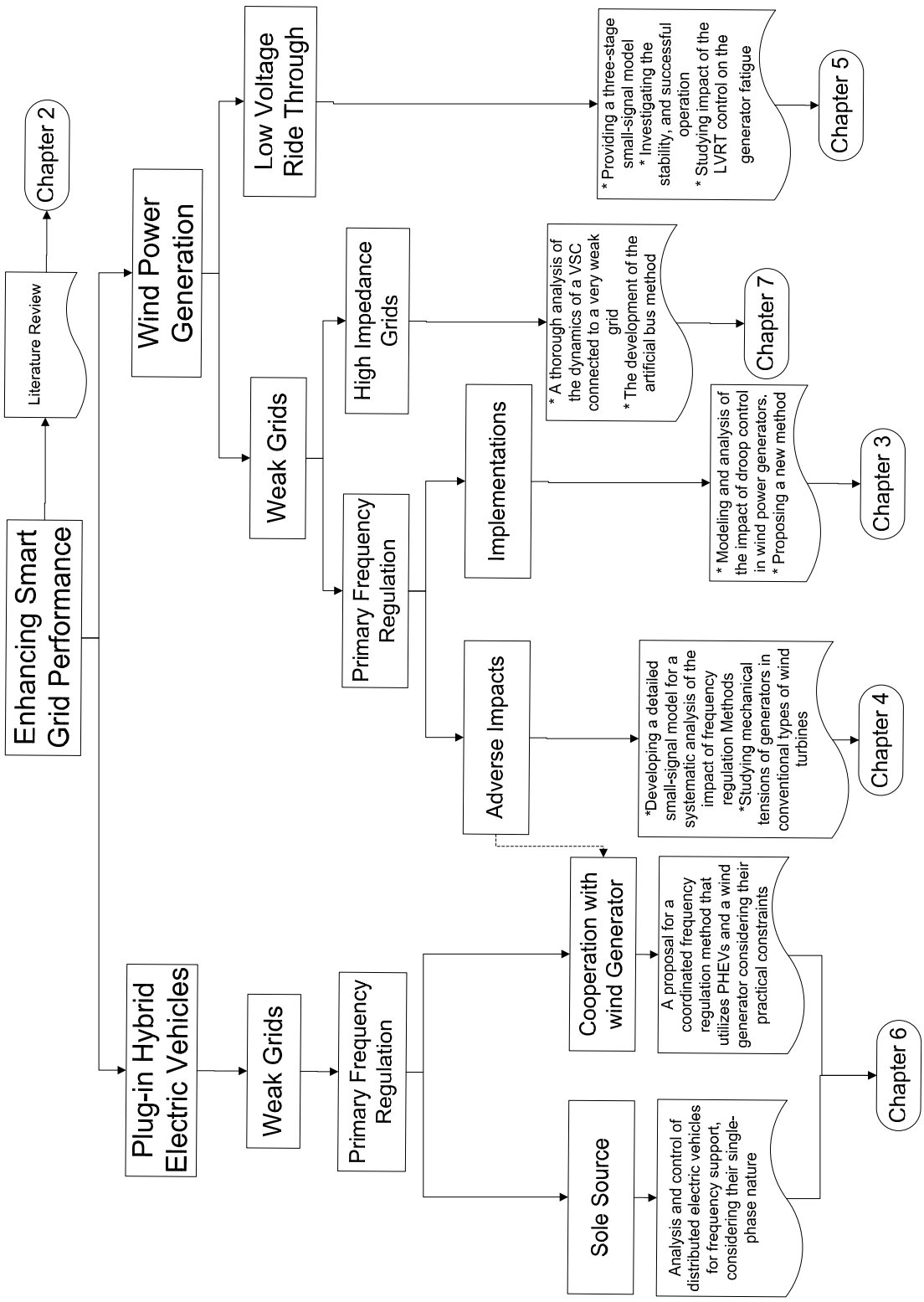

Figure 1-1 Illustration of the thesis structure. Dashed arrows show the relation between the concepts in different chapters.

Chapter 2
Literature Survey

Due to environmental, technical and financial issues, there is unprecedented interest in effective integration of new energy sources such as wind-based energy sources [3, 35, 36]. The intermittent nature of wind could be accounted as its most challenging characteristic. To extract the maximum available power from wind with fluctuating speed, a variable-speed turbine is required [35].

On the other hand, plug-in (hybrid) electric vehicles (PHEVs) are also gaining widespread acceptance by the automobile industry, customers and governments due to environmental and economic reasons [37]. PHEVs penetration is increasing rapidly and they are going to be significant parts of distribution systems in the near-term future [37, 38, 39, 40, 41].

Recently, by increasing the penetration level of these new types of generation and loads, it becomes essential for these resources to participate in system performance enhancement. Introducing the concept of smart grid and microgrid and increasing utilization of power-electronic-interfaced types of generation/load in power grids is magnified this necessity.

2.1 Wind Power Generators

Variable speed wind turbines based on a doubly-fed induction generator (DFIG) or permanent-magnet synchronous generator (PMSG) facilitate maximum power extraction and efficient operation [35, 42]. Although DFIG-turbines have dominated the market, the trend and market share of PMSG-based turbines are increasing due to several advantages associated with the PMSG-based topology such as higher reliability, lower losses, gear-less direct drive connection and higher energy density [42].

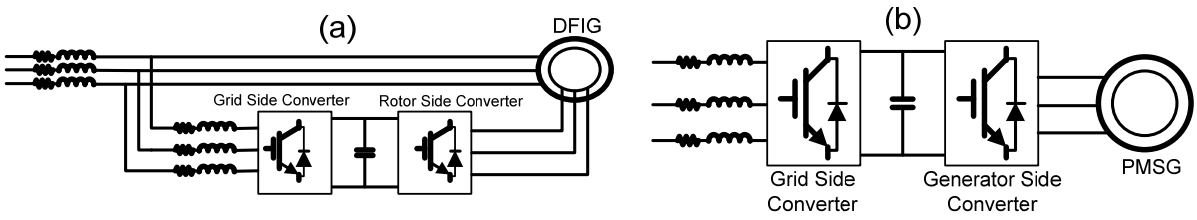

Figure 2-1 Wind power generators (a) Type C (b) Type D.

While the classical issues of wind power, such as capturing the maximum available wind energy, have been solved, increased the penetration level of wind power brings out new problems for power systems. Incorporating wind power generators in frequency regulation and low-voltage ride-thorough (LVRT) are among these serious issues.

2.1.1 Frequency Regulation

Recently, and especially after introducing the concept of microgrid to enhance supply reliability and increasing utilization of inertia-less types of generation in power grids, it becomes essential for wind turbines to participate in frequency regulation. Even in the grid-connected mode, many grid codes have changed to allow or even force wind power generation to participate in primary frequency regulation [43].

The main idea for incorporating wind turbines in frequency regulation is simply emulating the behavior of conventional generators in terms of droop control to mimic the speed governor characteristics, or virtual inertia control to mimic the behavior of the rotating mass.

2.1.1.1 Implementation Methods

The use of frequency deviation, i.e. frequency droop method, instead of frequency derivative, conventional inertia emulation, or at least a combination of both [43, 44, 45, 46, 47] is proposed. It is reported that this method has more advantages [43, 48]; however, detailed analysis is not provided to prove these arguments. It is worth to mention that in all of these works, a secondary, usually dispatchable, source of energy was employed to restore the frequency to its nominal value.

To incorporate wind resources in frequency regulation, different methods for providing the needed energy are employed. Significant part of research efforts is devoted to the use of wind turbine rotating mass [48, 49, 50], whereas several proposals are made to provide the energy by deviating from maximum power extraction point [44, 51], as shown by Figure 2-2. While almost all of the proposed methods for steady-state participation of wind in frequency/power regulation agreed on deloading and using droop control method, the adopted approaches are different.

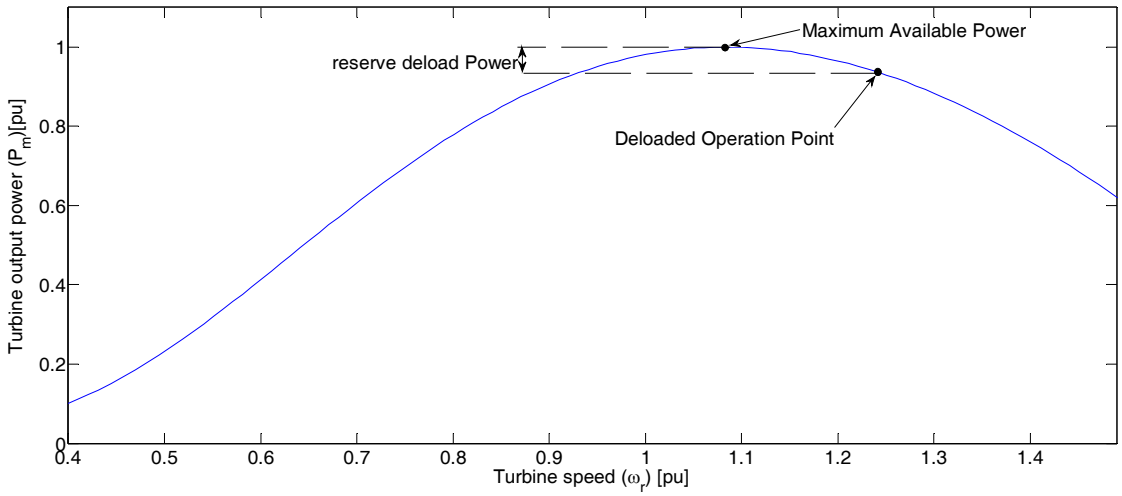

Figure 2-2 Wind turbine power characteristics showing the deloading and maximum power tracking (pitch angle is zero and wind speed is 12 m/s).

Many of these methods use wind speed for deloading; however, its accurate measurement does not seem easy [52]. On the other hand, the pitch-angle is used to deviate from optimum power extraction in [45, 53], whereas the DFIG torque control and over-speeding are used by [51, 52]. In [54], it is reported that pitch-angle control is fast enough for deloading; however, comparative results among other techniques reveal its slower behavior. It is also suggested that similar to the conventional wind control, pitch-angel could be utilized for high wind speed, whereas torque could be used for under-rated speeds [43, 52]. Despite its advantages, this approach needs wind speed measurement for switching between both control methods. Using both methods simultaneously based on a fuzzy control is proposed in [44]; however, similar to all discussed references, detailed stability analysis is not presented.

Due to these deficiencies, many references, such as [51], instead of measuring the wind speed or utilizing the pitch angle controller, preferred to modify the torque control. This method was investigated previously in the literature; however, it was noted that there are some major differences between wind-droop and the conventional dispatchable energy-based droop. The amount of reserved power from deloading is not constant, and using a constant droop gain, similar to that in the classic frequency control, may lead to power system destabilization. Reference [55] introduced an analytical method for finding the maximum possible droop gain to prevent any destabilization. However, the researchers did not provide

a solution, except for changing the droop gain with changes in the wind speed. Nevertheless, despite the relatively complicated analytical methods, the dynamics of the wind generator and wind turbine characteristics were approximated. References [56] and [57] acknowledged the same problem but proposed some modifications in the wind generator controller. By sending the droop reference power through a high-pass filter, [56] prevented any contribution to the steady-state power sharing, the main advantage of the droop method over the virtual inertia method. Reference [57] followed the same reasoning by adding a PI controller guaranteeing the restoration of the wind generator to the maximum power extraction. Reference [58] tried to approach this problem by updating the droop gain online. However, this method needs wind speed prediction and should be updated by a time interval of less than 0.1 s.

The droop method as one of the main solutions for primary frequency regulation in microgrids has been discussed and modified by many researchers. One of the main aspects receiving attention has been the stability problem. The power system is highly nonlinear, and a linear droop tailored for one operating point could face stability problems [59]. A proposed solution was the adaptive droop [60, 61]. A term containing the derivative of active power was added to the conventional droop. The gain of this component was adapted based on the operating point of the generator. Later, the concept of the adaptive droop was used by other researchers to consider the charging state of the energy storage of the generator and avoid over-charging or -discharging [62, 63]. On the other hand, using communication to determine the droop characteristics was proposed. This solution allowed considering the whole microgrid instead of only the generator and was useful for reactive power sharing, which usually does not happen perfectly in traditional droop methods [64]. The proposed method was also used for active power/frequency regulating in which the fuel cost of the microgrid was minimized [65, 66, 67]. However, this class of the droop method was criticized because of its reliability and the cost of the communication [68]. These criticisms led other researchers to focus on other possible solutions such as the nonlinear droop. The proposed nonlinear relation of frequency and power reflects the usually nonlinear relation of power generation and fuel cost. The complicated procedure of determining the nonlinear

characteristics of the proposed method has overshadowed its effectiveness [67, 68]. Moreover, all the previous references have used the droop for only the dispatchable generations.

The dynamic droop concept was discussed in [69, 70, 71, 72]. To consider the variable nature of renewable generation, a new type of frequency regulation with variable droop gain was proposed. References [69] and [70] focused on the power management among solar generation units while minimizing the auxiliary sources contributions. On the other hand, [71] and [72] avoided any deloading and the associated problems. [73] changed the external rotor resistance of a type-2 wind generator to enhance its natural frequency regulation. One of the best discussions about dynamic droop in type-3 (and similarly PMSG-based) generators is in [74]. It recognized the problem of the limited deloaded power of wind generators and proposed a method to solve it. However, the proposed method needs communication among the generators in a wind farm, and the droop gain of each generator in the wind farm is somehow dependent on other generators' performance. This method also used wind speed measurement, which makes the method less reliable than other methods. All these studies, however, suffer from the lack of thorough analytical studies.

In addition, none of mentioned papers, except Ref. [75], alluded to the stand-alone operation of DFIG-wind generators in the absence of any dispatchable sources. Despite its precious contributions, the work in [75] did not include any stability analysis. Further, it only considered constant wind speed with always excessive generation.

While droop method shows considerable enhancements, some serious difficulties can prevent its widespread application. First of all, droop implementation demands a power reserve, which is generated by a deviation from the maximum available wind power, to respond to steady-state frequency deviations [76]. Although this unavoidable deviation leads to frequency regulation enhancement, it is not desired economically [77]. Further, it has been reported that droop-based methods mainly improve the steady-state frequency behavior rather than the transient one [78].

Recently, several researchers have paid more attention to emulating the inertial response of conventional generators [48, 49, 79] via the so-called virtual inertia concept. Because this method does not incorporate wind turbines in steady-state frequency regulation, it does not require any permanent power deviation, and this may enhance the transient response significantly [78]. Such performance enhancements motivated the development of the combined droop and virtual inertia concepts [45, 46, 47].

2.1.1.2 Practical Concerns

Frequency regulation methods have been investigated in several studies [50, 76, 80]; however, their practicality has not yet been discussed thoroughly. In the current literature, the interactions between the double-mass dynamics and the frequency regulation methods in wind turbines are not thoroughly addressed. Instead, a single-mass model is usually adopted, or the contributions of droop and virtual inertia are completely ignored or assumed to be small [77, 81, 82]. The impact of implementing frequency support controllers on the wind turbine tear and wear needs to be studied. However, [81] pointed out that the rate of change of power (ROCOP) associated with the implementation of virtual inertia can be a limiting factor. A higher ROCOP leads to higher wear and tear in a wind generator and consequently faster aging and higher maintenance cost. This is a very important factor, because it has been recently found that aging in wind power generators, even in conventional units without frequency regulation, is faster than what was previously expected owing to mechanical breakdowns [83]. On the other hand, effective frequency regulation performance demands a higher permissible ROCOP. The impacts of this trade-off problem and possible mitigation strategies are not deeply investigated in the current literature. Conventionally, a simple rate limiter, usually with a threshold of approximately 0.2 per-unit (pu)/s, is commonly adopted [82, 84, 85] to limit the ROCOP. Even though the study in [81] addresses the importance of the ROCOP, it does not discuss—owing to the lack of theoretical analysis—the disadvantages and possible alternatives of the rate limiter block. Further, it does not explain why the ROCOP is not a concern in a conventional wind generator (i.e., without any frequency regulation controller implemented), and, therefore, the rate limit constraints could

be relaxed [86]. Furthermore, a single-mass mechanical model is usually adopted in droop- or virtual inertia-related studies.

It was also shown previously that practical direct-drive PMSGs are prone to mechanical resonance [87] due to the double-mass mechanical dynamics. However, the impact of the interactions between the system frequency and turbine shaft on the system stability has not been studied. References [88] and [89] pointed out that the natural resonance frequency of wind generators lies in the range of the resonance frequency of traditional large plants with synchronous generators. However, in a conventional variable-speed wind turbine, with no frequency regulation service, the drive-train dynamic is decoupled from that of the power system; therefore, it can be ignored in power system stability analyses [90]. Such decoupling does not exist after implementing frequency regulation methods in wind generators.

2.1.2 Low Voltage Ride Through

Incorporating wind power generators in low voltage ride through has gained significant attention in the literature in recent years, and grid codes have been standardized and implemented in several countries [91]. Generally, LVRT standards emphasize the need to keep a wind power generator connected to the grid and to improve the voltage profile during low-voltage transients. Reference [92] shows that all the generators in a wind farm are not required to provide LVRT capability; however, this reference does not question the need to implement LVRT implementation in wind power generators. The performance of a doubly-fed induction generator, as the most popular type of wind generator, has been extensively studied under LVRT [93]. Although the crowbar method is widely utilized in DFIGs, it is characterized by the loss of control and the waste of energy [94]. As an alternative, the demagnetizing control method has been proposed; however, it has not been widely adopted due to its complexity [95].

All these difficulties, besides some other problems, such as reliability, losses, and the cost of slip rings and gearboxes, reduce the advantages of DFIGs and result in an increasing trend toward using direct-drive permanent-magnet synchronous generators with full-scale back-to-back converters [42]. However, this topology with conventional control (i.e., dc-link voltage

control via the grid-side converter) yields high dc-link voltage during fault conditions [96]. Several approaches have been proposed to overcome this difficulty. Reference [97] proposes the use of a breaking resistor to dissipate excessive dc-link energy; however, this method increases the losses. The use of the rotating mass of a wind generator for storing the excessive generation during the fault is proposed in [98, 99]. The objectives of these studies were to not only enhance the dc-link voltage dynamics during faults, but also to improve different aspects of the grid voltage even under asymmetric faults [100]. The results of these studies are promising and present the PMSG as a generator with an inherent LVRT capability without the need for any additional components. However, the double-mass nature of the turbine-generator mechanical dynamics and its relatively soft shaft characteristics are not considered in these works. The natural resonance of PMSG-based wind power generators under conventional conditions has been investigated thoroughly [87, 101]. Interestingly, some of the earliest articles in this field have pointed out the risk of resonance and proposed mitigation strategies [88, 102]. In other words, adopting a realistic double-mass model for a PMSG-based wind turbine is necessary because using the single-mass model can lead to an incorrect and deceptive assessment of LVRT operation.

On the other hand, utilizing the rotating masses in a PMSG for storing the excessive energy during the fault will expose its shaft to the power system transients. Considering the softness of a direct-drive PMSG shaft, the LVRT control scheme may increase the fatigue and speed up the aging of the wind generator. Recently, it has been found that wind generators suffer from faster aging than expected, mainly because of mechanical fatigue [83]. Although addressing the fatigue caused by wind speed variation has gained significant attention [103], the impact of faults on the LVRT-capable PMSG fatigue is not addressed in the current literature. For conventional synchronous generators, the impact of power system faults on the generator fatigue is thoroughly addressed in the literature [104, 105]. It has been shown that these faults can increase the stresses and wear out the generator faster. Even DFIGs, which usually adopt crowbars during a fault, have been studied for possible mechanical tensions [106, 107].

2.1.3 Off-shore Winds: Voltage Source Converters Connected to Very Weak Grids

High voltage direct current (HVDC) transmissions have gained significant attention in recent years [108], partly because of increased offshore wind power generation and the high capability of HVDC to interface with this type of generation [3, 108, 109]. The implementation of HVDCs has increased so much that some countries have decided to standardize and regulate their application [110]. Modern HVDC systems are expected to exhibit a generator-like behavior in terms of frequency support and low-voltage ride-through.

HVDC systems face several problems, which have been discussed at length [111]. Research on line-commutated converters (LCC) is still ongoing [112]; however, voltage source converters (VSCs), despite their higher cost, seem to be more successful in resolving the problems of LCC-based HVDC systems [109, 110, 113]. VSCs suffer much less from output harmonic content and do not require reactive power consumption. They also perform better when connected to weak grids. However, problems occur when VSC-based HVDCs are connected to very weak grids [114]. Many efforts have been made to improve the performance of a very weak grid connected to a VSC. The authors of [115] tried to approach the problem by enhancing the ac-bus voltage regulation performance. However, later references such as [116] have argued that the problem stems from phase locked loop (PLL) performance in very weak grids. VSCs usually employ vector control, which requires a PLL [114]. PLLs have been investigated for a long time, and many different types have been introduced [117, 118, 119, 120]. Most articles have paid attention to the impacts of PLL on converter behavior, and some articles have even suggested rules of thumb for PLLs' utilization [121]. On the other hand, other research has concentrated on how a converter controller could also affect the performance of PLLs [122, 123]. Reference [124] showed that even in a strong grid with a high short-circuit ratio (SCR), under special circumstances such as faults, a PLL could be considerably influenced by the converter controller.

These factors convinced researchers to focus more on PLLs and their interaction with a VSC to improve its performance in very weak grids. The authors of [116] used only the PLL parameters to enhance the overall converter performance and stability, significantly decreasing the PLL bandwidth to prevent its interaction with other modes of the system.

Although the system remained stable, its performance was very poor. It also suffered from a lack of robustness. In other words, in case of a change in the power system SCR—i.e., switching or faults—the converter stability was not verifiably guaranteed.

Another interesting solution that eliminated the PLL by emulating the inherent synchronization behavior of synchronous machines in a VSC was developed in [125, 126]. However, the control scheme was completely changed and did not match the standard vector control scheme. In addition, similar to the previous method [116], this method did not achieve 1.0 per unit (pu) power injection in very weak grids (SCR = 1).

The newest efforts are still using vector control. In [127], the authors proposed the design of 35 H_∞ controllers for one converter and one specific SCR. The control strategy achieved the maximum power injection and guaranteed a smooth performance. However, the overall vector control system was very complex. Further, this research focused on only active power regulation. Dc-link voltage regulating has also been investigated in the literature [115, 116, 128, 129], but the maximum possible active power injection/absorption does not appear to have been reached.

Reference [130] suggested referring the PLL measurement point to a point with lower observing grid impedance; however, the study neglected any reactive power and/or ac-voltage regulation. Therefore, the VSC could not absorb/inject the maximum possible active power with a reasonable converter output voltage. Ref. [131] is one of the most recent articles which approached the same problem and they were successful to reach the maximum power injection limit. The authors also examined the method robustness against the balanced faults and frequency changes. Despite their achievement, this method suffers from the same problem, complexity. A state-space, containing at-least eighteen states, should be formed and eigenvalues of the system should be located properly. In addition, the system is sensitive to changes of parameters and the working point of the converter. On the other hand, Ref. [132] proved that even a simple vector control, without any additional loop or controller, is capable of achieving the same goal, just by retuning the parameters via a similar state-space and pole-placement method.

2.2 Plug-in Hybrid Electric Vehicles

This new type of load could result in new advantages and disadvantages for power systems. Early works on PHEVs have mainly discussed their negative impacts on system stability and possible mitigation strategies [38, 39]. Several works paid more attention to the use these sources to improve system performance.

2.2.1 Structure

Before focusing on the impact of PHEVs on power systems, it will be useful to have a brief discussion on their structure and characteristics to show their possible potential and challenges imposed on power systems.

Although many different topologies are introduced for PHEVs, Figure 2-3 depicts a general structure [37]. It consists of the parts needed for both traction and parking modes. However, the scope of this report is limited to the components needed in the parking mode, particularly the power train and the charger.

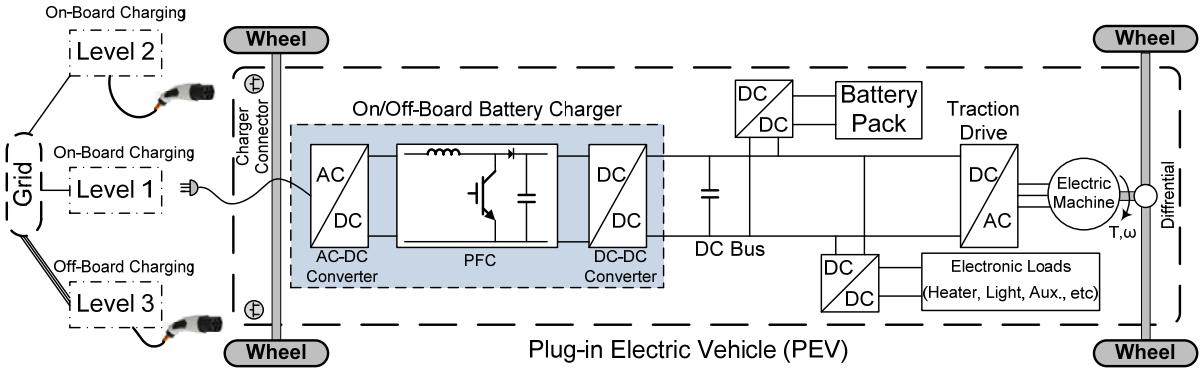

Figure 2-3 Plug-in hybrid electric vehicle structure.

2.2.1.1 Power Train

Batteries are used widely as energy storage source in hybrid electric vehicles due to their high energy density, reliability, compact sizes and relatively low cost [133]. Among different types of batteries, Lead-Acid, Nickel-Metal-Hydride (NiMH) and Lithium-Ion (Li-ion) have more popularity in electric vehicle industry.

All kind of batteries suffer from a relatively high equivalent series resistance (ESR) which decreases efficiency especially in low state of charges (SOC) [134]. The ESR is also different in charging and discharging modes. This could explain the much longer charging time of batteries. The disadvantages of batteries do not remain limited to the ESR. They cannot be discharged more than 50 percent in best cases otherwise their life time will be impacted [133]. Some types of batteries, such as NiMH, show memory effect which does not allow recharging to 100% SOC after a while.

Although batteries show much better power density and faster dynamics than fuel-cells, they are still slow considering the burst power needed in (plug-in hybrid) electric vehicles. Their relatively low life cycle is another problem which has encouraged industry to look for an alternative.

While none of other sources shows enough merit to be the sole source for PHEV, the hybridization has persuaded by many researchers. Lower cost, size, weight, higher reliability, and better performance of vehicle in traction mode are the same goals of all hybrid combinations. Electrolyte double layer capacitors (EDLC), more known as ultra-capacitors or super-capacitors, are among the choices extensively studied in the literature [133, 135]. This is because of their high energy density and much longer life cycle [136]. They could be completely charged and discharged with no harm to their life time [133, 134]. However, they suffer from low energy density.

The power train is also under study. Not only new topologies and circuits are still being proposed, the battery and ultra-capacitors are still advancing [133, 136, 137]. It is worthy to mention that all the efforts for improving the PHEV power train is focused on the traction mode where little attention is made to the parking mode.

2.2.1.2 Chargers

Research works have been underway in recent years to improve the charger features and consequently many different topologies have been proposed [138]. These chargers could be classified based on different major characteristics such as mounting location, power direction or connection method. One of the most important features is the power level. The higher the

charging rate (and consequently the lower the charging time), the level number is higher so that level 3 has the highest charging rate and lowest charging time, whereas level 1 has the lowest and the highest charging level and time, respectively. However, the most well-known and primary type is level 2 which is considered as a compromise between cost, size and charging time. This charger is usually connected to a single phase source [138]. Table 1 summarizes some of the main features of each charging level.

Table 1 Charger power levels [138].

Power Level Types	Voltage Level	Charger Location	Typical Use	Energy Supply Interface	Expected Power Level	Charging Time	Vehicle Technology
Level 1	120 Vac (US) 230 Vac (EU)	On-board 1-phase	Charging at home or office	Convenient Outlet	1.4kW (12A) 1.9kW (20A)	4-11 hours 11-36 hours	PHEVs (5-15kWh) EVs (16-50kWh)
Level 2	240 Vac (US) 400 Vac (EU)	On-board 1-phase or 3-phase	Charging at private or public outlets	Dedicated	4kW (17A) 8kW (32A) 19.2kW (80A)	1-4 hours 2-6 hours 2-3 hours	PHEVs (5-15kWh) EVs (16-30kWh) EVs (3-50kWh)
Level 3	208-600 Vac or Vdc	Off-board 3-phase	Commercial (analogous to a filling Station)	Dedicated	50kW 100kW	0.4-1 hours 0.2-0.5 hours	EVs (20-50kWh)

One of the important features especially for this study is the power direction of chargers. While industry prefers more reliable, simpler and cheaper unidirectional ones, employing the vehicles to improve the power system usually necessitates bidirectional power flow [138, 139].

The bidirectional converters of the vehicle motors can be used for vehicle-to-grid interactions in the parking mode. In the parking mode, both the motor windings and its inverter have left unused and could be employed as the converter interfacing the grid [140, 141]. This proposed method benefits from an on-board bidirectional inverter with a much higher rating while it does not add to the cost, weight and size of vehicle. However, this method adds to the complexity of PHEV and has not been commercialized yet.

2.2.2 Impacts on Power Systems

It is important to discuss the impacts of PHEVs on system performance. Not only because of the importance of these threats but also these studies could be considered as a historical prelude of studying the opportunities of vehicle for power systems.

By adding PHEVs as new type of load, the power system is responsible for providing energy for the vehicles which are moving in the streets. Therefore, these loads considered firstly as a new burden and new concern for power engineers.

One of the serious issues is well-known as uncoordinated charging. It means that if PHEVs like other appliances in the home could be connected to the grid independent of time, it would undesirably impact the load profile of system. There was the concern that this newly introduced load could increase the peak load. Many researches in different countries show that how dangerous could be the situation, if the charging happen uncoordinated [139].

The other reported issue associated with PHEVs is related to the power quality. A conventional vehicle is usually connected to the power system via an LCL filter. However, this filter can be subjected to resonance; the situation becomes much more complicated since the charger could be connected many different system. In other words, the inductance connecting vehicle to grid could vary drastically and it means a variable resonance frequency. In such cases, traditional passive damping could not be very beneficial. However, this problem was previously reported in 3-phase system when reconfiguration could lead to variable grid inductance and many solutions have been already investigated. Reference [142] employs one of them which is based on active resonance damping. In this method, a virtual resistor is considered in series with the capacitor to damp the resonance without physical power losses. On the other hand, its virtual nature allows the realization of an adaptive control system.

Another aspect investigated in the literature is related to impacts of PHEVs on the power stability. Reference [38] shows how simultaneous changes of PHEVs in a system could impact the power stability. Though it has pointed out an important issue, many oversimplifications has been made, which affect the accuracy of the results.

It is worth to mention that PHEVs could make serious issues for power system operation, power quality and stability. Meanwhile some researchers try to prove the benefits of employing PHEVs, some others are still trying to mitigate their undesired impacts. A realistic and general picture of PHEVs needs to consider all these aspects.

2.2.3 Vehicle-to-Grid: An Opportunity

These controllable loads could be employed for peak shaving and load leveling. On the other hand, they could be utilized to absorb the extra generation of unpredictable undispatchable renewable resources and inject this energy back when there is a shortage [139]. The utilization of PHEVs to improve the voltage and frequency stability is another aspect which gained attention. However, PHEVs are owned by customers, not utilities, and their storage devices should be charged to some acceptable levels before unplugging. These facts can be assumed as some of the most important challenges for PHEVs utilization as sources of active power. A coordinated control necessitates communication which could result in huge cost by considering the distributed nature of these resources [139]. These challenges should be considered in any proposed utilization of PHEVs for improving power system performance, otherwise the practicality will be lost.

2.2.3.1 Frequency Regulation

Using PHEVs to enhance the frequency, especially with high penetration of these resources and existence of fluctuating renewable resources, was one of the main ideas investigated in the literature in recent years [63, 143, 144, 145]. To contribute to frequency regulation and also eliminate one of the main barriers, the communication cost, researchers preferred to use one of the most famous concepts in power systems, droop control. As explained previously, the droop method has been employed for a long time in conventional generator governor and has been examined in 3-phase distributed generators (DGs). Therefore, the droop equations similar to (2-1) are adopted, where K_{V2G} is the droop gain, P_{V2G} is the vehicle power injected to the grid, and P_{max} is the limitation imposed on the injected power.

$$P_{V2G} = \begin{cases} K_{V2G}\Delta f & |P_{V2G}| \le P_{max} \\ \pm P_{max} & |P_{V2G}| > P_{max} \end{cases}. \quad (2\text{-}1)$$

However, another important challenge still exists. The utility does not own the PHEV energy storage and it could not be charged and discharged deliberately. To solve this problem, [143] proposed that K_{V2G} can be changed based on the SOC of battery to prevent any over-charging and -discharging and guarantee an acceptable average SOC. Figure 2-4(a) reveals the main idea. Obviously, when the battery is close to the maximum SOC, the PHEVs charging droop factor is very low which means that vehicle avoids overcharging due to extra absorption. On the other hand, discharging droop factor is close to its maximum. The other interesting suggestion by [143] is shown in Figure 2-4(b). This study discusses the situation in which vehicle prefers not to inject the active power to the system, and proposes that the vehicle can still incorporate in frequency regulation by switching to the "*Smart Charging*" mode, shown by red line in the figure.

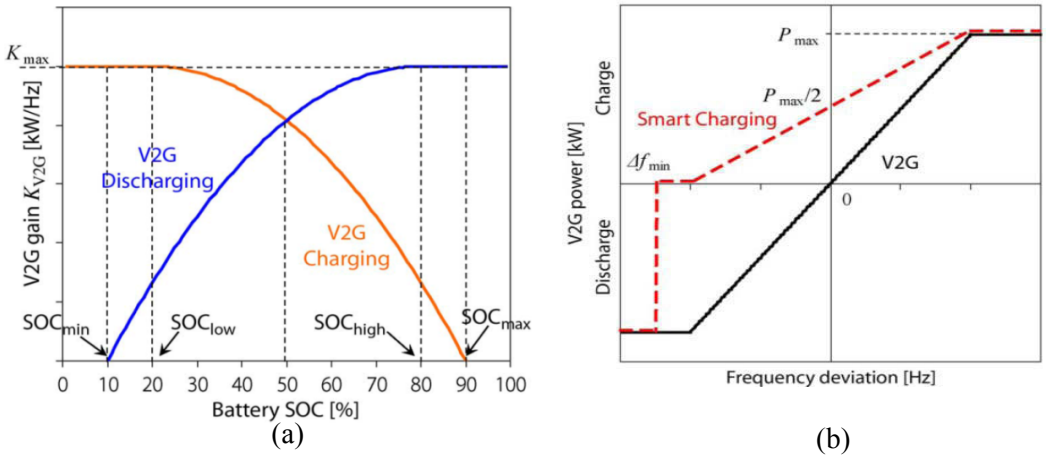

Figure 2-4 (a) Controlling droop factor (K_{V2G}) based on the battery SOC, (b) Smart Charging as an alternative for conventional V2G when vehicle owner prefer to stay longer in the charging mode [143].

They were some deficiencies in this study as well. They have considered only the case when the average SOC should remain close to half. Several efforts have been made to improve the method. One of the first efforts tried to solve the problem mentioned above is reported in [63]. Moving the average point of SOC is important especially in a case that vehicle has entered the parking with SOC greater than 50%. It seems obvious that the owner does not expect to leave the parking with a lower SOC. To move the average point in Figure 2-4(a), four new parameters (SOC_{min}, SOC_{low}, SOC_{high}, SOC_{max}) should be provided. It means for any working point, at least four parameters should be stored in a database for

each PHEV. To improve the smart charging mode, the expected leaving time of the vehicle should be known to find the average power, P_i^c, to assure enough charging. This additional information was used to modify the smart charging. In fact, in addition to limiting the vehicle to charging mode, a dc-bias, P_i^c is used and claimed that it is more useful. However, this method needs more information from the vehicle owner.

In [144], the same linearized model used in [63] and [143] was adopted to address the effect of uncertainties associated with wind power, load and even PHEVs on system frequency dynamics. Therefore, load frequency control (LFC) models of thermal power plants were used to cope with these uncertainties. The interesting part in this work is implementation of a robust control method, where a conventional LFC block is used for control design. Robust analysis was used to tune PI parameters of LFC so that system remains robust.

Reference [145] accepted the significant impact of the droop-based method but it questioned some other aspect of this method. The droop method is very common in power systems because of avoiding the cost of communication while in this method each PHEV needs one frequency sensor which in total is not much cheaper than communication. In addition, each sensor has some errors and noises that without any communication could not be mitigated easily. Therefore, it tried to use the same droop method but instead of one sensor for each PHEV benefits from several sensors in the whole power system which transmit the frequency information to PHEVs. In fact, the main focus of this paper was more on constructing and analyzing the communication system. They have shown that the proposed method is robust against noises and even delays.

All of the aforementioned research works have tried to have a macro or system-level perspective and use large number of vehicles in the adopted models. Further, only droop-based methods are employed to incorporate PHEVs in primary frequency control.

Other researchers paid attention to the dispersed and distributed nature of these resources, which necessitates some communication among them [146, 147, 148]. Furthermore, the possibility of asymmetrical contributions to the power system was investigated [149].

Because of these limits, PHEVs are considered as part of larger solutions in many studies, such as [150, 151, 152]. They can be an effective choice to complement the dynamic characteristics of wind generators and facilitate effective participation of wind generators in primary frequency regulation. Implementing frequency regulation methods in wind generator may have some adverse impacts on the mechanical resonance, wear and tear and aging of wind generators [153, 154, 155]. Due to the importance of incorporating wind generators in the power system frequency regulation, the utilization of some other sources in combination with wind generators to mitigate the undesired side-effects was also proposed. These methods, however, used ineffective cost choices, i.e., large energy storage units, or weak components, i.e., the generator dc-link capacitance. Other hybrid solutions available in the literature, such as [156, 157, 158, 159, 160], did not even consider the wear and tear of wind generators.

2.3 Summary

In this chapter, a critical literature survey on the utilization of wind generators and electric vehicles for enhancement of weak grids performance has been presented. The main outcome of this chapter is to pinpoint the lack of thorough analyses of barriers and adverse impacts of employing these sources in existing literature. Accordingly, developing a detailed modeling and proposing solutions for the wind power generators and electric vehicles that overcome the aforementioned difficulties demand a special attention.

Chapter 3
Frequency Regulation in Wind Turbines – Analysis and New Methods

3.1 Introduction

Wind power will provide a significant portion of electricity generation in the near future. This important role requires wind power generators to contribute to the system frequency regulation. Moreover, the use of wind generators for autonomous frequency regulation is becoming an essential objective in power grids with reduced inertia and isolated microgrid operation. The droop method is one of the most popular methods to be implemented in these generators to mimic the governors of conventional generators and contribute to primary frequency regulation. While droop-control is studied by many researchers, detailed analysis of droop-controlled wind generators in microgrids has not been reported.

In this chapter, the conventional wind-based droop methods are studied. Thorough analyses are employed to demonstrate the methods' effectiveness. It is also shown that the employment of conventional power droop in non-dispatchable wind power generation could result in problems which could not be observed and even discussed in conventional dispatchable distributed generation (DG) units. This chapter proposes a new solution which allows the droop gain to be tuned regardless of the unpredictable variable wind speed. The role of the proposed method in the both transient and steady-state frequency control is investigated and discussed.

The contributions of this chapter to the field are the following:

1) Developing a small-signal model for the present wind droop methods (power- and torque-droop) in DFIG-based wind generators. The models are used for comparative analysis and sensitivity studies.

2) Investigating the impact of wind-droop on microgrid frequency stability by eigen-values studies, and comparing the impact of wind-droop to real inertia. Providing a

systematic approach to coordinate wind-droop with other energy sources available in a typical microgrid system (e.g. inverter- and turbine-based generators).

3) Examining stand-alone operation of wind generation (without any dispatchable sources) in a microgrid with real wind speed pattern.

4) Proposing a new frequency regulation for wind generators in order to resolve the stability issues of variable deloaded reserve power;

5) Analyzing the impact of the proposed method on the transient and steady-state behaviors of the frequency dynamics, and comparing the stability and performance of the proposed method to those of the two famous present ones, the power and torque droop methods.

This chapter is organized as follows. The modeling is described in Section 3.2. In Section 3.3, implementation of the conventional droop methods, their performance and impacts on system stability are discussed. The proposed solution and its detailed analyses are discussed in the next section. Section 3.5 presents comprehensive simulation results to validate analytical results. Finally, conclusions are drawn in Section 3.6.

3.2 Modeling

Figure 3-1 shows a DFIG-based wind power generator with interactive control for stiff-grid-connected and weak/microgrid operation modes. The DFIG system is not required to contribute to voltage regulation when the generator is connected to a stiff grid. In this mode, the DFIG is controlled to work at unity power factor. On the contrary, in islanding or weak grid mode the DFIG is forced to control its terminal voltage via the rotor-side converter (RSC) whereas the grid-side converter is controlled to operate at unity power factor to minimize the converter rating. The terminal voltage controller generates the reference reactive current component. More details on DFIG control structures can be found in [47, 161].

During connection to a stiff grid, a DFIG is controlled to extract the maximum available power/torque, and it does not incorporate in frequency/active power regulation. On the

contrary, in the islanding/weak grid mode, it switches to the droop control, which is usually realized by torque-droop or power droop. The reference torque is used to generate the reference active current component. Conventional proportional-integral (PI) controllers are used to control the RSC currents. To incorporate wind in microgrid frequency regulation and implement droop, enough reserve power should be considered in wind power generation.

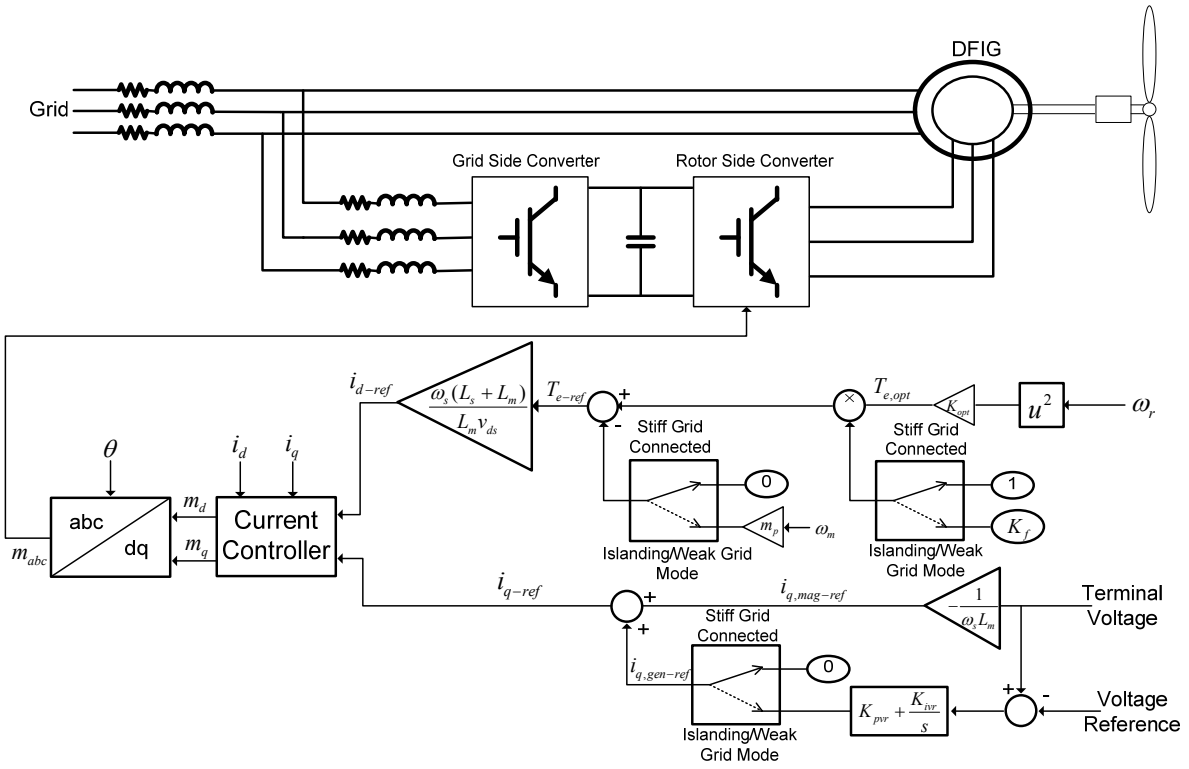

Figure 3-1 DFIG-based wind power generator with interactive control for stiff-grid connected and weak/microgrid operation modes

Following the tradition of power system stability studies, the primary frequency regulation behavior can be studied in the two modes of *steady-state* and *transient* [162]. As mentioned, the main problem in implementing a frequency droop in the wind generator is the lack of a constant reserve power. The needed power can be obtained by deloading; however, the amount of this power is a function of the unpredictable variable wind speed.

3.2.1 Conventional Generation: Maximum Power Extraction

The energy extracted by a wind turbine can be described by (3-1), where the wind speed is represented by v_w, the air density by ρ, and the area covered by the turbine blades by A_r. In

[90], C_p is called the efficiency coefficient, which is a function of two other parameters: β, referring to the pitch angle of the turbine blades, and λ, known as the tip speed ratio, formulated in (3-2). R and ω_r denote the blade radius and the rotational speed of the turbine, respectively. C_p is introduced in (3-3), and its parameters are given in the Appendix A, and the λ_i is presented in (3-4) [163]. Obviously, C_p is highly nonlinear so that some references, such as [55], preferred to estimate it. However, this study remains committed to using the original equation shown in (3-3).

$$P_m = C_p(\lambda, \beta)0.5\rho A_r v_w^3. \tag{3-1}$$

$$\lambda = R\omega_r / v_w. \tag{3-2}$$

$$C_P(\lambda, \beta) = c_1(\frac{c_2}{\lambda_i} - c_3\beta - c_4)e^{-\frac{c_5}{\lambda_i}} + c_6\lambda, \tag{3-3}$$

$$\frac{1}{\lambda_i} = \frac{1}{\lambda + 0.08\beta} - \frac{0.035}{1+\beta^3}. \tag{3-4}$$

In conventional wind generators, the controller regulates the turbine so that it eventually extracts the maximum available power at any wind speed. In other words, the desired rotational speed of the wind turbine makes the derivative of the wind power in respect to the turbine speed ($dP_m/d\omega_r$) zero. At an arbitrary wind speed, but not sufficient to activate the pitch angle controller, this derivative can be represented as shown in (3-5). In the last part of this equation, $d\lambda/d\omega_r$ is replaced by R/V_{w0}. The "0" subscript denotes the initial equilibrium point around which the turbine performance is studied. The final result shows that to achieve the maximum power extraction, a special tip speed ratio, λ_{opt}, is needed regardless of the wind speed. For this reason, some controllers prefer to regulate the tip speed ratio instead of the rotational speed of the turbine [164].

$$\frac{\partial P_m}{\partial \omega_r}|_{V_{w0}} = K_p V_{w0}^3 \frac{\partial C_p}{\partial \lambda}.\frac{\partial \lambda}{\partial \omega_r} = K_p R V_{w0}^2 \frac{\partial C_p(\lambda, 0)}{\partial \lambda}. \tag{3-5}$$

The constant amount of the tip speed ratio needed to maximize the wind power extraction means that the optimal rotational speed and the maximum available power are the linear and 3rd-degree functions of the wind speed, respectively, as long as the pitch angle controller is not active. These equivalences are formulated in (3-6):

$$\omega_{r,opt} = \frac{\lambda_{opt}}{R} v_w \Rightarrow P_{opt} = K_{vopt} v_w^{\ 3} = K_{wopt} \omega_r^{\ 3}. \tag{3-6}$$

3.2.2 Reserve Energy: Deloading

As discussed, deloading is implemented differently. In some methods, the optimal power derived in (3-6) is simply multiplied by a deloading factor, K_{vf}. Figure 3-2(a) shows the result of this method. To find the new operating point, (3-7) should be solved. Obviously, the answer is dependent only on the tip speed ratio and is independent of the wind speed. In other words, once more for a constant deloading factor, there is a constant tip speed ratio, λ_{del}, independent of the wind speed. Figure 3-2 (b) demonstrates this phenomenon. As discussed in [74] and [76], any under-speed deloading, which yields an operating speed lower than the optimal value, should be avoided.

$$P_m - P_{deloaded} = 0.5 \rho A_r C_p(\lambda, 0) v_w^{\ 3} - K_{vf} K_{vopt} v_w^{\ 3} = 0. \tag{3-7}$$

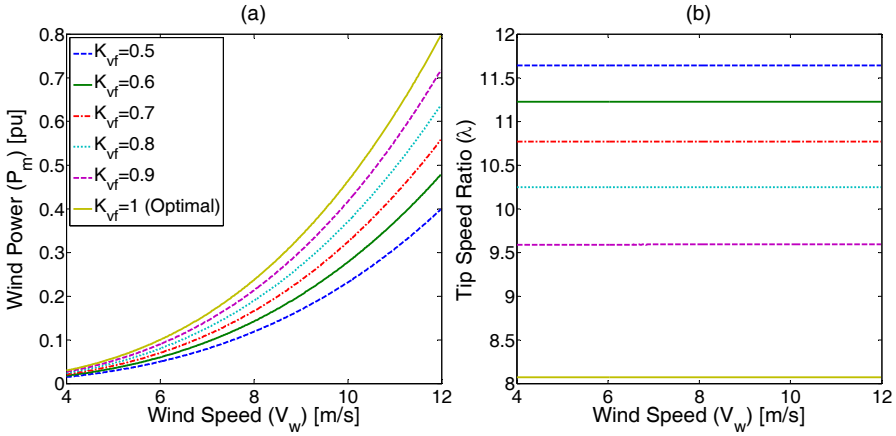

Figure 3-2 Optimal and deloaded wind generator; (a) the output power, (b) the tip speed ratio.

Similar to (3-4), here the relation of the desired rotational speed of the turbine and the wind speed is linear. As a result, the new operating point can also be described with ω_r as in (3-8). This equation is important because it proves that deloading by using either the wind speed measurement (such as in [52]) or the power/torque control (such as in [51]) leads to the same results, although the former, as discussed, requires some practical constraints to be implemented. Figure 3-3 shows the relation of K_{vf} and K_{wf}, which results in the same amount of deloading. Turbines rotate faster with a lower deloading factor at the same wind speed. This phenomenon can be understood by using Figure 3-2(b), which shows the tip speed ratio.

This higher rotating speed explains why K_{wf} is not equal to K_{vf} for the same amount of deloading in the turbine output power.

$$\omega_{r,del} = \frac{\lambda_{del}}{R} v_w \Rightarrow P_{deloaded} = K_{vf} K_{vopt} v_w^{\ 3} = K_{wf} K_{wopt} \omega_r^{\ 3}. \tag{3-8}$$

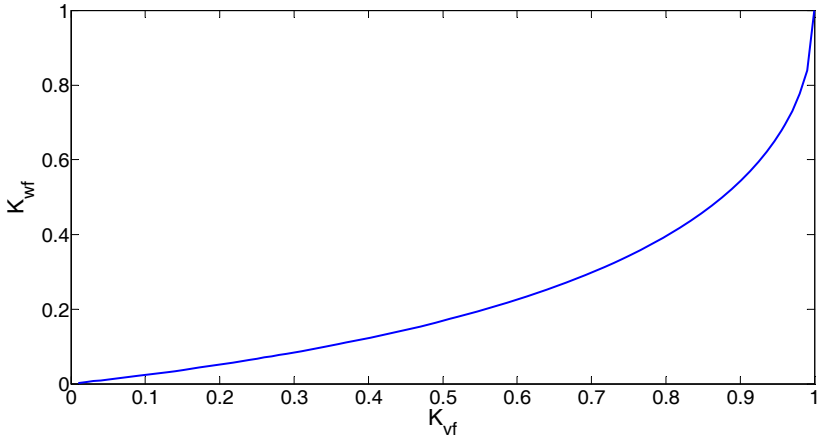

Figure 3-3 Relation between deloading factors using wind speed measurement and power/torque controller.

This equation also reveals that the reserved power obtained by deloading is changed drastically by changes in wind speeds. Such a reliance on the unpredictable variable wind speed can threaten the system stability and will be discussed later.

3.2.3 Wind Based Frequency Regulation

To provide the complete picture of the problems involved in implementing wind-based frequency regulators, the frequency regulation method should also be considered. Equation (3-9) represents the behavior of the mechanical part of the wind generator, assuming a single rotational mass [90]. P_e is the electrical output power of the generator, and H_{DFIG} is the inertia constant of the generator:

$$P_m - P_e = 2H_{DFIG} \omega_r d\omega_r / dt. \tag{3-9}$$

Reference [51] has shown that in frequency stability analyses, the dynamics of the generator's electrical part is fast enough to be ignored. Consequently, the desired and actual output electrical power can be assumed to be equal. Equation (3-10) represents the desired output power of the wind generator. The first term on the right side of the equation is derived from (3-8), and P_{reg} refers to the active power injected/absorbed by the generator to regulate the system frequency.

$$P_e = K_{wf} K_{wopt} \omega_r^{\,3} + P_{reg}. \tag{3-10}$$

Equations (3-10) and (3-1) can be substituted in (3-9) to continue the modeling. Some of the wind power generator equations are highly nonlinear. There is a long history of using linearization and small-signal analyses for investigating wind generator stability in the literature including [50, 165] and [166]. To cope with the nonlinear nature of a wind generator, its performance at different (initial) operation points is studied. To linearize (3-1), new parameters are introduced in (3-11)-(3-14). Because the pitch angle controller is not activated, the first term ($A_1.\Delta\beta$) in the right-hand side of (3-11) can be neglected.

$$\Delta P_m = A_1.\Delta\beta + A_2.\Delta\omega_r + A_3.\Delta v_w. \tag{3-11}$$

$$A_1 = \partial P_m / \partial\beta = 0.5\rho A_r V_{w0}^{\,3} \partial C_P / \partial\beta. \tag{3-12}$$

$$A_2 = \partial P_m / \partial\omega_r = 0.5\rho A_r V_{w0}^{\,3} (\partial C_P / \partial\lambda).(\partial\lambda / \partial\omega_r). \tag{3-13}$$

$$A_3 = \frac{\partial P_m}{\partial v_w} = 0.5\rho A_r \left(3C_P V_{w0}^{\,2} + V_{w0}^{\,3} \frac{\partial C_P}{\partial\lambda}.\frac{\partial\lambda}{\partial v_w}\right). \tag{3-14}$$

After replacing the linearized forms and doing some calculations, the output power of the generator can be formulated as (3-15). "*s*" is the Laplace operator. The intermediate calculations are not included in this chapter. The first term in (3-15) shows how the wind generator reacts to the changes in the wind speed, and the second term represents the response of the generator to the desired frequency regulation power.

$$\Delta P_e = \frac{3K_{wf}K_{wopt}\omega_{r0}^{\,2}A_3}{2H_{DFIG}\omega_{r0}s + 3K_{wf}K_{wopt}\omega_{r0}^{\,2} - A_2}\Delta v_w + \frac{2H_{DFIG}\omega_{r0}s - A_2}{2H_{DFIG}\omega_{r0}s + 3K_{wf}K_{wopt}\omega_{r0}^{\,2} - A_2}\Delta P_{reg}. \tag{3-15}$$

The contribution of the wind generator to the steady-state frequency regulation can be determined by deriving the steady-state response of the wind generator to ΔP_{reg}. The subscript "*ss*" represents the steady-state response. As (3-16) reveals, the response seems to depend on the desired steady-state regulation power as well as the operating point of the generator before the disturbance. A_2, which represents the partial derivative of the turbine input power in relation to the turbine rotating speed, needs to be discussed.

$$\Delta P_{e.ss} = \lim_{s\to 0} s\Delta P_e = \frac{-A_2}{3K_{wf}K_{wopt}\omega_{r0}^{\,2} - A_2}\lim_{s\to 0} s\Delta P_{reg}. \tag{3-16}$$

Given that the wind generator works at a constant tip speed ratio as long as the deloading factor remains unchanged, $d\Delta C_p/d\Delta\lambda$ is constant for different wind speeds. As a result, A_2 is a quadratic function of the initial wind speed. Moreover, (3-8) shows that the relation between the turbine rotational speed and the wind speed is linear so that A_2 can also be formulated as a quadratic function of the turbine rotating speed. The coefficient a_2 is a function of the deloading factor. Figure 3-4 shows these relations graphically.

$$A_2 = 0.5\rho A_r R V_{w0}{}^2 \frac{\partial \Delta C_P}{\partial \Delta\lambda}\Big|_{\lambda = \lambda_{del}} = a_2 \omega_{r0}{}^2. \tag{3-17}$$

Substituting (3-17) in (3-16) leads to the derivation of (3-18), which provides a much clearer picture of the relation of the wind power steady-state response to the frequency regulation active power command. Despite the misunderstanding that (3-16) might cause, the final response of the wind generator does not depend on the initial wind speed. Instead, this response depends only on the deloading factor, and trivially, the steady-state commanded active power.

$$\Delta P_{e.ss} = \frac{-a_2 \omega_0{}^2}{3K_{wf}K_{wopt}\omega_0{}^2 - a_2\omega_0{}^2}\Delta P_{reg,ss} = \frac{-a_2}{3K_{wf}K_{wopt} - a_2}\Delta P_{reg,ss}. \tag{3-18}$$

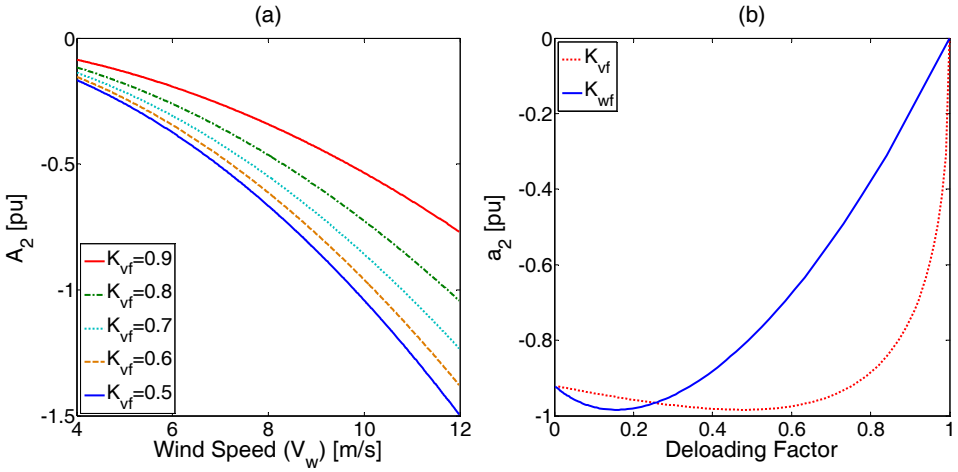

Figure 3-4 Dependence of the rotational speed coefficient of wind power on (a) wind speed, (b) deloading factor

3.3 Present Droop Methods

3.3.1 Steady-State Performance

The main problem in implementing a droop in wind generators can now be understood completely. With a conventional droop used as P_{reg}, as described by (3-19), the wind generator tries to inject/absorb the same amount of power for the same amount of frequency deviation, regardless of the wind speed, as long as the deloading factor is constant. However, the amount of energy reserved for injecting changes with the cube of the wind speed, as revealed in (3-20). m_p, ω_m and τ represent the droop gain, system frequency and droop time constant, respectively. The superscript "*" refers to the nominal value.

$$P_{reg} = P_{PoDr} = \frac{m_p}{1+\tau s}(\omega_m^{*} - \omega_m). \tag{3-19}$$

$$P_{reserve} = (1-K_{vf})K_{vopt}V_{w0}^{3}. \tag{3-20}$$

Tuning the droop gain for a high wind speed may make the system unstable, whereas choosing the droop gain based on low wind speeds is too conservative.

If the regulation power command is forced to be a function of the wind speed itself, the problem may be mitigated. Reference [167] recommends such a solution based on trial and error. Without explaining why, [76] used the same idea to implement the droop in the generator torque instead of the power, where P_{reg} is described by (3-21). A closer look will indicate that (3-21) is basically very similar to (3-19) multiplied by the rotating speed of the wind generator. This difference can be justified by the relation of the torque and power, in which $P=T\omega$, and the fact that this time the droop is implemented in the generator torque instead of the power. This equation can be substituted in (3-18) to find the response of the generator in the steady-state. The result of the torque-droop is shown in (3-22). Obviously, the effective droop gain, $a_2\omega_{r0}m_p/(3K_{wf}K_{wopt}-a_2)$, differs from the tuned one, m_p.

$$P_{reg} = P_{TrDr} = \omega_r m_p \frac{(\omega_m^{*} - \omega_m)}{1+\tau s}. \tag{3-21}$$

$$\Delta P_{e-TrDr,ss} = \frac{a_2\omega_{r0}}{3K_{wf}K_{wopt} - a_2} m_p \Delta\omega_{m,ss}. \tag{3-22}$$

The maximum power that $\Delta P_{e\text{-}TrDr,ss}$ can gain is the reserve power represented in (3-18). Because more power injection is not possible, it is reasonable to tune the droop gain so that it happens in the maximum frequency deviation. This method can be used to find the maximum allowable droop gain. This index was previously used in conventional dispatchable distributed generators [168]. However, in the original application, the effective and actual droop gains are the same, whereas in the wind-based droop, they are different. Moreover, the reserved power is also variable here. The maximum allowable droop gain for the torque-droop is formulated in (3-23). Whereas K_{wopt}, K_{vopt}, R and $\Delta\omega_{m,max}$ are constant, K_{wf}, a_2 and λ_{del} are functions of the deloading factor, K_{vf}. In other words, the maximum allowable torque-droop-gain is a function of the wind speed and deloading factor.

$$m_{p-TrDr,\max} = \left| \frac{(3K_{wf}K_{wopt} - a_2)(1-K_{vf})K_{vopt}\lambda_{del}}{a_2 R\Delta\omega_{m,\max}} \right| {V_{w0}}^2. \tag{3-23}$$

The same reasoning can be used to find the maximum allowable gain for the power-droop, as shown in (3-24). Whereas the power-droop is also a function of both the deloading factor and the wind speed, this droop shows more sensitivity to wind speed changes where their relation is the third degree.

$$m_{p-PoDr,\max} = \left| \frac{(3K_{wf}K_{wopt} - a_2)(1-K_{vf})K_{vopt}}{a_2\Delta\omega_{m,\max}} \right| {V_{w0}}^3. \tag{3-24}$$

The effective droop factors $m_{eff,TrDr}$ and $m_{eff,PoDr}$ are introduced in (3-25)- (3-26), for torque- and power-droop methods, respectively. Equations (3-25) and (3-26) indicate that several unconventional factors impact power/frequency regulation and may result in deviation of the effective droop factor from its expected constant value, m_p.

$$m_{eff,TrDr} = m_p.K_{eff,TrDr} = m_p. - \frac{\omega_{r0}a_2}{3K_{wopt}K_{wf} - a_2} \tag{3-25}$$

$$m_{eff,PoDr} = m_p.K_{eff,PoDr} = m_p. - \frac{a_2}{3K_{wopt}K_{wf} - a_2}. \tag{3-26}$$

Figure 3-5 shows the effective droop factor versus wind speed considering different deloading factors. This figure reveals why the lower than unity K_{wf} should be chosen even if a larger than unity one also results in deviation from maximum power tracking point. In fact, a higher than unity K_{wf} leads to a negative effective droop factor which works as a positive

feedback for power/frequency regulation and is highly undesirable. While some references, such as [51, 52, 74], previously advised to avoid higher than one K_{wf}, the reason behind this criterion is neither given nor quantified by analysis.

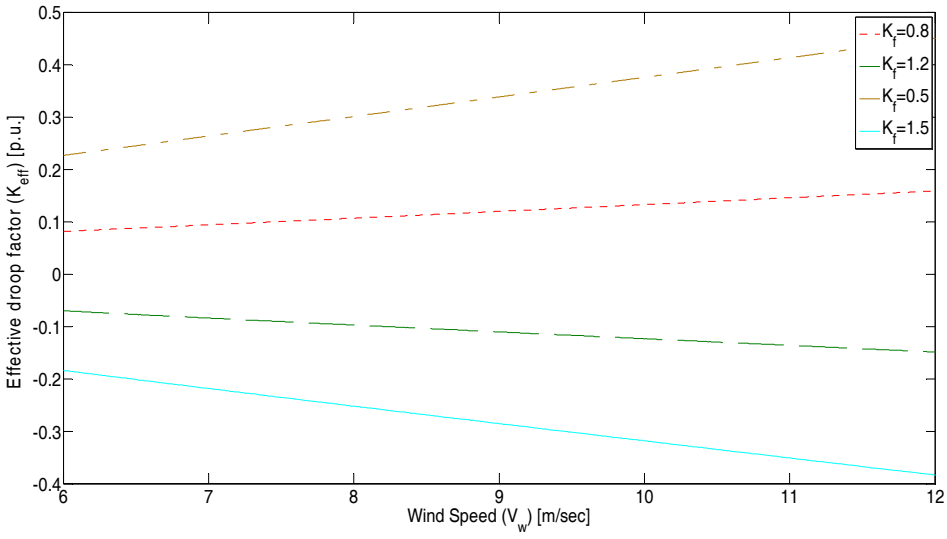

Figure 3-5 Effective droop factor, $K_{eff,TrDr}$, versus wind speed, V_w.

3.3.2 Transient Performance

The "$2H_{DFIG}\omega_{r0}s$" term in the numerator of (3-15) resembles inertial response; and questions may be asked about the effects of these terms. Figure 3-6 depicts the magnitude response of (3-15), when P_{reg} is substituted with P_{TrDr}. As shown, in the medium-frequency range, it emulates a physical inertia but it is not a wide or even constant range as it depends on wind speed. On the contrary, the major impact of a real inertia is in the high-frequency range, equivalently right after a power disturbance. Although this term is not going to act exactly as inertia, it seems to be useful in overall system stability, which will be discussed in more details. This resemblance could also explain why in references, such as [47], the wind-droop method is utilized merely for short-term power/frequency regulation and how it influences the system transient stability. On the other hand, the droop method is generally recognized for its positive impact in steady-state conditions. The explanation, which is absent in those references, is due to lack of detailed analysis.

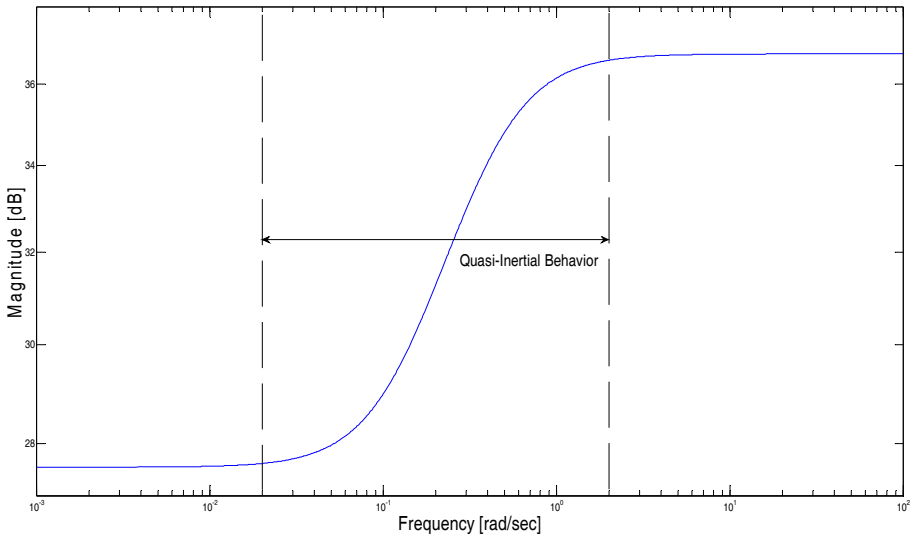

Figure 3-6 Magnitude response of wind output power dynamics with droop control.

For further investigations, a typical medium-voltage rural distribution system, a real system in Ontario, Canada, shown in Figure 3-7, is adopted. The segment after the circuit breaker B2 has the ability to work in islanded mode and constitutes the microgrid. The overall load of this section is 3.77MW/1.24MVAr. It contains two DG units. DG1 is a variable-speed wind turbine connected to a 2.5MVA DFIG with its rotor interfaced by back-to-back converters. DG2 is a 2.5MVA synchronous generator with droop and excitation control systems. System parameters are given in Appendices. The stability analysis could be extended to larger microgrid or weak grids which suffer from reduced inertia.

The wind generation model presented in the last section can be combined with the gas turbine generator model to form the overall frequency dynamics model of the system [162] as shown in Figure 3-8, where $H_1(s)$ and $H_2(s)$ can be obtained from (3-15) depending on the droop-method used. This model can be effectively used to show how wind droop could impact the frequency stability.

Figure 3-9 shows the root-locus of system dominant poles when m_p, the wind torque-droop factor, is increased. In addition to its expected positive impact on the steady-state response, poles move toward the left-half-plane which implies enhancement in system dynamic performance. It should be noted that for other wind speeds and power-droop, similar pattern was observed. It is worthy to mention that m_p could not be increased more than the maximum

calculated in (3-23). Figure 3-10 shows the impact of K_{wf} and initial system frequency on the torque-droop behavior. As shown, their influence could be neglected even if the parameters (K_{wf} and initial system frequency) are varied in relatively wide ranges. In fact, it should concluded here, especially with consideration of the results of Figure 3-2, what limits the deloading factor is not a dynamic concern but it is both economic reasons and the risk of high rotational speed of DFIG. The effect of the high rotational speed will be discussed later.

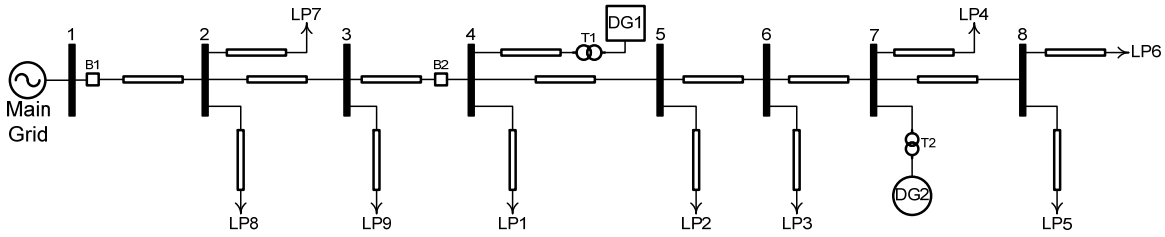

Figure 3-7 System under study.

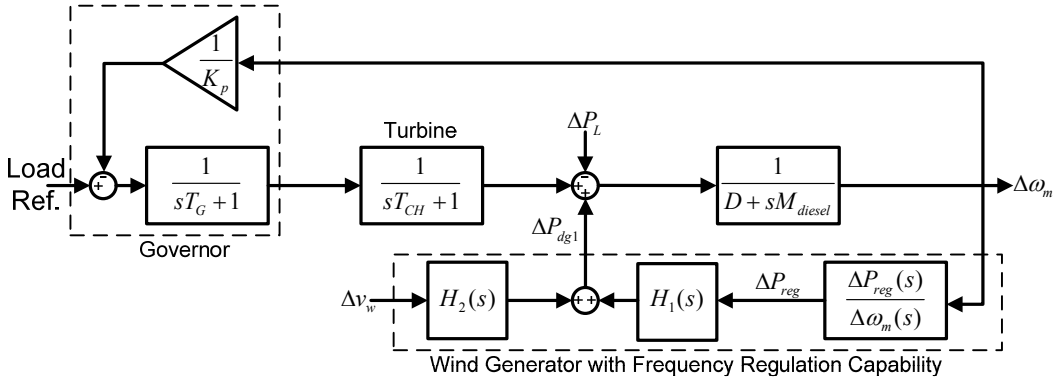

Figure 3-8 Block diagram representation of system dynamics.

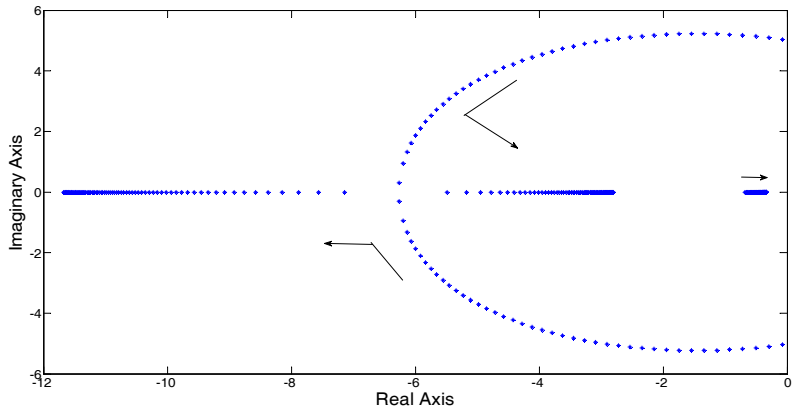

Figure 3-9 Root-locus of the system dominant poles when m_p is increasing from zero to 80p.u.

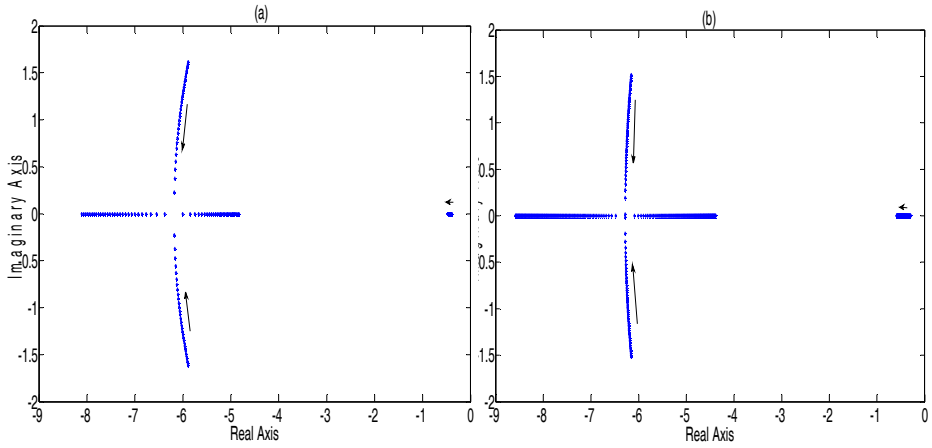

Figure 3-10 Root-locus of the system dominant poles at V_w=12m/s and m_p =40 (a) K_{wf} is decreasing from 1 to 0.4p.u. and (b) Initial (equilibrium point) frequency is increasing from 59.4 to 60.6Hz.

The small-signal model could be also employed to investigate the quasi-inertial characteristics of wind droop. To compare with a real inertia, the impact of increasing gas turbine generator inertia, M_{diesel}, is also studied. Figure 3-11 shows the overshoot for both cases. Obviously, both diagrams have similar trends and even lower overshoots are more achievable with wind droop than increased inertia. In other words, to decrease overshoots to some desirable values (around 5%), the turbine inertia should be increased ten times, while similar overshoot with reasonable wind-droop factor is possible. However, it does not mean that the real inertia in the system could be replaced by wind droop. Figure 3-12 shows one of the most important reasons. While inertia decreases the maximum *df/dt*, the wind droop has no impact. *df/dt* as an useful and meaningful measurement of frequency stability improvement is used here, especially that many protection relays operate based on frequency derivative measurement. This phenomenon could be explained by Figure 3-6 which previously showed that the wind droop does not behave as inertia in the very high-frequency region, equivalently right after the disturbance and when the maximum rate of change of frequency (ROCOF) occurs. In other words, wind-droop cannot be considered as substitution of real inertia for compensating high *df/dt*. However, it should not be misunderstood that wind droop has no impact on ROCOF entirely. Figure 3-13 reveals the considerable impact of wind droop on the rise-time of system frequency which implies lowering the ROCOF in

general. It could be concluded that system inertia could be helped by wind-droop in the medium-frequency range.

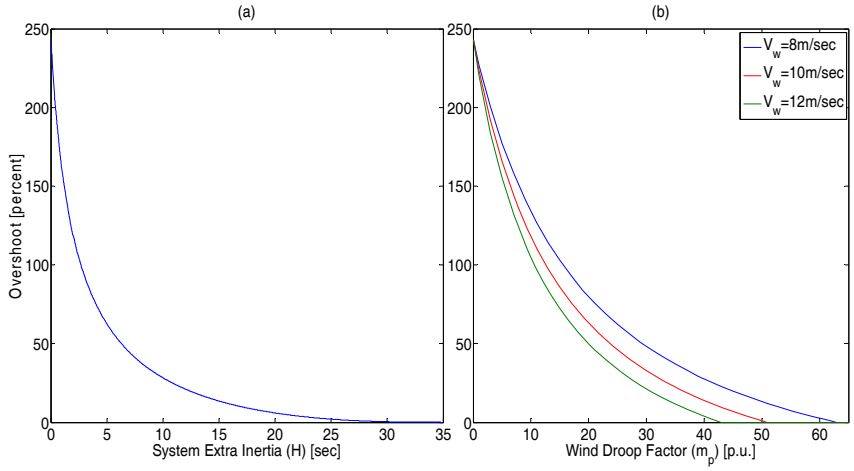

Figure 3-11 Overshoot of the system frequency in case of a load step disturbance versus (a) extra inertia and (b) wind power droop.

3.3.3 Interactions and Coordination with Other Units

Although it seems that the wind-droop (both torque- and power-droop methods) solely has positive impact on system performance, its interactions with other system units, e.g. turbine and inverter-based DG units could be a concern. Further, interactions with the pitch-angle controller should be investigated.

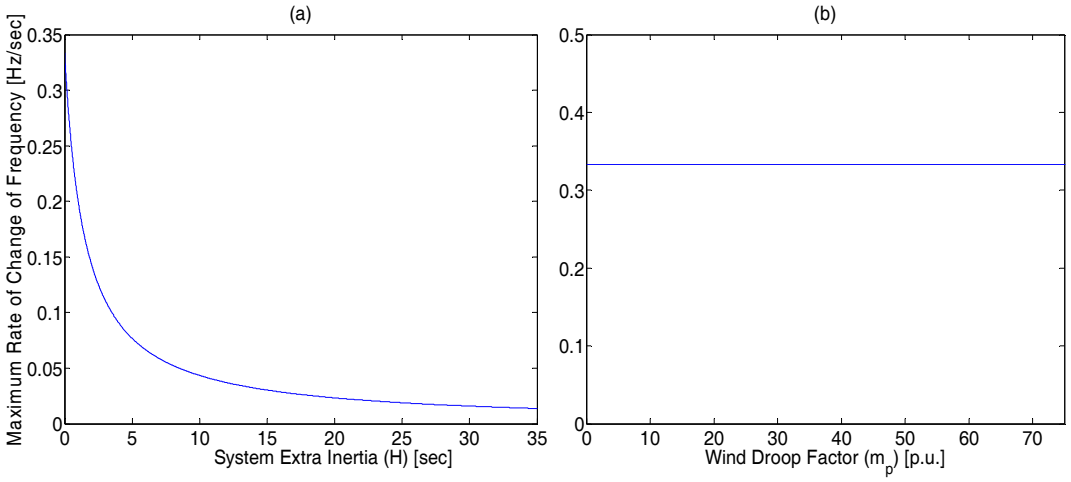

Figure 3-12 Maximum ROCOF of the system frequency in case of a load step disturbance versus (a) Extra inertia and (b) Wind power droop.

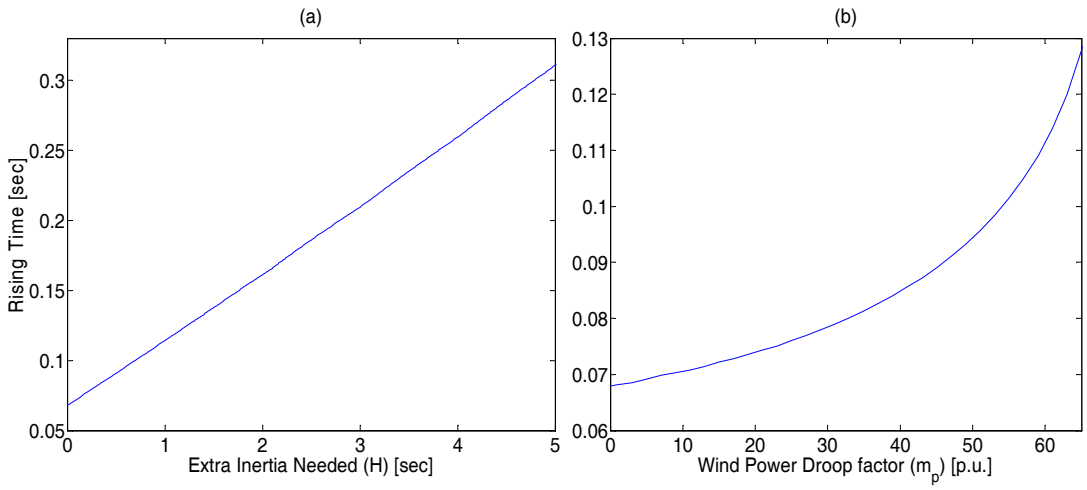

Figure 3-13 Rise-time of the system frequency in case of a load step disturbance (a) With extra inertia and (b) With wind power droop.

3.3.3.1 Gas Turbine

Gas turbine, as the other source and only dispatchable source in this case-study, plays an important role in both dynamic and static system behavior. Its governor, which is responsible for frequency regulation, is also equipped with droop, similar to (3-27). In order to have a better frequency regulation and lower deviation, it is desired to have a lower K_p. Blue poles in Figure 3-14 represent the root-locus of the system dominant poles in absence of wind droop. It shows the trade-off between steady-state performance and dynamic stability. Eventually, instability (Hopf bifurcation) can be yielded with inappropriate selection/coordination of droop gains. It should be noted that variable droop operation is required in order to optimize the economic aspects of microgrids. On the other hand, the red locus shows the system poles trend in presence of wind droop. Therefore, wind droop improves the steady-state frequency regulation not only by its direct contribution to frequency dynamics but also by allowing turbine to have lower K_p (i.e. increases the possible coordination range of system parameters).

$$P = P_n - \frac{(\omega_m^* - \omega_m)}{K_p}. \tag{3-27}$$

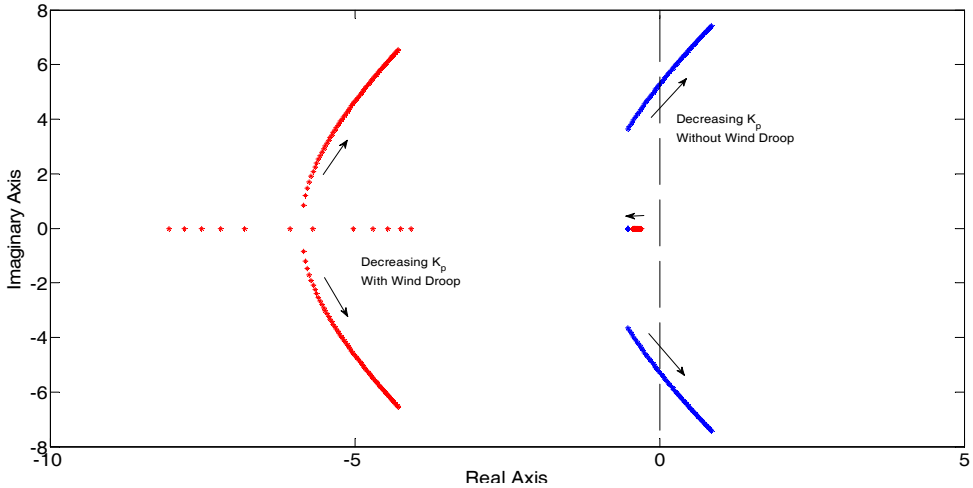

Figure 3-14 Root-Locus of the system dominant poles at V_w=12m/s and m_p=40 when K_p is decreasing in presence (red poles) and absence (blue poles) of wind droop.

3.3.3.2 Inverter

Nowadays, many DG units are inverter-interfaced and this may lead to interactions between wind-droop and inverter-based droop units. To investigate this scenario, first of all, the inverter model should be added. Previously, [60] and [168] have shown that with well-tuned control parameters, an inverter could be represented by a power-controller block in frequency dynamics studies. Thus, a transfer function, based on (3-28), should be fed-back to the input of the turbine inertia block. In (3-28), P_{inv}, and m_{inv} are the power and droop gain of the of the inverter-based DG unit, respectively; and τ_{inv} is the time-constant of the equivalent low-pass filter model of the inverter dynamics (mainly due to the low-pass filter applied to extract the average power, and inner control loop dynamics).

$$\Delta P_{inv} = -\frac{m_{inv}}{\tau_{inv}s+1}\Delta\omega_m \quad (3\text{-}28)$$

Figure 3-15 depicts the impact of lowering the inverter droop factor, m_{inv}, on the system stability. As predicted by references such as [169], the inverter droop gain may result in instability (Hopf bifurcation) as shown by the blue poles in Figure 3-15. Fortunately, the presence of wind-droop could solve this problem by adding more damping to the dominant modes as shown by the red poles in Figure 3-15. In other words, the presence of wind-droop allows the system operator to change the inverter parameters in a wider range to meet the

economic operation constraints. It is worthy to mention that wind-droop could also eliminate stability problems associate with inappropriate tuning of the inverter average power filter.

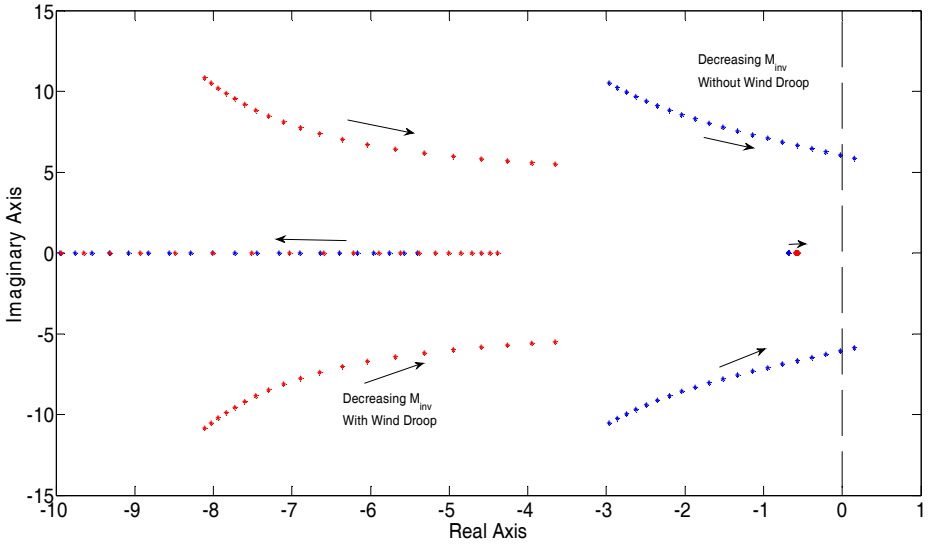

Figure 3-15 Root-Locus of the system dominant poles at V_w=12m/s and m_p =40 while m_{inv} is decreasing in presence (red poles) and absence (blue poles) of wind droop.

3.3.3.3 Pitch-Angle Controller

Up till now, the pitch-angle controller is not considered; however, in reality, a wind generation unit might operate in this regime for a considerable time, especially when wind generation output is at its maximum. The pitch-angle controller is used to limit the wind power output and its rotational speed [53]. In conventional wind generation, the reference torque value changes into a constant torque. Here, because of wind-droop, it should change according to (3-29) implying that the wind generator will always generate less than the rated torque. This fact results in bypassing the pitch compensation block which normally tries to reduce the output power to the rated value. Thus, the pitch-angle controller will merely try to regulate the rotational speed while the output power is set by the RSC controller. Now, the dynamics of the wind power generator could be represented by (3-29)-(3-35), along with (3-9) and (3-11), where K_{pp}, K_{pi} are the pitch-angle controller parameters; β_{cmd} and τ_p are desired pitch-angle and turbine pitch mechanical time-constant, respectively; and T_{max} represents the rated torque.

$$T_{e,TrDr-ref} = K_f T_{\max} - m_p(\omega_m^* - \omega_m). \tag{3-29}$$

$$\Delta\beta_{cmd} = (K_{pp} + K_{pp}/s)\Delta\omega_r. \tag{3-30}$$

$$\Delta\beta = \frac{1}{\tau_p s+1}\Delta\beta_{cmd}. \tag{3-31}$$

$$\Delta P_e = K_f T_{\max}\Delta\omega_r - \omega_{r0} m_p \Delta\omega_m \tag{3-32}$$

$$\Delta P_e = \frac{A_3 K_f T_{\max}(\tau_p s^2+s)}{D(s)}\Delta v_w + \frac{N(s)}{D(s)}\Delta\omega_m \tag{3-33}$$

$$D(s) = 2H_{DFIG}\omega_{r0}\tau_p s^3 + (2H_{DFIG}\omega_{r0} + (K_f T_{\max} - A_2)\tau_p)s^2 + (K_f T_{\max} - A_2 - A_1 K_{pp})s - A_1 K_{pi} \tag{3-34}$$

$$N(s) = -m_p\omega_{r0}(2H_{DFIG}\omega_{r0}\tau_p s^3 + (2H_{DFIG}\omega_{r0} - A_2\tau_p)s^2 + (-A_2 - A_1 K_{pp})s - A_1 K_{pi}). \tag{3-35}$$

After mathematical manipulation, the wind power output, P_e, could be derived as given in (3-33) which should be used in Figure 3-8. This new model reveals how wind-droop acts in the presence of pitch-angle control dynamics. Dominant eigenvalues are shown in Figure 3-16, which shows that wind-droop still influences positively, and indeed, the pitch-angle controller does not impact the wind-droop dynamics significantly. This is due to the fact that the pitch-angle controller is much slower than the RSC controller. Furthermore, it shows that the major disadvantage of deloading, i.e. high rotational speed, could be solved simply by employing a conventional pitch-angle controller.

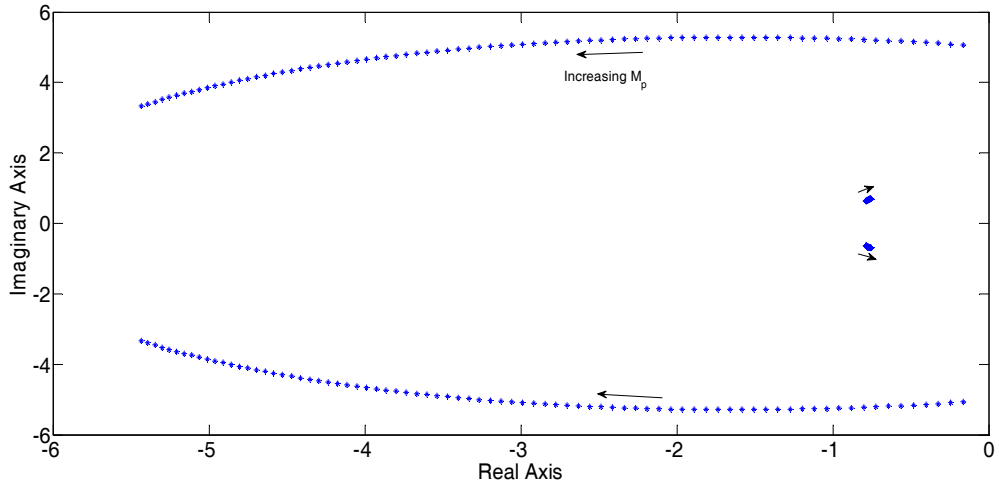

Figure 3-16 Root-locus of the system dominant poles when m_p is increasing from zero to 80p.u and pitch-angle controller is activated.

3.4 The Proposed Solution

On the one hand, the reserve power obtained from the deloading is variable and a function of the cube of the wind speed. On the other hand, the impact of the wind behavior on the frequency regulation power is independent of the wind speed.

3.4.1 Efficiency Droop

To solve these problems, this thesis proposes a new method for implementing the droop in wind power generators. This method is shown in (3-36).

$$P_{reg} = P_{EffDr} = \omega_r^{\,3} m_p \frac{(\omega_m^{\,*} - \omega_m)}{1+\tau s}. \tag{3-36}$$

The same procedure used for the previous methods can be utilized here to calculate the maximum allowable gain for the efficiency droop. Equation (3-37) formulates this value, and Figure 3-17 compares the maximum tuning gain for the droop implemented in the power, torque, and efficiency for the same deloading factors and wind speeds. Obviously, the maximum allowable efficiency droop gain is not a function of the wind speed as this gain also appears in (3-37) and depends only on the deloading factor. In contrast, the power- and torque maximum allowable droop gain are functions of the square and cube of the wind speed, as (3-24) and (3-23) demonstrate. As mentioned in the discussion about Equation (3-23), the components of the maximum allowable efficiency droops are constants such as R, K_{wopt} and K_{vopt} or, like a_2, λ_{del} and K_{wf} are solely dependent on the deloading factor, K_{vf}. Thus, operators, regardless of the wind speed, can choose the droop gain just after selecting the deloading factor, just as they can with the conventional droops. This capability is the main advantage of the proposed droop over the present ones. In other words, the droop gain can be chosen regardless of the wind speed, and with no concern about instability or wasting an available capacity.

$$m_{p-EffDr,\max} = \left| \frac{(3K_{wf}K_{wopt} - a_2)(1-K_{vf})K_{vopt}\lambda_{del}^{\,3}}{a_2 R^3 \Delta\omega_{m,\max}} \right|. \tag{3-37}$$

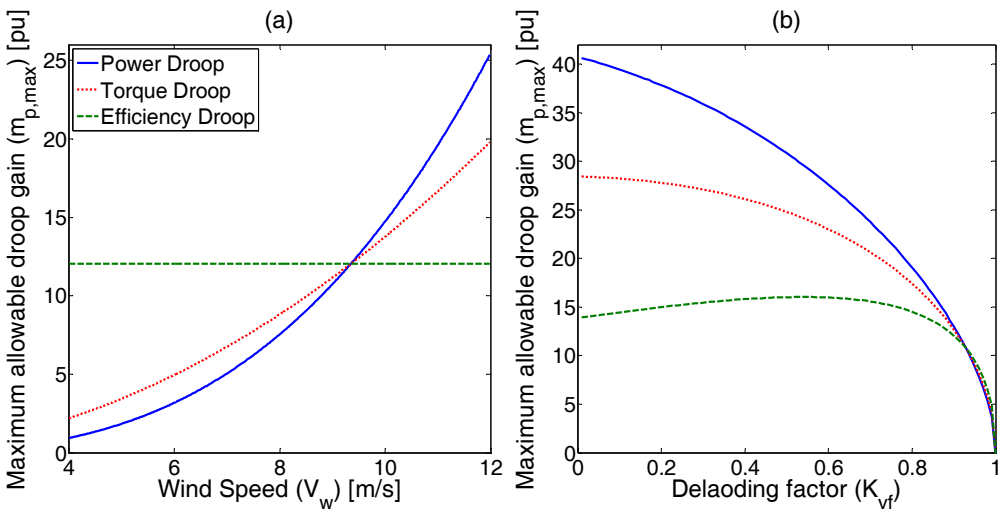

Figure 3-17 Maximum allowable droop gain versus (a) wind speed when K_{vf}=0.9, (b) deloading factor when V_w=9.6 m/s.

Before proceeding further, a few questions need to be answered. First, the proposed method needs to be physically justified. Equation (3-36) seems very similar to both power and torque droop methods, (3-19) and (3-21) respectively. However, ω_r makes them different. Power and torque droops have no and simple rotating speed element, respectively, while in the proposed method, the cube of ω_r is employed. Equation (3-38) shows the wind generator output power at the steady state when the proposed method is implemented.

$$P_{e.ss} = K_{wf} K_{wopt} {\omega_{r0}}^3 + \frac{-a_2}{3K_{wf} K_{wopt} - a_2} {\omega_{r0}}^3 m_p ({\omega_m}^* - \omega_{m,ss}). \tag{3-38}$$

By using (3-6) and (3-1), (3-38) can be rewritten as follows:

$$P_{e.ss} = (\frac{2K_{vf} K_{vopt}}{\rho A_r} + \frac{-2a_2 {\lambda_{del}}^3}{(3K_{wf} K_{wopt} - a_2)\rho A_r R^3} m_p ({\omega_m}^* - \omega_{m,ss}))0.5\rho A_r {V_{w0}}^3. \tag{3-39}$$

The comparison between (3-1) and (3-39) shows that the term in the parenthesis is equivalent to the efficiency coefficient. Reference [90] has explained that $0.5\rho A_r {V_w}^3$ is the total energy in the wind generator and that C_p describes the fraction of this power which can be extracted by the wind turbine. In other words, the proposed droop changes the wind turbine efficiency linearly. This efficiency tuning can explain why the maximum allowable droop gain is independent of the wind speed. The first term in the parenthesis, $2K_{vf}K_{vopt}/\rho A_r$, is, in fact, the deloaded efficiency coefficient. The maximum droop gain can be determined

by subtracting the deloaded efficiency factor from the maximum one and then dividing by the product of the maximum frequency deviation and the factor multiplied into the droop term, $-2a_2\lambda_{del}^3/(3K_{wf}K_{wopt}-a_2)\rho A_r R^3$. In the discussions of (3-3) and (3-7), all these values and parameters were shown to be independent of the wind speed. In fact, the only influential factor is the tip speed ratio, which is constant as long as the deloading factor is constant. Note that the analyses have not been simplified.

The second important question involves the effective droop gain shown in (3-40) and derived from (3-38) and (3-8). This relation is depicted in Figure 3-18. Obviously, the effective droop gain is a function of the variable wind speed. The impact of the wind speed's reliance on the system stability might be questioned. In other words, at high wind speeds, the proposed droop is more sensitive to the frequency changes and injects/absorbs more power for the same amount of frequency changes than occurs at low wind speeds. Although this dependency is not similar to that of the dispatchable generator, it is still desired. At low wind speeds, some other sources should also participate in the generation to meet the demands of the system. These sources usually contribute to the frequency regulation as well. However, at high wind speeds, these generators may be turned off because they are no longer needed for power generation. Thus, the wind generator should also involve more than low wind speed conditions in the frequency regulation. The efficiency droop regulates this behavior automatically, and its effective droop gain is also a function of the wind speed in the desired way.

$$m_{p-EffDr,effective} = \frac{-a_2\lambda_{del}^{\ 3}V_{w0}^{\ 3}}{(3K_{wf}K_{wopt}-a_2)R^3}m_p. \tag{3-40}$$

3.4.2 The Transient Response

The proposed method has the desired behavior in steady-state frequency regulation. However, the transient response of the proposed droop (also called the transient droop [162]) needs to be investigated to obtain a complete understanding of this method. This section analyzes these effects.

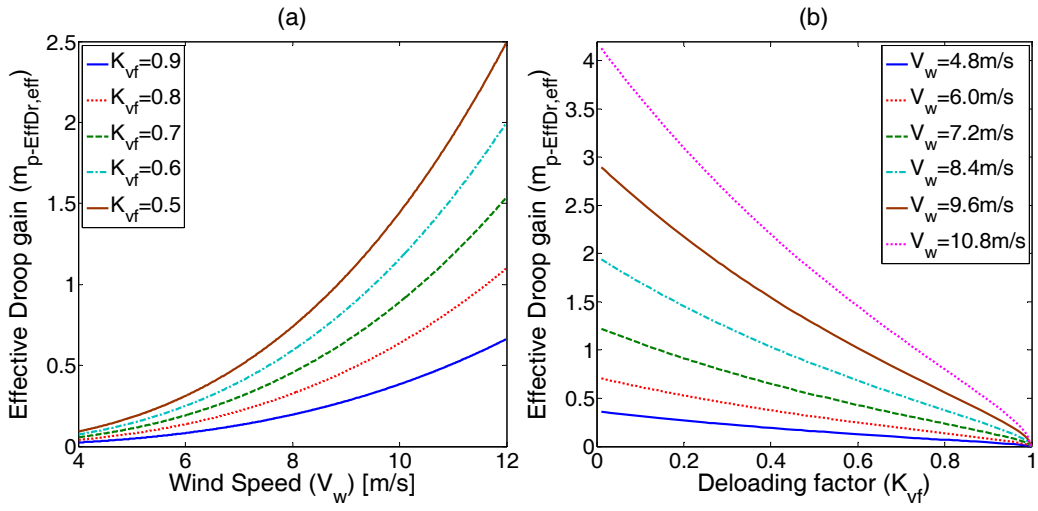

Figure 3-18 Effective efficiency droop gain reliance on (a) wind speed and (b) deloading factor when m_p is equal to 1.

3.4.2.1 Inertial Response

Figure 3-19 shows the frequency response of the wind generator active power output responding to the changes in the system frequency. To obtain the results in this figure, the linearized form of (3-36) was substituted in (3-15). Apparently, the proposed method for a range of frequencies behaves very similarly to the physical inertia of the conventional generator. However, the range of frequency, despite the real inertia, is limited and also a function of the wind speed. In other words, at higher wind speeds, the proposed method has a higher gain in the higher frequencies. Therefore, at high wind speeds, the proposed method contributes more to the transient frequency regulation than at low speeds. This behavior is very similar to its steady-state frequency regulation behavior, as discussed in the previous section. For very similar reasons, this behavior is also desired.

Figure 3-19(b) reveals the impact of the deloading factor. Apparently, lower factors can participate more effectively than higher factors in transient frequency regulation. This difference can be attributed to the higher speed of the wind turbine and the larger amount of energy stored in the rotating mass of the generator.

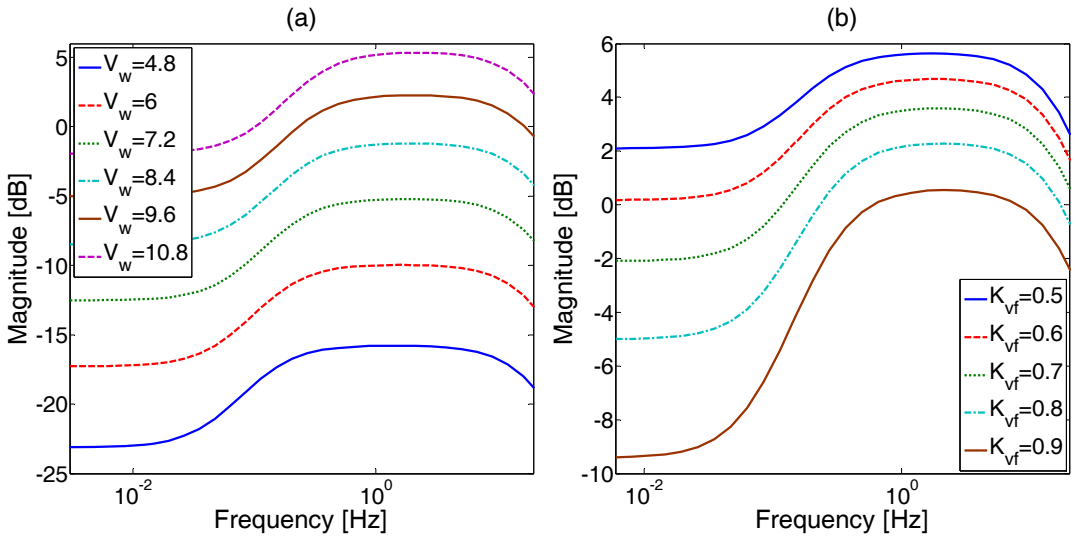

Figure 3-19 Bode diagram of efficiency droop ($H_1(s)\Delta P_{EffDr}$) in (a) different wind speeds when K_{vf}=0.8, (b) Different deloading factors when V_w=9.6 m/s. The droop gain, m_p, is constantly one in all the cases.

3.4.2.2 Parameters Sensitivity

Figure 3-20 reveals the dominant modes of the system when the droop gain of the efficiency droop is increased from almost zero to its maximum allowable amount at both relatively high (blue) and low (red) wind speeds. Apparently, in both cases, the closest poles to the imaginary axis move significantly toward the left-half plane, although this replacement at a high wind speed is considerably more. This result is matching the findings of the previous section and the frequency response shown in Figure 3-19(a).

These modes show no sign of instability, even if the droop gain is larger than the maximum allowable gain shown in Figure 3-17. This stability can be explained by the nature of the small-signal analysis, in which the instability discussed in the previous section was caused by the nonlinearity of the wind power relation and the limited amount of stored energy. In fact, the model suggested in Figure 3-8 is incapable of showing that asking for more power than the reserved power can make the wind generator unstable. However, such analysis does correctly show that the use of a wind-based droop improves the stability of the whole power system. For this reason, the previous section was devoted to finding the maximum allowable droop gain.

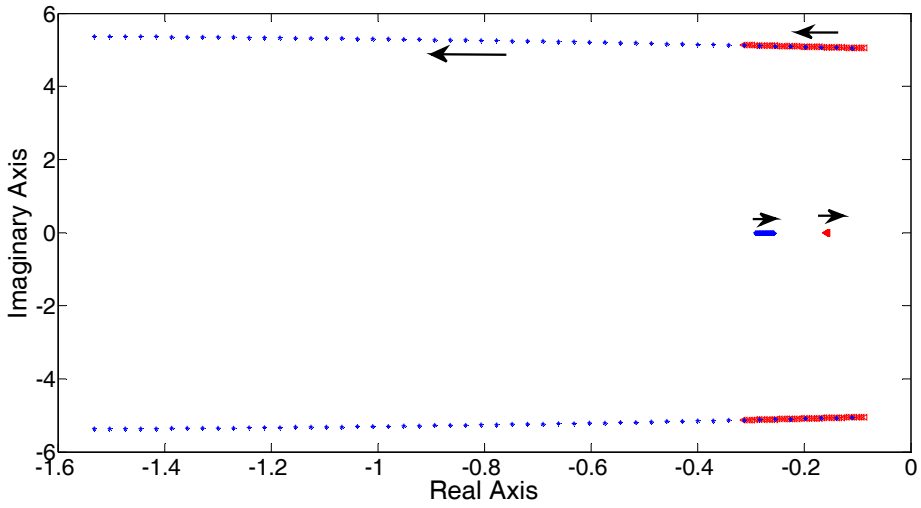

Figure 3-20 Dominant poles of the system when the droop gain is increasing in V_w=11 m/s (blue stars) and V_w=6 m/s (red triangles).

Figure 3-21(a) reveals the impact of the wind speed more clearly by showing how increasing the wind speed influences the dominant poles of the system. Not surprisingly, the higher the wind speed is, the more stable modes can be observed. Figure 3-21(b) completes this discussion by revealing the impact of the deloading factor. K_{vf}, is decreased from almost 1 to 0.5 and, again, the dominant modes have moved toward the left. These results were predicted previously in Figure 3-19(b), where the proposed method shows a higher gain in the middle range of the frequency with lower deloading factors.

Figure 3-22 compares the transient behavior of different wind-based droops by depicting the overshoot in the frequency response of the system in the case of a step load disturbance. This figure shows that at high wind speeds, the proposed efficiency-droop regulates the frequency better than the two other methods, whereas the power-droop performs the best at lower wind speeds. However, the inability of small-signal analyses to consider the maximum allowable droop gain should be noticed here. Although the efficiency droop shows a higher oscillation for the same amount of droop gain at low wind speeds, the efficiency droop is allowed to adopt much higher gains than those allowed to power- and torque-droops. The same argument can be used against the efficiency droop at higher wind speeds. More scrutiny of Figure 3-22 reveals more interesting results where the maximum droop gain for each

droop method is specified by the dashed lines. Amazingly, the maximum overshoots for the maximum droop gain of all three methods are the same. This observation is valid regardless of the wind speed and deloading factor. On the other hand, the same steady-state frequency deviation, and, consequently, also the maximum overall frequency deviation, will be obtained by using the maximum droop gain, regardless of the adopted method. These similar results mean that the maximum improvements that can be achieved by all the droop-based methods are the same. However, for the efficiency droop method, this maximum is obtained by a constant droop gain regardless of the wind speed, whereas, for the other two methods, the droop gain should be modified by any change in the variable wind speeds, as [58] showed. This point is an important advantage of the proposed methods over the existing ones.

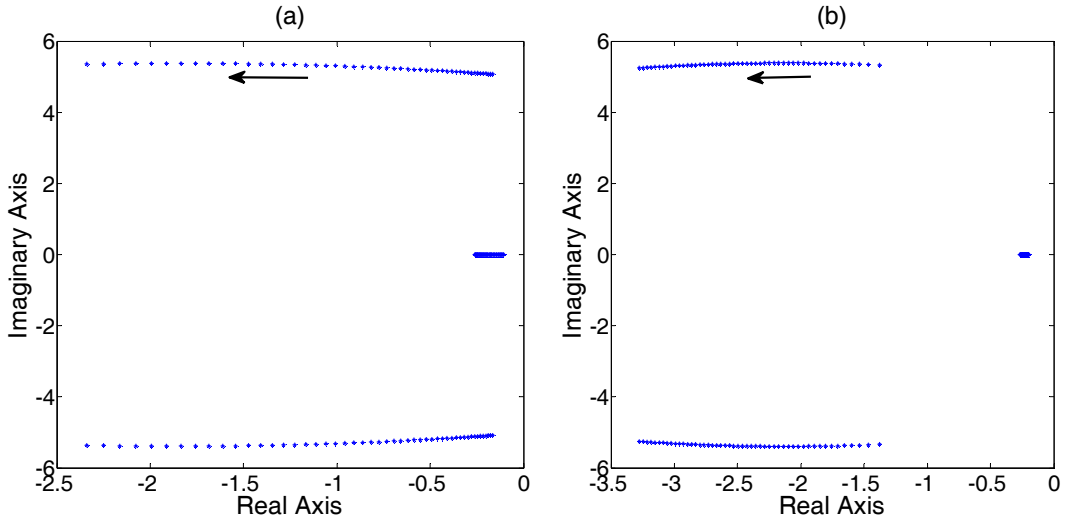

Figure 3-21 Dominant poles of the system when (a) wind speed is increasing from 4 to 12m/s with K_{vf}=0.9 and m_p=15, and (b) deloading factor is decreasing from almost one to 0.5 when m_p=15 and V_w=11 m/s.

Finally, it is easy, but space-consuming, to show that none of these (transient and steady-state) problems occur when the pitch angle controller is enabled at very high wind speeds and all droop-based methods perform equally well in this region. In such high wind speeds, the wind generator rotating speed, ω_r, is kept constant by the pitch angle controller, and the large amount of available unused wind energy solves the problem of limited variable reserve power.

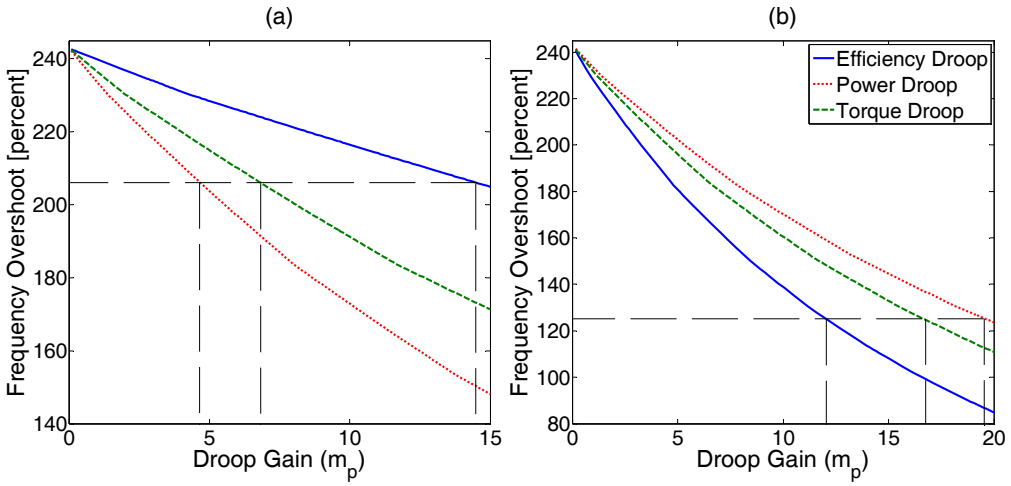

Figure 3-22 Frequency overshoot versus the droop gain when (a) V_w=6 m/s, K_{vf}=0.8 and (b) V_w=11 m/s, K_{vf}=0.9 m/s.

3.5 Time-Domain Simulation Results

Time-domain simulation, using Matlab/Simulink®, is used to verify the analytical results discussed in the previous section. These simulations benefit from detailed nonlinear models when the system shown in Figure 3-7 is also adopted here. In most of the analyses, a DFIG wind generator is used as the wind generator. The detailed modeling of the DFIG system was discussed in [50] and [76], whereas the modeling of the conventional generator DG2 was discussed in detail in [162]. Typical distribution system lines, with a low X/R ratio (X/R =2), are modeled as lumped R-L, whereas loads are modeled by parallel R-L circuits. The system parameters are given in the Appendices, and more details are provided in [161]. An intentional islanding at t=35 s is used as the disturbance for the system. This disturbance leads to a mismatch between the demand and the generation. In Figure 3-8, this mismatch is modeled as the load change, represented by ΔP_L.

3.5.1 Present Wind Droop Methods

Two different scenarios are investigated. The first deals with the case of both wind and gas turbine generators, whereas the second uses only wind power generation. Each scenario consists of different cases.

3.5.1.1 Gas Turbine plus Wind

Firstly, to reduce the complexity, constant wind speed is considered. Later, to present a more realistic case, a real wind speed pattern will be used.

1) Constant Wind Speed

The system frequency is shown in Figure 3-23 without wind-droop and with wind-droop implemented as power- or torque-droop at different droop gains. As depicted, not only the final frequency but also the transient behaviors are improved as predicted by the analytical findings reported in the previous sections and despite the low X/R ratio. It also confirms the results of Figure 3-9; i.e. larger m_p results in better dynamic behavior.

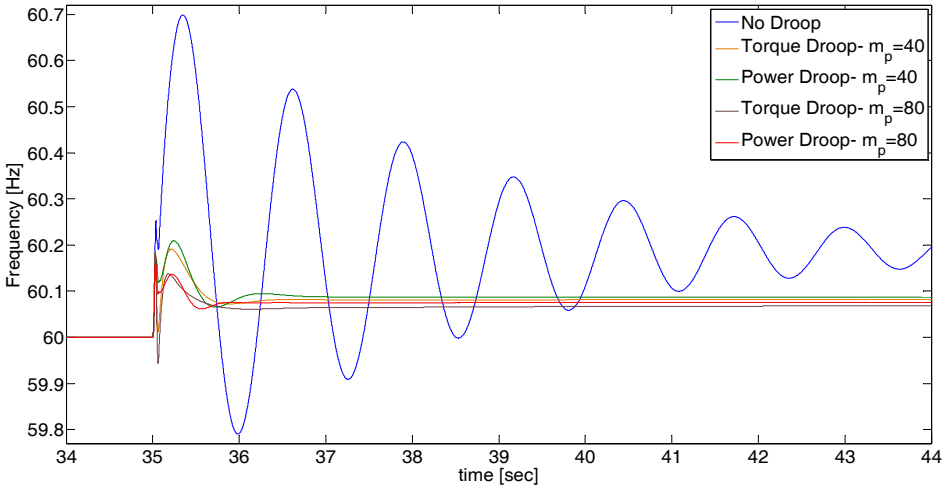

Figure 3-23 Frequency response when wind speed is 13m/s and K_{wf}=0.5.

It was previously shown that choosing K_{wf} higher than one may result in negative effective droop. Figure 3-24 shows the wind generator output when K_{wf}=1.5. While the system has excessive generation similar to the pervious case, and the frequency has increased after islanding, the wind power output, despite the philosophy of implementing droop, has also increased. Indeed, wind-droop with under-speeding dictates higher fluctuations to dispatchable sources outputs and it is not capable of feeding a microgrid alone.

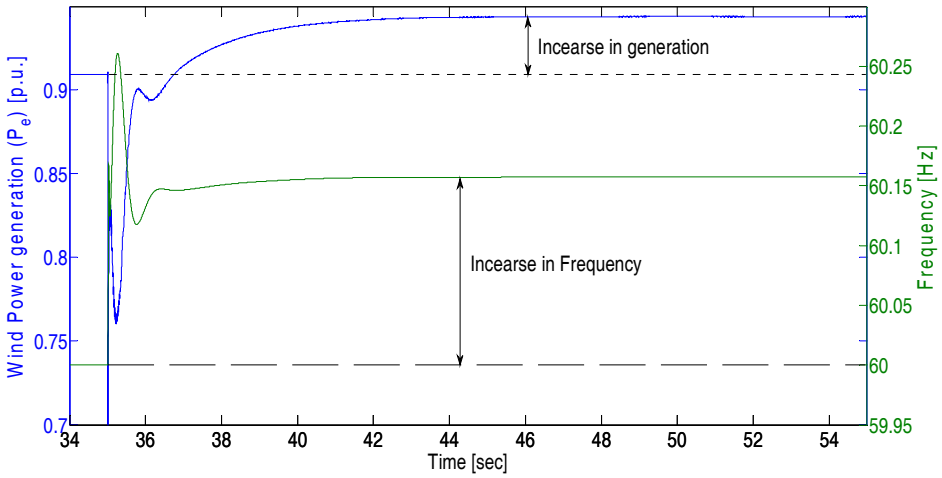

Figure 3-24 Frequency and wind power generation responses when wind speed is constant at 13m/s and K_f=1.5, m_p=40.

In this scenario, an inverter-based DG unit is added to bus 8 in the system and turbine droop factor has also been modified. The inverter is modeled based on [169]. Figure 3-25 shows the system frequency in several scenarios. While decreasing the inverter droop factor has worsen both the steady-state and the dynamic behaviors, the presence of wind-droop improves the system stability. It can even stabilize the unstable system as predicated by the analytical results.

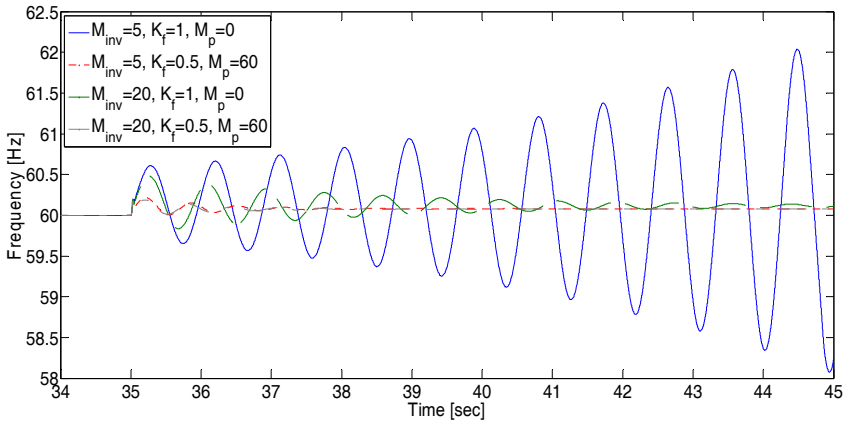

Figure 3-25 Frequency and wind Power generation responses when wind speed is constant at 13m/s and K_{wf}=1.5, m_p=40.

2) Variable Wind Speed

In this scenario, a real wind speed pattern, which is derived from a real measured wind speed [170] is used, and it is shown in Figure 3-26.

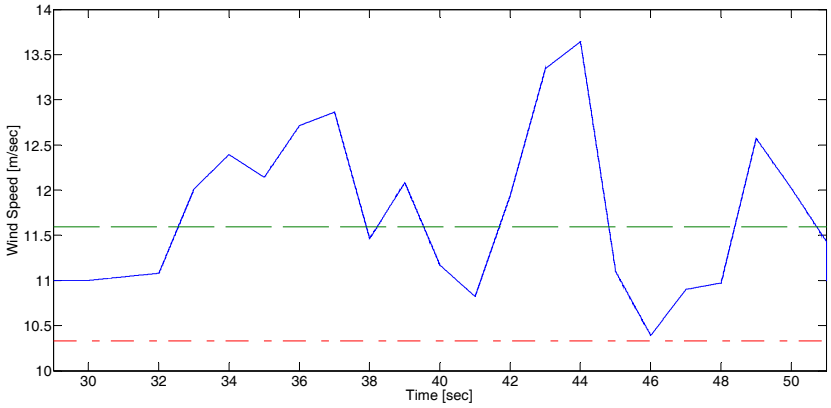

Figure 3-26 Real wind speed pattern (blue solid line). The minimum wind speed needed for stand-alone wind operation (green and red dashed lines) will be illustrated in Section IV.B.1.

To prevent the interference between the intentional islanding disturbance and impacts of variable wind speed, islanding has taken place long enough before t=30s, and wind speed is kept constant until t=30s, at which wind speed start to change gradually. Figure 3-27 shows how wind droop has made the frequency smoother with less fluctuation. The other important observation here is the improvement in the gas turbine generator active power output with and without wind-droop, as shown in Figure 3-28. It reveals how the proposed method reduces the fluctuations in dispatchable source output. It should be also noted that even if dispatchable DG is not limited by any ramp constraint and could afford these oscillations, more fluctuations will lead to a faster aging and frequent maintenance. This could be accounted as one of the hidden economic benefits of wind-droop.

The presented analysis predicted that lowering K_p, despite its positive impact on steady-state frequency deviation, may result in instability. Figure 3-29 confirms this argument. It also verifies that the presence of wind-droop allows the turbine to experience lower K_p without facing stability problems.

3.5.1.2 Stand-Alone Wind

With appropriate energy management, sensitive loads can be fed from a wind generation under the outage of dispatchable resources or other microgrid contingencies. In this scenario, it is assumed that wind generation is enough for essential loads in a microgrid and merely studies short-term frequency stability issues (not long-term power dispatching). With the excessively increasing penetration of wind power in power systems and advances in the forecasting and energy management methods, this scenario is very likely to happen in near-term microgrids.

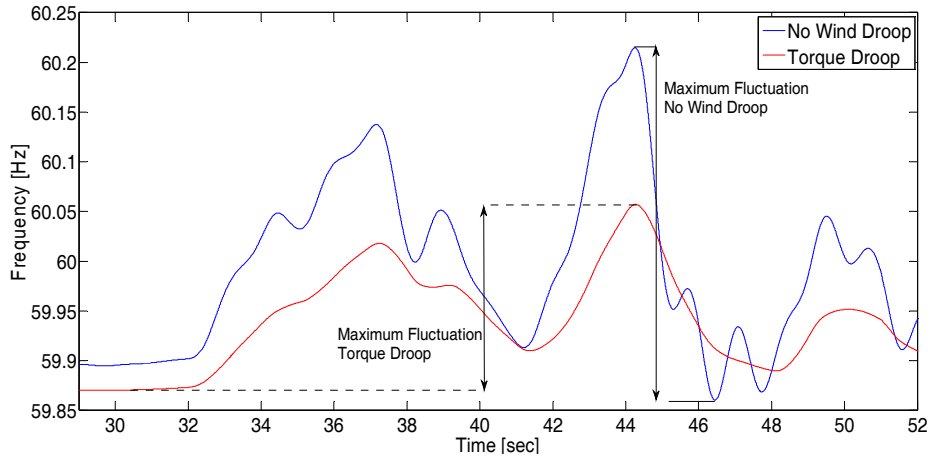

Figure 3-27 Frequency responses when wind speed is varying. Islanding had taken place long enough before wind speed starts to change.

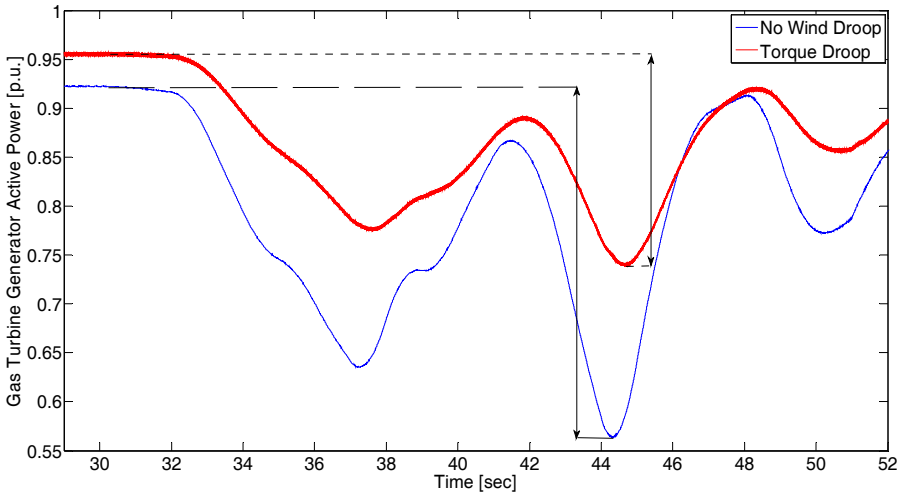

Figure 3-28 Gas turbine generator output power response when wind speed is varying. Islanding had taken place long enough before wind speed starts to change.

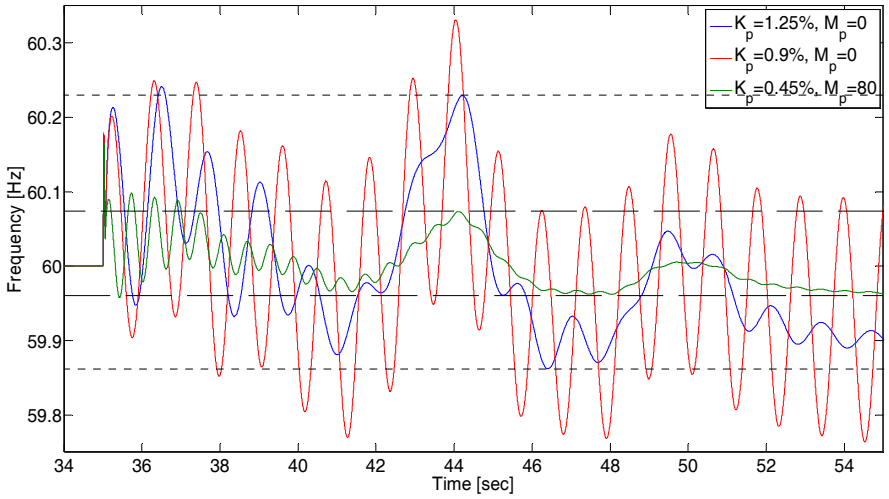

Figure 3-29 Frequency response when different turbine droop factors, K_p, are adopted.

1) Single Wind Generation Unit

In this part, the gas turbine generator unit is removed and load 2 is changed for generation-load matching. Green and red-dashed lines in Figure 3-26 show system loading levels regarding wind speed; indeed, they specify the minimum wind speed required to feed the loads. It should be noted that that in steady-state in both cases, available wind power is sufficient. However, in some cases, e.g. for the green line, some short-term deficiencies occur. Figure 3-30 and Figure 3-31 depict the frequency and wind generator output power, respectively, in both cases, which are stable. This experiment reveals that short-term deficiency in available wind power could be afforded due the kinetic energy provided by the rotating mass.

2) Multiple Wind-Power Generators

In this scenario, load 2 is restored and another wind power generator is added to bus 7, the same place of the gas turbine unit. Similar to the pervious part, firstly, constant wind speed is utilized; then a typical wind speed profile is employed.

One of the generators works at 14 m/s whereas the other operates at V_w=9.5 m/s and the droop factor is the same for both. Figure 3-32(a) shows the output power responses of both generators when torque droop is implemented, whereas Figure 3-32(b) shows the same when power droop is used. With torque-droop, generator with higher wind speed has higher share

in power regulation. In contrast, power-droop yields almost equal power sharing. These differences can be explained by discussions about the effective droop factor. As expected, in torque-droop, the wind generator with higher wind speed has a higher effective droop factor.

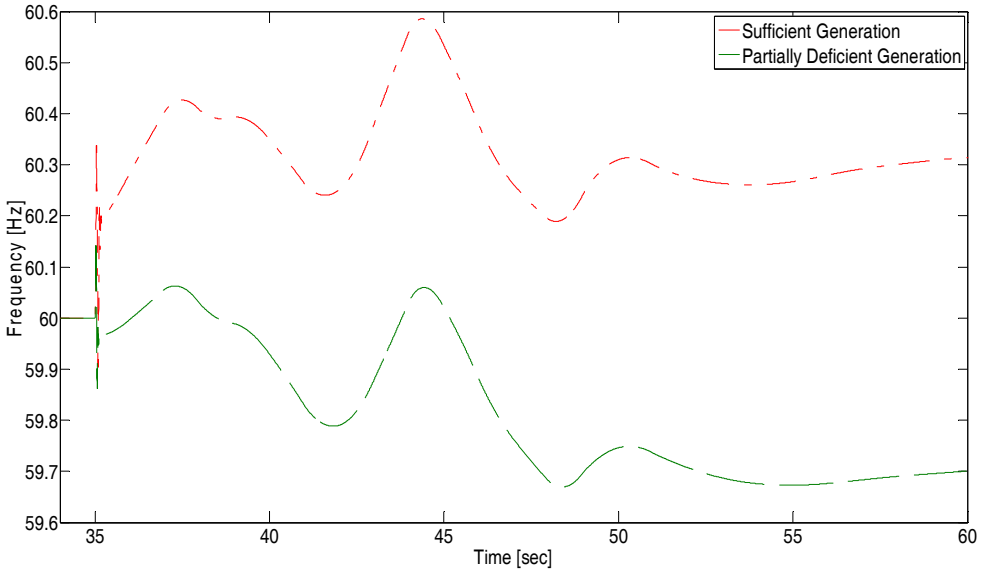

Figure 3-30 Frequency response for stand-alone wind power generation.

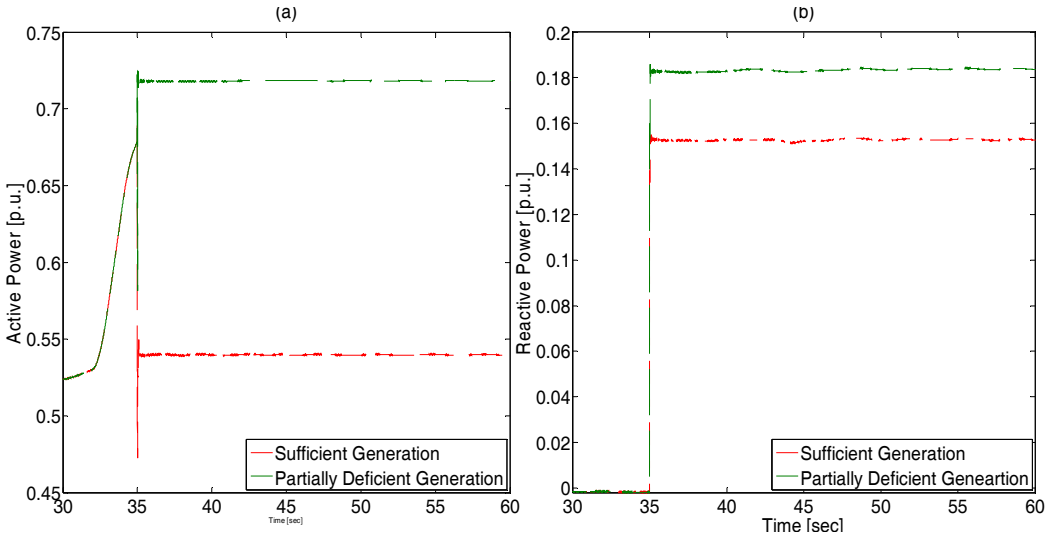

Figure 3-31 Wind (a) Active power response, (b) Reactive power response.

In the previous sections, it was reported that the almost constant effective droop factor of power-droop, while the deloaded power is not constant, could result in instability. The case of Figure 3-33 confirms this argument which is similar to the case of Figure 3-32 but now the

lower wind speed is decreased from 9.5 to 9m/s. Again in power-droop method, the DG with lower wind speed and less available power is forced to provide almost the same power as the other unit with higher wind speed so the incapability of this DG unit leads to instability and consequently microgrid failure. It is worthy to mention that exactly the same scenario but with torque-droop remains stable (Figure 3-33(a)).

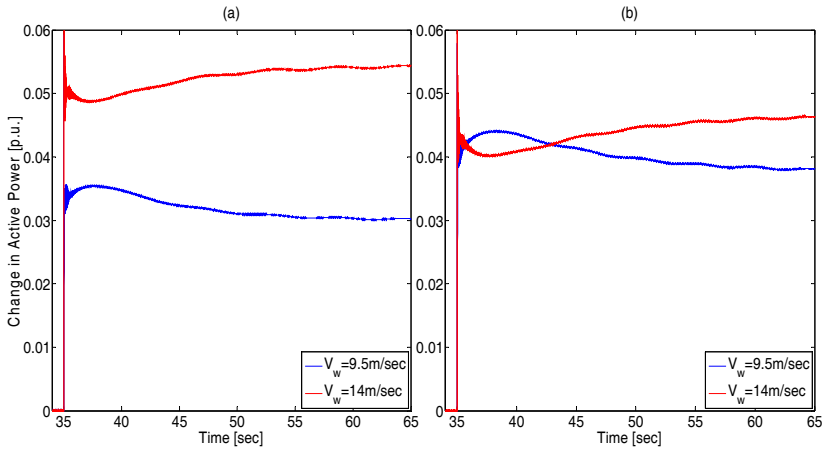

Figure 3-32 Changes in active power output of stand-alone wind power generations with different wind speeds, Vw, when droop is implemented in (a) Torque (b) Power.

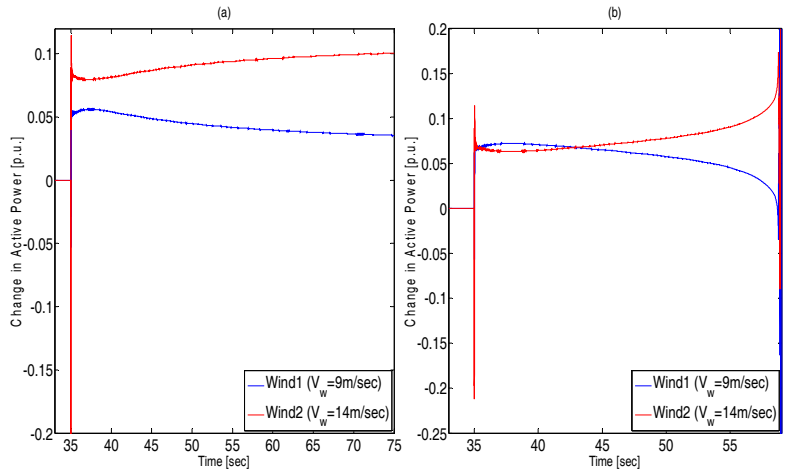

Figure 3-33 Changes in active power output of stand-alone wind power generations with different wind speeds, Vw, when droop is implemented in (a) Torque, (b) Power.

In this part, both wind power generators experience the same wind speed pattern shown in Figure 3-26. Figure 3-34 and Figure 3-35 show the frequency regulation and the power

sharing, respectively. Since both DG units have same parameters, they share the active power equally.

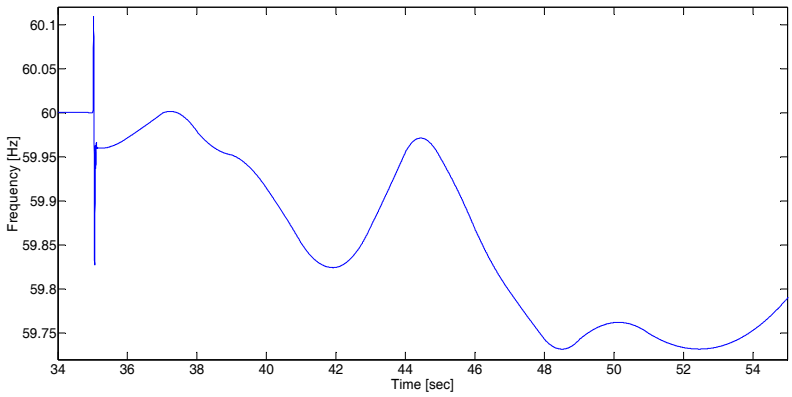

Figure 3-34 Frequency vs. time when two stand-alone wind generators with identical wind speeds regulating the microgrid frequency.

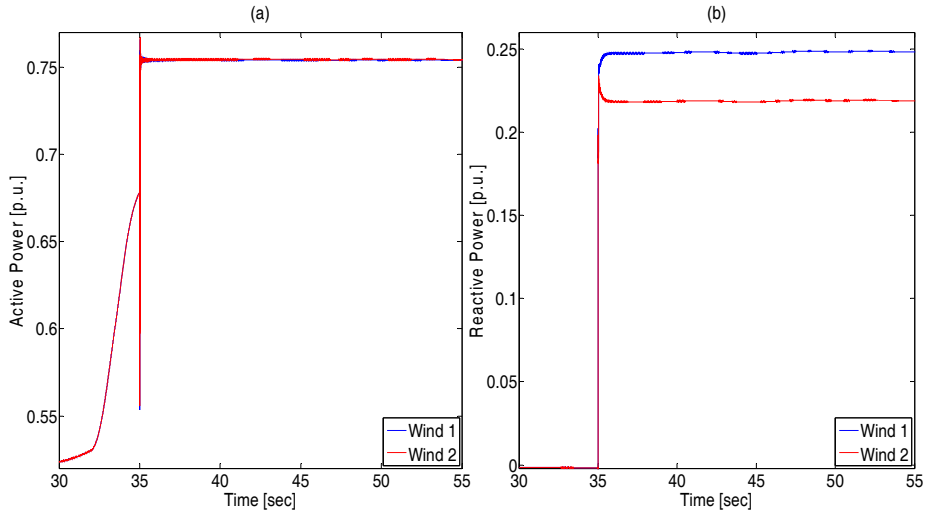

Figure 3-35 Wind (a) Active Power, (b) Reactive Power generation when two stand-alone wind generators with identical wind speeds regulating microgrid frequency.

A different wind speed pattern, derived from [170] and shown in Figure 3-36, is used for one DG unit whereas the other unit still works with the previous wind speed pattern shown in Figure 3-26 (shown by blue solid line in Figure 3-36).

Figure 3-37 illustrates the power sharing performance. Because of variable wind speed and dependency of the effective droop factor, a unit with higher wind speed generates more

power which seems reasonably beneficial. Figure 3-38 reveals the microgrid frequency response in this case.

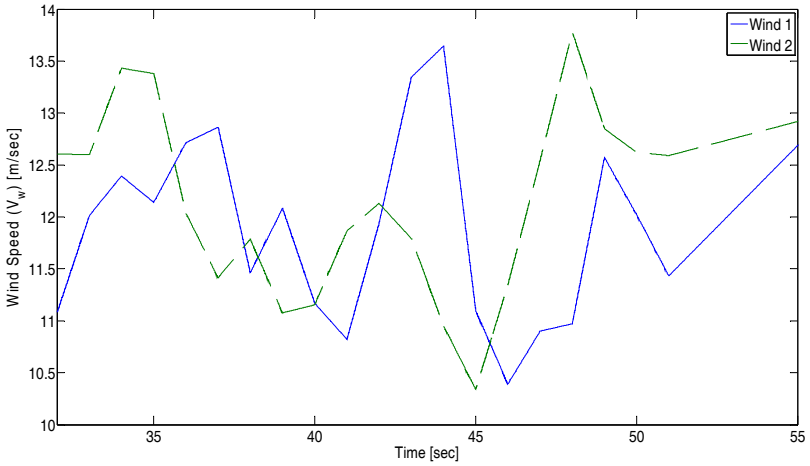

Figure 3-36 Real wind speed pattern.

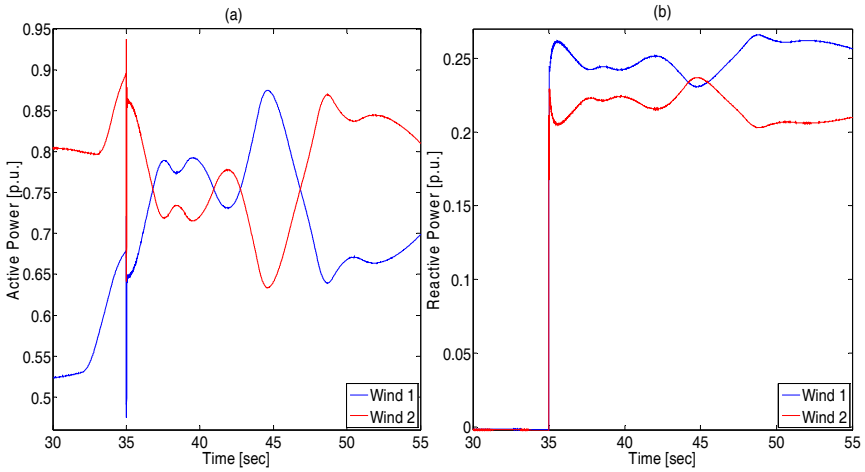

Figure 3-37 Wind (a) Active Power, (b) Reactive Power generation responses.

A question may arise about the compatibility between the power and torque droop as two possible droop methods. With wind speed patterns are exactly the same, one of DG units is equipped with torque-droop whereas the other unit adopts power-droop. Comparing Figure 3-39, showing the power sharing in this case, with Figure 3-35, reveals that despite the same parameters, power sharing is not completely equal due to the impact of the effective droop factor as explained before. The micro-grid frequency response is also shown in Figure 3-40.

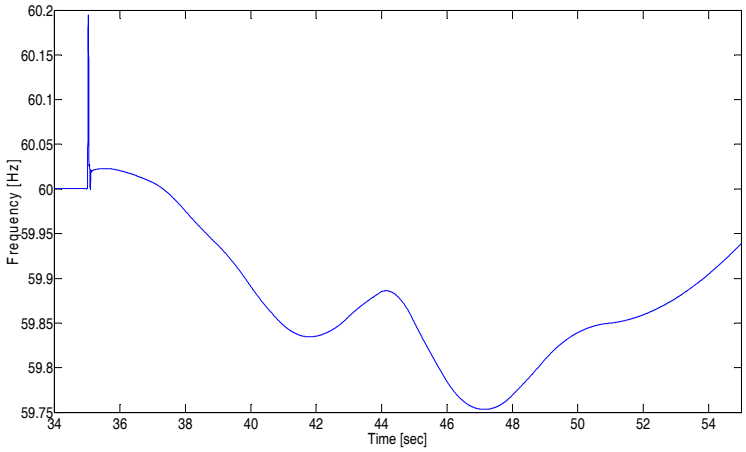

Figure 3-38 Microgrid frequency response with different variable wind speed patterns.

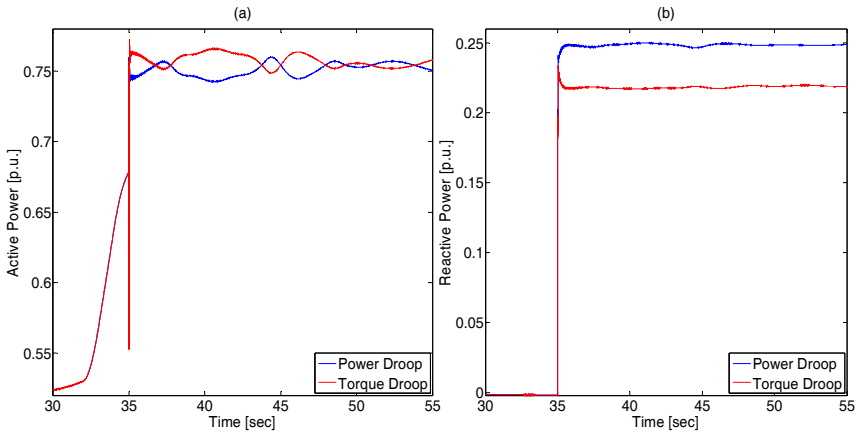

Figure 3-39 Wind (a) Active power, (b) Reactive power generation responses.

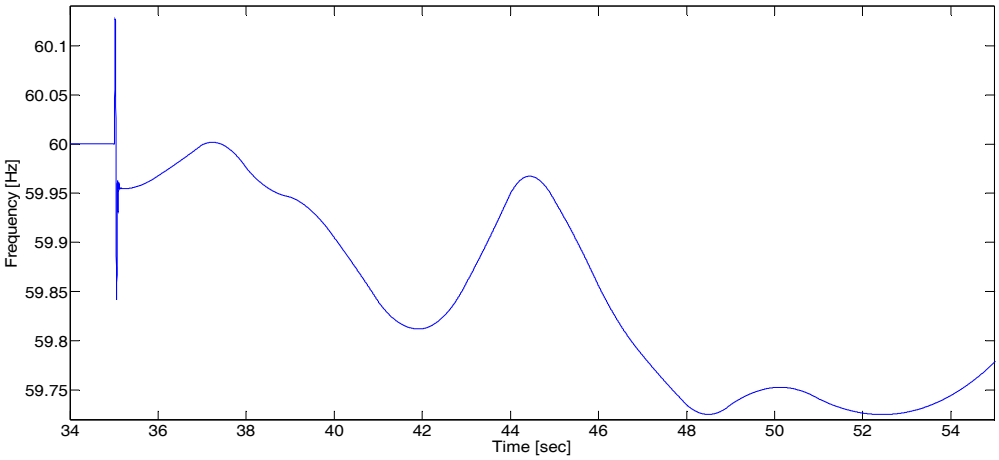

Figure 3-40 Microgrid frequency response.

3.5.2 The Proposed Method

3.5.2.1 Constant Wind Speed

To avoid any confusion, a constant wind speed is considered in this section. Figure 3-41(b) shows the system frequency when the wind speed is constantly as high as 11 m/s. Obviously, all the methods improve the frequency regulation in the system. In addition, this figure verifies this thesis's argument that at relatively high wind speeds, the efficiency droop shows a better performance than that of the other methods with equal droop gain.

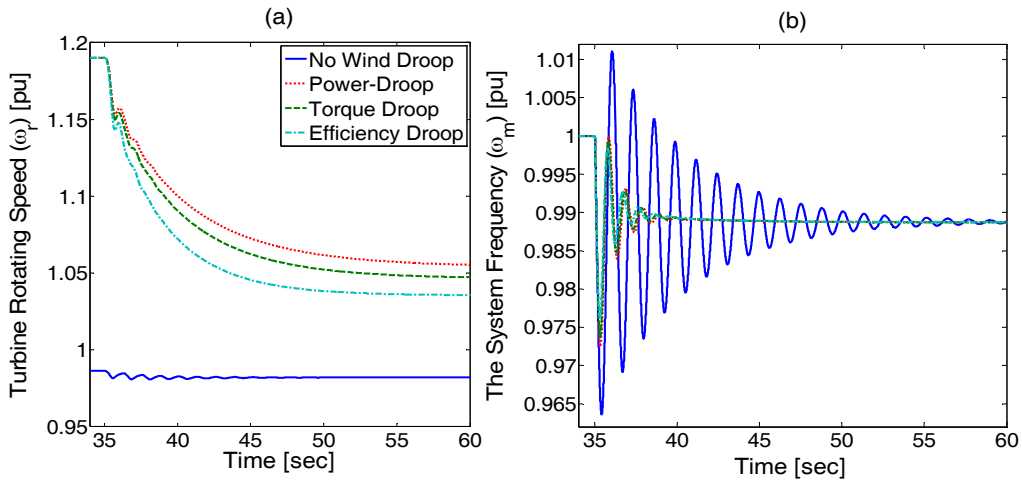

Figure 3-41 Utilizing wind-droop when wind speed is constantly 11m/s. (a) The wind turbine speed, (b) the system frequency when in droop-based methods K_{wf}=0.5, m_p=20pu.

Figure 3-42 depicts the impacts of the wind droop methods at a relatively low wind speed, 5.5 m/s. Each of these droop methods' gains is selected to be close their maximum allowable amount. A huge difference exists among these droop gains, 3 and 27 pu for the power- and efficiency droop, respectively, as was predicted in the previous section. Moreover, the simulations verify that using a droop gain as high as that used in the high wind speed case can make the wind generator unstable. Thus, the present methods, power- and torque-droop, are highly dependent on the wind speed, but the proposed method's droop-gain can be chosen regardless of the wind speed. On the other hand, despite the vast differences between the gains, the methods' performances are very similar to each other. This observation was also expected based on the discussion in the previous section, especially the discussion of Figure 3-22.

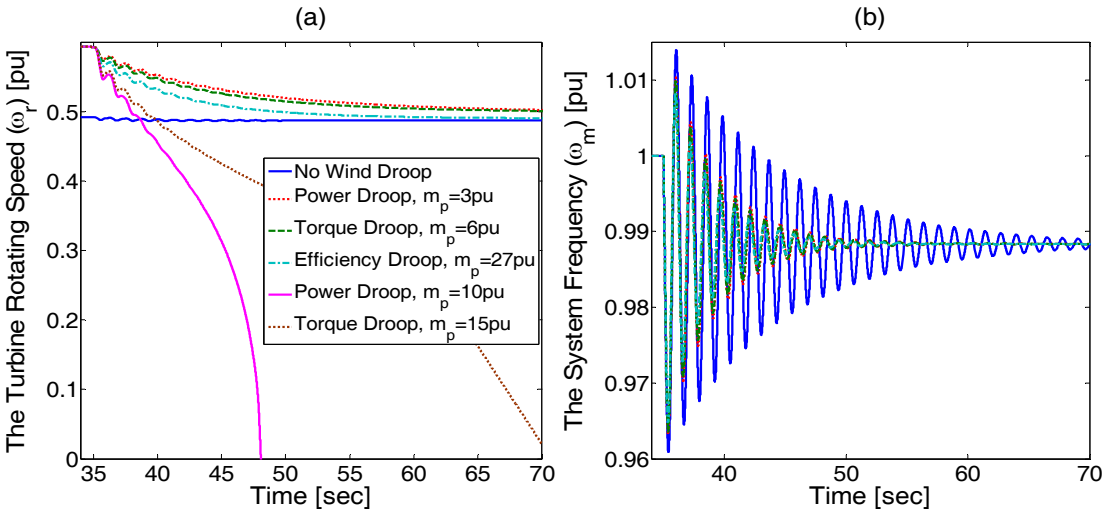

Figure 3-42 Utilizing wind-droop when wind speed is constantly 11m/s. (a) The wind turbine speed, (b) the system frequency when in droop-based methods K_{wf}=0.5.

The comparison between Figure 3-41 and Figure 3-42 is also informative. It shows how much more effective the efficiency droop is at a higher wind speed when an even lower droop gain is employed, as in Figure 3-41. In these simulations, to have a similar frequency response in the steady-state, the diesel generation is reduced from 0.55 pu at 5.5 m/s wind speed to 0.05 pu at 11 m/s. This reduction means that if two dispatchable generators were used, one of them would be shut down at the high wind speed. This generator shut-down would lead to less mechanical inertia in the system and worse frequency regulation.

3.5.2.2 Variable Wind Speed

In reality, the wind speed is always changing. In this section, a real wind speed pattern, shown in Figure 3-43(a), similar to the pattern used in Figure 3-26, is employed [170]. This figure verifies the appropriate function of the droop in a practical case. Figure 3-43(c) is also useful for discussing the impact of the wind droop on the both transient and steady-state frequency regulation. The wind-based droops respond not only to very fast changes of the islanding but also to relatively slow changes caused by a variable wind speed, the other source of disturbance for the system. After t=40 s, when the islanding disturbance is almost damped, the droop-implemented wind generators fluctuate less with changes in the wind speed to keep the frequency constant.

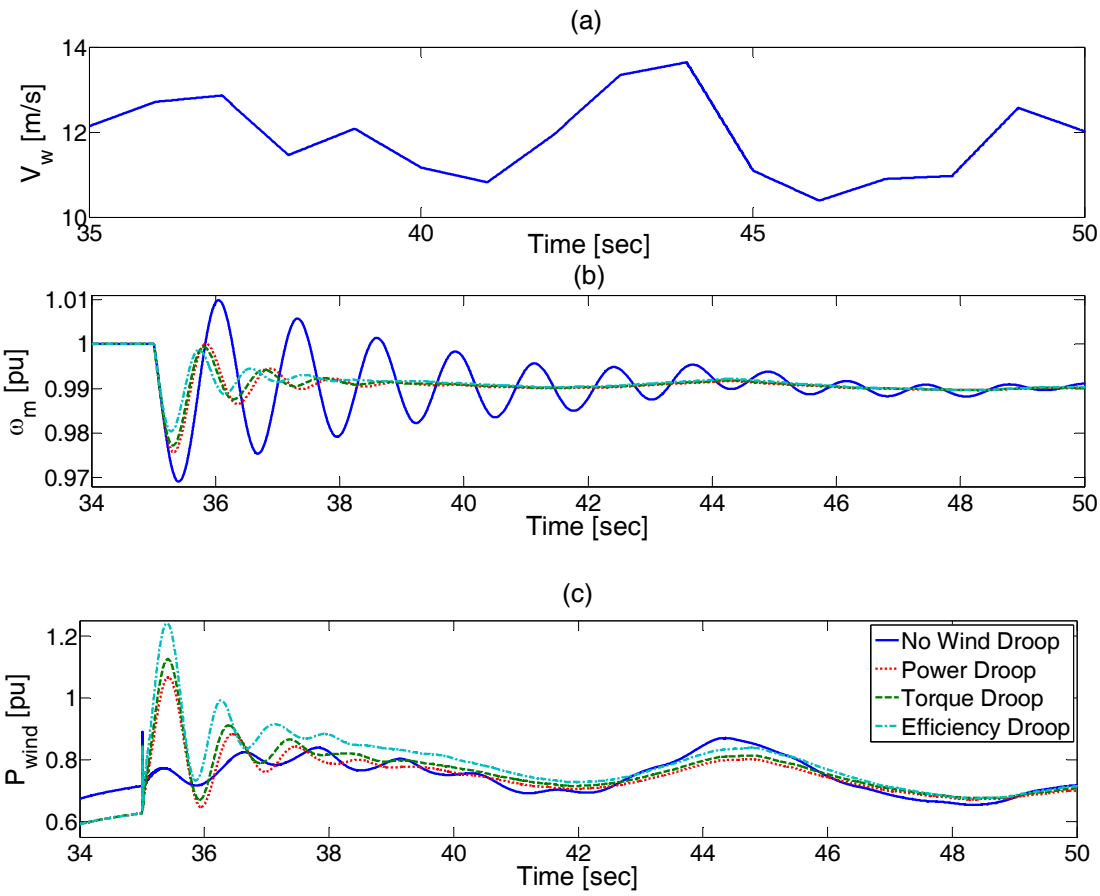

Figure 3-43 Wind-droop with changing wind speed. (a) real pattern of wind speed, (b) the system frequency, (c) The wind generator output active power when in droop-based methods K_{wf}=0.5, m_p=20pu.

3.6 Summary

This chapter presented torque- and power-droop implementations in DFIG-based units by some simple modifications in the conventional control and then, by means of small-signal modeling and eigen-value studies, showed how both techniques influence frequency stability. Sensitivity studies, with respect to the presence of turbine- and inverter-based generators in microgrids; and impacts of pitch-angle controller, wind speed variation and isolated mode operation with only wind-generators, were conducted.

In the present wind-based droop methods, the maximum allowable droop gain is a function of the wind speed. This dependency means either that the entire available capacity of the wind generator will not be used or that instability will threaten the implemented droop wind

generators. This chapter proposed the efficiency droop, a new droop-based method, which can be tuned regardless of the wind speed. Small-signal analyses were used to study the method in depth and compare its influences on both the transient and steady-state frequency performance to the influence of the present methods while adopting minimum approximation. Detailed time domain analyses were used to verify the analytical results of this chapter.

Chapter 4

Impacts of Implementing Frequency Regulation in Wind Turbines – Assessment and Mitigation Strategies

4.1 Introduction

Droop and virtual inertia are two key methods for involving wind power in frequency regulation. However, when these methods are applied, undesirable effects can be induced. Their impact on the generator and system frequency stability and fatigue when the double-mass mechanical dynamics of a wind power generator are considered has not been addressed thoroughly. Consequently, the mitigation of such impacts has not yet been analyzed, as well. The rate of change of power (ROCOP) of a wind generator can be a major factor limiting the effective implementation of frequency regulation methods. Whereas high ROCOP leads to wear and tear and increases the maintenance cost, simply limiting the ROCOP of the generator by a ramp-limit control function will neutralize the desired impact of frequency regulation. Different practical solution methods (i.e., the use of dc-link bandwidth re-tuning or an active damping controller, and a newly developed filter-based method) are discussed, compared and analyzed. This chapter presents a detailed analysis of a complete wind power generator when frequency regulation is implemented.

The contributions of this chapter to the research field are:

1) Developing a detailed small-signal model for analyzing the impact of virtual inertia and droop control on the mechanical tensions of a two-mass wind-turbine generator.
2) Investigating the ROCOP characteristics with and without frequency regulation methods. Analyzing the impact of the rate limiter on the effectiveness of virtual inertia control. Proposing and comparing different methods to mitigate the impact of virtual inertia on the ROCOP.
3) An investigation of the mechanical resonance phenomenon in double-mass wind generators in the presence of droop and virtual inertia,

4) A comparison of the performance of the present solutions: the dc-link bandwidth re-tuning and active damping stabilization methods, and a proposal for a new filter-based stabilizing method to overcome the drawbacks of the former methods.

This chapter is organized as follows. Modeling is presented in Section 4.2. In Section 4.3, the complete model for a wind power generator is used to analyze the ROCOP of a conventional wind power generator. This section discusses the impacts of droop and virtual inertia on the wind generator fatigue, and then, the existing and proposed solutions. Section 4.4 presents the mechanical resonance conflicts associated with droop and virtual inertia implementation. Possible solutions are discussed in this section, as well. In Section 4.5, time-domain simulation results are presented to validate the theoretical analysis. Conclusions are drawn in Section 4.6.

4.2 Modeling

Figure 4-1shows a PMSG-based wind power generator connected to a power network via a back-to-back converter. This physical structure is common among the different control methods. The traditional control uses the generator side converter to extract the maximum available power, whereas the grid side converter is used to regulate the dc-link voltage [87, 101, 164]. Some low-voltage ride through (LVRT) problems motivated researchers to propose a new control scheme (named LVRT-capable PMSG in the reminder of this dissertation) [98, 99, 100]. In this scheme, the generator side converter regulates the dc-link voltage, whereas the grid side converter is used for extracting the maximum available wind power. Such a simple modification does not affect the regular operation of a wind power generator and has advantage of making the generator more robust against severe faults.

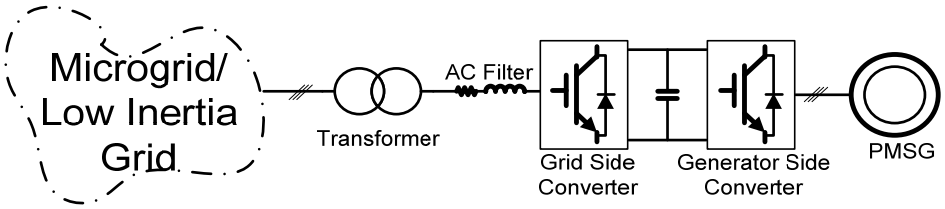

Figure 4-1 PMSG-based wind generator connected to a microgrid/low-inertia grid.

The main function of a wind generator is to extract the maximum available power. Equation (4-1) describes the wind turbine power where; ω_g is the generator speed; and P_m is the mechanical input power. This equation was previously introduced as (3-1) and it is repeated here for the sake of integrity and readibility.

$$P_m = 0.5\rho C_p(\lambda,\beta)A_r v_w^{\ 3}. \tag{4-1}$$

$$P_{g-ref} = K_f K_{OPT}\omega_g^{\ 3} + P_{reg} + P_{ad}. \tag{4-2}$$

Equation (4-2) represents the desired electrical output power of the generator. As described in the previous chapter, the first term on the right side is related to the maximum power extraction, whereas the second term reflects the active power needed for frequency regulation, either by droop or virtual inertia control. When droop necessitates a deviation from maximum power extraction, the deloading factor, K_f, will be less than 1. In other words, in a conventional wind power generator, or virtual inertia-equipped ones, K_f is equal to 1. Reference [171] has discussed why K_{OPT} remains constant as long as the pitch angle is kept zero. The third term is added to actively damp the resonance in the double-mass mechanical system.

In a double-mass mechanical system, a resonance is possible; thus, references such as [88, 102] proposed the use of an active damping method, such as that given by (4-3), to solve the problem. However, the authors of [87] have proved that any generator torque with a positive derivative is enough to suppress the resonance. Therefore, it is easy to prove that even the maximum available power tracking is enough to suppress the resonance. As a result, the active damping controller is not employed in most of conventional wind generators.

$$P_{ad} = \frac{\tau_{ad}s}{\tau_{ad}s+1}\cdot\frac{2\xi_{ad}\omega_{ad}s}{s^2+2\xi_{ad}\omega_{ad}s+\omega_{ad}^{\ 2}}D_v\omega_g. \tag{4-3}$$

The desired generator power is compared to the actual one and fed to a PI power controller to generate the desired current as shown in (4-4). The reference signal $i_{q\text{-}ref}$ is fed to another PI controller to calculate the desired voltage that should be generated by a voltage-source converter. However, it is easy to show that, by proper tuning of the PI current controller, the final actual current of a PMSG, i_q, is dependent on the desired amount, $i_{q\text{-}ref}$, as shown by (4-5), where τ_i is the closed-loop current control time constant.

$$i_{q-ref} = (P_{g-ref} - P_g)(K_p + K_i / s). \tag{4-4}$$

$$i_q = \frac{1}{\tau_i s + 1} i_{q-ref}. \tag{4-5}$$

The electrical output power of the generator, P_e, is related to the q-axis current, i_q through the electromagnetic torque, T_g, as shown by (4-6) and (4-7), where λ_m is the magnet's flux, which is constant in a PMSG; and P represent number of poles.

$$T_g = 0.75 P \lambda_m i_q. \tag{4-6}$$

$$P_g = T_g \omega_g. \tag{4-7}$$

Equations (4-8)–(4-10) describe the mechanical dynamics of the two mass generator-turbine system, where H, T, K_s, D, θ, and ω represent inertia constant, torque, shaft stiffness, damping factor, shaft angle, and rotating speed, respectively; and subscripts B, 0, t, and g denote base, initial, turbine and generator, respectively. Obviously, the initial values of the generator and turbine torque and speed are the same. It is worth mentioning that in some references, a damping proportional to the difference between turbine and generator speeds (i.e., axis damping) is also modeled. However, in the case of a direct-drive PMSG-based wind generator, this damping is very small and is usually neglected [87, 88, 90].

$$\dot{\omega}_t = \frac{1}{2H_t}(T_t - K_s \theta - D_t \omega_t). \tag{4-8}$$

$$\dot{\theta} = \omega_B (\omega_t - \omega_g). \tag{4-9}$$

$$\dot{\omega}_g = \frac{1}{2H_g}(K_s \theta - T_g - D_g \omega_g). \tag{4-10}$$

Equations (4-1)–(4-10) are enough to construct a model of a wind power generator, yet linearization is needed. To avoid repetition and save space, only linearized equations that introduce new states or parameters are presented here.

$$\Delta P_m = A_1 . \Delta\beta + A_2 . \Delta\omega_r + A_3 . \Delta v_w. \tag{4-11}$$

Equation (4-11) represents the linearized form of (4-1), whereas its parameters are previously given in (3-12)–(3-14). Obviously, in a generator with constant pitch angle, A_1 is zero. Similarly, when the generator works at the maximum power extraction point or with virtual inertia implementation, A_2 is zero. However, in droop control, where some deviation from maximum power occurs, A_2 is nonzero.

$$\Delta\dot{\phi}_1 = \frac{-2\xi_{ad}\omega_{ad}\tau_{ad}-1}{\tau_{ad}}\Delta\phi_1 - \frac{{\omega_{ad}}^2\tau_{ad}+2\xi_{ad}\omega_{ad}\tau_{ad}}{\tau_{ad}}\Delta\phi_2 - \frac{{\omega_{ad}}^2}{\tau_{ad}}\Delta\phi_3 + \Delta\omega_g . \tag{4-12}$$

$$\Delta\dot{\phi}_2 = \Delta\phi_1 . \tag{4-13}$$

$$\Delta\dot{\phi}_3 = \Delta\phi_2 . \tag{4-14}$$

$$\Delta\dot{\phi}_4 = \Delta P_{g-ref} - \Delta P_g . \tag{4-15}$$

$\Delta\phi_1$, $\Delta\phi_2$, $\Delta\phi_3$, and $\Delta\phi_4$ are artificial states introduced to augment the dynamics of the controllers in (4-3) and (4-4). All linearized models are utilized to provide the state-space equations of a wind power generator as shown by (4-16) and (4-17).

$$\frac{d}{dt}\begin{bmatrix}\Delta\phi_1\\ \Delta\phi_2\\ \Delta\phi_3\\ \Delta\phi_4\\ \Delta i_q\\ \Delta\omega_g\\ \Delta\theta\\ \Delta\omega_t\end{bmatrix} = \begin{bmatrix} -\frac{2\xi_{ad}\omega_{ad}\tau_{ad}+1}{\tau_{ad}} & -\frac{{\omega_{ad}}^2\tau_{ad}+2\xi_{ad}\omega_{ad}}{\tau_{ad}} & -\frac{{\omega_{ad}}^2}{\tau_{ad}} & 0 & 0 & 1 & 0 & 0\\ 1 & 0 & 0 & 0 & 0 & 0 & 0 & 0\\ 0 & 1 & 0 & 0 & 0 & 0 & 0 & 0\\ 2D_v\xi_{ad}\omega_{ad} & 0 & 0 & 0 & -0.75\omega_0 P\lambda_m & 2T_0 & 0 & 0\\ \frac{2D_v\xi_{ad}\omega_{ad}K_p}{\tau_i} & 0 & 0 & \frac{K_i}{\tau_i} & -\frac{4+3\omega_0 P\lambda_m K_p}{4\tau_i} & \frac{2T_0K_p}{\tau_i} & 0 & 0\\ 0 & 0 & 0 & 0 & -\frac{3P\lambda_m}{8H_g} & -\frac{D_g}{2H_g} & -\frac{K_s}{2H_g} & 0\\ 0 & 0 & 0 & 0 & 0 & -\omega_B & 0 & \omega_B\\ 0 & 0 & 0 & 0 & 0 & 0 & -\frac{K_s}{2H_t} & \frac{A_2-T_0-\omega_0 D_t}{2H_t\omega_0} \end{bmatrix}\begin{bmatrix}\Delta\phi_1\\ \Delta\phi_2\\ \Delta\phi_3\\ \Delta\phi_4\\ \Delta i_q\\ \Delta\omega_g\\ \Delta\theta\\ \Delta\omega_t\end{bmatrix} + \begin{bmatrix}0\\0\\0\\0\\0\\0\\0\\ \frac{A_3}{2H_t\omega_0}\end{bmatrix}\Delta v_w + \begin{bmatrix}0\\0\\0\\1\\ \frac{K_p}{\tau_i}\\0\\0\\0\end{bmatrix}\Delta P_{reg} \tag{4-16}$$

$$\Delta P_g = \begin{bmatrix}0 & 0 & 0 & 0 & 0.75\omega_0 P\lambda_m & T_0 & 0 & 0\end{bmatrix}\begin{bmatrix}\Delta\phi_1 & \Delta\phi_2 & \Delta\phi_3 & \Delta\phi_4 & \Delta i_q & \Delta\omega_g & \Delta\theta & \Delta\omega_t\end{bmatrix}^T \tag{4-17}$$

The developed model could represent both droop and virtual inertia as well as the active damping dynamics. This could be simply adapted to the conventional wind generator case by assigning K_f to 1 and D_v, A_2, and P_{reg} to zero. The state-space model permits observation of the other states and variable in a wind power generation system. Equation (4-18) shows how generator torques could be derived.

$$\begin{bmatrix}\Delta T_g\\ \Delta T_s\\ \Delta T_t\end{bmatrix}=\begin{bmatrix}0 & 0 & 0 & 0 & \dfrac{3\omega_0 P\lambda_m}{4} & 0 & 0 & 0\\ 0 & 0 & 0 & 0 & 0 & 0 & K_s & 0\\ 0 & 0 & 0 & 0 & 0 & 0 & 0 & \dfrac{A_2-T_0}{\omega_0}\end{bmatrix}\begin{bmatrix}\Delta\phi_1\\ \Delta\phi_2\\ \Delta\phi_3\\ \Delta\phi_4\\ \Delta i_q\\ \Delta\omega_g\\ \Delta\theta\\ \Delta\omega_t\end{bmatrix}+\begin{bmatrix}0\\ 0\\ A_3/\omega_0\end{bmatrix}\Delta v_w \tag{4-18}$$

A very similar approach can be used to model LVRT-capable PMSG-based wind generators. The model in (4-16)–(4-17) could also be utilized to model a DFIG-based wind power generation system with very slight modifications. Figure 4-2 shows the frequency responses of PMSG- and DFIG-based wind generators to a change in the wind speed or P_{reg}. Apparently, the responses are very similar, and this allows the result of one type to be generalized for the other as well. The only negligible difference comes from different parameter ranges [90]. The parameters used for typical DFIG- and PMSG-based wind generators are given in the Appendix A.

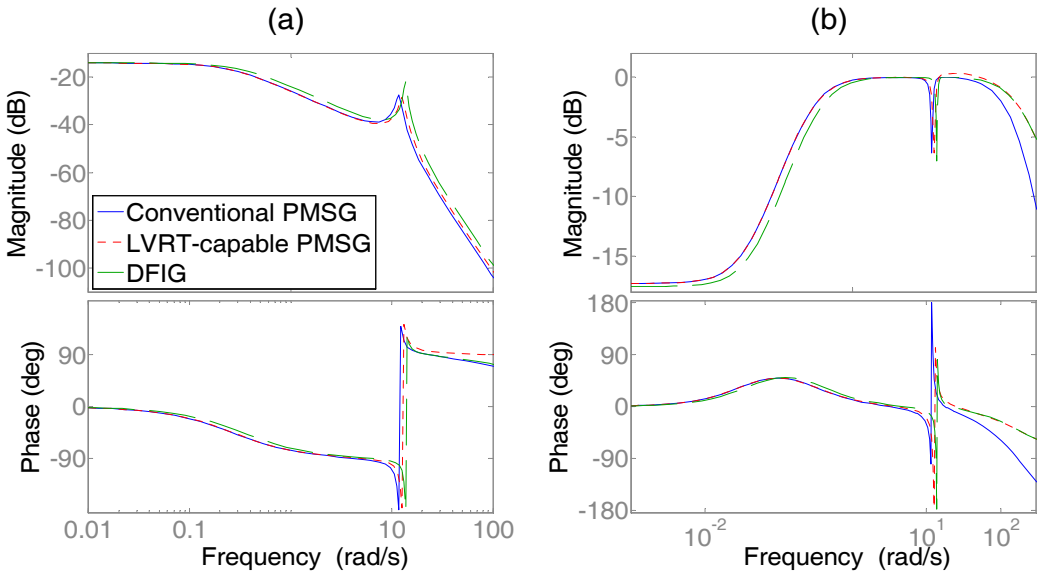

Figure 4-2 Frequency response of (a))$\Delta P_g(s)/\Delta V_w(s)$ (b) $\Delta P_g(s)/\Delta P_{reg}(s$ with V_{w0} = 12 m/s, K_f = 0.8, and D_v = 0 (Disabled Active Damping).

Obviously, all different types of variable-speed wind turbines act very similarly in terms of the frequency regulation. This fact and detailed simulation results allow generalizing the

results of this study, to other variable speed wind generators. These wind generators are compared only in terms of power regulation and frequency stabilization point of view because the main focus of this study is the active power and frequency regulation. Although the different types of wind generators are similar in this manner, they respond differently to voltage disturbances and faults. More basically, their structures and converters ratings are different. In fact, one of the advantages of this modeling approach is its generalizable results despite all the differences among variable-speed wind turbines.

4.3 Fatigue

Whereas the ROCOP concern has already been pointed out in the literature, many questions related to the impacts of implementing frequency regulation methods in wind power generators have been left unanswered. Important among these are the following: (1) What are the reasons for loose ROCOP protection in a conventional wind generator? (2) What is the impact of the frequency regulation method and different levels of frequency regulation implementation? (3) What is the impact of the double-mass mechanical model of a wind turbine? (4) What is the impact of using a simple rate limiter to limit the ROCOP? To thoroughly address these questions and concerns, detailed modeling and analysis are essential.

The model can be utilized to investigate the ROCOP of the generator as shown in Figure 4-3. When the wind speed severely changes from 12 m/s to 10 m/s as a step function, the ROCOP of the generator remains relatively very small. This could explain the absence of strict constraints on the ROCOP in conventional wind power generators. Further, it shows that the parameters of the PI power controller do not play any significant role in determining the ROCOP of the generator.

However, Figure 4-4 gives more insights by showing the rate of changes of torques (ROCOTs). Whereas the maximum torques of the shaft and generator are very close (thus not shown here), the rate of change of the shaft torque, a variable that could not be measured easily or calculated without proper modeling, is much higher than that imposed on the generator. The shaft torque and its derivative are important in characterizing the mechanical

stress on the generator shaft. Very recently, the authors of [103] have shown that these variables could be used to estimate the fatigue in a wind generator. Wind generators are expected to withstand tensions caused by wind speed changes during their lifetime. This means that tensions caused by changes in wind speed should not add up to the fatigue of the generator; thus, the maximum ROCOT of the shaft could be utilized as a threshold for tensions that may result in wearing out of the mechanical system. Despite all of these expectations, and whereas the shaft torque remains acceptably low in this case, adopting the maximum shaft torque and its derivative responding to wind speed change as indices could be questioned because faster aging of wind generators is observed in England and Denmark [83].

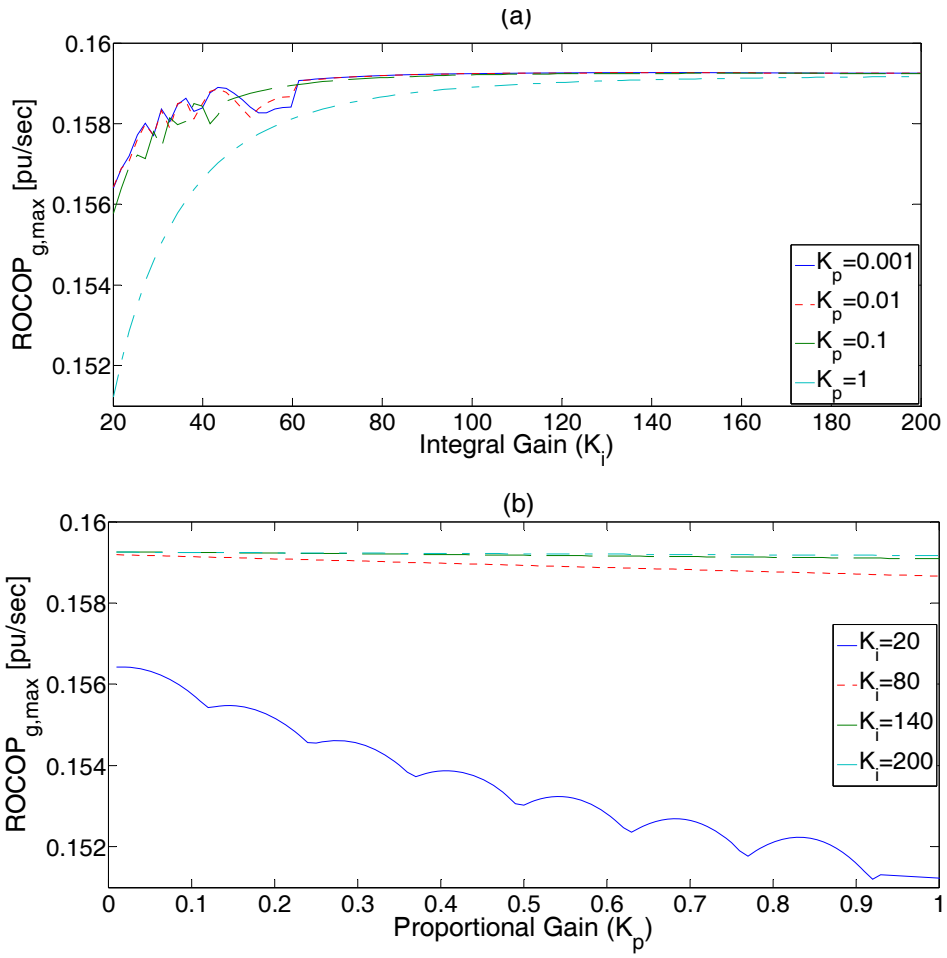

Figure 4-3 Rate of change of power of the wind generator when the wind speed instantaneously changes from 12 m/s to 10 m/s.

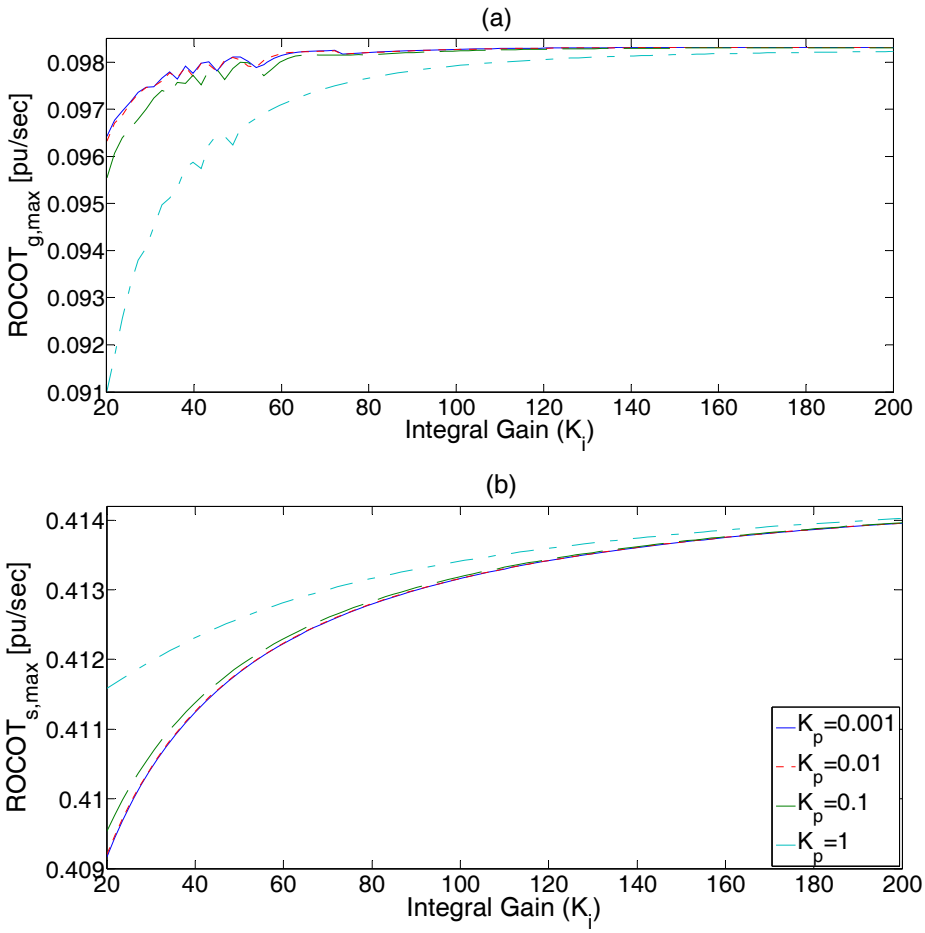

Figure 4-4 Rate of change of torque of (a) the wind generator (b) its shaft when the wind speed instantaneously changes from 12 m/s to 10 m/s.

The model in (4-16) already augments the frequency regulation dynamics implemented in a wind power generator; however, a complete power system is needed to study the impact of these methods on a wind power generator contributing to system frequency regulation.

The system used in the last chapter, Figure 3-7, is studied here too. DG1 that is a variable-speed wind turbine is connected to either a 2.5 MVA DFIG with its rotor interfaced by back-to-back converter or a 2.5 MVA PMSG with full-scale converter. Detailed system parameters are given in the Appendices. The overall system model is also shown in Figure 3-8. Whereas $H_2(s)$ is simply the transfer function that relates the wind speed, v_w, and output power of generator, P_g, and could be easily derived from (4-16) and (4-17), understanding $H_1(s)$ and its

impacts on the rate of change of frequency (ROCOF) and ROCOP needs further discussion, particularly when droop and virtual inertia are implemented.

4.3.1 Droop Method

In the droop-based method, P_{reg} is a linear function of the system frequency, ω_m, as shown by (4-19), where m_p and τ_m are the droop gain and time constant, respectively. Whereas most of the references neglect the time-constant τ_m, it is unavoidable and dictated by the frequency measurement device or practical implementation constraints (e.g., the need for frequency-scale separation between the outer droop control loop and inner power control loop) and could play a significant role in system dynamics.

$$P_{reg} = P_{drp} = \frac{m_p}{\tau_m s + 1}(\omega_{m,ref} - \omega_m). \tag{4-19}$$

Figure 4-5 reveals the impact of droop implementation on the system frequency and the generator power when the load demand, ΔP_L, changes 1.0 pu as a step function. As expected, and as discussed previously in [76, 78], it enhances the maximum frequency deviation without any serious influence on the ROCOF. For further enhancement, the droop gain, m_p, should increase. However, it is limited by some stability problems as discussed in [76]. Even in the stable range, it leads to a higher ROCOP as shown in Figure 4-5(c), which could be undesired. It should be noted that this result is for a severe change of 1.0 pu in the demand. Because the model is linear and the demand is acting as an external disturbance on the linearized system dynamics [162], the impact of any change in the demand on the linearized model could be easily obtained by scaling the response due to the 1.0 pu change.

Instead of using the maximum instantaneous ROCOF, the average rate, $ROCOF_{ave}$, is used. Owing to the finite response time of the power regulator loop, which is modeled by a low-pass filter with a time-constant τ_m in (4-19), the frequency regulation controller (either droop or virtual inertia), cannot respond instantaneously to a mismatch between load and generation. As a result, the maximum instantaneous ROCOF, which occurs as a spike right after the disturbance, is out of control with these frequency regulation methods. Consequently, the maximum instantaneous ROCOF does not convey enough information. On

the contrary, the $ROCOF_{ave}$ which is obtained by dividing the maximum frequency deviation, $|\Delta f_{max}|$, by its occurrence time, Δt_{max}, as shown in (4-20), is much more meaningful. The ROCOF will be discussed in more details in the following sections.

$$ROCOF_{ave} = \frac{|\Delta f_{\max}|}{\Delta t_{\max}}. \tag{4-20}$$

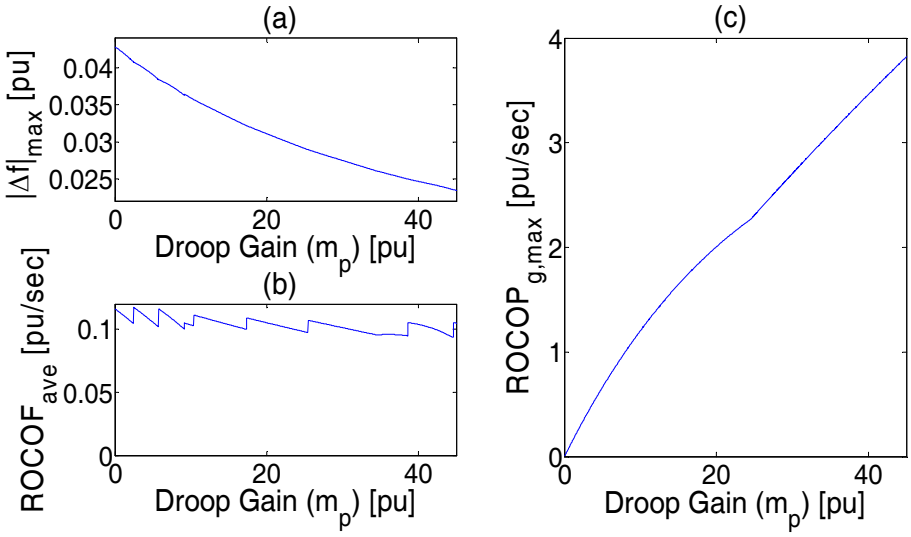

Figure 4-5 Impact of increasing the droop gain on (a) maximum frequency deviation, (b) average rate of change of frequency, and (c) maximum rate of change of power of the generator with $D_v = 0$, $v_w = 12$ m/s, $\tau_m = 0.1$ s, and $K_f = 0.8$.

Observing the torques could help understand the situation in a better way. Figure 4-6 illustrates the maximum torque and ROCOT applied to the generator, shaft and turbine. The turbine never experiences a high torque, and this could be attributed to its much heavier rotating mass and relatively soft shaft. On the other hand, the maximum values of the generator and the shaft torques are near each other.

Despite the large change in the load demand ΔP_L, and the relatively large range of the droop gain, m_p, the maximum torques of the generator and the shaft also remain acceptable**.** However, from the ROCOT perspective, the situation is different. The ROCOT tolerated by the shaft is almost twice that in the generator, and in high droop gains, it could be damaging. This figure proves why relying solely on the maximum torque or ROCOT of the generator

could lead to misleading results. This point is missed in the literature, where only the ROCOP or ROCOT of the generator is considered.

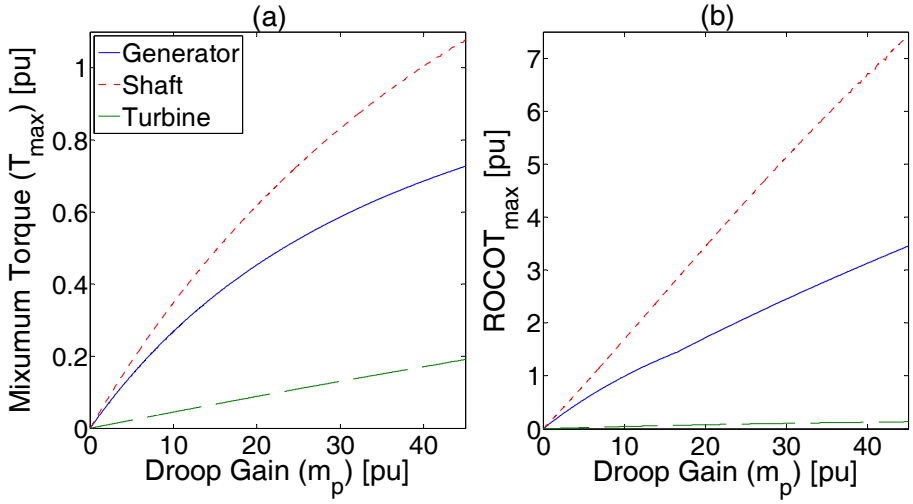

Figure 4-6 Impact of increasing the droop gain on (a) maximum torque, and (b) maximum rate of change of torque of the generator, shaft and turbine with $D_v = 0$, $v_w = 12$ m/s, and $K_f = 0.8$.

The other interesting observation is the impact of the droop time constant on the system performance as shown in Figure 4-7. Whereas it shows that increasing the time constant could reduce both the shaft and the generator ROCOT, it also neutralizes the desired effect of droop control.

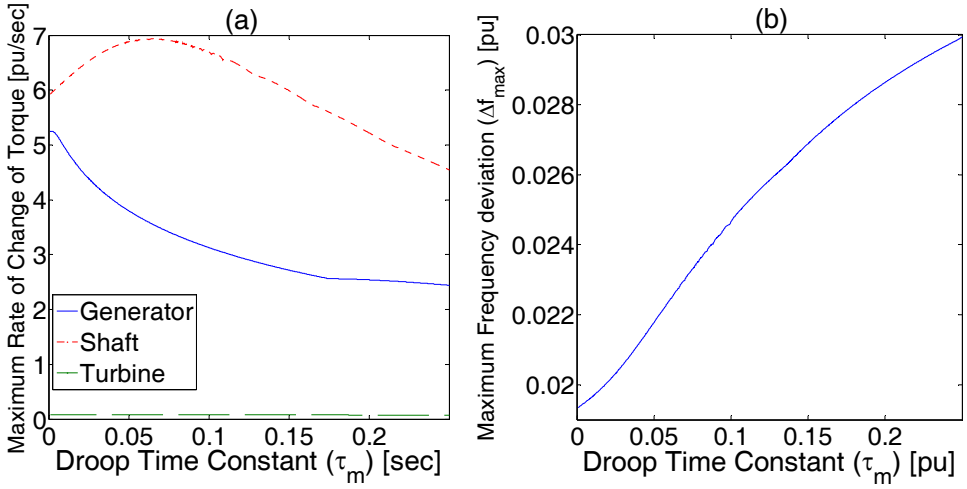

Figure 4-7 Impact of the droop time-constant on (a) maximum rate of change of torque of the generator, shaft and turbine, and (b) maximum frequency deviation with $D_v = 0$, $v_w = 12$ m/s, $m_p = 40$ pu, and $K_f = 0.8$.

Although active damping is added to solve the problem of the mechanical resonance in a two-mass wind generator, its impact on the frequency regulation method could be questioned. Figure 4-8 shows that this impact, whether on the frequency response or torques, is not significant.

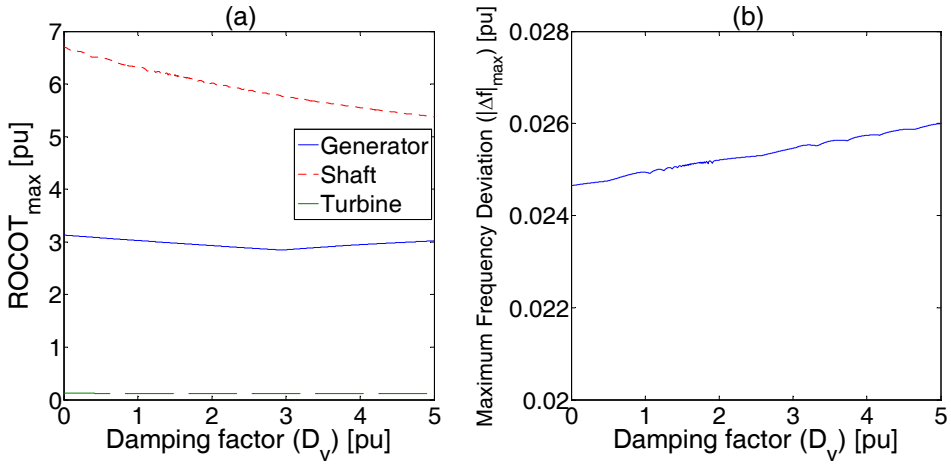

Figure 4-8 Impact of active damping on (a) maximum rate of change of torque of the generator, shaft and turbine, and (b) maximum frequency deviation with τ_m = 0.1 s, v_w = 12 m/s, m_p = 40 pu, and K_f = 0.8.

4.3.2 Virtual Inertia

Virtual Inertia is the alternative method proposed to cope with the deficiencies of the droop method. First, it does not require any permanent deviation from the maximum power point, i.e., K_f = 1. Secondly, it emulates the inertia of a synchronous generator as shown in (4-21), where M_{vi} and τ_{vi} are the virtual inertia gain and time-constant, respectively. In addition, it could impact the ROCOF significantly as shown in Figure 4-9. It is worth mentioning that ROCOF relays in 60-Hz systems are usually set to react to a threshold between 0.1 and 1.2 Hz/s [172, 173].

$$P_{reg} = P_{vi} = -\frac{M_{vi}s}{\tau_{vi}s+1}\omega_m \tag{4-21}$$

Whereas virtual inertia is capable of enhancing both the maximum frequency deviation and ROCOF, the maximum rate of change of power applied to the generator is very high compared to droop or wind speed change. Figure 4-10 reveals the torque characteristics in the wind generator with virtual inertia implemented. Here, virtual inertia is much faster than

the mechanical system; therefore, the ROCOT sensed by the shaft remains close to that imposed on the generator. However, the oscillations, appearing because of the two-mass nature of the mechanical system, result in a higher torque (not its rate of change) imposed on the shaft. Similar to the droop method, the virtual inertia time constant does not play a significant role in changing the ROCOTs; slight reductions in the ROCOTs can be gained at the cost of worse system frequency behavior, which is not desired.

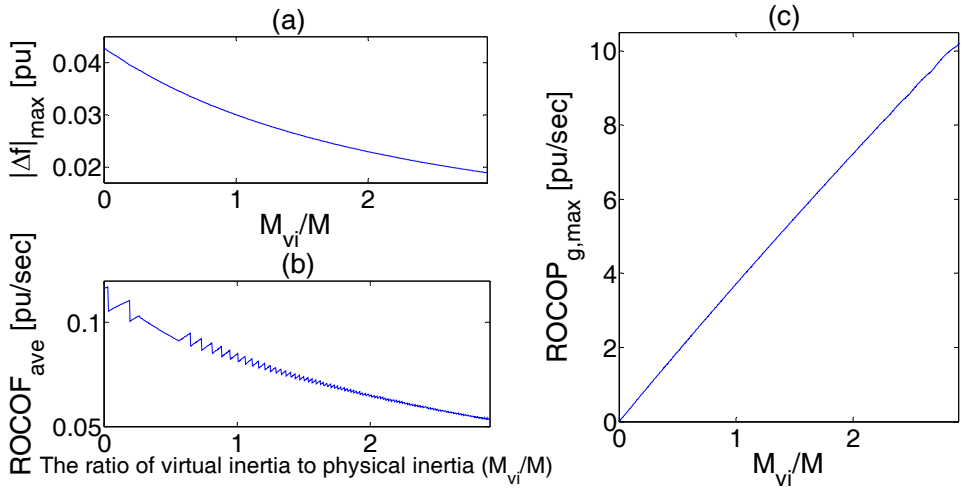

Figure 4-9 Impact of increasing the virtual inertia on (a) maximum frequency deviation, (b) average rate of change of frequency, and (c) maximum rate of change of power of the generator with $D_v = 0$, $v_w = 12$ m/s, $\tau_m = 0.2$ s, and $K_f = 1$.

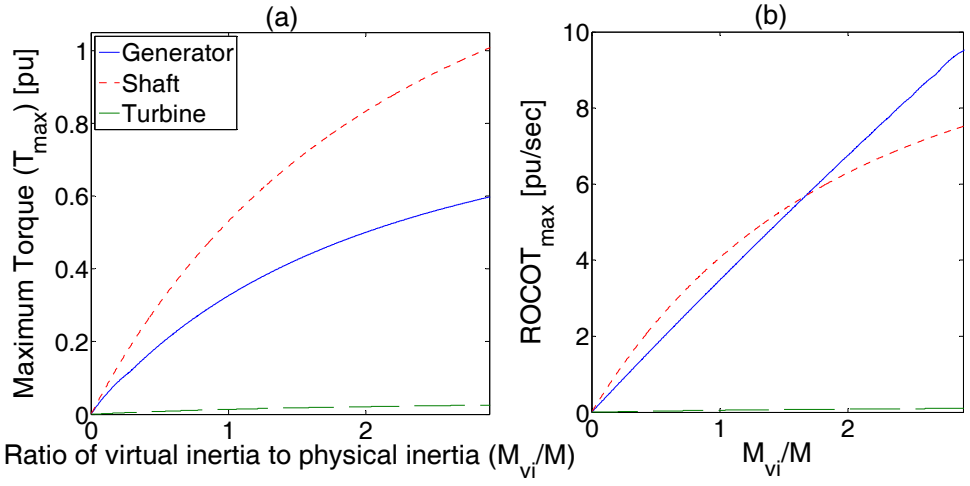

Figure 4-10 Impact of increasing the virtual inertia gain on (a) maximum torque, and (b) maximum rate of change of torque of the generator, shaft and turbine with $D_v = 0$, $v_w = 12$ m/s, and $K_f = 1$.

Similar to the droop control case, the active damping dynamics does not affect the frequency behavior or the ROCOT significantly when virtual inertia is implemented as shown in Figure 4-11. However, suppressing the mechanical oscillations enhances the shaft torque characteristics slightly. Figure 4-10 shows that in the case of virtual inertia, both the shaft and generator suffer from mechanical tensions.

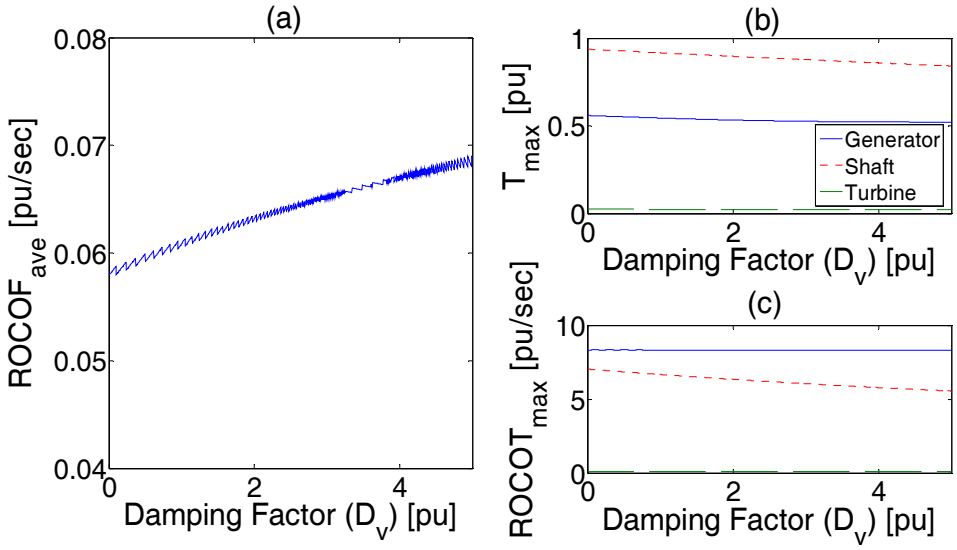

Figure 4-11 Impact of active damping on (a) maximum rate of change of frequency (b) maximum torque and (c) maximum rate of change of torques of the generator, shaft and turbine with τ_{vi} = 0.23 s, v_w = 12 m/s, M_{vi}/M = 2.5, and K_f = 1.

Although active damping has been previously utilized to damp the mechanical resonance in double-mass systems, the presented analysis in this chapter shows that it is not helpful to mitigate possible violation of the ROCOP limit associated with frequency regulation implementation. This phenomenon could be explained by considering the bandpass nature of the active damping controller, which is only devoted to actively damp the resonance frequency of the mechanical system. The soft shaft and double-mass dynamics are still present under frequency regulation implementation and contribute to increase the mechanical tensions on the wind power generator. Therefore, there is a need to develop a solution that is more comprehensive.

4.3.3 Solutions

The previous analysis shows that frequency regulation can expose the mechanical parts of a wind generator to much higher tension than a conventional generator. Although this problem has never been explored thoroughly, a simple solution based on the use of a ramp-rate limiter (RRL), has been adopted by some researchers with no further investigation.

4.3.3.1 Ramp-Rate Limiter—Conventional but Limited Effectiveness

Intuitively speaking, an RRL could constrain the rate of change of the generator power or torque. This method, however, has serious drawbacks. First of all, in all cases reported in the literature, the shaft torque is completely ignored, and only the generator torque is considered. Secondly, only the impact of the RRL on the maximum frequency deviation is studied whereas the ROCOF, which is another very important index in characterizing the effectiveness of frequency regulation, is not considered. In addition, the impact of different levels of virtual inertia or droop incorporation is not studied.

To address these deficiencies, a thorough analysis is conducted. Thus, in the simulated system, P_{reg} has been processed by an RRL, with the parameters suggested in [82, 84, 85], before being applied to the wind model in (4-16). Figure 4-12 shows the impact of the RRL on the system frequency regulation when virtual inertia is adopted. Clearly, the RRL neutralizes the impact of virtual inertia when its contribution is high. Also, the impact of the RRL on the ROCOF is more drastic. In other words, the RRL is useful when wind power does not play an important role in frequency regulation.

Whereas the fast nature of virtual inertia and its high ROCOP makes these results expectable, the impact of the RRL on the droop performance is more interesting. As Figure 4-13 reveals, with higher droop gains of wind power, the RRL could make the system unstable; this situation has never been discussed in the literature. However, this situation could also be explained as follows. The RRL makes the droop sluggish and slow. Previously, in a synchronous machine with a slow governor, it has been observed that increasing the droop gain could result in instability while it enhances the steady-state behavior of the system [50, 76].

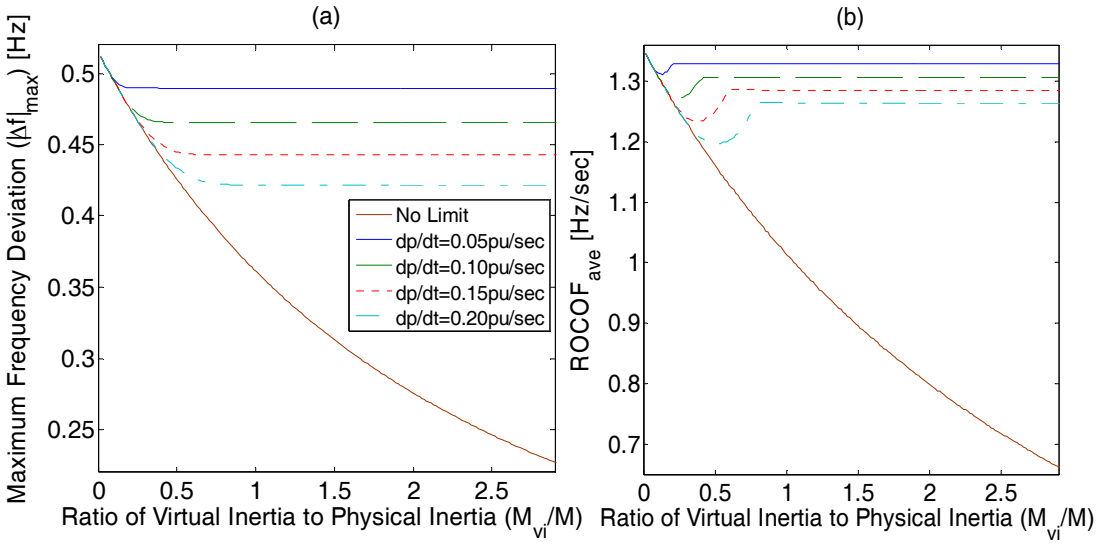

Figure 4-12 Impact of the power RRL on virtual inertia. $\Delta P_L = 0.2$ pu and $\tau_{vi} = 0.23$ s, $v_w = 12$ m/s, and $K_f = 1$.

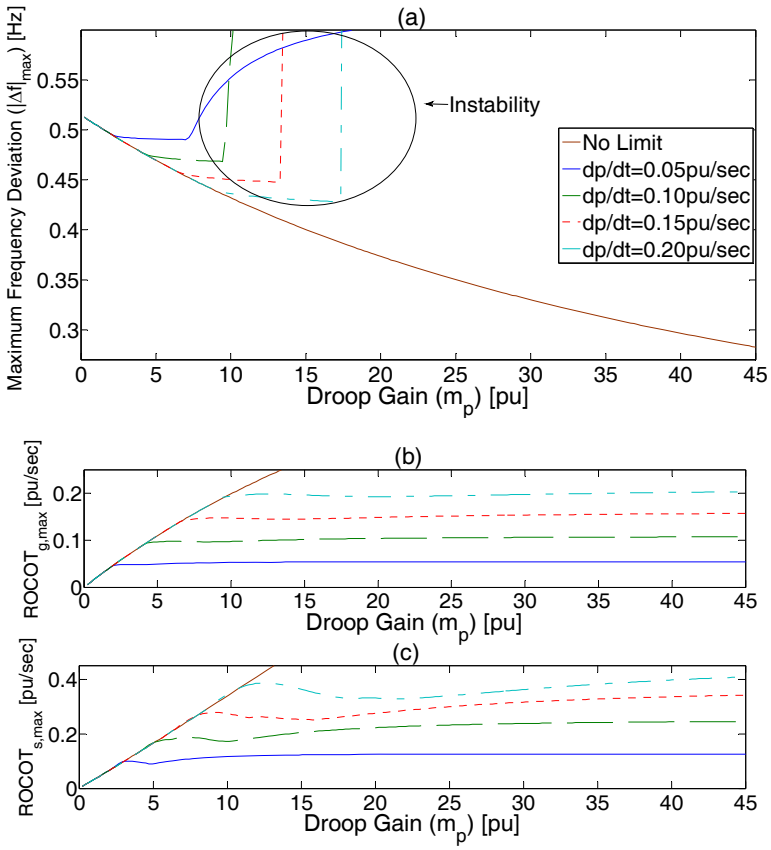

Figure 4-13 Impact of power RRL on droop. $\Delta P_L = 0.2$ pu, $\tau_{vi} = 0.1$ s, $v_w = 12$ m/s, and $K_f = 0.8$.

Another interesting observation is related to the ROCOT of the shaft. Although it is also limited, its maximum value is still higher than what the generator experiences. The shaft torque and its rate of change can be calculated by considering the relation between maximum ROCOTs of the shaft and the generator and using the detailed modeling approach presented in this chapter.

4.3.3.2 Another Source of Energy

On the one hand, employing wind power for frequency regulation leads to mechanical tensions in the wind generator; on the other hand, the RRL, if it does not result in instability, neutralizes the impact of frequency regulation. To solve this problem, another limited-size source of energy is needed to respond to the fast transient changes and relieve the stress imposed on the wind generator. A possible solution is the utilization of a dc-link capacitor. It is already present in the generator configuration and could minimize the cost. However, it is worth mentioning that the main duty of this component is the dc-link voltage regulation, and this new responsibility should not interfere with its main function.

Different methods could be used to manage the energy between these two sources; a simple yet effective method is the use of a second-order filter as given by (4-22). It is a well-behaved linear function that allows the elimination of nonlinearities induced by the RRL. The input of the filter is either the virtual inertia or droop power, whereas the output is fed as P_{reg} to (4-16). The remaining power, denoted here as P_{comp}, could be produced by the dc-link. Assuming that the closed-loop dc-link voltage control is fast enough, the reference value of the dc-link voltage, V_{ref}, could be corrected as given in (4-24) to generate P_{comp}, where V_{nom} and C_{dc} are the nominal value and the capacitance of the dc-link, respectively, and ω_n and ξ_n refer to the cutoff and damping factor of the second-order filter, respectively. It is worth mentioning that this implementation method guarantees the restoration of the dc-link voltage to its nominal value after disturbance. The controller is depicted in Figure 4-14.

$$P_{reg} = \frac{2\zeta\omega_n s + {\omega_n}^2}{s^2 + 2\zeta\omega_n s + {\omega_n}^2} P_{vi/drp}. \tag{4-22}$$

$$P_{comp} = P_{vi/drp} - P_{reg}. \tag{4-23}$$

$$V_{ref}{}^2 = V_{nom}{}^2 + (2/C_{dc}s)P_{comp}. \tag{4-24}$$

The impact of the proposed method on the droop and virtual inertia could be observed in Figure 4-15 and Figure 4-16, respectively. It improves the frequency regulation slightly because the dc-link voltage is much faster than the mechanical parts of a wind generator. Unsurprisingly, this could reduce the ROCOTs significantly. To make a comparison, without this method, the maximum ROCOT observed by the shaft with the same droop gain or virtual inertia was more than 6 pu/s as shown in Figure 4-6 and Figure 4-10.

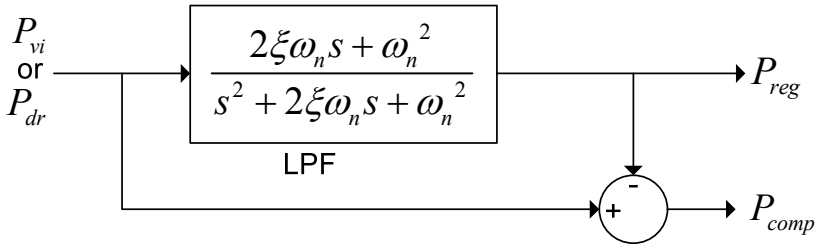

Figure 4-14 The proposed controller.

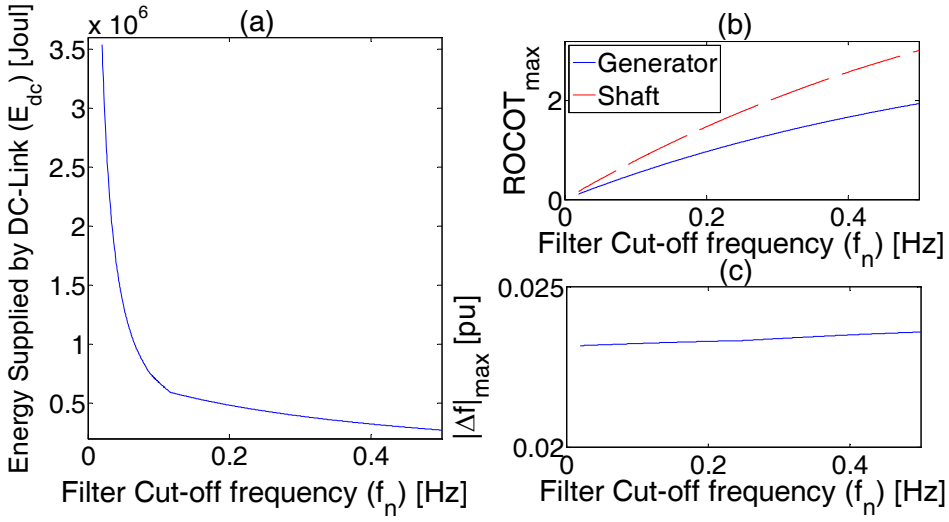

Figure 4-15 Impact of the filter cutoff frequency on droop. ΔP_L = 0.2 pu, m_p = 40 pu, τ_{vi} = 0.1 s, v_w = 12 m/s, and K_f=0.8.

Such a huge enhancement is achieved at the cost of fluctuations in the dc-link voltage. Here, these oscillations are presented in terms of energy; however, they could easily be interpreted in terms of voltages as shown by (4-25) and (4-26), where subscripts “max” and

"min" denote the maximum and minimum, respectively; E stands for energy; and the "+" and "-" superscripts describe the absorption and injection modes of energy, respectively.

$$E_{\max}^{+} = 0.5C_{dc}(V_{\max}^{2} - V_{nom}^{2}). \tag{4-25}$$

$$E_{\max}^{-} = 0.5C_{dc}(V_{nom}^{2} - V_{\min}^{2}). \tag{4-26}$$

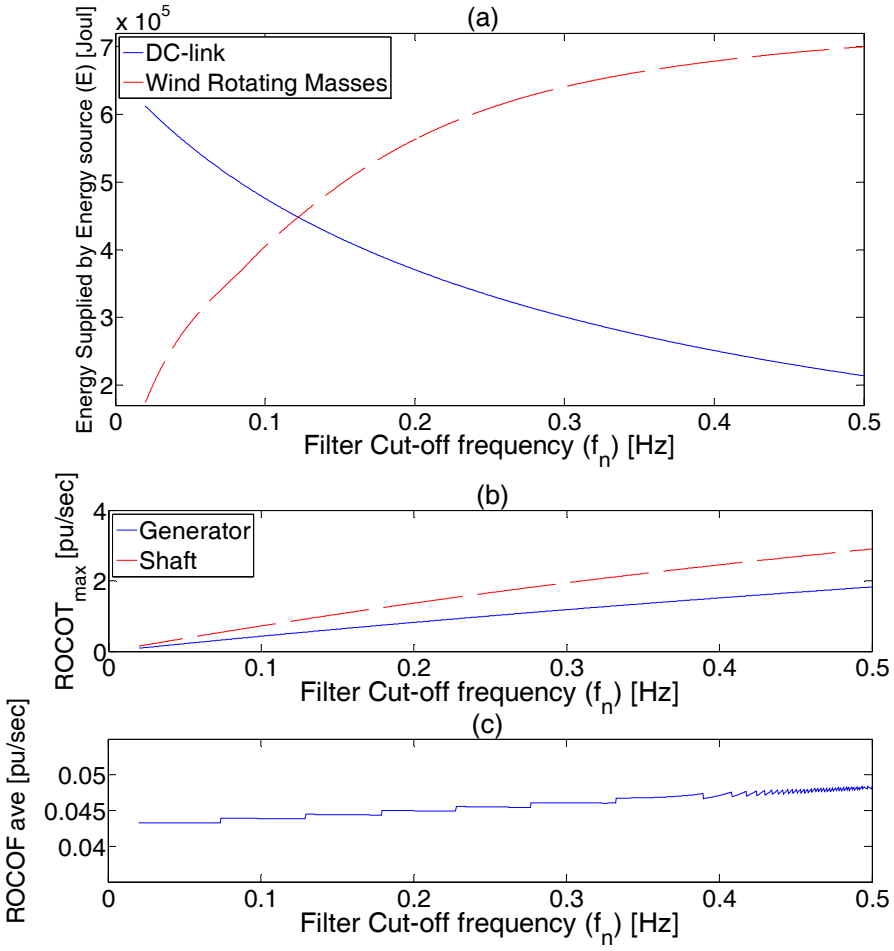

Figure 4-16 Impact of the filter cutoff frequency on virtual inertia. $\Delta P_L = 0.2$ pu, $M_{vi}/M = 2.5$, $\tau_{vi} = 0.1$ s, $v_w = 12$ m/s, and $K_f = 0.8$.

Because there are usually some restrictions on the dc-link voltage fluctuations, (4-25) and (4-26) in addition to the energy diagram shown in Figure 4-15(a) and Figure 4-16(a) could be utilized to calculate any possibly needed upgrade in the dc-link capacitance. Here, one of the advantages of a PMSG-based turbine over a DFIG-based one could be mentioned. Because a full-scale back-to-back converter is utilized in a PMSG, it benefits from a dc-link with higher stored energy. This could remove the need for any upgrade or, at least, minimize the upgrade.

The converters in a PMSG-based generator do not need any upgrades whereas both the dc-link and converters may need upgrades in a DFIG generator.

On the other hand, Figure 4-15(a) and Figure 4-16(a) show that by proper tuning of the second-order filter cutoff frequency, a reasonable ROCOT could be gained with a reasonable amount of energy supplied by the dc-link. Figure 4-16(a) provides more insights. When the dc-link is used to incorporate a wind power generator in frequency regulation, the use of the wind generator rotating mass could be questioned. However, this figure shows that even with very tight filters, a considerable amount of energy is still supplied by the rotating masses of the generator. In other words, if the stored kinetic energy is not used for frequency regulation, a much larger source of energy in the dc-link is needed. This situation is more obvious in droop implementation, which supplies energy for a longer time.

4.4 Mechanical Resonance

The risk of the resonance in the mechanical part of a PMSG-based turbine was initially mentioned and discussed because the turbine was responding to wind speed changes. In conventional wind generators, the resonance is damped even when the active damping controller is disabled, as Figure 4-2(a) demonstrates. Such stability is caused by the maximum power point tracking (MPPT) implementation in the wind power generator. A positive derivative of the generator torque in respect to the generator speed ($dT_g/d\omega_g$) is needed to remove the risk of resonance [87], and, in a conventional wind generator, MPPT guarantees this derivative to be always sufficiently positive, and thus no additional damping is needed [174]. This observation explains why many conventional wind generators still work properly without any active damping method.

Therefore, conventional wind generators with no frequency regulation do not usually face the stability problem. However, the implementation of frequency regulation can have adverse impacts on the mechanical resonance of the generator, and this risk shows the importance of studying the impact of frequency regulation methods on the mechanical system of wind generators.

Analyzing the impacts of incorporating the frequency regulation methods in a wind generator on its drive-train necessitates studying a complete power system as shown in Figure 3-7. A LVRT-capable PMSG, whose complete model can be found in Appendix A, is used for this part of study. Similarly, The wind power generation model can be combined with the synchronous generator model to form the overall frequency dynamics model of the system, as shown in Figure 3-8 and discussed the last section.

Figure 3-8 also reveals the differences between the conventional and frequency-regulating wind generators. In the former, $H_1(s)$ is zero since the generator is not involved in the frequency regulation, and, therefore, the generator responds to only the wind speed change. In the regulation frequency mode, the wind power generator becomes a part of the closed-loop feedback system. This feedback can intensify the oscillatory response and increase the risk of the mechanical resonance in the generator. This phenomenon needs a detailed investigation as follows.

4.4.1 Droop

Figure 4-17 depicts the root locus of the dominant poles and zeros of the power system, shown in Figure 3-7 and Figure 3-8, when the droop gain is increasing. While the poles, which were initially more influential on the system frequency behavior, become more stable, some other poles move toward the right-half plane. These poles are related to the natural resonance frequency of the double-mass dynamics of the wind power generator. Accordingly, implementing the droop in the wind power generator exposes its mechanical system to forces that can stimulate the resonance. This phenomenon becomes more serious as the contributions of the wind power generator to the system frequency regulation increases. This instability does not show up when droop is not applied.

One important factor to be considered is the effect of the initial wind speed. Figure 4-18(a) shows the dominant system poles whereas more focused results are revealed in Figure 4-18(b) and (c). By increasing the initial wind speed, the rotational mass poles, Figure 4-18(b), start to move toward the right half-plane whereas the other dominant non-canceled poles do not move significantly, Figure 4-18(c). This movement of poles means that

contributing to the frequency regulation by using the droop method at higher wind speeds is riskier. This higher risk is the reason for conducting most of the analyses in a relatively high-speed range here.

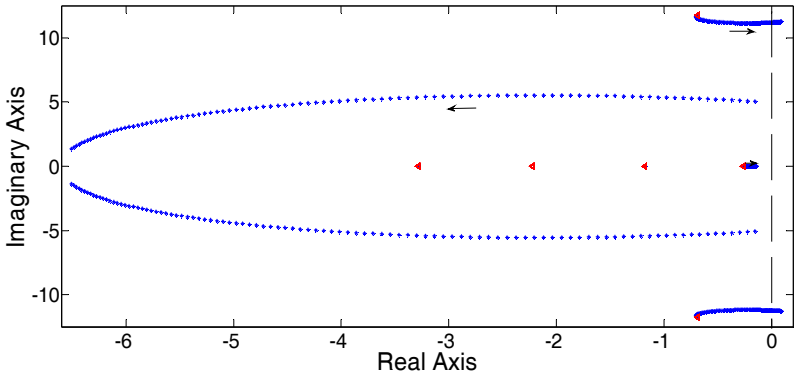

Figure 4-17 Root locus of dominant poles and zeros of the system when m_p is increasing V_w=12 m/s, and τ_m=0.01 s.

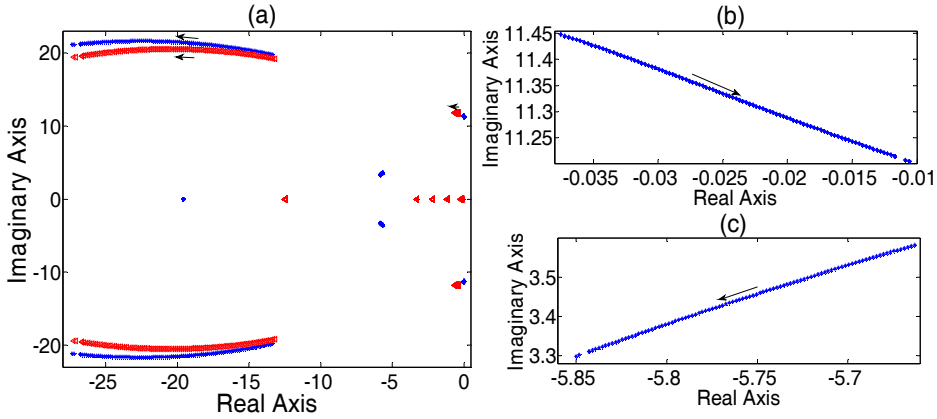

Figure 4-18 Root locus of dominant poles (blue) and zeros (red) of the system when wind speed is increasing from 6 m/s to 12 m/s and m_p=80pu, τ_m=0.01 s.

The other interesting information that can be obtained from this analysis is the impact of the deloading factor. Previously, references like [74] and [76] avoided sub-synchronous deloading, obtained by using a deloading factor, K_f, greater than one. These references argued that this kind of deloading may result in some problems. Although using K_f>1 is desirable because of its under-speeding feature, especially in high wind speeds, the literature does not thoroughly quantify or describe the impacts of such a selection on the system stability. Figure 4-19 shows the dominant system eigenvalues when K_f is increasing from 1 to 1.5 in high and low wind speeds. In high wind speeds, where under-speeding is desired, a

sub-synchronous deloading can make the system unstable. On the contrary, K_f>1 does not yield a stability problem for the wind generator in relatively low wind speeds, as shown in Figure 4-19. Some other difficulties, rather than the mechanical resonance, may prevent the utilization of a higher than one deloading factor in low wind speeds, as discussed in [74, 76].

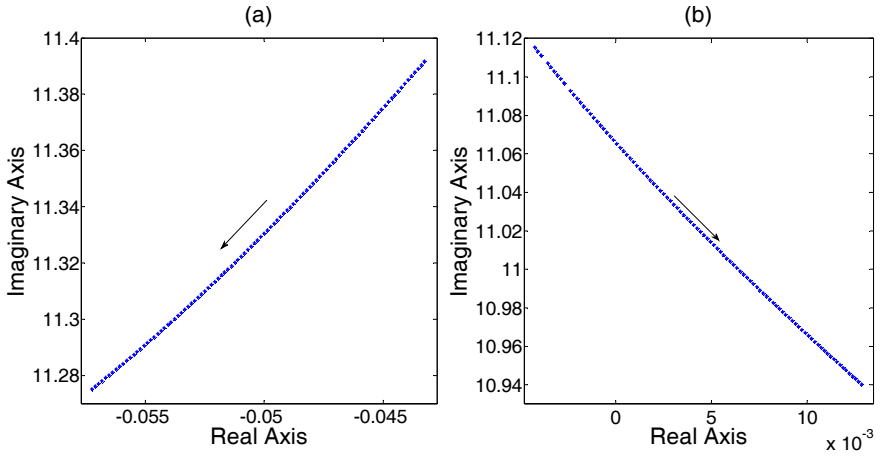

Figure 4-19 Root locus of dominant poles and zeros of the system when deloading factor, K_f, is increasing from 1 to 1.5, m_p=80 pu, τ_m=0.01 s and (a) V_w= 6 m/s; (b) V_w=12 m/s.

Further, the modes that move toward the right half-plane are related to the mechanical system of the wind power generator. In other words, choosing K_f higher than one makes the wind generator shaft more vulnerable to the mechanical resonance when the turbine contributes to the frequency regulation. A single-mass model of the wind generator is incapable of revealing this phenomenon.

Another point that demands further investigation is the use of a dead-banded droop. This frequency regulation method does not respond to disturbances until the frequency violation from the nominal frequency exceeds a pre-defined dead-zone. The presented model in this thesis can be simply modified to implement a dead-band. A dead-band block should be added before a simple droop, such as (3-19), denoted as $\Delta P_{reg}/\Delta\omega_m$ in the block-diagram representation in Figure 3-8.

Although the new model is not linear and cannot be used for eigenvalues analyses, it can be very beneficial. Consider Figure 4-20, which depicts the system frequency responding to a load demand disturbance when the wind droop has a relatively high contribution to the

frequency regulation. The simple droop stimulates the mechanical resonance, and dead-bands with small zones are incapable of preventing the instability. On the other hand, large dead-zones can solve the instability problem but at the cost of neutralizing or reversing the desired influence of the droop method, as shown in Figure 4-21. In these analyses, the conventional control method of PMSG is used.

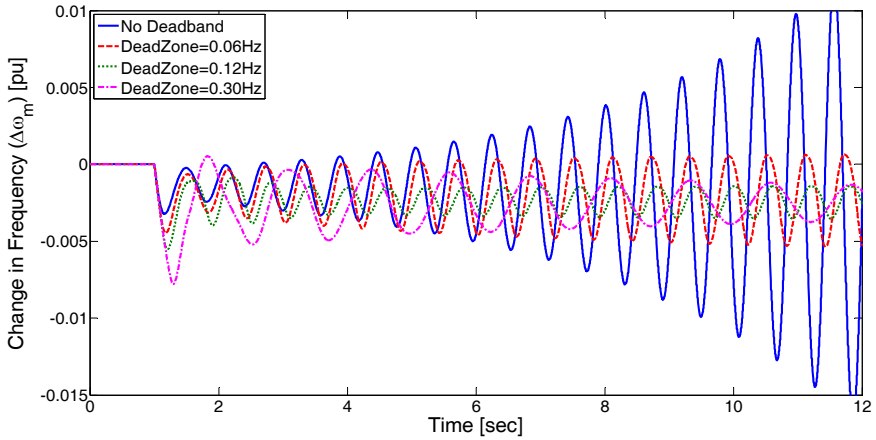

Figure 4-20 Impact of dead-band on droop implantation in wind generator, K_f=0.8, m_p=80, v_w=12m/s, ΔP_L=0.2pu.

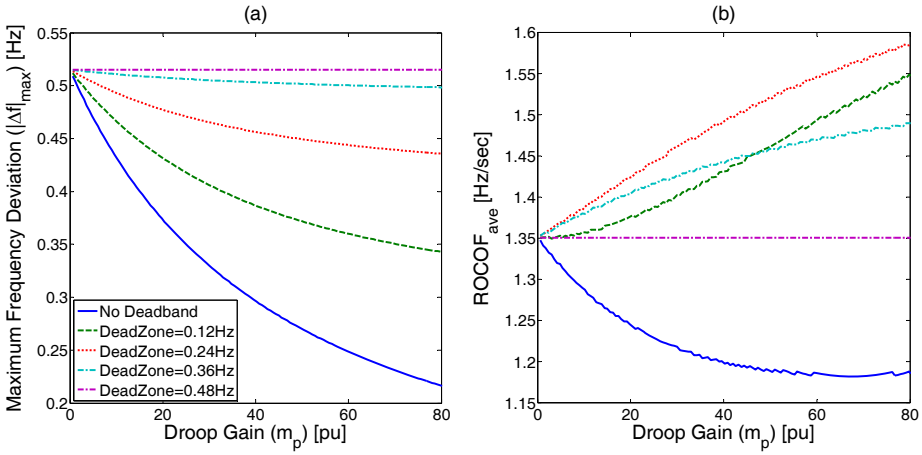

Figure 4-21 Impact of adoption of dead-band in wind droop on the system frequency, K_f=0.8, m_p=80, v_w=12m/s, ΔP_L=0.2pu.

4.4.2 Virtual Inertia

Similar to the droop control, the virtual inertia can result in stability problems for wind power generators contributing to the power system frequency regulation. Figure 4-22 verifies this argument, showing that increasing the virtual inertia gain leads to instability. The unstable

modes also correspond to the mechanical system of the wind power generator. The case of virtual-inertia-related instability is more demanding since the large droop gains may endanger the system stability even in a single-mass model by extracting a power larger than the reserve delaoded power, and thus they are usually restricted [76]. On the other hand, no threat has been previously observed in implementing virtual inertia in a single-mass model [55]. The obtained results have significant meaning: a wind power generator with no contribution to the frequency regulation does not experience any stability problem with its natural resonance. The analysis indicates that when a wind generator contributes to the frequency regulation (either droop or virtual inertia), its stability cannot be understood or characterized separately, as has been done in the classical studies so far. The frequency regulation acts as a feedback mechanism that makes the interaction between the system frequency and the wind-turbine mechanical dynamics possible. Consequently, the stability of wind generators should be studied as a part of the integrated system dynamics. This point has never been considered in the literature.

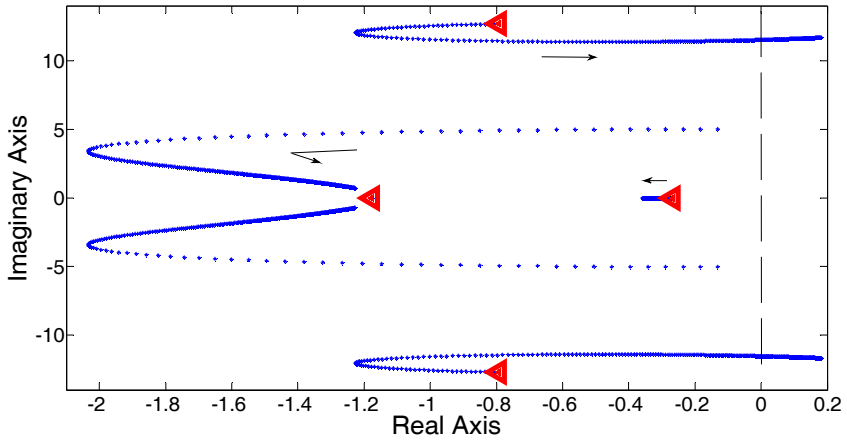

Figure 4-22 Power system dominant poles (blue stars) and zeros (red triangles) when virtual inertia gain is increased.

4.4.3 Mutual Impacts

Another interesting case is the impact that several wind generators has on each other when they contribute to the frequency regulation. One of the advantages of the model presented in Figure 3-8 is its straightforward extension, where a new wind power generator can be simply added as a parallel block to the existing wind generators model.

Many different situations can be studied, the mutual interactions of the droop and the virtual inertia. Figure 4-23(a) shows the system eigenvalues in such a case where one wind generator is equipped with a constant droop gain, and the other wind generator employs the virtual inertia with an increasing gain. In the presence of only one generator, the system remains stable, whereas the presence of both generators simultaneously leads to instability. Figure 4-23(b) presents the system eigenvalues under different wind generator parameters, showing that instability happens sooner when wind generators have the same resonance frequency. In other words, when wind generators contributing to the frequency regulation have similar parameters, they can amplify the resonance phenomenon and increase the severity of the problem. Traditional wind generators do not use the system frequency as a medium to intensify their natural mechanical resonance.

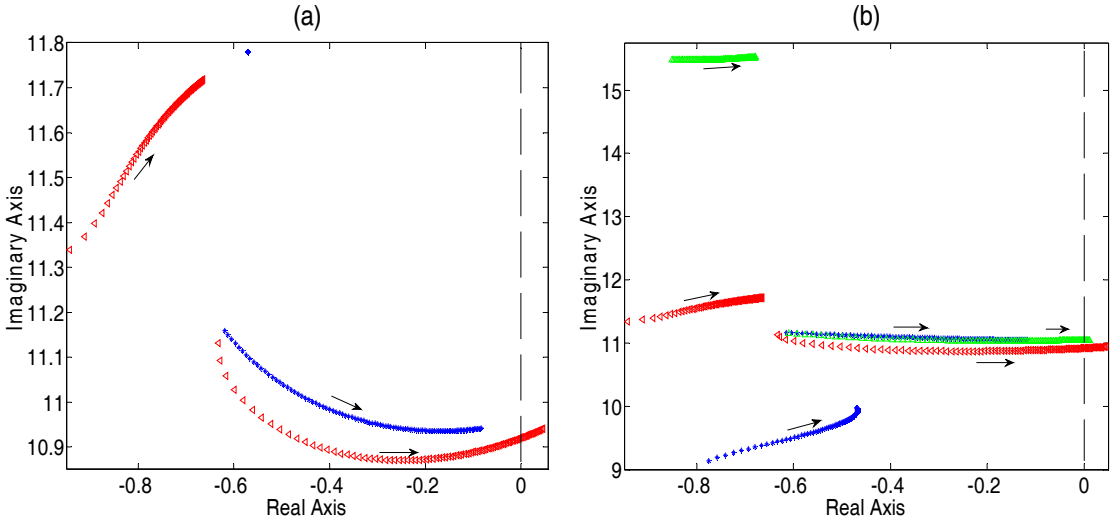

Figure 4-23 System dominant poles with two wind generators, one is equipped with a droop and virtual inertia gain implemented in the other increases from zero. (a) no droop (blue) versus m_p=40 (red) (b) m_p=40 for all generators whereas the stiffness of shaft of droop-based wind is 1.2 (blue), 1.6(red) and 2.8 pu (green), and the stiffness of the other generator is fixed at 1.6 pu.

4.4.4 Solutions

The analysis presented in the previous section showed that a high contribution of the wind generator to the frequency regulation, whether by the droop or the virtual inertia, can stimulate the natural resonance of a wind generator. The undesirable stimulation is a very serious concern in the wind power generators participating in the frequency regulation. On

the contrary, in conventional wind generators, with no frequency regulation, MPPT guarantees enough damping, and no passive or active damping is needed.

A very conservative approach for addressing the problem can be to limit the contribution of wind power generators to the frequency regulation. Although the presented analysis can be employed to find the safe penetration limits as well, a more efficient and permanent solution that ensures the system stability at higher contributions of wind generators to the frequency regulation seems necessary. Utilizing a ramp rate limiter cannot be also considered as a solution, for when the last section has already questioned its effectiveness.

Because the problem stems from the lack of mechanical damping, a trivial and passive solution can be the adoption of a physical damper. However, the theoretical analysis shows that some relatively high virtual inertia gains require a high damping gain which is not acceptable due to high losses.

A better solution can be utilizing the controller to damp the resonance or prevent the stimulation of the rotating masses unstable dynamics. These methods, however, are usually based on using another source of energy. An available alternative is to use the dc-link capacitor of the back-to-back interfacing converter. However, the main responsibility of this component is regulating the dc-link voltage, and this new duty should not seriously interfere with in the voltage regulation requirements.

The following section discusses three possible solutions and their advantages and disadvantages. Their impacts on the natural resonance frequency and the dc-link voltage regulation are also investigated.

4.4.4.1 DC-Link Bandwidth Tuning

The control scheme in a LVRT-capable PMSG (which regulates the dc-link voltage by the machine-side converter) allows the implementation of a simple yet effective method. It is based on supplying a considerable amount of the needed energy by the dc-link so that the rotating mass is not exposed to high torques that can stimulate the resonance. This goal can be achieved by re-tuning the PI-controller of the dc-link voltage regulator.

By assuming a relatively fast current controller, the bandwidth can be estimated as a function of the dc-link regulator parameters. By proper tuning of the integral gain, the desired bandwidth can be obtained. Reducing the dc-link voltage controller bandwidth to save the system stability allocates the poles related to the dc-link behavior close to the right half-plane; however, zeros accompany these poles. These zeros remarkably mitigate the dc-regulating poles' influence on the system frequency behavior. This method, however, can be used in only a LVRT-capable PMSG controller. As well, it negatively affects the dc-link voltage regulation during the wind speed change or LVRT since the dc-link controller is not as fast as it should be. Although these problems can be addressed by some modifications in the controller, the method loses its most important advantage, which is simplicity.

4.4.4.2 Active Damping Method

As discussed, although the active damping method is not usually adopted in a conventional wind generator, but has been adopted in some studies, usually those related to fault ride-through [88] and [174]. Here, the same method is utilized to address the conflicts of the frequency regulation. Equation (4-27) formulates the active damping method in which ω_{ad} is the natural frequency of the shaft. As expected (shown in Figure 4-24), by increasing the active damping gain, D_v, the system becomes more stable in both the droop and the virtual inertia methods. While the rotating masses modes move significantly to the left, the poles related to the frequency behavior do not change considerably.

$$V_{ref}{}^2 = V_{nom}{}^2 + \frac{D_v}{\tau_{ad}s+1}.\frac{2\xi_{ad}\omega_{ad}s}{s^2+2\xi_{ad}\omega_{ad}s+\omega_{ad}{}^2}\omega_g. \tag{4-27}$$

Classically, the active damping gain is tuned by considering only the wind generator dynamics. However, the resonance in the frequency regulating wind turbines occurs because of the mutual impact of the wind generator and the rest of the power system. Therefore, the integrated system can still become unstable when active damping is implemented in individual wind generators. In other words, designing the active damping gain necessitates studying the complete power system. With any major change in the system, e.g., the incorporation of another wind generator in frequency regulation or changes in a droop gain of a thermal generator, re-tuning of the active damping controller may be necessary.

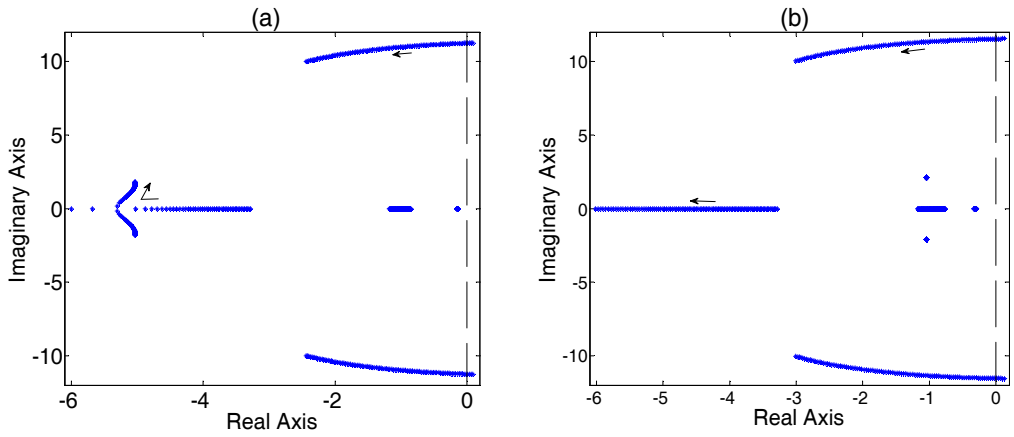

Figure 4-24 Dominant poles of the system when the active damping gain, D_v, increases from 0 to 5 pu. (a) Droop (b) Virtual inertia.

4.4.4.3 Filter Method

Similar to the first method, the dc-link is used here to respond to the faster changes in the power due to the frequency regulation, but does not use the controller bandwidth as a lever. Instead, the filter method like the active damping method modifies the reference to the dc-link voltage [153]. The needed modification is shown in (4-28), which, with slight modifications, can also be employed in the conventional PMSG controller. The added term is the power needed for the frequency regulation, which is processed by a high-pass filter (responding to faster changes) and integrated to change the power to the needed energy. The integration is essential because the controller regulates the square of the dc-link voltage, which is proportionally related to its energy.

$$V_{ref}{}^2 = V_{nom}{}^2 - \frac{2}{C}\cdot\frac{1}{s}\cdot\frac{s^2}{s^2 + 2\zeta\omega_n s + \omega_n{}^2}P_{reg}. \tag{4-28}$$

Figure 4-25 depicts the frequency responses of the transfer functions relating the wind generator rotating speed, $\Delta\omega_g$, to changes in the load demand, ΔP_L. Firstly, the results once again support the main argument of this chapter: with the frequency regulation implementation in a wind power generator, the network and the load disturbances can stimulate the resonance of the wind generator. On the contrary, a conventional wind turbine is, ideally, supposed to show no significant reaction to changes in the load demand, and also no contribution to the frequency regulation. Secondly, these results verify that all the

discussed compensation methods work, but both the filter and the active damping methods are more successful in resolving the resonance problem. The active damping (red curve) and filter (purple curve) methods yield smoother and more damped responses at the resonance frequency. On the other hand, the undamped case (blue curve) and the dc-link bandwidth tuning method yield a high-gain peak at the resonance frequency.

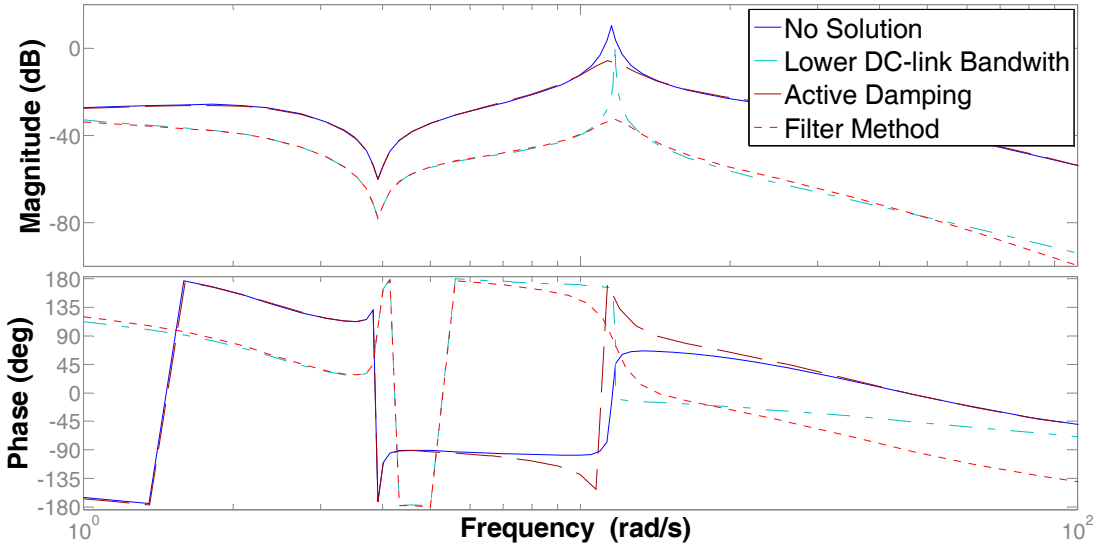

Figure 4-25 Frequency response of $\Delta\omega_g(s)/\Delta P_L(s)$.

The proposed filter method has another advantage over the previous methods. It never imposes fluctuations on the dc-link voltage while the generator is responding to wind speed changes. In conventional wind generators, the dc-link voltage remains very close to its nominal value when it responds to the perpetual unpredictable wind speed changes, as is desired in a VSC with a vector control. Obviously, the red curve in Figure 4-26(b), representing the energy provided by the dc-link reacting to a wind speed change, remains very close to zero, no matter which frequency is chosen for the filter. The undesired needed energy increases when the active damping gain increases, as shown by the red curve in Figure 4-26(a). The filter method also reduces the mechanical tensions caused by frequency regulation methods. The rate of change of power (ROCOP) shown in Figure 4-26(d) is associated with the mechanical tensions of the wind turbine shaft [153]. On the contrary, the active damping method has almost no influence on the mechanical tensions (see

Figure 4-26(c)). Therefore, both methods succeed in stabilizing the mechanical system. However, the filter method also reduces the mechanical tension and fatigue caused by the frequency regulation. Reducing the generator fatigue leads to longer lifetimes of the generator. This phenomenon occurs because the filter method takes responsibility for the higher frequency content of the frequency regulation power whereas the active damping method acts only around the resonance frequency. However, this superiority is gained at the cost of a higher contribution of the dc-link capacitance to the frequency regulation. The blue curves in Figure 4-26(a) and (b) depict the energy provided by the dc-link. A high amount of needed energy means that employing these methods may necessitate re-rating the dc-link capacitance. As compared with the filter method, the active damping method demands less energy from the dc-link.

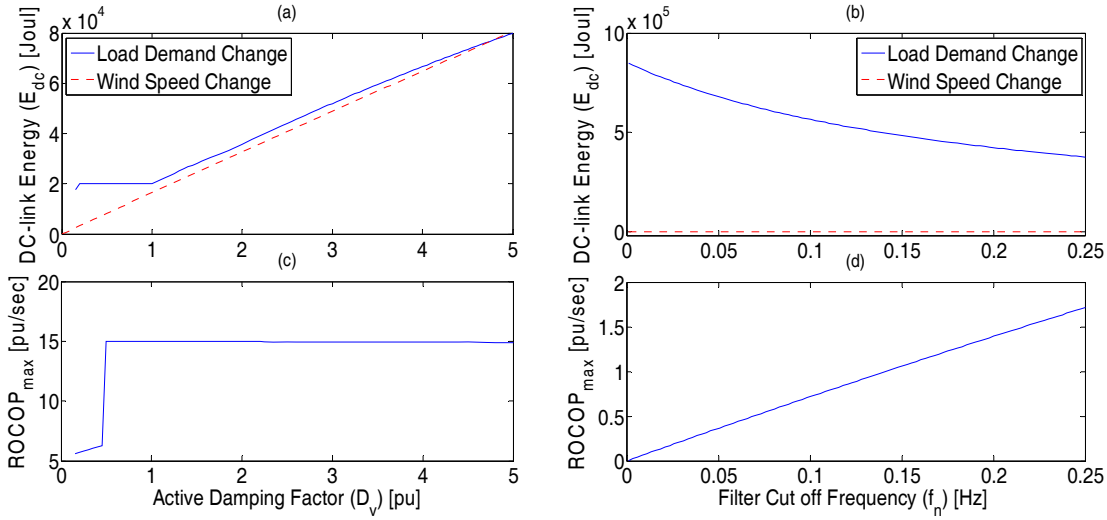

Figure 4-26 (a), (b) DC-link energy required by the active damping and filter methods, (c), (d) generator ROCOP. In the active damping method, the system becomes stable with D_v>0.5 pu while in the filter method, for the whole bandwidth range used here, the system is always stable.

A comparison between (4-27) and (4-28) can explain the roots of their differences. The filter method receives the frequency regulating power as the input and does not allow the stimulating forces of this reference power to reach the mechanical system. On the other hand, the active damping method uses the generator rotating speed, as an input, to produce a damping torque around the mechanical system natural resonance frequency, regardless of the source of the disturbance, the wind speed change or the frequency regulating power.

4.5 Time-Domain Simulation Results

In this section, time-domain simulation, based on detailed nonlinear models of the system components, is used to verify the analytical results discussed in the previous sections. The system shown in Figure 3-7 is used here as well. The studied disturbance in almost all cases is an intentional islanding occurring at t = 35 s. The Matlab/Simulink package is employed for the simulation studies.

4.5.1 Model Verification

Figure 4-27 compares the responses of the small-signal model and the detailed nonlinear time-domain simulation model. Both models have the same parameters and are excited by the same disturbance, which is an intentional islanding event at t = 0. The responses of both models are very close. The negligible difference between the responses could be attributed to linearization and neglecting copper loss in the small-signal model. However, it should be noted that for contingencies which lead to large changes in the operating point (e.g., frequency control), the small-signal model may lead to inaccurate results.

Figure 4-27(c) also shows how wind-based droop uses over-speeding (the optimal rotating speed is 1.08 pu) to utilize some reserve power for frequency regulation. More details on this issue can be found in [76].

4.5.2 Fatigue

4.5.2.1 No External Limitation

In this part, no limitation on the ROCOP or ROCOT is applied. First of all, Figure 4-28 shows the ROCOP and ROCOT when, instead of islanding, wind speed abruptly changes from 12 m/s to 10 m/s at t = 35 s. This verifies the analytical finding in this chapter that despite the severe change in the wind speed, the ROCOP of the generator remains relatively very low. It also verifies that the shaft experiences a higher ROCOT compared to the generator.

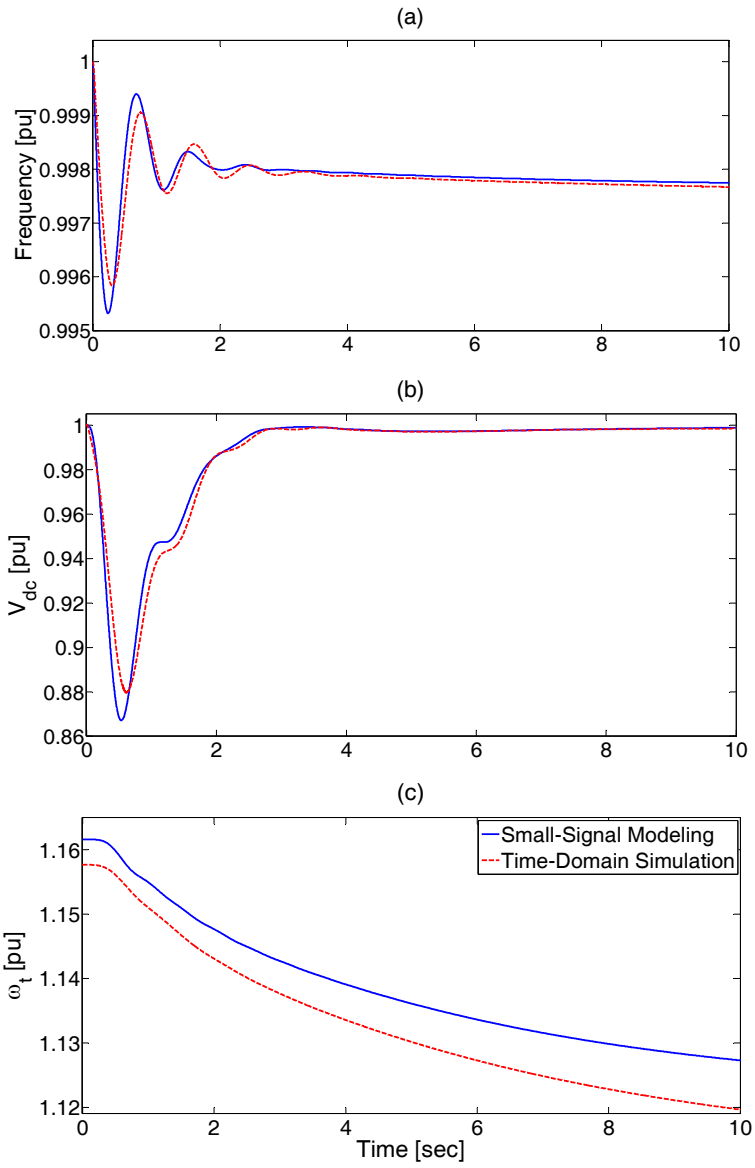

Figure 4-27 Comparing the responses of the time-domain simulation and small-signal models. (a) System frequency, (b) Wind generator dc-link voltage, (c) Turbine rotating speed. Droop is implemented in the wind generator with m_p = 40 pu, V_w = 12 m/s, and K_f = 0.8.

Figure 4-29 shows the impact of implementing frequency regulation in a wind power generator. Whereas the frequency behavior is enhanced significantly, the high ROCOTs are not negligible. Comparing this scenario, Figure 4-29(c) and (d), to the case of wind speed change, Figure 4-28(b), proves that frequency regulation leads to a high ROCOT issue that does not exist in conventional wind generators. Such high tensions could speed up the aging and complicate the already present problem of wear and tear of wind generators.

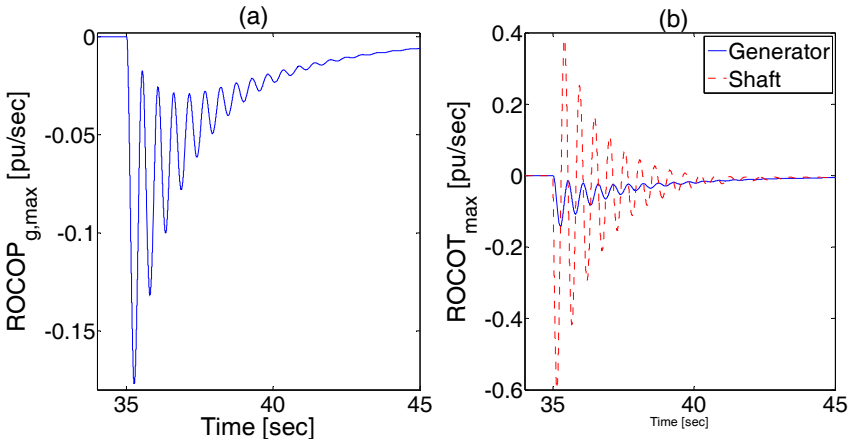

Figure 4-28 Response of the wind generator to a step change in wind speed from 12 m/s to 10 m/s. (a) ROCOP of PMSG, (b) ROCOT of the shaft and the generator.

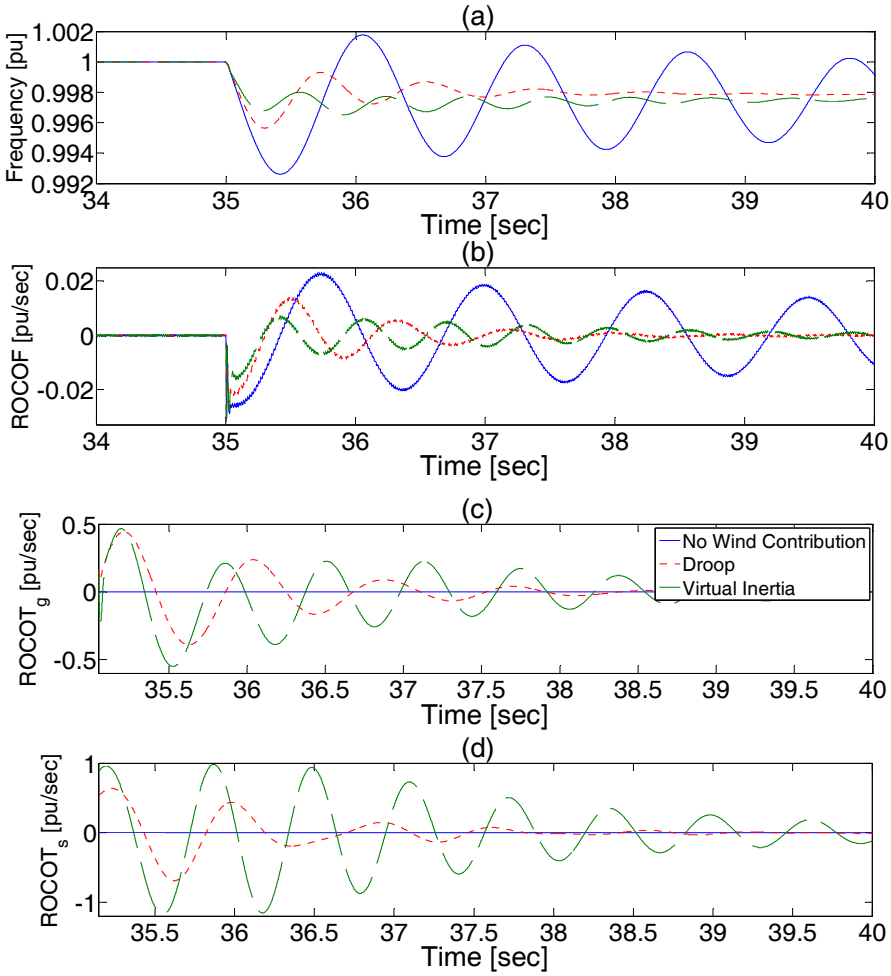

Figure 4-29 Impact of implementing frequency regulation in a wind power generator on (a) system frequency (b) ROCOF (c) ROCOT of the generator (d) ROCOT of the shaft. m_p=40 pu and M_{vi}/M=5.

4.5.2.2 Ramp-Rate Limiter

As discussed, this solution, despite its availability and wide utilization in the literature, yields several problems when frequency regulation is implemented. Figure 4-30 confirms how the desired virtual inertia impact is neutralized by the RRL. It is worth mentioning that, owing to lack of space, only the high contribution of virtual inertia is shown here, whereas in lower contributions, the impact of the RRL is not that severe.

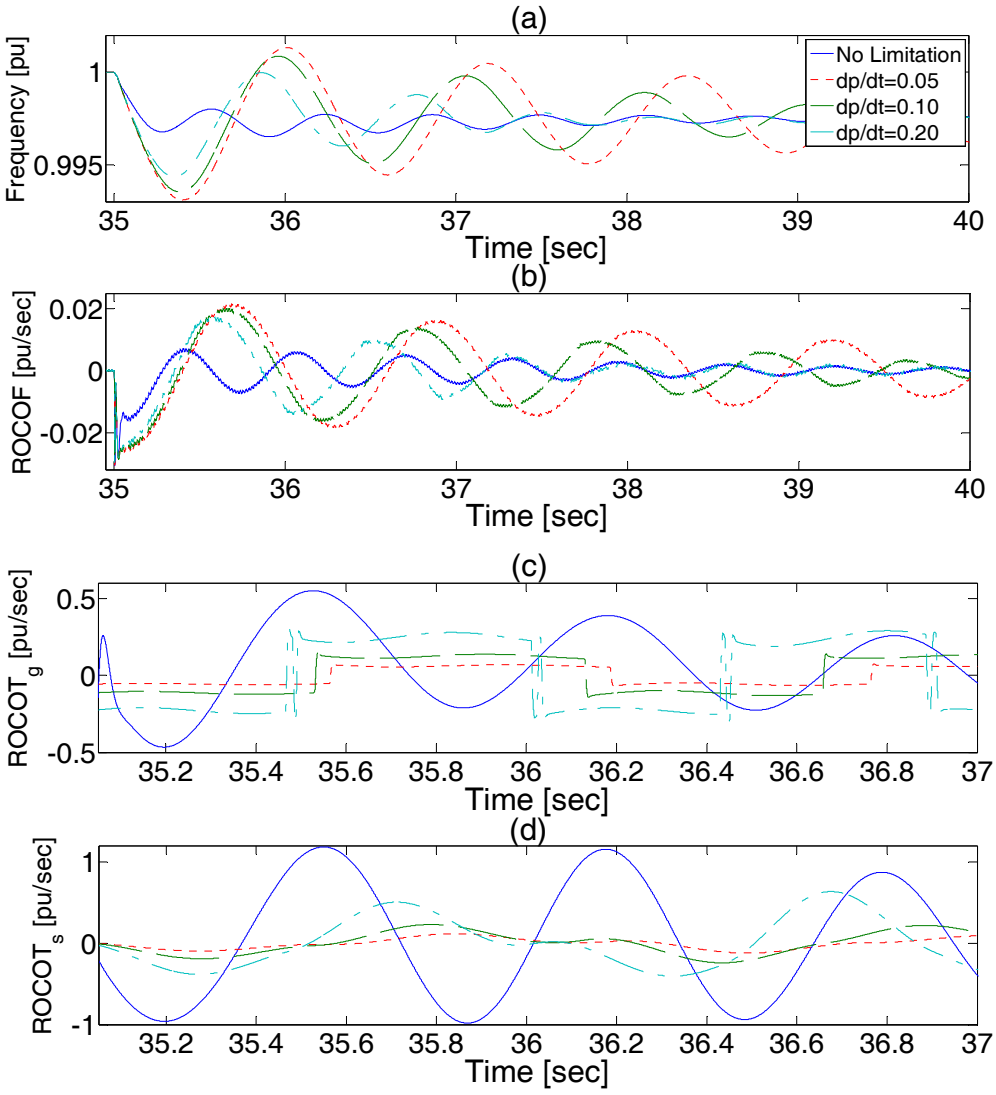

Figure 4-30 Impact of using a power RRL on wind-based virtual inertia. (a) System frequency (b) ROCOF (c) ROCOT of the generator (d) ROCOT of the shaft. M_{vi}/M=5.

Figure 4-31 depicts the interaction of droop and RRL. It verifies the analytical findings of neutralizing the frequency regulation and destabilizing the power system. Thus, in the presence of the RRL, the droop function, which was added to improve the frequency stability of the system, makes it unstable.

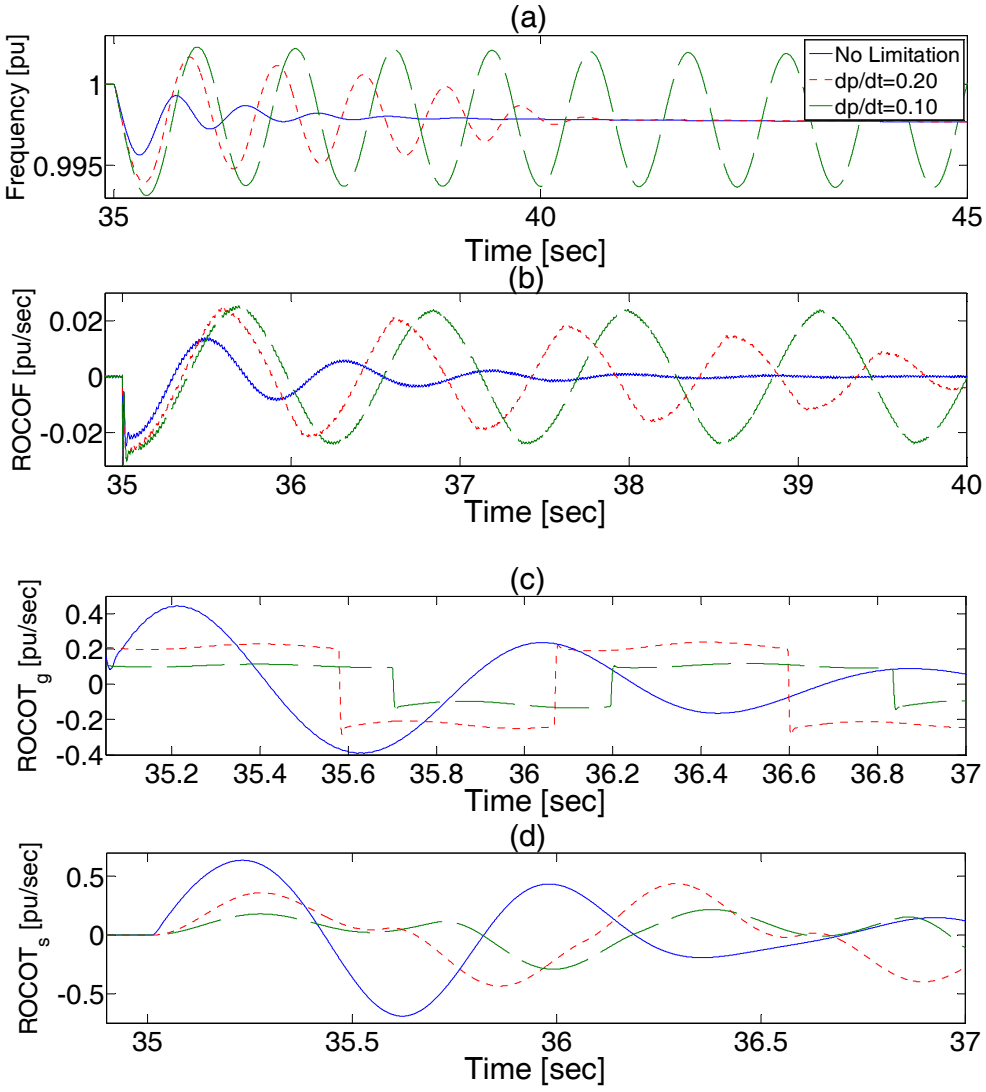

Figure 4-31 Impact of using a power RRL on wind-based droopwith m_p=40 pu (a) System frequency (b) ROCOF (c) ROCOT of the generator (d) ROCOT of the shaft.

All of these problems make the RRL an unacceptable solution or, more precisely, acceptable only in low contributions of wind power to frequency regulation. In addition, it

should be noted that the RRL increases the nonlinearity of the system, which results in much higher complexity in analyzing and understanding the system behavior.

4.5.2.3 Filter Method

Figure 4-32 and Figure 4-33 show the system performance with the proposed filter method. Obviously, it is effective in preventing high mechanical tension, and at the same time, the filter method does not interfere with the frequency regulation controllers. These figures also depict the dc-link voltage as the source responding to the fast transients of frequency regulation methods. First of all, the voltage is finally, and relatively shortly, restored to its nominal value to prevent any undesired impact on converter operation. Second, as discussed, the depth of the dc-link voltage disturbance is dependent on the filter cutoff frequency.

4.5.3 Mechanical Resonance

4.5.3.1 Frequency Regulation and Instability

Figure 4-34 shows the impact of a relatively high virtual inertia gain on the system stability. As predicted, the high contribution of the virtual inertia stimulates the natural resonance of a wind power generator. The results in this figure also verify that all the investigated solutions work properly. The frequency behaviors of all solution methods are very similar. However, as Figure 4-35 shows, some methods have an advantage over others. Figure 4-35(a) shows the ROCOP in the PMSG; the active damping method has almost no significant effect. However, the characterization is not complete unless the impact on the dc-link voltage is considered. Figure 4-35(b) shows the dc-link voltage response when the virtual inertia is implemented. As shown, the desired results of the filter and the re-tuned dc-link bandwidth methods are achieved at the cost of more fluctuation in the dc-link voltage.

The impacts of the wind speed and the deloading factor are depicted in Figure 4-36. As predicted by the theoretical analysis, the lower the wind speed, the higher the robustness against the resonance. Figure 4-36(b) also confirms the analysis related to the higher chance of instability in the sub-synchronous mode, i.e., when K_f is greater than one. Some loads are shed for the lower wind speed to make the droop implementation possible.

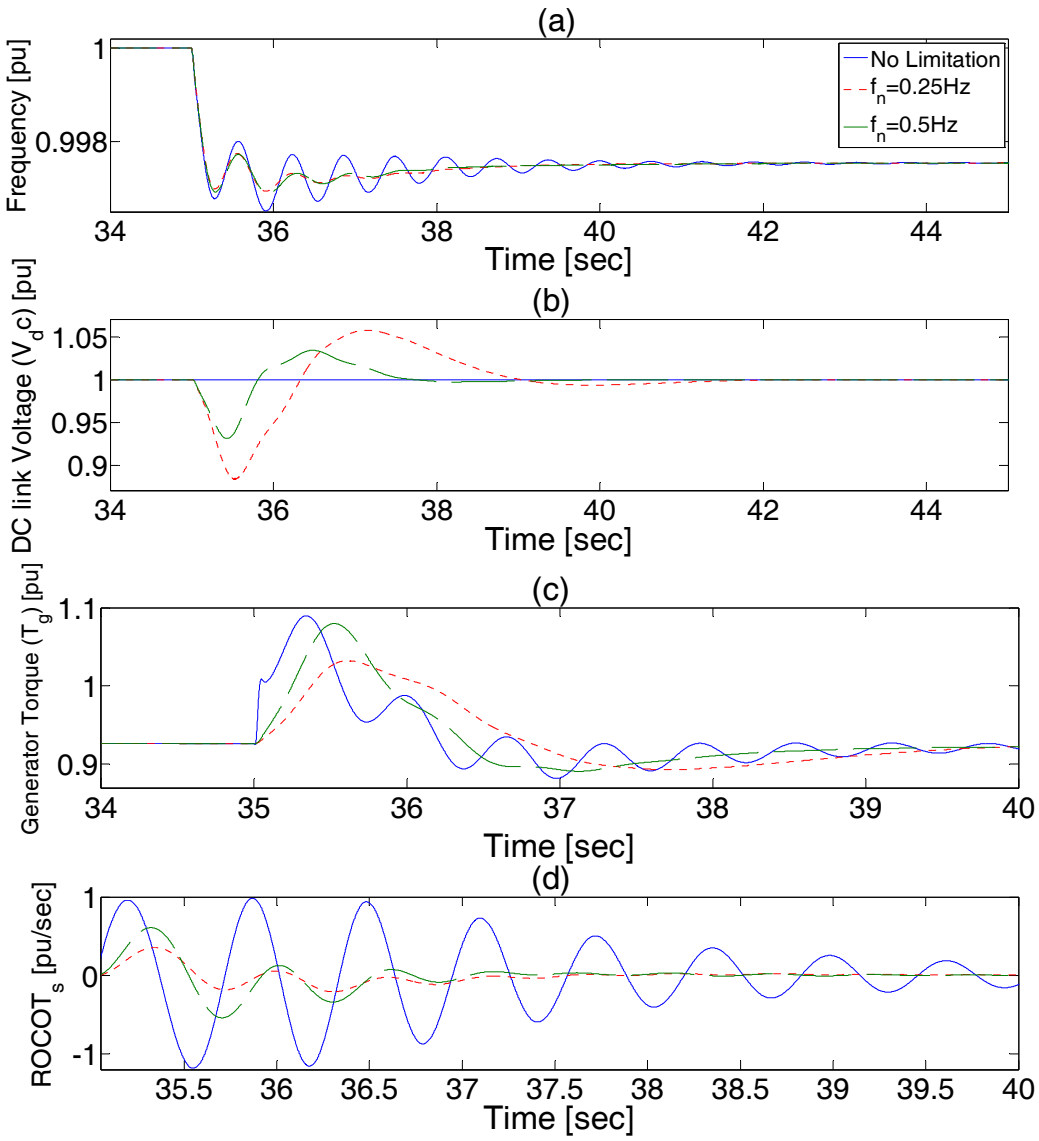

Figure 4-32 Impact of the proposed method on wind-based virtual inertia with M_{vi}/M=5. (a) System frequency (b) Wind generator dc-link voltage (c) Wind generator torque(d) ROCOT of the shaft.

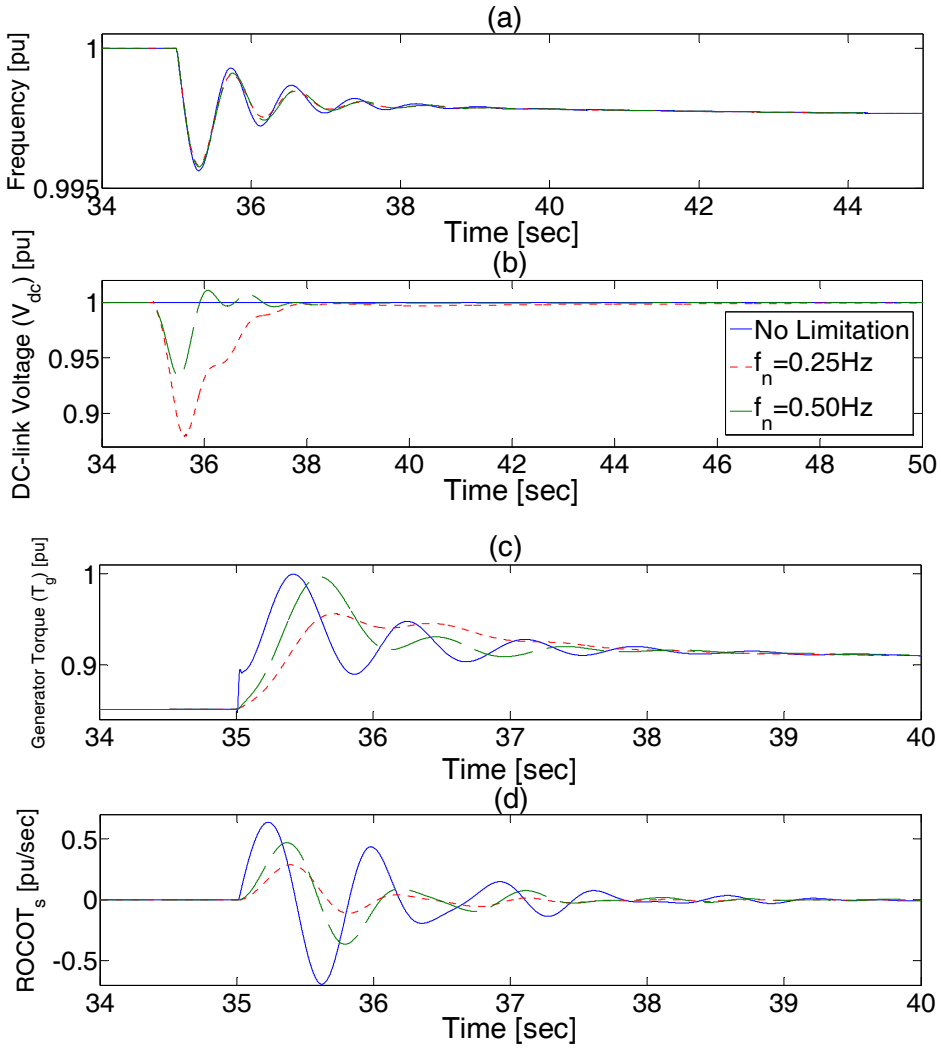

Figure 4-33 Impact of the proposed method on wind-based droop. (a) System frequency (b) Wind generator dc-link voltage (c) Wind generator torque (d) ROCOT of the shaft. m_p =40 pu.

4.5.3.2 Wind Speed Changes

The proposed methods must not negatively interact with the conventional control functions in a wind power generator. This design objective is examined here by applying a severe step change in the wind speed and observing the dc-link voltage. Figure 4-37 verifies the discussions in the previous section, in which the filter method's impact on the dc-link voltage is negligible. As expected, considerable changes can be seen when the active damping method is applied, yet these changes are much less than those resulting from the dc-link re-tuning method.

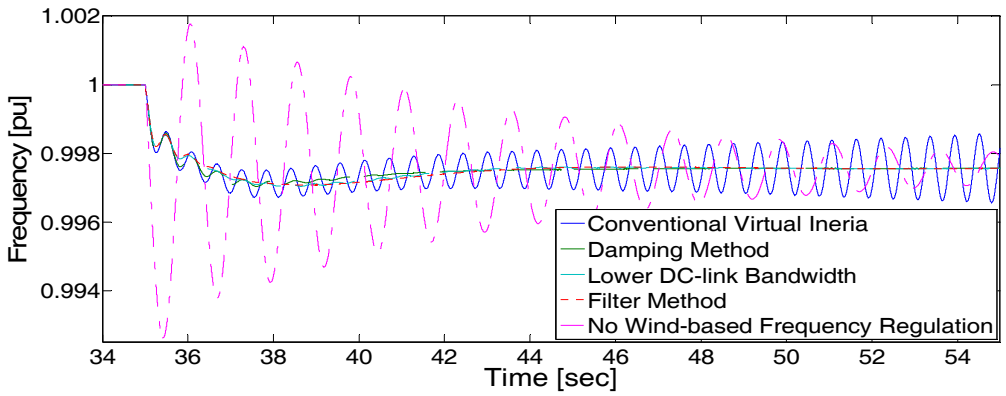

Figure 4-34 System frequency with and without virtual inertia and proposed solutions.

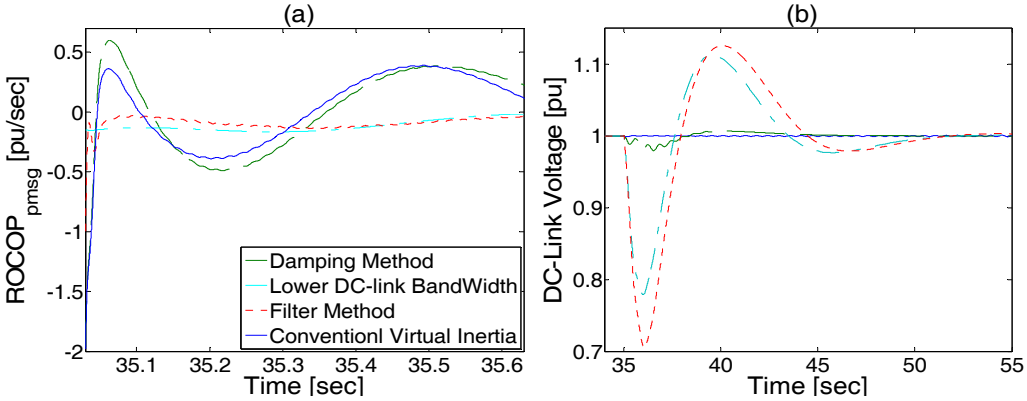

Figure 4-35 (a) PMSG ROCOP, (b) DC-link voltage with virtual inertia, $M_{vi}/M_{diesel}\approx 10$.

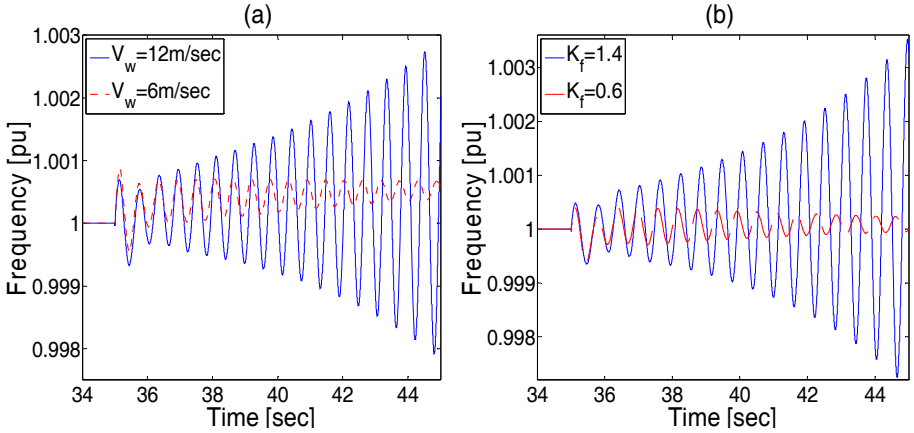

Figure 4-36 System frequency with wind based-droop (a) Different wind speeds at K_f=0.8, (b) Different deloading factors at V_w=12 m/s.

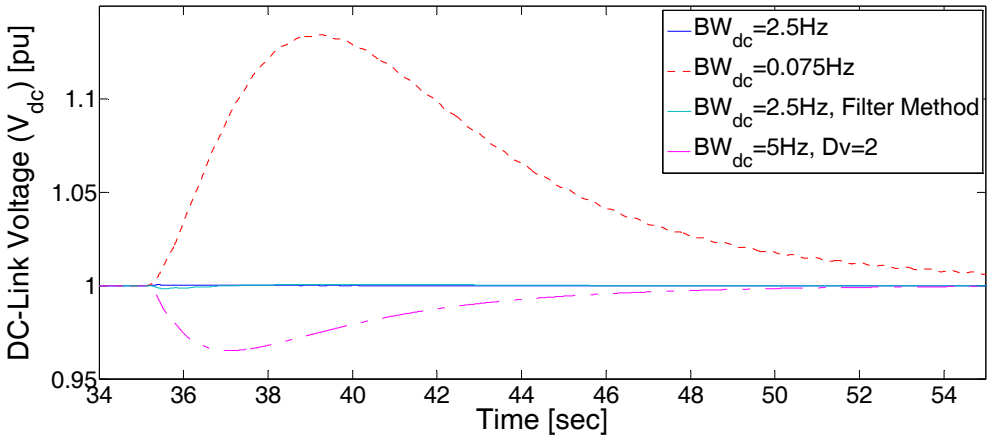

Figure 4-37 DC-link voltage when wind speed changes suddenly from 12 to 10 m/s.

4.5.3.3 Mutual Impact of Wind Generators

Here, another wind generator, with similar specifications, is added to Bus 6, referred to as DG3. While DG1 is equipped with the virtual inertia, the droop is implemented in DG3. To verify that the presented analysis is applicable to the other control topology in PMSG-based wind turbines, both wind generators, DG1 and DG3, employ the conventional control strategy (i.e., the dc-link voltage is regulated by the grid-side converter). Figure 4-38 shows that how the accumulative impact of both generators leads to the instability whereas each of them alone can operate in a stable manner. In this part, different shaft stiffnesses, K_s, are employed. The worst case happens when both generators have a similar K_s. This behavior means that their resonance frequencies are close, and their impacts are amplified by each other. As the presented analysis predicts, even a softer, but not similar, shaft can prevent the instability. Figure 4-38(b) shows the cases when a damping method is adopted. Passive damping of 0.03 pu cannot stabilize the system and also increases the losses. On the other hand, the active damping implementation is effective. However, the same amount of active damping in different generators has different impacts. The theoretical analysis, not provided here due to lack of space, predicted the same results. These results confirm that the resonance of a wind generator participating in the system frequency regulation should be studied as a part of the integrated system dynamics.

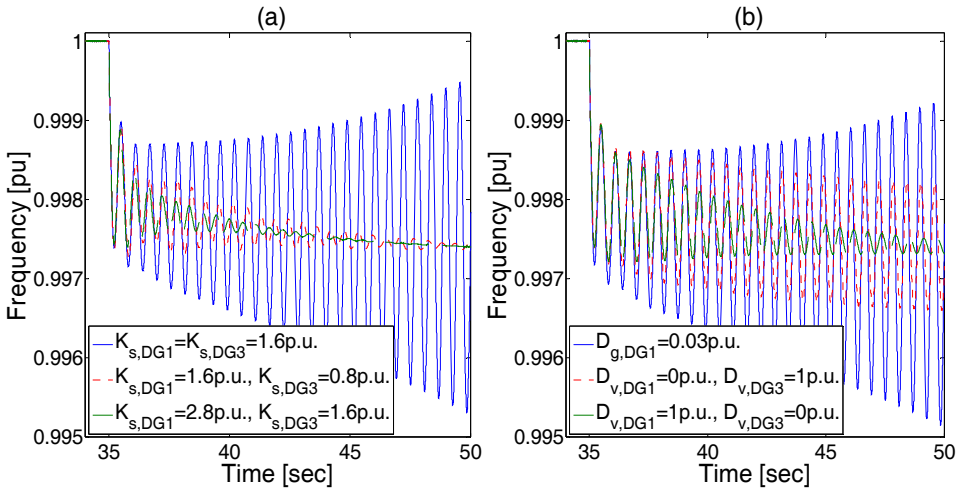

Figure 4-38 System frequency when two wind generators contribute to the system frequency. $M_{vi}/M_{diesel} \approx 6.5$, m_p=40. (a) Different wind generators shaft stiffness is examined (b) Passive and active damping methods are employed.

4.6 Summary

In this chapter, small-signal analysis was employed to study the impact of frequency regulation methods on the ROCOP of wind turbines considering the two-mass mechanical dynamics. Both doubly fed induction generator- and permanent-magnet synchronous generator-based turbines were considered. An effective solution, based on utilizing the converter dc-link capacitor, was proposed, analyzed, and compared to the conventional ramp-rate limit method in different aspects.

Small-signal modeling, analysis, and eigenvalues studies were also used to show that incorporating a wind power generator in the frequency regulation can expose its shaft to forces stimulating its natural resonance frequency dynamics and lead to instability. This study showed that the mechanical resonance of frequency-regulating wind generators must be studied and enhanced not individually but as a part of the whole power system stability analyses. To overcome the stability problem caused by implementing frequency regulation in wind generators, this chapter investigated different alternatives to stabilize the generator dynamics and, at the same time, minimize undesirable interference in the conventional wind power generator controllers. Time-domain simulation results validate the analytical results and discussions.

Chapter 5
Dynamic Modeling and Performance Enhancement of PMSG-Based Wind Turbines under Faults

5.1 Introduction

A full-scale permanent-magnet synchronous generator (PMSG)-based wind turbine with dc-link voltage control via the machine-side converter has the potential to provide inherent low-voltage ride-through (LVRT) performance without additional hardware components.

Figure 5-1 shows a PMSG-based wind power generator. Classically, the grid-side converter (GSC) is utilized to regulate the dc-link voltage whereas the wind-generator-side converter (WSC) extracts the maximum available power. During a fault, the GSC loses its capability to inject or sink active power, partially or completely; thus, a voltage violation may occur in the dc-link voltage. Alternatively, to utilize the generator rotating mass for storing the excessive energy during a fault, switching the control functions of the WSC and GSC has been proposed [87, 98, 99, 100, 101]. This switching could be either permanent [87, 100, 101] or only temporarily during faults [98, 99]. In this chapter, the performance of an LVRT-capable PMSG-based wind generator in which the control functions of the WSC and GSC are permanently switched is analyzed. It is easy to show that no major difference exists in the behavior of a PMSG-based wind generator under normal operating conditions with the dc-link voltage regulated by either the GSC or the WSC.

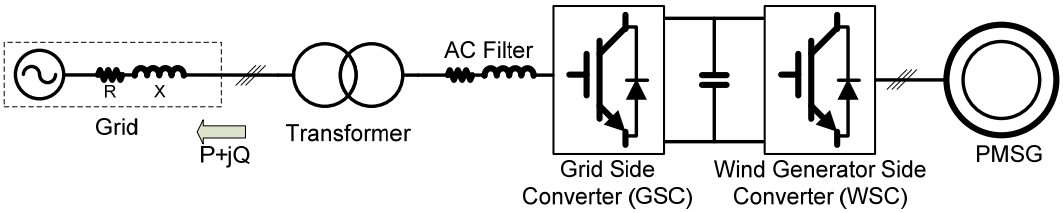

Figure 5-1 PMSG-based grid-connected wind power generator.

However, several important performance aspects related to this topology are not addressed in the current literature. To characterize the pros and cons of the LVRT-capable control method, detailed modeling and thorough analysis are needed.

The contributions of this chapter to the research field are:

1) Providing a three-stage small-signal model for a PMSG-based wind generator to analyze the fault ride-through dynamics by considering the double-mass mechanical dynamics and typical LVRT characteristics.

2) Investigating the stability, risk of resonance, and successful operation of a PMSG-based wind power generator under LVRT.

3) Studying the impact of the LVRT control on the generator fatigue.

4) Studying and comparing the performance of two possible solutions for performance enhancement and fatigue reduction in a PMSG-based wind generator with LVRT.

This chapter is organized as follows. The modeling is presented in Section 5.2. Detailed analysis and mitigation methods are discussed in the next section. Time-domain simulation results are presented in Section 5.4. Finally, conclusions are drawn in Section 5.5.

5.2 Modeling

Deriving linearized models for a wind power generator is crucial to analyze the generator dynamic performance during LVRT and to coordinate different controllers. Under LVRT, a wind generator will be subjected to different operating conditions and huge changes; therefore, utilizing one linearized model does not seem reasonable. Instead, three models are adopted in this chapter. The first model characterizes the wind power generator dynamics in the pre-fault condition. In this case, the model input is the wind speed. The second model considers the generator dynamics in the "during fault" period, where the generator output power is dictated by the power system conditions instead of extracting the maximum available wind power. The third model characterizes the wind power generator dynamics after fault clearance when the generator has complete control over its output power. The wind power generator dynamics, which is moved from its steady-state mode during the fault, tries to restore the pre-fault condition. Here, the system is responding mainly to its initial states rather than any external forces. This initial state is, in fact, the final state obtained from

the "during fault" model. The process is depicted in Figure 5-2. Each of these modes and the corresponding linearized models will be discussed in the following subsections.

5.2.1 Pre-Fault

This state can be identified as a normal operating condition, but it has a significant common feature with the "during fault" period. In fact, when the WSC controls the dc-link voltage, the WSC and consequently the generator, in both normal and fault conditions, work similarly to regulate the dc-link. The GSC performance during a fault may yield different dynamics and disturbances imposed on the dc-link.

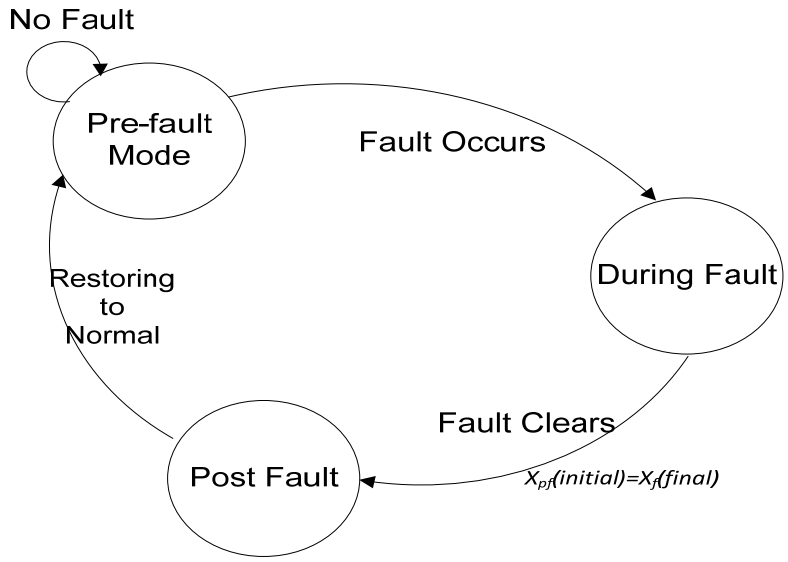

Figure 5-2 Schematic view of the LVRT modeling approach.

To facilitate the close control of a PMSG, a field-oriented control system implemented in the *d*-*q* reference frame is usually employed. This frame associates the *q*-axis current i_q with the active power production, whereas the reactive power is dependent on the *d*-axis current component, i_d, which is usually regulated to zero. The reference of the *q*-axis current component is generated to regulate the dc-link voltage, V_{DC}, as shown by (5-1), where K_{pc} and K_{ic} are the proportional-integral (PI) regulator parameters, and the "ref" subscript denotes the desired value [175]:

$$i_{q-ref} = ({V_{ref}}^2 - {V_{DC}}^2)(K_{pc} + \frac{K_{ic}}{s}). \tag{5-1}$$

The reference current is compared to the actual value and fed to a PI current controller as depicted in Figure 5-3. In most cases, the current dynamics, the relation between the actual and desired *q*-axis currents can be approximated by (5-2), where τ_i is the closed-loop current control time-constant [175]. This current is related to the electromagnetic torque by (5-3), where T_g, P, and λ_m are the electromagnetic torque, pole-pair number, and the electromagnetic flux constant of a PMSG, respectively:

$$i_q = \frac{1}{\tau_i s+1} i_{q-ref}. \tag{5-2}$$

$$T_g = \frac{3}{4} P \lambda_m i_q \tag{5-3}$$

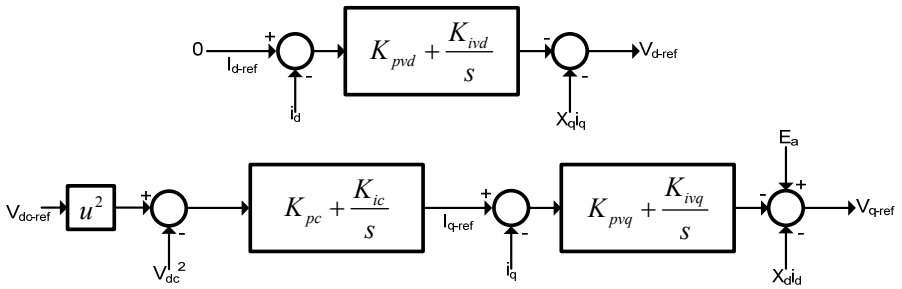

Figure 5-3 Block diagram of the WSC controller.

On the one hand, the electromagnetic torque impacts the dc-link voltage via the generator electric output power P_{gen}, as given by (5-4), where ω_g is the rotational speed of the generator. Equation (5-5) relates the PMSG output power and GSC output power, P_{grid} to the dc-link voltage, where C and P_{nom} represent the dc-link capacitance and nominal power. P_{gen} and P_{grid} here are in per unit whereas the other parameters have their well-known SI units (Watt, Farad, and Voltage).

$$P_{gen} = T_g \omega_g \tag{5-4}$$

$$P_{nom}(P_{gen} - P_{grid}) = C \frac{d}{dt} V_{DC}^2. \tag{5-5}$$

On the other hand, T_g is an important variable in the mechanical part of the generator as shown by (5-6)-(5-8), where the equations and their parameters were previously introduced

in the last chapter, (4-8)-(4-10), and are repeated here, only for the sake of integrity and readability.

$$\dot{\omega}_t = \frac{1}{2H_t}(T_t - K_s\theta - D_t\omega_t). \tag{5-6}$$

$$\dot{\theta} = \omega_B(\omega_t - \omega_g). \tag{5-7}$$

$$\dot{\omega}_g = \frac{1}{2H_g}(K_s\theta - T_g - D_g\omega_g). \tag{5-8}$$

The wind turbine performance can be described by (5-9), as it was described in (3-1). and P_m is the mechanical input power and is equal to the product of T_t and ω_t.

$$P_m = 0.5\rho C_P(\lambda,\beta)A_r v_w^{\ 3} = T_t\omega_t. \tag{5-9}$$

In normal operating conditions, the reference grid-power is set to extract the maximum available power, as Figure 5-4 shows. Reference [171] shows that if the pitch angle is constantly kept at zero, this optimum power can be expressed by (5-10) in which K_{OPT} is a constant. The GSC controller is fast enough to assume that the actual amount of P_{grid} is equal to its reference value [50].

$$P_{grid-ref} = K_{OPT}\omega_g^{\ 3}. \tag{5-10}$$

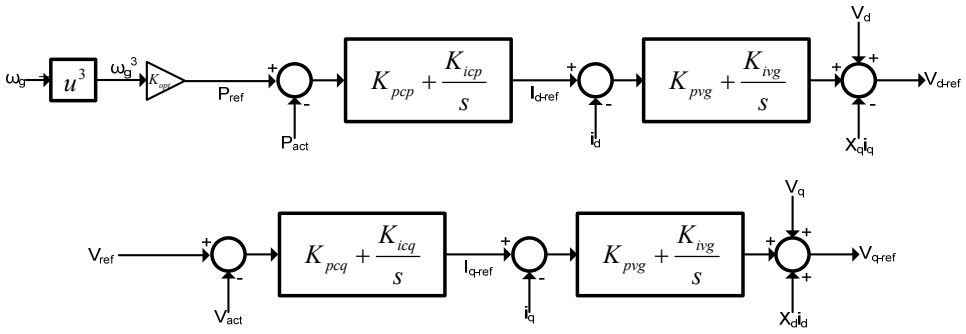

Figure 5-4 Block diagram of the GSC controller.

In a double-mass mechanical system, resonance is possible; therefore, an active damping controller can be used to suppress resonance without the physical losses associated with a passive damping solution. To complete the model, a typical active damping controller is augmented in the system dynamics. Equation (5-11) describes the active damping method, initially suggested in [88, 102]. Basically, it is a band-pass filter aiming to increase the

damping of the natural resonance frequency, ω_{ad}, of the generator. This damping can be discarded simply by assigning D_v, the active damping gain, to zero. In (5-11), V_{nom} is the nominal dc-link voltage. The application of the active damping in both normal and fault situation will be discussed later.

$$V_{ref}{}^2 = V_{nom}{}^2 + \frac{D_v}{\tau_{ad}s+1}.\frac{2\xi_{ad}\omega_{ad}s}{s^2+2\xi_{ad}\omega_{ad}s+\omega_{ad}{}^2}\omega_g. \tag{5-11}$$

To construct the final model, the system dynamics need to be linearized; however due to lack of space, this step is not detailed here except when it has resulted in introducing new states or parameters such as (5-12)-(5-15), where $\Delta\phi_1$, $\Delta\phi_2$, $\Delta\phi_3$ and $\Delta\phi_4$ are introduced to realize (5-11) and (5-1). The change in the mechanical input power, ΔP_m, in general is a function of the pitch angle, rotor rotational speed and wind speed. However, the pitch angle is usually zero, and because of the maximum power point tracking (MPPT), $dP_m/d\omega_t=0$. Therefore, the mechanical power can be expressed as a single-variable function of the wind speed as in (5-16). The linearization point in the modeling is the system's equilibrium point, which is a function of wind speed.

$$\Delta\dot{\phi}_1 = \frac{-2\xi_{ad}\omega_{ad}-1}{\tau_{ad}}\Delta\phi_1 - \frac{\omega_{ad}{}^2\tau_{ad}+2\xi_{ad}\omega_{ad}}{\tau_{ad}}\Delta\phi_2 - \frac{\omega_{ad}{}^2}{\tau_{ad}}\Delta\phi_3 + \Delta\omega_g. \tag{5-12}$$

$$\Delta\dot{\phi}_2 = \Delta\phi_1. \tag{5-13}$$

$$\Delta\dot{\phi}_3 = \Delta\phi_2. \tag{5-14}$$

$$\Delta\dot{\phi}_4 = \Delta v^2{}_{ref} - \Delta v^2{}_{dc}. \tag{5-15}$$

$$A = \frac{\partial\Delta P_m}{\partial\Delta v_w} = 0.5\rho A_r\left(3C_P V_{w0}{}^2 + V_{w0}{}^3\,\partial\Delta C_P \Big/ \partial\Delta\lambda . \partial\Delta\lambda \Big/ \partial\Delta v_w\right). \tag{5-16}$$

Equation (5-17) represents the complete linear model. In this small-signal model, the equilibrium point is the origin.

$$\frac{d}{dt}\begin{bmatrix}\Delta\phi_1\\ \Delta\phi_2\\ \Delta\phi_3\\ \Delta v^2_{dc}\\ \Delta\phi_4\\ \Delta i_q\\ \Delta\omega_g\\ \Delta\theta\\ \Delta\omega_t\end{bmatrix}=\begin{bmatrix} -\frac{2\xi_{ad}\omega_{ad}+1}{\tau_{ad}} & -\frac{\omega_{ad}{}^2\tau_{ad}+2\xi_{ad}\omega_{ad}}{\tau_{ad}} & -\frac{\omega_{ad}{}^2}{\tau_{ad}} & 0 & 0 & 0 & 1 & 0 & 0\\ 1 & 0 & 0 & 0 & 0 & 0 & 0 & 0 & 0\\ 0 & 1 & 0 & 0 & 0 & 0 & 0 & 0 & 0\\ 0 & 0 & 0 & 0 & 0 & \frac{3P_{nom}\omega_0}{2C} & -\frac{4P_{nom}T_0}{C} & 0 & 0\\ 0 & \frac{4P_{nom}D_v\xi_{ad}\omega_{ad}K_p}{\tau_d C} & 0 & -1 & 0 & 0 & 0 & 0 & 0\\ 0 & \frac{4P_{nom}D_v\xi_{ad}\omega_{ad}K_p}{\tau_i\tau_d C} & 0 & -\frac{K_p}{\tau_i} & \frac{K_i}{\tau_i} & -\frac{1}{\tau_i} & 0 & 0 & 0\\ 0 & 0 & 0 & 0 & 0 & -\frac{3P\lambda_m}{8H_g} & -\frac{D_g}{2H_g} & -\frac{K_s}{2H_g} & 0\\ 0 & 0 & 0 & 0 & 0 & 0 & -\omega_B & 0 & \omega_B\\ 0 & 0 & 0 & 0 & 0 & 0 & 0 & -\frac{K_s}{2H_t} & \frac{-T_0-\omega_0 D_t}{2H_t\omega_0} \end{bmatrix}\begin{bmatrix}\Delta\phi_1\\ \Delta\phi_2\\ \Delta\phi_3\\ \Delta v^2_{dc}\\ \Delta\phi_4\\ \Delta i_q\\ \Delta\omega_g\\ \Delta\theta\\ \Delta\omega_t\end{bmatrix}+$$
$$\begin{bmatrix}0 & 0 & 0 & 0 & 0 & 0 & 0 & 0 & \frac{A}{2H_t\omega_0}\end{bmatrix}^T\Delta v_w. \qquad (5\text{-}17)$$

5.2.2 During Fault

During the fault, a model modification is needed, due mainly to the inability of a wind power generator to inject the available wind power to the system.

Figure 5-5 clarifies the situation, presenting a typical LVRT standard [91]. Figure 5-5(a) shows the voltage limits for LVRT, where Figure 5-5(b) shows the reactive power injection code requiring a wind power generator to reserve its entire thermal limit for reactive power injection for a voltage dip of more than 50%. This requirment means that for a slow recovery (e.g., up to 900 ms), no active power can be injected into the system, and even after that occurs, the active power injection should be increased gradually to respect the grid codes and converter rating, as shown by (5-18).

$$P_{grid}=\sqrt{S_{conv}{}^2-Q_{grid}{}^2} \qquad (5\text{-}18)$$

Therefore, the main difference here is the grid power, which can no longer be described by (5-10). Instead, and based on the standards in Figure 5-5 and (5-18), Figure 5-6 depicts a typical trajectory of P_{grid} during the fault. In other words, Figure 5-5(b) dictates no active power injection whereas the voltage drop is more than 50 percent, which means 900 and 150

ms for limit lines 1 and 2, respectively, shown in Figure 5-5(a). Because any point above these two lines should be endured by the generator, the fast recovery represents a scenario where the line voltage is restored to a neighborhood of 10 percent voltage deviation right after 150 ms. In this case, the active power injection is not restricted by the reactive power mandate, and the system is not in the "During fault" condition after this short time interval. In the slow recovery, the limit line 1 is considered where the voltage is increasing linearly with time, and thus, after 900 ms, the mandatory reactive power injection is decreasing linearly. By obtaining the reactive power profile from Figure 5-5(b) and substituting in (5-18), the maximum allowed active power injection for the limit line (1), depicted as the slow recovery case in Figure 5-6, can be calculated. It is obvious that to obtain ΔP_{grid}, P_{grid0} should be subtracted from the present curves. Equation (5-19) shows the system model under the fault condition. This model adopts the final equilibrium point of the pre-fault stage as the linearization point. As well, the ac-system is assumed to be strong enough so that the interaction of the ac-system with the wind generator after fault recovery can be neglected.

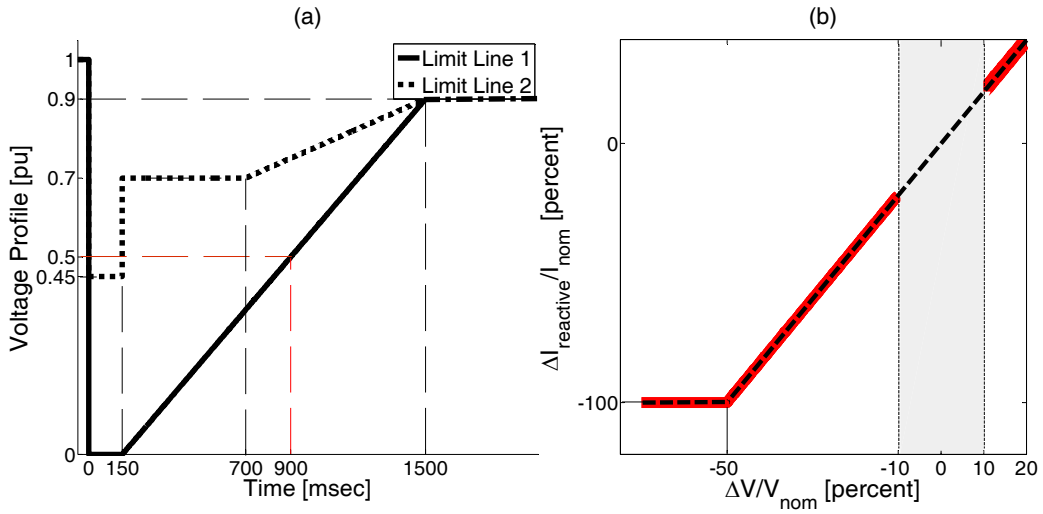

Figure 5-5 Grid code for LVRT (a) Voltage limits (b) Reactive current injection by the generator during a fault.

$$\frac{d}{dt}\begin{bmatrix}\Delta\phi_1\\ \Delta\phi_2\\ \Delta\phi_3\\ \Delta v^2_{dc}\\ \Delta\phi_4\\ \Delta i_q\\ \Delta\omega_g\\ \Delta\theta\\ \Delta\omega_t\end{bmatrix}=\begin{bmatrix}-\frac{2\xi_{ad}\omega_{ad}+1}{\tau_{ad}} & -\frac{{\omega_{ad}}^2\tau_{ad}+2\xi_{ad}\omega_{ad}}{\tau_{ad}} & -\frac{{\omega_{ad}}^2}{\tau_{ad}} & 0 & 0 & 0 & 1 & 0 & 0\\ 1 & 0 & 0 & 0 & 0 & 0 & 0 & 0 & 0\\ 0 & 1 & 0 & 0 & 0 & 0 & 0 & 0 & 0\\ 0 & 0 & 0 & 0 & 0 & \frac{2P_{nom}\omega_0}{2C} & \frac{2P_{nom}T_0}{C} & 0 & 0\\ 0 & \frac{4P_{nom}D_v\xi_{ad}\omega_{ad}K_p}{\tau_d C} & 0 & -1 & 0 & 0 & 0 & 0 & 0\\ 0 & \frac{4P_{nom}D_v\xi_{ad}\omega_{ad}K_p}{\tau_i\tau_d C} & 0 & -\frac{K_p}{\tau_i} & \frac{K_i}{\tau_i} & -\frac{1}{\tau_i} & 0 & 0 & 0\\ 0 & 0 & 0 & 0 & 0 & -\frac{3P\lambda_m}{8H_g} & -\frac{D_g}{2H_g} & -\frac{K_s}{2H_g} & 0\\ 0 & 0 & 0 & 0 & 0 & 0 & -\omega_B & 0 & \omega_B\\ 0 & 0 & 0 & 0 & 0 & 0 & 0 & -\frac{K_s}{2H_t} & \frac{-T_0-\omega_0 D_t}{2H_t\omega_0}\end{bmatrix}\begin{bmatrix}\Delta\phi_1\\ \Delta\phi_2\\ \Delta\phi_3\\ \Delta v^2_{dc}\\ \Delta\phi_4\\ \Delta i_q\\ \Delta\omega_g\\ \Delta\theta\\ \Delta\omega_t\end{bmatrix}+\begin{bmatrix}-\frac{2P_{nom}}{C} & 0 & 0 & 0 & 0 & 0 & 0 & 0 & 0\end{bmatrix}^T\Delta P_{grid}. \quad (5\text{-}19)$$

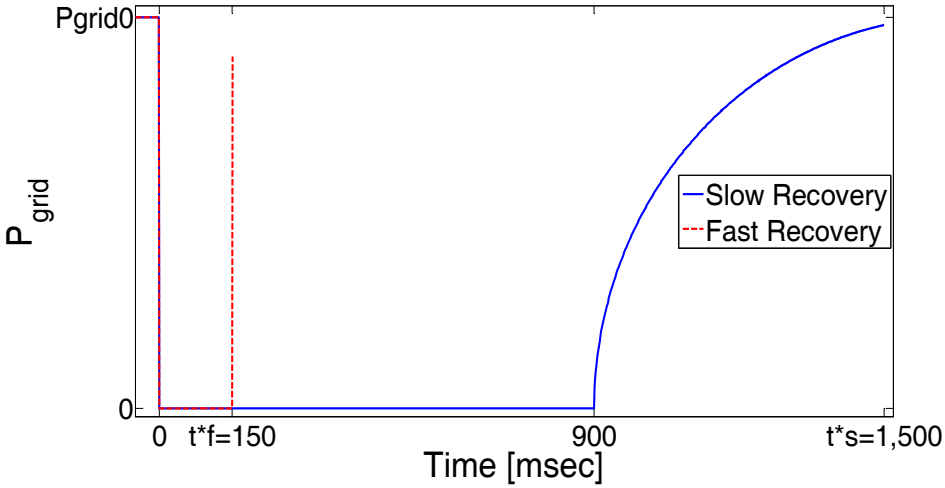

Figure 5-6 Generator output power during a fault, considering fast (red) and slow (blue) recovery scenarios.

5.2.3 After Fault Clearance

After the time instant denoted by t^* in Figure 5-6, the GSC returns to its previous control, introduced in (5-10), trying to restore its initial pre-fault operating point. It means that (5-17) is once more valid to describe the system; however, it is not in its equilibrium point anymore. This initial point could be easily extracted from the previous part. In other words, the final states of the fault part could be used as initial values for this mode. To simplify the model,

the wind speed changes could be ignored here. Then this mode could be understood as an initial value response.

5.2.4 Model Verification

To validate the proposed model, a typical 2.0 MVA PMSG-based wind turbine is simulated for detailed time-domain simulation studies. The turbine and generator parameters are given in the Appendix A, and the controllers are depicted in Figure 5-3 and Figure 5-4. The time-domain simulation model utilizes a well-tuned Phase Locked Loop (PLL) as well [117]. The proposed model and the time-domain simulation model have the same parameters and are excited by a three-phase solid fault occurring at the point of common coupling. Both the fast and slow recovery scenarios are simulated and compared as shown in Figure 5-7. Figure 5-7(a) shows the fast recovery responses without any active damping, whereas Figure 5-7(b) shows the slow recovery responses with active damping. As shown in Figure 5-7, in spite of the large variation in the operating point, the developed model predicts the generator performance almost as accurately as the time-domain simulation results do.

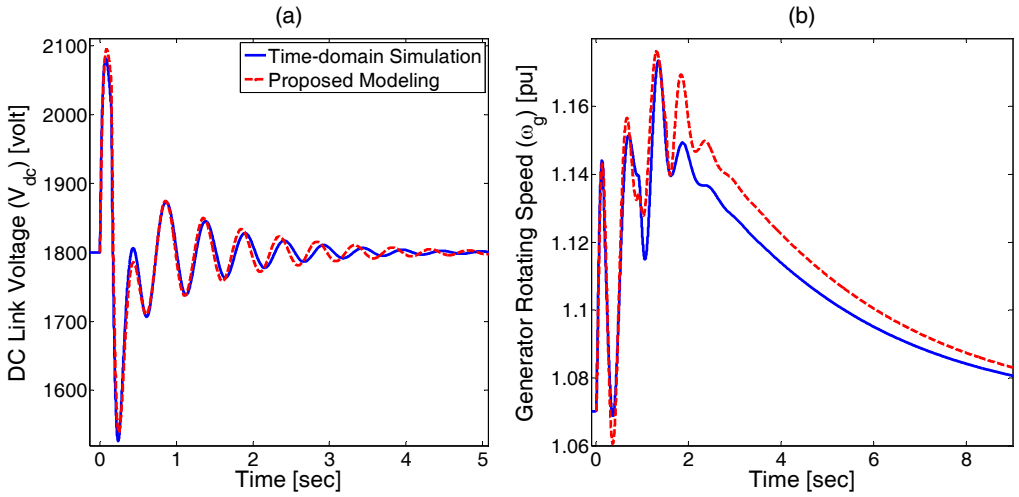

Figure 5-7 Comparing the proposed (3-stage) model with time-domain simulations (a) DC-link voltage when fast recovery is implemented and D_v=0, (b) The generator rotating speed during slow recovery and D_v=3.0 pu.

5.3 Double-Mass PMSG and LVRT

The detailed state-space model allows (1) studying the stability and characterizing the performance of the system under fault conditions, (2) observing different states and

parameters, (3) tuning and coordinating the generator system control parameters, and (4) testing the performance of the new controllers needed to improve the generator stability and performance under faults. The analysis and solutions presented in this section illustrate the usefulness of using the proposed analytical model.

5.3.1 Successful LVRT Operation

A conventional PMSG-based wind generator usually has no active or passive damping mechanism. Therefore, many researchers have discussed the risk of resonance in these generators, especially because of the relatively soft shaft dynamics [87, 89, 101]. In fact, the active damping introduced in (5-11) is one of the solutions discussed to solve this problem. However, [102] has shown that an electromagnetic torque with positive derivative with respect to the generator speed ($dT_g/d\omega_g=2K_{OPT}\omega_g>0$) is sufficient to guarantee the generator stability. In normal situations where the GSC and WSC active powers are equal, the generator torque is equal to $K_{OPT}\omega_g^2$. Therefore, the MPPT produces a stabilizing torque in the generator, and no additional remedy is necessary. For this reason, active damping is not usually employed in conventional wind generators; however, this reason is not clearly discussed in the literature.

5.3.1.1 Problem Description

The positive $dT_g/d\omega_g$ condition can totally change if a fault occurs. During faults, as Figure 5-6 depicts, P_{grid} is reduced to zero, and the generator no longer follows the MPPT control. Although the WSC can still regulate the dc-link, the risk of instability in the mechanical system of the generator exists. Figure 5-8 shows the dominant poles of the system before and during a three-phase fault at the generator terminals. Whereas the system in the normal (*pre-fault*) condition is reasonably damped, the faulty ("*During fault*") system is vulnerable to resonance.

Using the pre-fault model for the post-fault situation implies that the system stability before a fault guarantees the stability after the fault clearance. Thus, regardless of the conditions that the generator experiences during the fault, the generator will be restored to its pre-fault status if it were a stable point. However, the situation is much more complicated. In

reality, some relays will disconnect the generator if the observed parameters (e.g., generator speed, dc-link voltage, etc.) violate their allowed range. Not only stability, but also the system limitations should not be violated. The system designer must check the limit violation as well. Figure 5-9 shows a flowchart for studying the LVRT performance by using the proposed model.

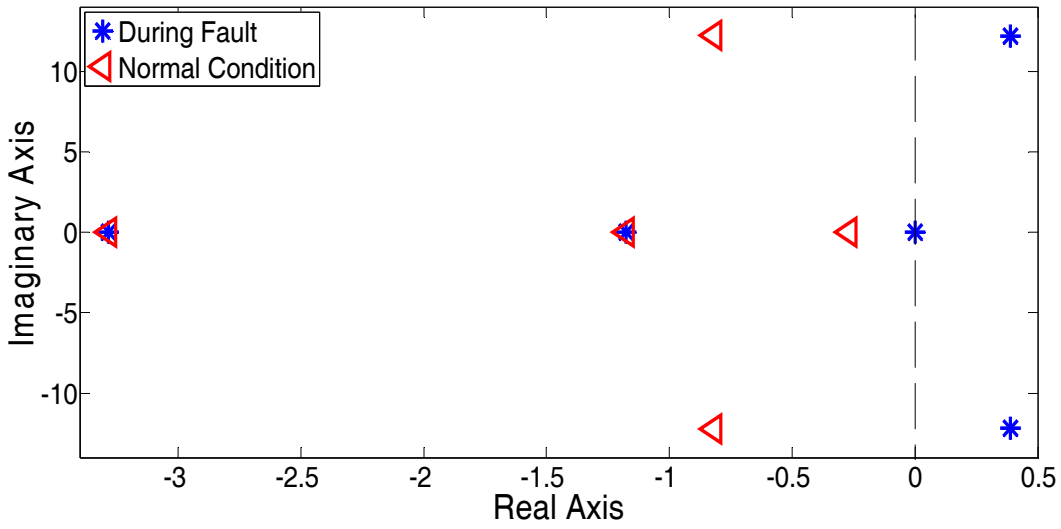

Figure 5-8 Root locus of the dominant poles of the wind power generator in normal condition (red triangles) and during a fault (blue stars).

The limited time of the fault does not allow the unstable modes to generate severe unstable responses; however, these models may lead to a violation of the limits of the dc-link voltage or generator rotating speed. The soft shaft of the mechanical system does not permit equal involvement of both rotating masses in storing energy. The generator rotating mass, which is more controllable, stores a larger portion of excessive energy than what is stored in a system with a stiff shaft, or equivalently, with a single-mass model. However, this mass is usually much lighter than the turbine mass. A single-mass (or a stiff shaft) model predicts equal changes in the angular speeds of the masses, and consequently, division of the excessive energy between them will be based on their inertia. The energy stored in a rotating mass is a function of the square of its angular speed, ω, and its inertia H. Figure 5-10 clarifies this situation, showing the impact of shaft stiffness and the weight ratio of the generator mass to the total masses weight. The figure reveals that when the turbine generator is lighter, or the shaft is softer, deviation from the single-mass model becomes more obvious, and energies

become stored in the masses more disproportionally. This disproportion increases the chance of very high generator speeds. In Figure 5-10, the practical ranges for these parameters are utilized [90]. In high wind speeds, a change in the generator rotating speed equal to or greater than 20% can trigger the over-speed relay [99]. In other words, a generator with a soft shaft or a light rotating mass (while the turbine and, consequently, the total rotating masses are heavy enough) cannot override the fault. Therefore, the utilization of a single-mass model of the turbine-generator does not facilitate accurate LVRT study, and can lead to deceiving LVRT capability results. This important finding is missing in the current literature supporting the LVRT control method for PMSG-based wind generators.

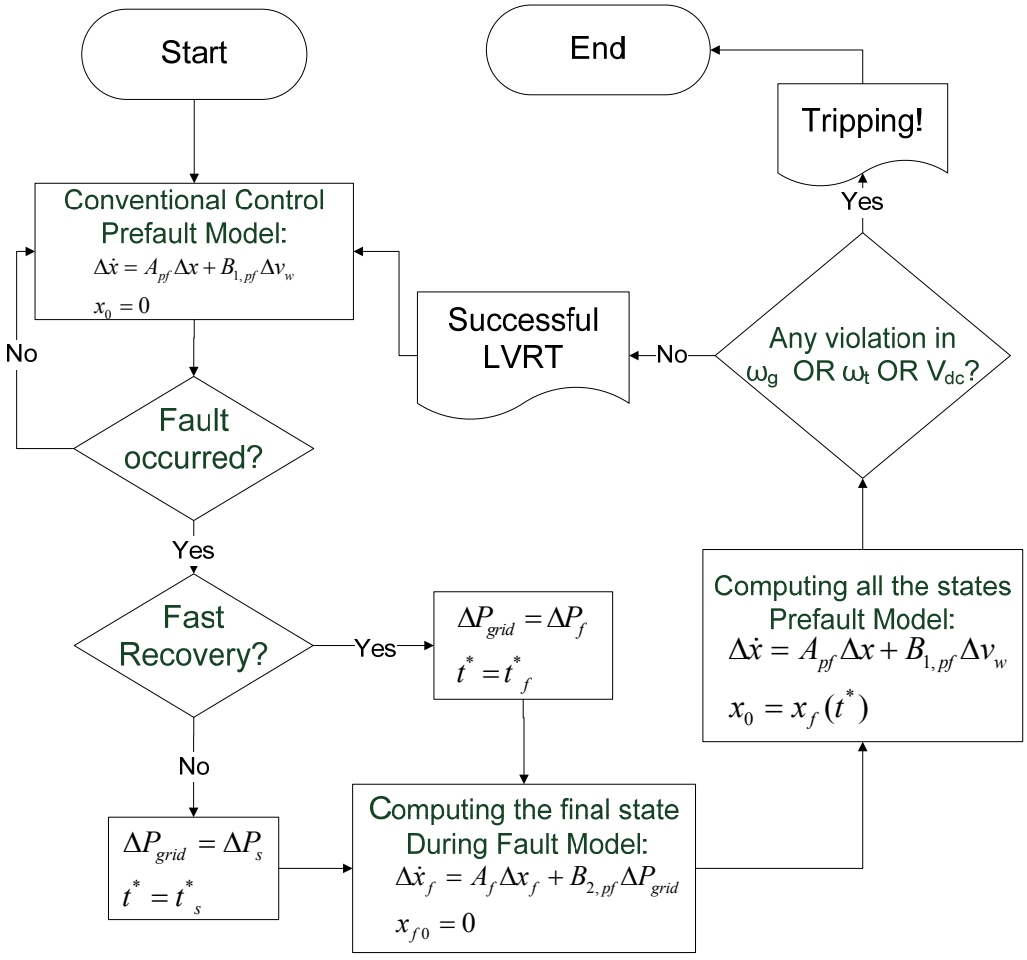

Figure 5-9 Flowchart of the complete LVRT model.

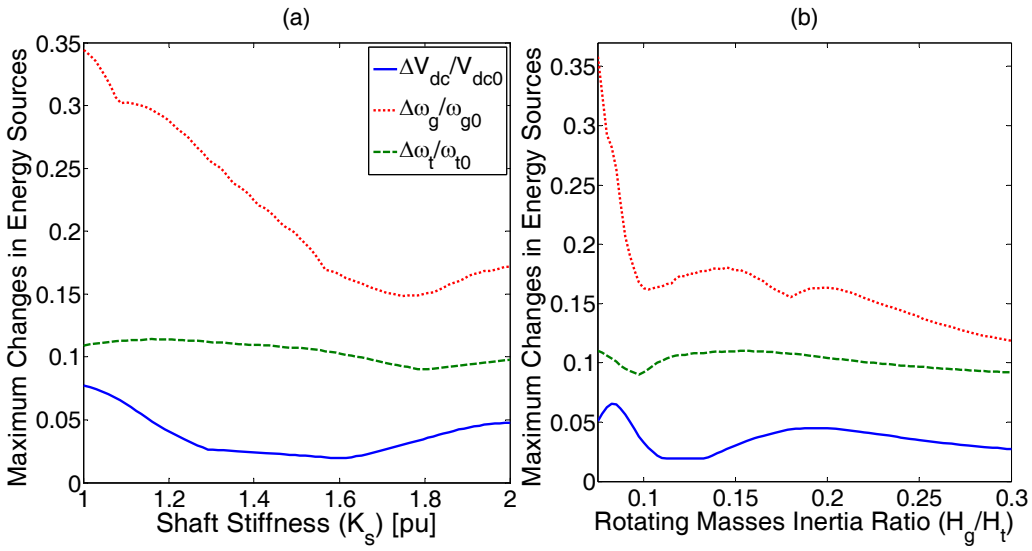

Figure 5-10 Impact of the double-mass model parameters (a) shaft stiffness, (b) the ratio of inertia of rotating masses on fluctuations in the energy sources.

5.3.1.2 Remedy

To stabilize the system during the fault and control the states, the dc-link voltage control bandwidth, as one of the already available control levers, can be used. The dc-link voltage control bandwidth f_{dc} can be calculated, as given by (5-20), by assuming a fast current controller, i.e., a small enough τ_i. The K_{ic} parameters can be adopted to control f_{dc}.

$$f_{dc} = \frac{1}{2\pi}\sqrt{\frac{3P\lambda_m}{2}P_{nom}\omega_{r0}K_{ic}/C}. \tag{5-20}$$

A smaller bandwidth means that the controller is slower, and a wind generator is not responding to changes rapidly. In other words, now the dc-link should play the role of a buffer that does not allow the generator to be exposed to fast changes. In this case, fault transients will be suppressed by the dc-link slow dynamics instead of being directly imposed on the rotating masses of the generator. This major role of the dc-link in stabilizing the system under faults is in contrast with the philosophy of LVRT in a PMSG-based wind generator, in which the rotating mass of the generator is preferred over the dc-link to store the excessive energy. Figure 5-11 clarifies the situation by providing more details. First, the differences in the changes in the speeds of the turbine and generator rotating-masses seem significant. More importantly, this figure shows that to reduce the maximum generator speed

considerably, a relatively low dc-link bandwidth is needed. However, this enhancement in the generator speed will be gained at the cost of undesired large dc-link fluctuations.

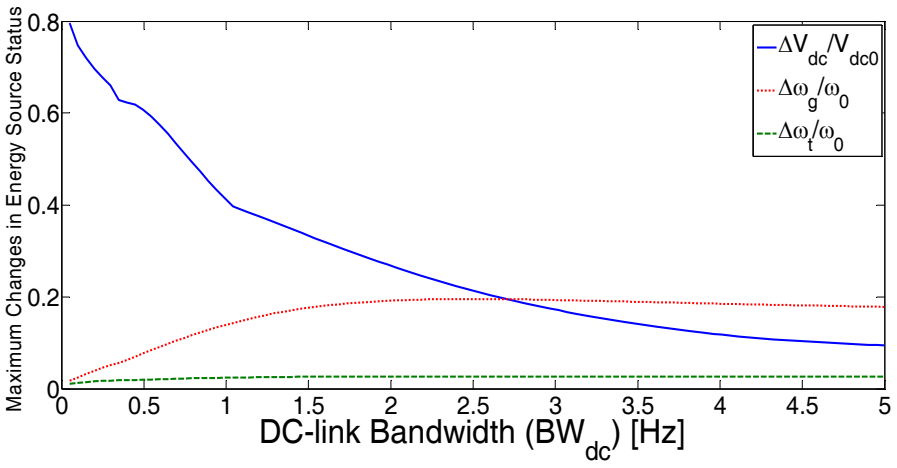

Figure 5-11 Impact of the dc-link bandwidth on fluctuations in energy sources of PMSG-based wind generators with a fast recovery.

On the one hand, during a fault, the system becomes temporarily unstable, and there is no control of the energy management between sources. On the other hand, the dc-link voltage control bandwidth cannot solve the problem. Active damping may be a proper solution. Figure 5-12 shows the impact of adding active damping on the stability of the generator in normal and faulty situations. Even in the normal condition, the stability is significantly improved.

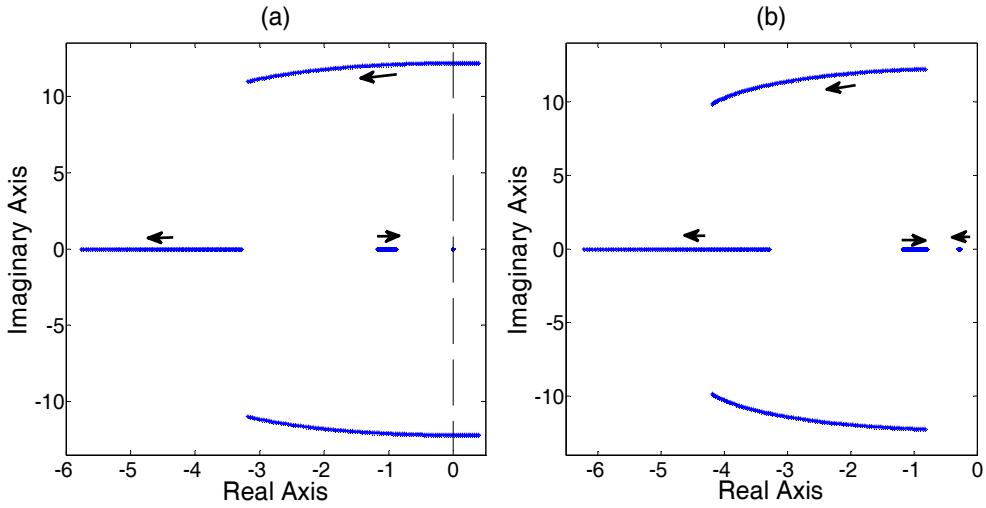

Figure 5-12 Impact of increasing the active damping gain, from zero, on the wind generator modes, (a) during a fault (b) normal condition.

Figure 5-13 provides more details about the impact of active damping on the PMSG operation during and after the fault. Obviously, such damping can be utilized to manage the excessive energy during the fault. Compared to the dc-link voltage control bandwidth, Figure 5-11, active damping can reduce the maximum generator rotating speed with a much lower contribution of the dc-link capacitor in storing the excessive energy. This phenomenon can be attributed to the band-pass nature of this controller and the damped resonance of the shaft. In other words, active damping seems to be an important tool to guarantee the stable operation of the wind generator and manage the excessive energy in the fault condition. The algorithm shown in Figure 5-9 can be used to tune the active damping controller parameters.

5.3.2 Fatigue Analyses

Researchers understood the importance of fatigue analysis of power generators a relatively long time ago. In the literature, fatigue is associated with the notion of *stress*. When the stress is higher than a certain limit, the shaft material will go through the *plastic strain region*. In this region, the shaft material deforms irreversibly, and this nonreversible deformation can be interpreted as fatigue.

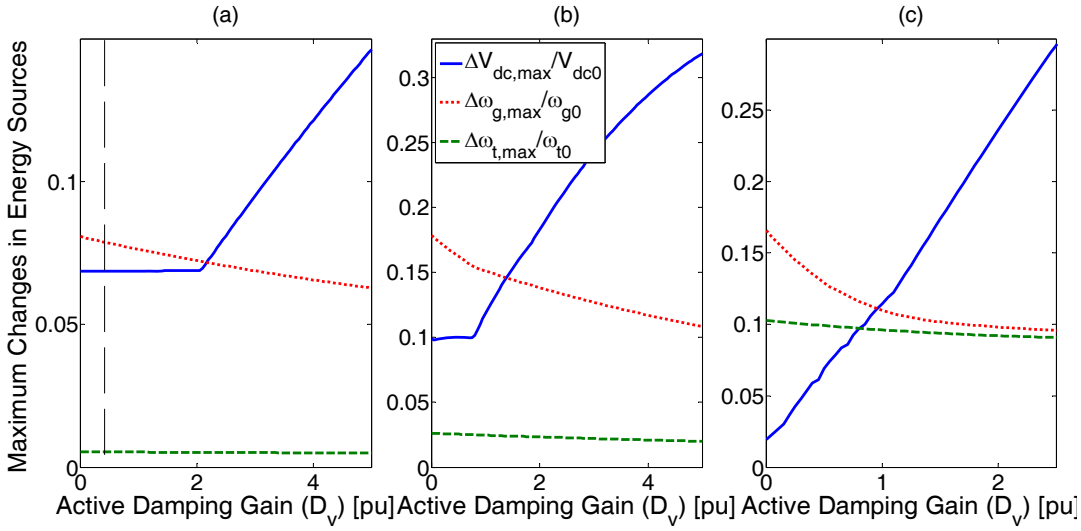

Figure 5-13 Impact of active damping gain on the fluctuations in energy sources of PMSG-based wind generators (a) During a fault, (b) Fast recovery, and (c) Slow recovery.

On the other hand, this result also implies that under that at a certain stress limit, the shaft remains in the *elastic stress region*, and the machine experiences no faster aging. A machine

in this condition has not yet reached its *fatigue limit*, which describes the maximum stress that does not result in any fatigue.

Though the shaft stress is a linear function of the shaft torque, the relation of fatigue and the shaft torque is much more complicated. The relation of stress and strain makes hysteresis cycles, and to calculate the impact of stress on the fatigue, the maximum stress, average stress and number of each cycle during a relatively long time should be calculated. The method used is highly nonlinear, cumulative, and complicated [104, 105]. Recently, a new study presented a method for estimating the fatigue in wind turbines [103]. After some further calculation, it can be formulated as (5-21):

$$F = aT_{shaft}^{\ 2} + g\dot{T}_{shaft}^{\ 2}. \tag{5-21}$$

Obviously, the fatigue estimation, F, is a function of the shaft torque and its derivative. The positive parameters a and g are calculated online, and, because of the cumulative nature of fatigue, they vary over time.

On the one hand, the shaft torque and its derivative can be used as indices for the fatigue investigations. On the other hand, limiting the mechanical tensions can prevent them from adding to the generator fatigue [104]. Thus, the shaft torque and its derivative can be gauged and controlled to restrict the shaft fatigue.

5.3.2.1 Problem Description

Faults that do not expose the wind generator shaft to stresses higher than the fatigue limit do not add any burden to the generator. For a meaningful comparison, the shaft torque and its derivative under fault conditions are compared to the corresponding quantities under wind speed variation. A typical wind turbine is designed to withstand the mechanical tensions associated with wind speed changes during its lifetime. Figure 5-14 shows the shaft torque and its derivative during and after a fast recovery of a three-phase to ground fault. The maximum amount observed during a relatively severe change in the wind speed from 12 m/s to 10 m/s is shown in the same figure by the red dashed lines. The fault-induced mechanical stresses are much higher. On the contrary, in a conventionally controlled PMSG-based wind turbine, much less and, ideally, no, tensions are inducted on the shaft of the generator

because of power system faults. A conventional generator continues to extract the maximum available energy from wind regardless of faults, and all tensions should be handled by the dc-link capacitor and GSC [96, 97]. Therefore, the LVRT control method eliminates the need for new components to dissipate the excessive energy during the fault, but this method can increase the aging of the generator. The mechanical stress can be reduced via active damping control or dc-link voltage control bandwidth re-tuning, but at the cost of higher stress on the dc-link capacitors. This mechanical stress issue, associated solutions, and trade-offs are not addressed in the literature.

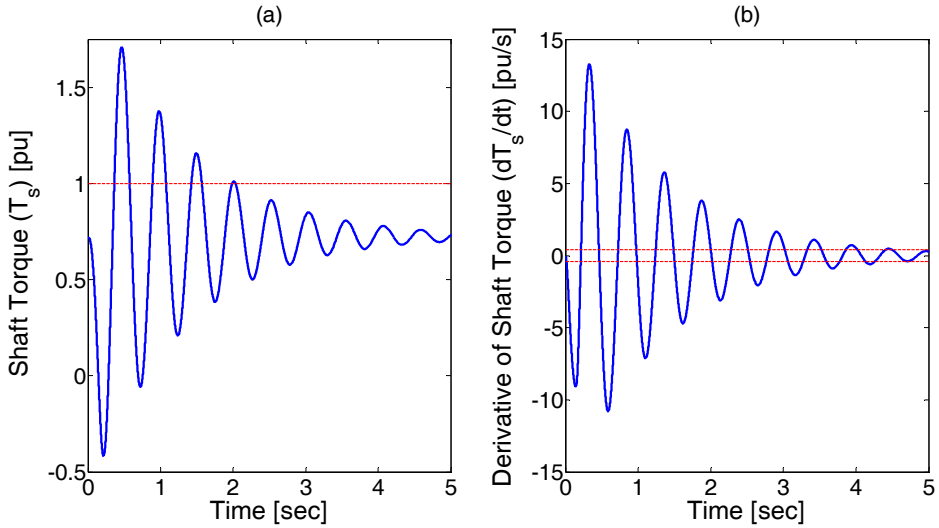

Figure 5-14 (a) Shaft torque and (b) its derivative when a fast recovery is used; fault occurs at t=0. The red-dashed line determines the maximum observed values when the generator responds to a step wind speed change from 12m/s to 10 m/s.

5.3.2.2 Remedy

The active damping control is examined here as well. Figure 5-15 shows the maximum shaft torque and its derivative at different active damping gains. Obviously, both indices can be reduced significantly; however, the impact on the shaft torque is higher than its derivative.

The dc-link voltage control bandwidth method can be also employed to reduce the mechanical stress; however, this method suffers from the same performance issues discussed in the previous section (e.g., Figure 5-11). Figure 5-16 compares the performances of the active damping and dc-link voltage bandwidth methods, showing the maximum dc-link voltage needed to reduce mechanical stresses. As expected, the active damping method can

provide the same reduced maximum shaft torque or its maximum derivative, with much lower energy injected into the dc-link capacitor. However, even the active damping method yields high oscillations in the dc-link voltage for an acceptable reduction mechanical tension. Considering that the dc-link capacitors are the weakest components in power converters, [176, 177], a system designer can be faced with a strong trade-off.

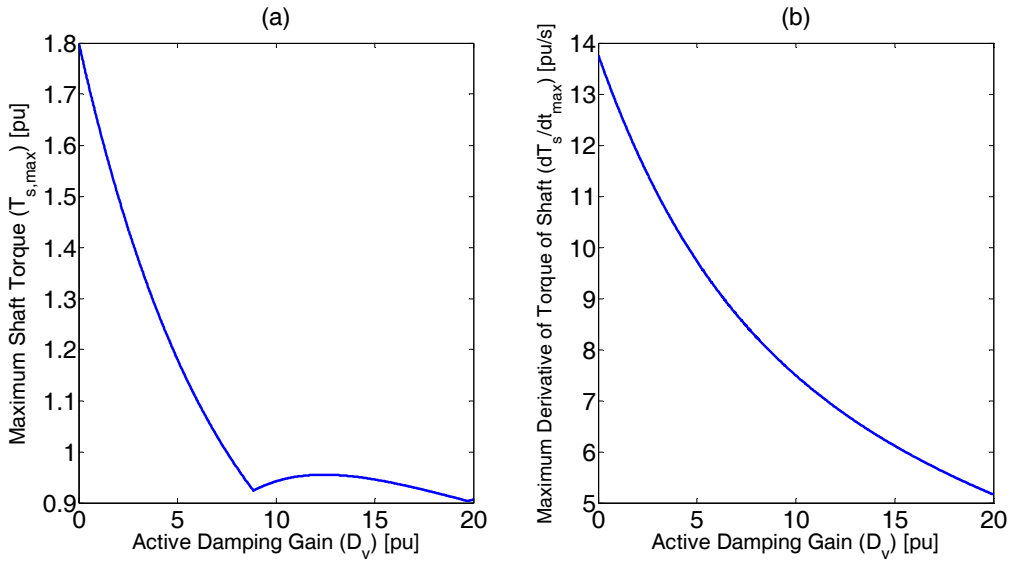

Figure 5-15 Mechanical stress imposed on the generator during and after a fast recovery versus active damping gain, (a) The maximum shaft torque, (b) the maximum shaft torque derivative.

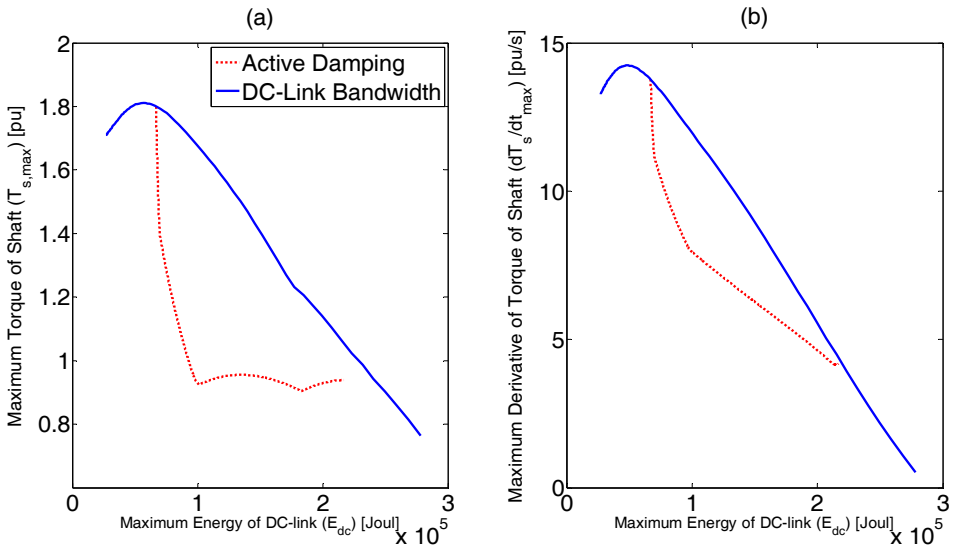

Figure 5-16 (a) The maximum shaft torque, (b) the maximum shaft torque derivative vs. the maximum voltage of the dc-link.

On the one hand, with either no or a small amount of active damping, the dc-link capacitor does not experience any serious over-voltage, but the turbine-generator shaft wears out more quickly. On the other hand, the active damping controller can reduce or eliminate the mechanical stresses at the cost of wearing out the dc-link capacitor. Such issues can limit the effectiveness and adoption of the LVRT-capable control method for PMSGs.

To increase the breadth of the analysis, two aspects need to be analyzed:

1) Impact of Fault Duration

In a fast recovery, the fault clears relatively quickly. This situation is desirable; however, the fault clearance acts as another disturbance stimulating the resonance of the mechanical system again. The clearance disturbance might add to the previous disturbance, the fault itself, which created mechanical oscillations in the first place. These initial oscillations are not usually completely damped before the fault clearance. On the contrary, in the slow recovery situation, the mechanical system has more time to be damped before the second disturbance, or the fault clearance. Figure 5-17 compares the energy needed to mitigate the mechanical stresses in both fast and slow recovery trajectories. First, without any active damping (which yields the minimum $V_{dc,max}$), the mechanical stresses are almost the same. Therefore, even in a slow recovery, the mechanical system is exposed to high stresses and wearing out. However, much less energy is needed from the dc-link to suppress these tensions in this case. On the other hand, these reductions are swiftly saturated, and for a slight further reduction in the shaft torque or its derivative, a considerably higher contribution from the dc-link becomes necessary. Even in a slow recovery, huge mechanical stresses are imposed on the shaft, and their mitigation results in compromising the dc-link performance and stress levels.

2) Impact of Unsymmetrical faults

Unsymmetrical faults are not usually as severe as symmetric three-phase-to-ground faults (at the same location), but they occur more frequently in typical power systems. Because of the accumulative nature of fatigue, they can play an important role in wearing out the generator. The main difference in the unsymmetrical fault condition is only in the “during fault” stage,

where the input grid power usually does not go to zero, and instead, a second-order oscillating power is superimposed on the average value of P_{grid}. These fluctuations disappear as soon as the fault clears. Figure 5-18 shows the frequency response of the shaft torque responding to the input, P_{grid}. The magnitude response at the second-harmonic frequency is about -100 dB, which is very small. In other words, the shaft performance is not compromised by the power oscillating component associated with unsymmetrical faults, and the only part that impacts the shaft is the non-oscillatory part of ΔP_{grid}, which is inherently less than its corresponding value under a symmetrical fault. These results are expected as the dc-link and the mechanical system each act as a low-pass filter with relatively low cut-off frequencies and excellent ability to filter out the second-order oscillation before it reaches the generator shaft. The power oscillations will affect mainly the dc-link capacitor.

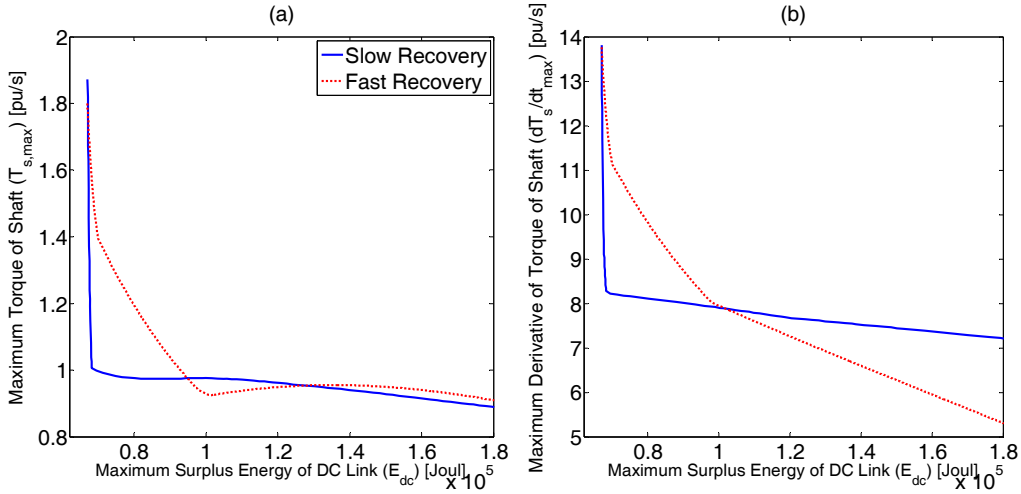

Figure 5-17 (a) The maximum shaft torque, (b) the maximum shaft torque derivative vs. the maximum voltage of the dc-link.

Figure 5-19 compares the responses of the energy sources in the wind generator to the input of a system during a fault condition. Whereas the rotating masses respond to the low-frequency content, the dc-link capacitor is responsible mainly for higher frequencies including second harmonic oscillations caused by asymmetric faults. In other words, asymmetric faults neither increase the fatigue of the mechanical system nor result in over-speeding of rotating masses that may threaten successful LVRT. This analysis also shows that the LVRT-capable PMSG is not inherently capable of reducing electrical tensions

imposed on the dc-link during asymmetric faults. However, some, usually relatively complicated, methods such as those in [100, 178] that allow mitigating the unbalanced fault tensions on the dc-link.

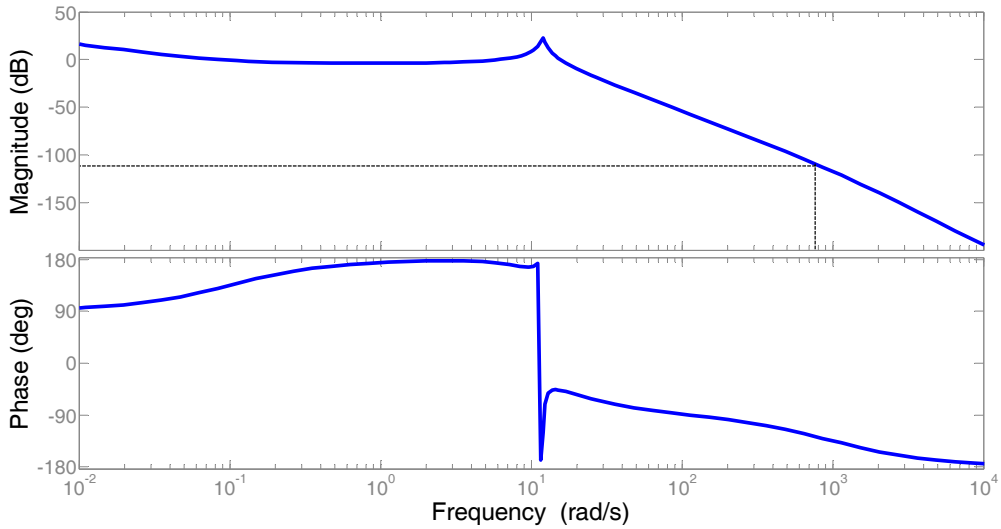

Figure 5-18 The bode diagram of the shaft torque responding to grid power changes during fault phase ($\Delta T_s(s)/\Delta P_{grid}(s)$).

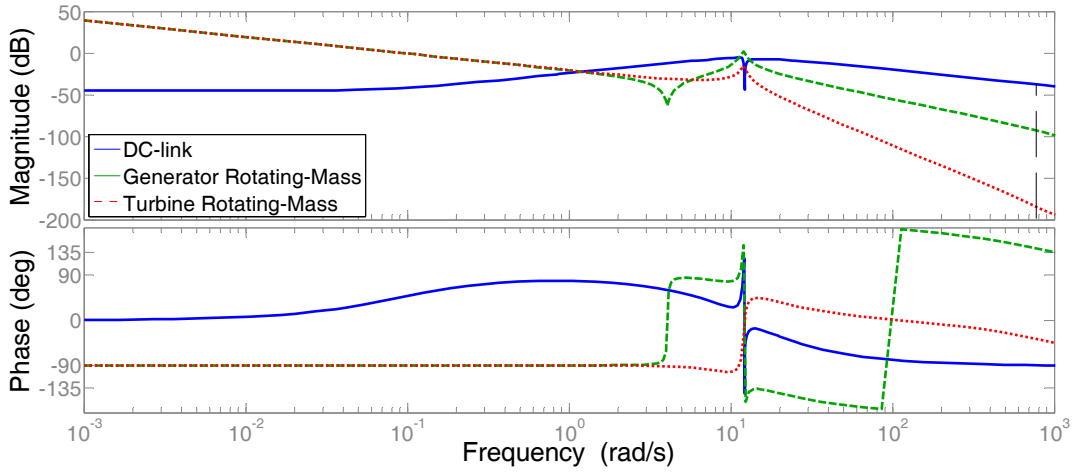

Figure 5-19 Frequency response of the energy sources responding to grid power changes during fault condition.

5.4 Time-Domain Simulation Results

To verify the theoretical analysis in the previous sections, time-domain simulations based on the detailed nonlinear model of a typical Ontario, Canada-based system, shown in Figure 3-7, are employed. The wind generator converters controllers are depicted in Figure 5-3 and Figure 5-4, and the system parameters are given in the Appendices.

The disturbance used for studying this system is a three-phase to-ground fault that occurs at bus #4 at t=35 s in most the cases. Such a severe fault close to the wind generator allows for observing the worst-case scenario. The Matlab/Simulink® package is employed for simulation studies.

5.4.1 Shaft Stiffness

The shaft stiffness and weight ratio of the rotating masses are changed to examine the analytical results. The slow recovery scenario is adopted here, where the active power injection of the GSC is forced to follow the slow recovery scenario, shown in Figure 5-6, to examine the worst-case scenario. The results are shown in Figure 5-20. While these changes do not impact the dc-link voltage, the generator rotating mass can experience a 30% over-speed. Meanwhile, the turbine rotating speed does not exceed 1.18 per unit. The results, once more, show that the utilization of the single-mass model can lead to misleading results.

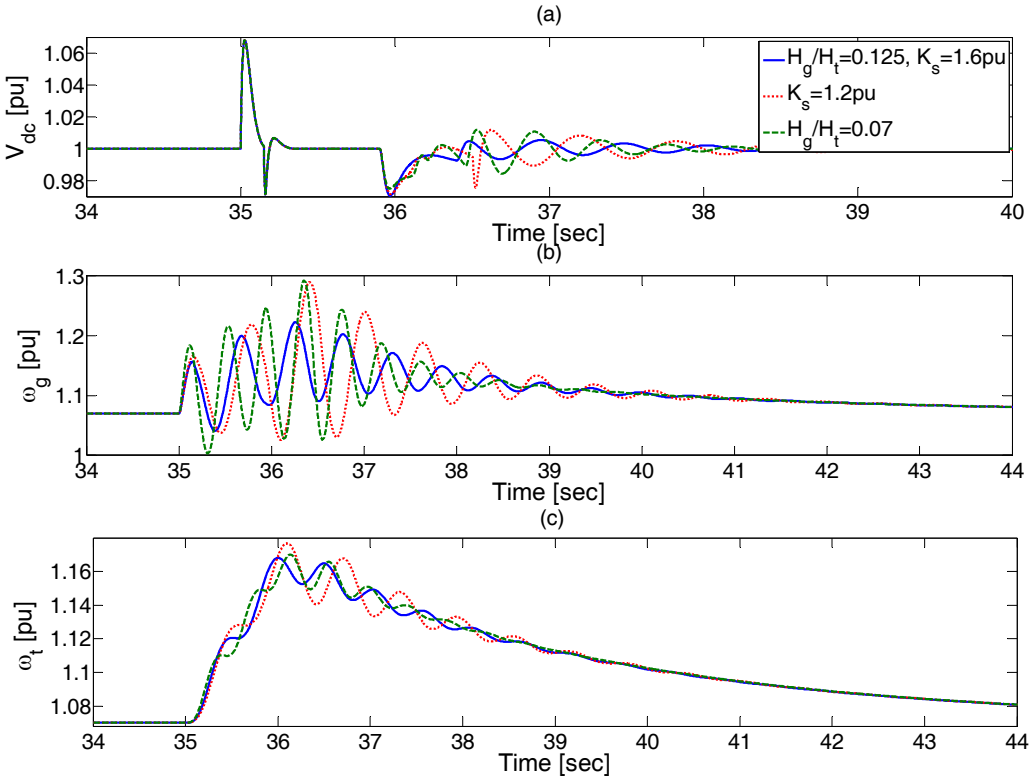

Figure 5-20 Impact of doubly-mass model specifications when a slow recovery occurs after fault; (a) Dc-link voltage, (b) Generator rotating speed, (c) Turbine rotating speed.

5.4.2 DC-link Controller Bandwidth

A fast recovery scenario is also tested; the results are shown in Figure 5-21. As predicted by the theoretical analysis, a lower dc-link voltage control bandwidth reduces the amplitude of oscillations on the rotating masses speeds at the cost of larger changes in the dc-link voltage. The figure also depicts the mechanical tensions and how using the dc-link as a buffer can save the generator shaft from higher stresses. Although the stress on the mechanical system of the generator is reduced, the capacitor will wear out faster.

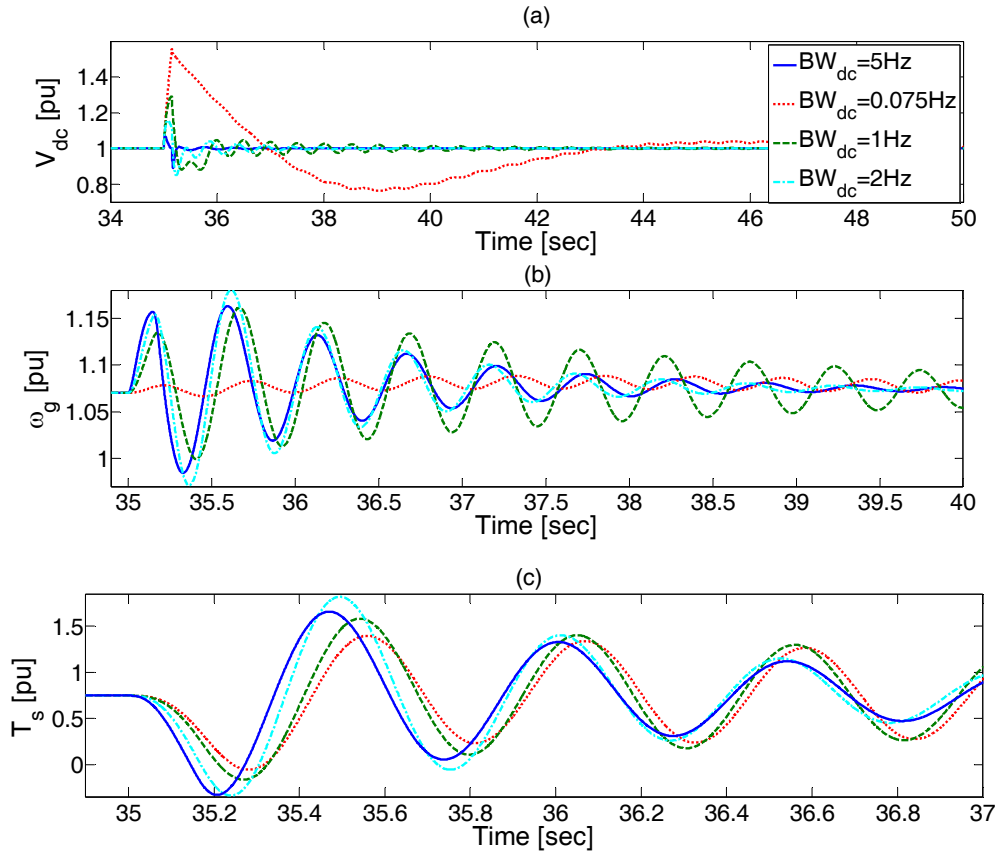

Figure 5-21 Impact of dc-link controller bandwidth when a fast recovery occurs after fault; (a) Dc-Link Voltag, (b) Generator rotating Speed, (c) Torque of Shaft.

5.4.3 Active Damping

Figure 5-22 shows the generator performance when the active damping is applied in the slow voltage recovery case. Again, time-domain simulations confirm the theoretical findings, where the active damping method reduces the fluctuations in the generator rotating mass speed at the cost of higher deviations in the dc-link voltage. Figure 5-22(b) reveals that at a

wind speed of 12 m/s, the generator rotating speed can exceed 1.20 pu, which is close to the over-speed threshold of wind turbines [99]. The active damping method yields a successful LVRT and reduces the mechanical stresses on the turbine shaft, as predicted by the analysis (Figure 5-22(c)).

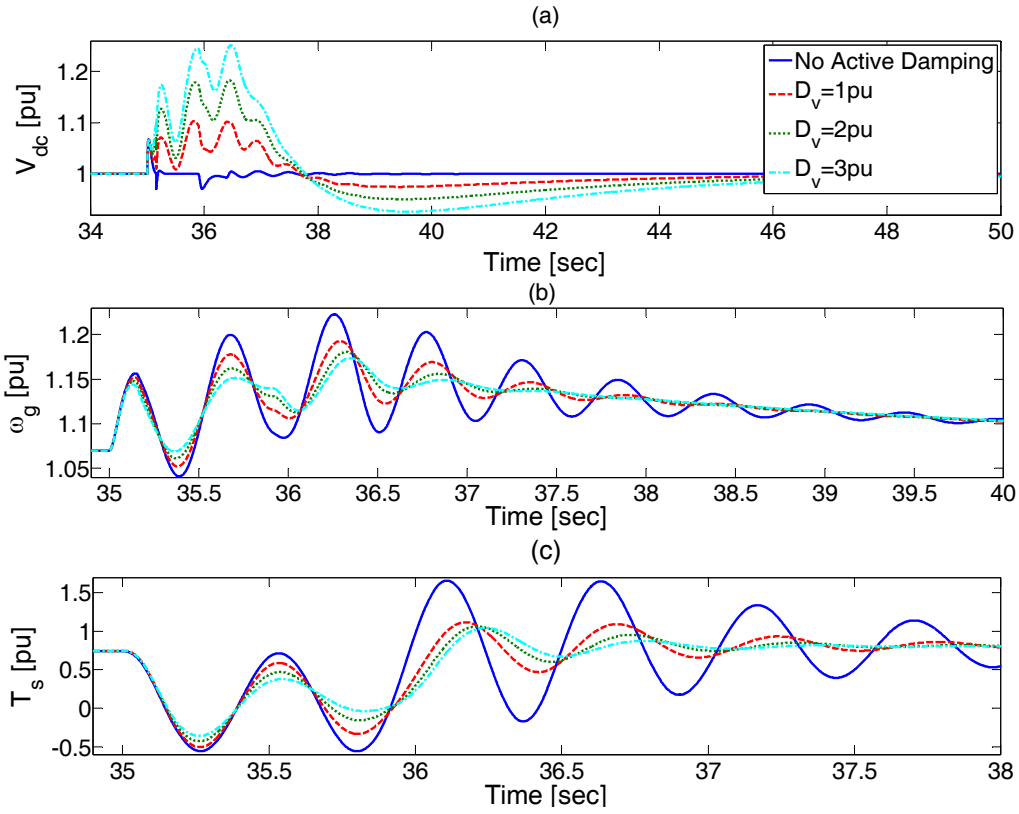

Figure 5-22 Impact of the active damping when a slow recovery happens after fault; (a) Dc-Link Voltag, (b) Generator rotating Speed, (c) Torque of Shaft.

5.4.4 Asymmetric Fault

Figure 5-23 shows the wind power generator performance when a single-phase fault occurs at the generator terminals. Obviously, with a 1.20 pu thermal limit of the power converter, the healthy phases are capable of injecting the active power of the faulted phase. In such a case, the average power remains constant, but the second-order harmonic appears on the generator output active power, P_{wind}. However, these oscillations do not yield observable oscillations on the shaft torque and its derivative. Only negligible fluctuations, because of the

transients associated with the fault and its clearance, are observed. Instead, the dc-link voltage fluctuates because of the asymmetrical fault.

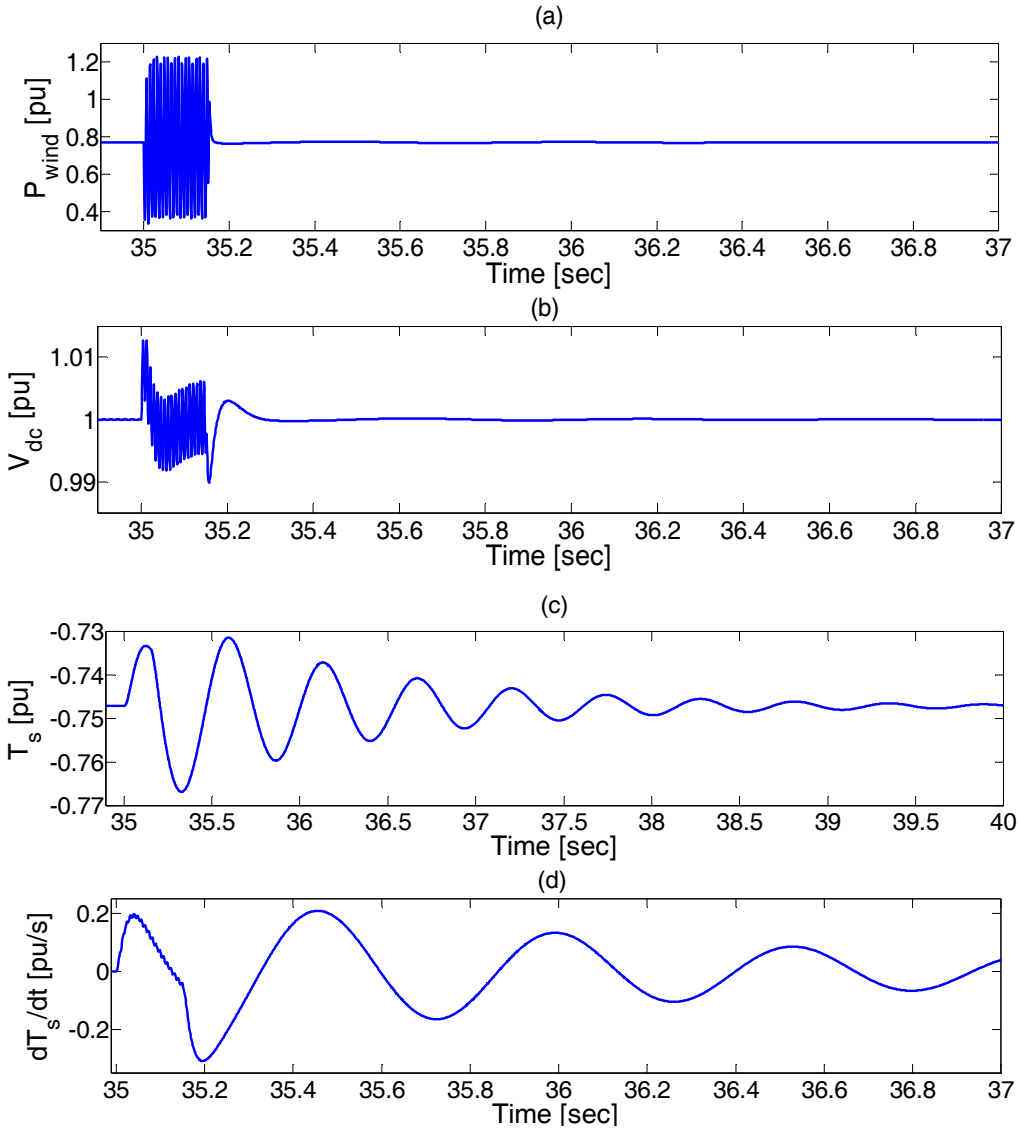

Figure 5-23 Impact of a single-phase fault that occurs at the generator terminal; (a) Output power of wind generator, (b) DC-link voltage, (c) Torque of shaft, (d) Derivative of torque of shaft.

5.5 Summary

This chapter investigated the impacts of the LVRT control on the stability and risk of resonance, successful operation, and fatigue in a full-scale PMSG-based wind power generation system. An analytical model, considering the double-mass nature of the

turbine/generator and typical LVRT requirements, was developed, validated, and used to characterize the dynamic performance of the wind generation system under LVRT control and practical generator characteristics. To enhance the operation and reduce the fatigue under LVRT control, two solutions, based on active damping control and dc-link voltage bandwidth retuning, were proposed, analyzed and compared. The detailed nonlinear time-domain simulation results validated the accuracy of the developed model and analytical results.

Chapter 6
Application of Plug-in Hybrid Vehicles in Frequency Regulation

6.1 Introduction

In spite of the potential capability of PHEVs to participate in dynamic frequency regulation, several technical challenges need to be addressed. A central controller for single-phase distributed electric vehicles may result in delay while a distributed control may lead to asymmetry. Both of these situations may result in instability. In the presence of such loads/generators, the coupling between frequency and voltage stability is not valid anymore. In this research, both centralized and distributed control will studied and an improved hybrid control solution will be proposed. The mutual impact of voltage and frequency stabilization will be investigated and practical solutions will be suggested.

The development of a coordinated control method for incorporating both wind and PHEVs in the power system frequency regulation while considering their practical constraints is not only useful but also necessary, particularly for systems with reduced inertia, such as microgrids. The aging of wind generators, state of charge (SOC) limits of PHEVs, and delays in communications are the main constraints that should be investigated to realize the practical and effective utilization of wind generators and PHEVs in primary frequency regulation.

The contributions of this chapter to the research field are:

1) Utilizing PHEVs for virtual inertia. Comparing droop to virtual inertia as solutions for systems with insufficient physical inertia.

2) Considering the impacts of single-phase nature of PHEVs. Investigating both centralized and distributed control strategies and proposing a hybrid method.

3) A proposal for a coordinated frequency regulation method that utilizes PHEVs and a wind generator and considers their practical constraints.

4) An investigation and comparison of the virtual inertia and droop as tools for coordinated frequency regulation.

5) A thorough investigation and comparison of the impacts of two frequency-regulating coordination structures, centralized and distributed, for wind generation and PHEVs.

In Section 6.2, incorporating electric vehicle in frequency regulation is studied. The centralized control is investigated and the droop method is compared to virtual inertia. It also focuses on distributed control with its disadvantages and remedies. The cooperation of wind and PHEVs in the power system frequency regulation is described in Section 6.3. The centralized and distributed cooperative solutions and their dynamic analysis are discussed. Simulation results are presented in Section 6.4 to validate theoretical analysis and discussions. Finally, conclusions are drawn in Section 6.5.

6.2 EVs as a sole source

6.2.1 Centralized Control

Virtual inertia is previously discussed in literature [50, 80, 179]. It tries to emulate the rotating-mass inertia by injecting power as a function of frequency derivative. The important question that may arise is why a centralized control could or could not be used for virtual inertia, whereas successful application of centralized droop has been reported previously [145]. On the other hand, the advantages/disadvantages of virtual inertia as compared to the droop method may be questioned. This section tries to answer these questions.

6.2.1.1 Virtual Inertia

While distributed control of virtual inertia, with local measurement, may result in asymmetric power injection, a centralized control (as shown in Figure 6-1) could guarantee a balanced incorporation. In this scheme, every PHEV measures its output and transmits its available active and reactive power to the computation center. The computation center analyzes the received information to find out how much symmetric resources are available. Then based on its availability and measured voltage and frequency at the substation bus and its control

method (e.g. droop, virtual inertia …), the computation center decides the power that will be injected by each PHEV to participate in frequency stabilization. This reference power is transmitted to each participating PHEV via the communication network. The demanded power will be shared between different PHEVs so that the total active and reactive powers at the substation bus remain symmetric.

However, such a control system needs communication, and the wide-spread nature of PHEVs makes a devoted communication line inefficient. On the other hand, general communication lines are highly developed and widely used nowadays. Although these communication lines are economically desirable, they may lead to some delay, which impacts system stability.

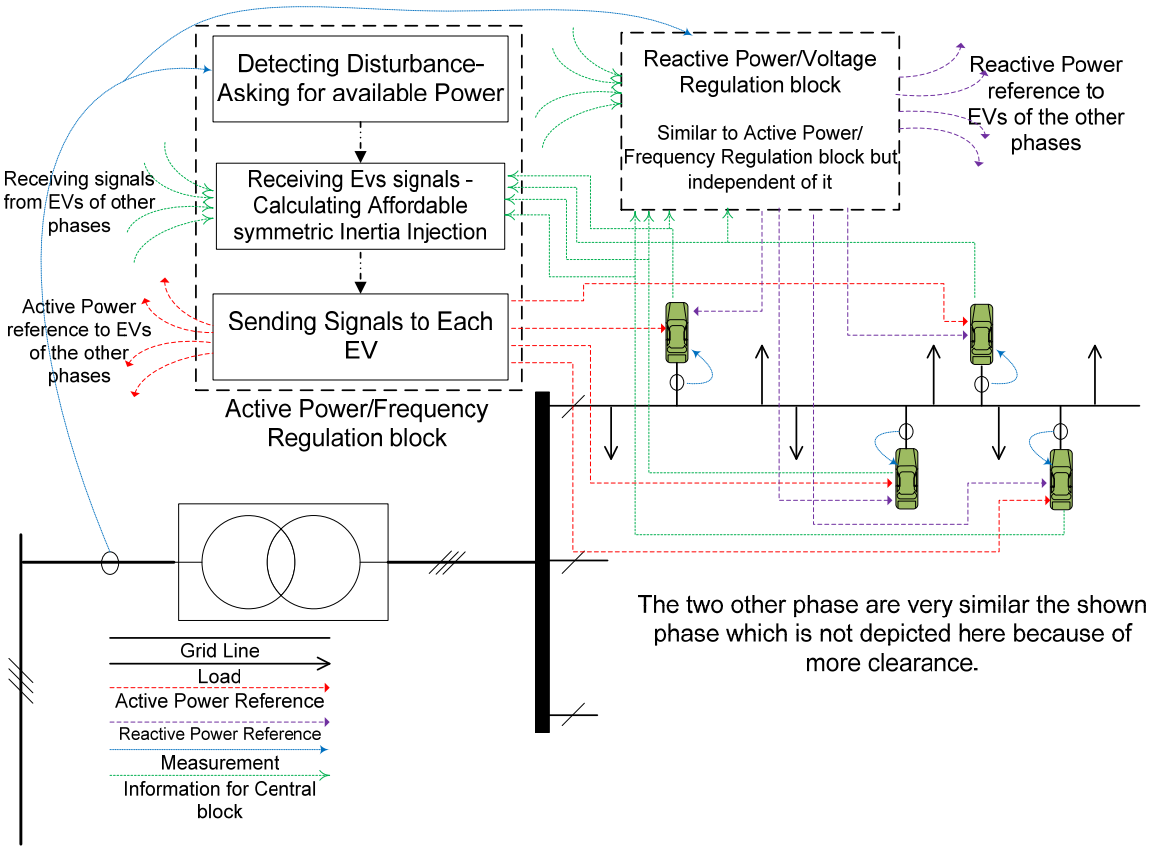

Figure 6-1 Centralized PHEV-based virtual inertia control. The central control receives signal form each PHEV to measure the available symmetric inertia and then specifies and communicates to each PHEV its contribution.

To investigate the impact of distributed inertia, the system shown in Figure 6-2 is employed. The network after the breaker has the capability to constitute a microgrid and work autonomously. In fact, the microgrid is utilized for this study since the asymmetrical power injection is complicated enough and this relatively simple, yet practical, model allows better understanding.

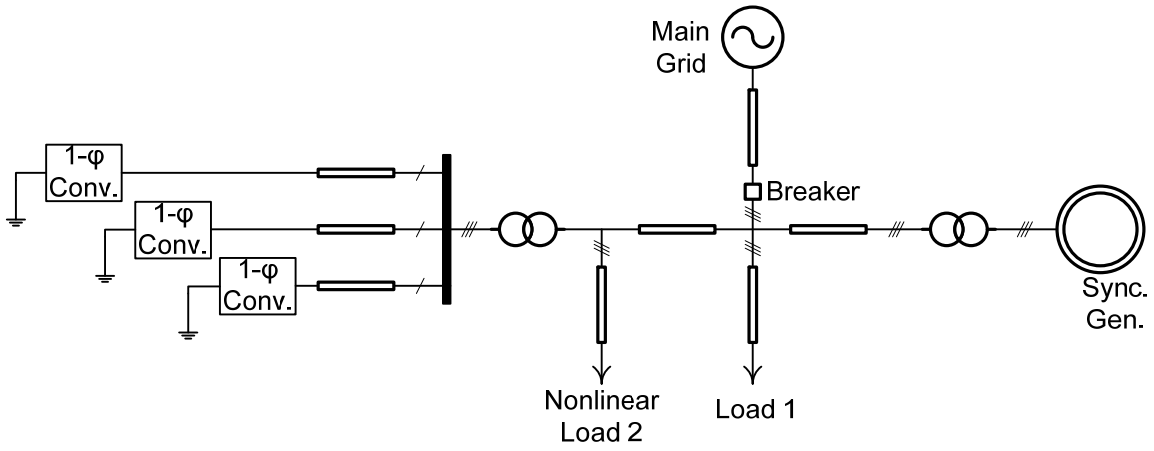

Figure 6-2 System under study.

In [180], it is shown that if controller parameters are appropriately tuned, then the fast controller details (e.g. current controllers) could be neglected even with typical dynamic loads (e.g. induction motor loads). By considering the typical fast response of single-phase converters, the injected power can be simply assumed equal to the desired reference power as given in (6-1).

$$\Delta P_{ev,vinertia-ref} = \frac{M_{ev}s}{\tau_{ev}s+1}\Delta\omega. \tag{6-1}$$

where M_{ev} and τ_{ev} are EV-based inertia factor and time constant, respectively; and ω is the system frequency. It is worthy to mention that M_{ev} could not be simply regarded as a substitute of M_{diesel}, as it is a controller gain designed to emulate the performance of actual inertia to damp frequency oscillations.

The rest of the system could be modeled as discussed in [162] and shown in Figure 6-3. This model reveals how increasing M_{ev} in symmetric virtual inertia could enhance the system performance. Figure 6-4 shows the eigen-values derived from the small-signal model shown in Figure 6-3. Obviously, the dominant poles move toward the left-half plane (LHP) as the

virtual inertia increases. However, the delay has not been considered yet. Reference [181] shows that, a centralized control could suffer from three source of delays: transmitting information from sensors (in our case PHEVs which are sparsely distributed), computation, sending the required action to actuators (which are again sparsely distributed PHEVs). The absence of a dedicated communication line will increase the delay. Reference [182] states that in "one way" communication, the maximum delay is 150 ms.

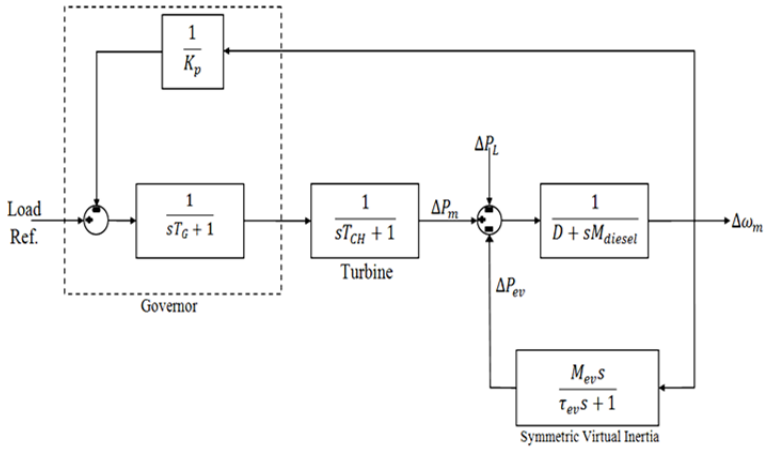

Figure 6-3 System schematic block diagram.

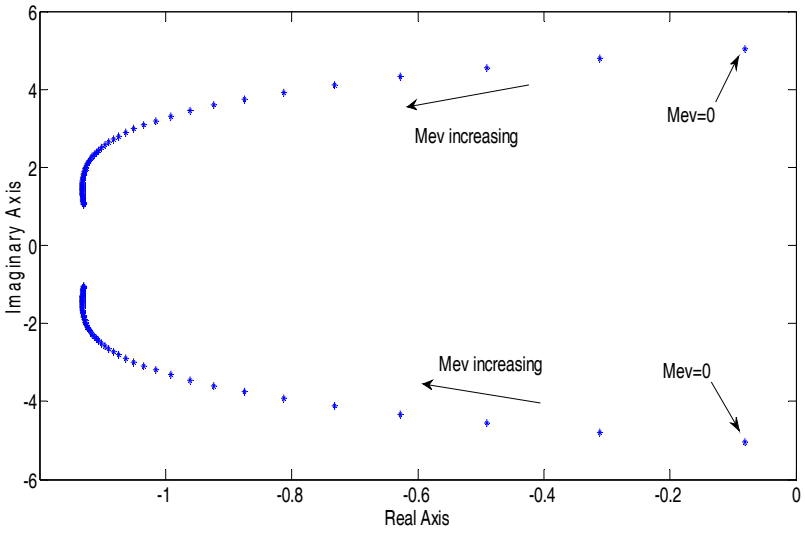

Figure 6-4 System dominant poles' root-locus when symmetric virtual inertia is applied.

Although previous works did not address such a distributed single-phase regulation, references such as [183] and [184] discussed the delay impact on conventional generators. Similar to [183, 184], one delay for the overall network is considered here. In fact, if

different phases may have different delays, the most severe scenario occurs when all delays are equal. In other words, if delay is considered as a late power injection, less delayed phases could compensate the impact of more delayed phase. In the next sections, this scenario will be simulated and discussed. Equations (6-2) and (6-3) formulate the symmetric virtual inertia with a time delay τ_d in time- and s-domains, respectively.

$$\Delta P_{ev,vinertia-actual}(t) = \Delta P_{ev,vinertia-ref}(t-\tau_d). \tag{6-2}$$

$$\Delta P_{ev,vinertia-actual}(s) = \Delta P_{ev,vinertia-ref}(s)e^{-s\tau_d}. \tag{6-3}$$

The delay element can be approximated as follows [185]:

$$e^{-\tau_d s} \approx \frac{1-\tau_d s/2}{1+\tau_d s/2}. \tag{6-4}$$

By replacing (6-4) by (6-3) in Figure 6-3, more realistic system will be obtained with

$$\Delta P_{ev,vinertia-actual} = \frac{M_{ev} s e^{-\tau_d s}}{\tau_{ev} s+1}\Delta\omega \approx \frac{M_{ev} s}{\tau_{ev} s+1}.\frac{1-\tau_d s/2}{1+\tau_d s/2}\Delta\omega. \tag{6-5}$$

Figure 6-5 depicts the root-locus of system dominant poles when virtual inertia is adopted and delay is increasing from 0 to 300 ms. With small incorporation of electric vehicles (EVs) in frequency regulation, the system is not too vulnerable to time delay whereas in high contribution cases, a very small delay could lead to instability. Indeed, these figures illustrate why employing centralized virtual inertia is not reasonable under high penetration level of PHEVs.

6.2.1.2 Droop Control

Droop is a well-known method of incorporating generation units in frequency/power regulation. While droop method has been usually implemented distributed with local measurement, [145] has shown that in case of distributed EV sources, a centralized droop controller could be more effective. Equations (6-6) and (6-7) represent ideal and delayed droop functions, respectively. Figure 6-6 depicts the delay impact on the dominant poles. Although time delay forces the poles toward the right-half-plane too, much higher amount of delay is needed to destabilize the microgrid, even in high contribution of PHEVs in frequency regulation.

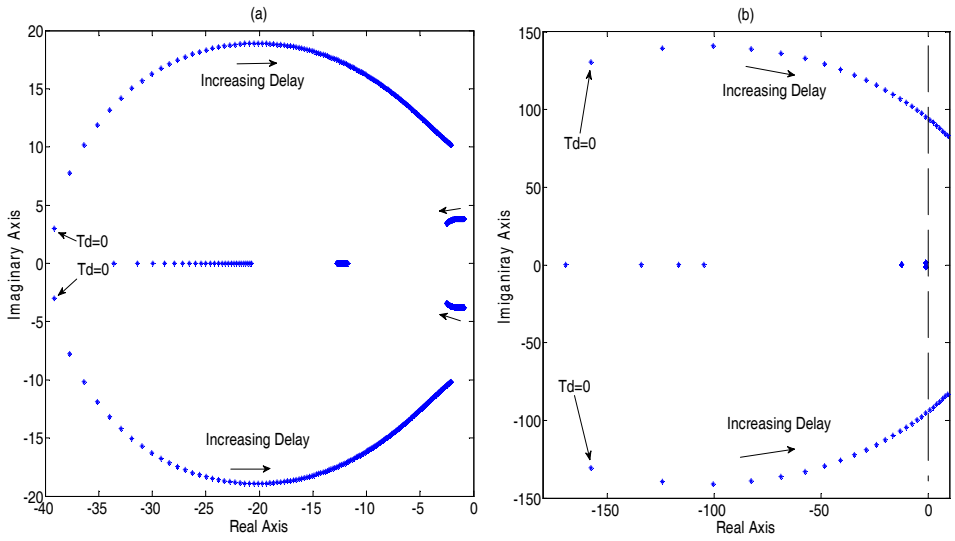

Figure 6-5 Root-locus of the dominant poles of the system equipped virtual inertia when (a) $M_{ev}/M_{diesel}\approx 1$ and τ_d=0-300ms. (b) $M_{ev}/M_{diesel}\approx 10$ and τ_d=0-30ms.

$$\Delta P_{ev,droop-ref} = \frac{1/K_{ev}}{\tau_{ev}s+1}\Delta\omega. \tag{6-6}$$

$$\Delta P_{ev,droop-delay} = \frac{(1/K_{ev})e^{-\tau_d s}}{\tau_{ev}s+1}\Delta\omega \approx \frac{1/K_{ev}}{\tau_{ev}s+1}.\frac{1-\tau_d s/2}{1+\tau_d s/2}\Delta\omega. \tag{6-7}$$

While τ_{ev} is used as EV-based droop time-constant, similar to inertia, K_{ev} introduces EV droop factor. It should be noted that τ_{ev} for droop is usually constant and dictated by the line frequency [180]. The robustness of the droop control method against time-delay may incorrectly imply that it should be preferred over the virtual inertia control method. Figure 6-7 compares the impacts of using virtual inertia, droop method and increasing the physical inertia. Obviously, virtual inertia is much more similar to real inertia while droop could not influence the transient behavior of the system in many aspects. In fact, all of these differences, advantages and disadvantages, could be explained by considering the nature of droop. It is very similar to a low-pass filter and slower than a virtual and physical inertia. That is why its influence in steady-state is more significant and more robust to the delay. On the other hand, this inherent feature prevents a comparable impact on system transient. While droop is not a good replacement for virtual inertia and centralized control of virtual inertia may significantly impact the stability, another approach should be employed.

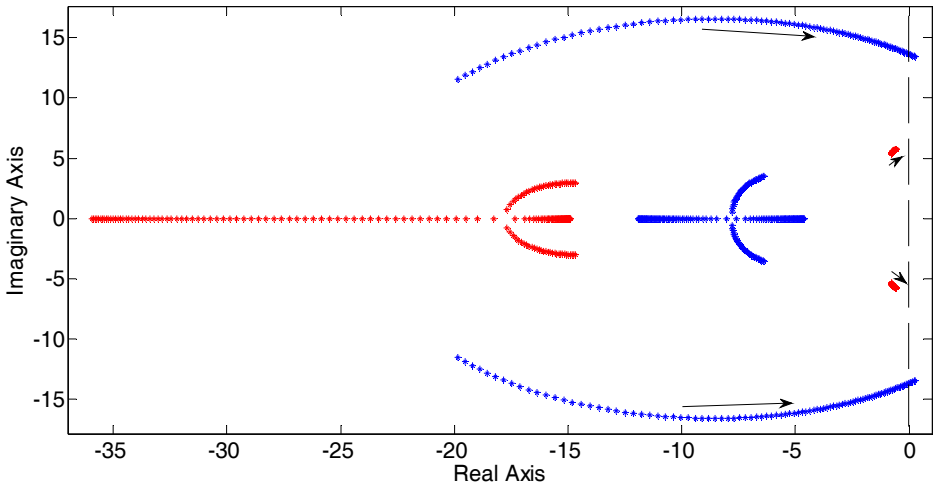

Figure 6-6 Root-locus of the dominant poles of the system equipped centralized droop controller and τ_d=0-100ms when $K_{ev}/K_p \approx 8$ and (red poles) and $K_{ev}/K_p \approx 1$ (blue poles).

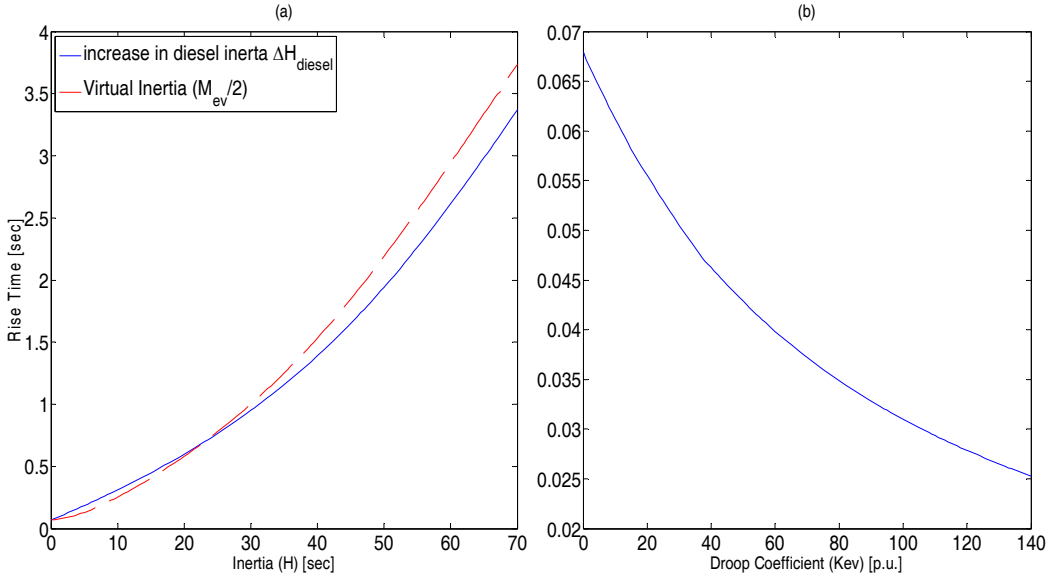

Figure 6-7 Change of rise-time of the system frequency response when a step changes takes place in load in case of (a-blue) increase in physical inertia, (a-red) implementing virtual inertia and (b) droop. τ_d and τ_{ev} for both droop and virtual inertia are constantly zero and 0.05 respectively.

6.2.2 Distributed Control

The other possible method for implementing virtual inertia is distributed local control. It means that every PHEV responds to frequency based on its own measurement and no communication for active power is needed anymore as shown in Figure 6-8. By this method,

communication delay and its undesired consequences will be removed but it may have its own and new conflicts. The following part investigates this issue.

6.2.2.1 Asymmetric Active Power Injection

One of these possible scenarios is asymmetric power injection; in other words, a situation in which the three phases do not incorporate equally in power/frequency regulation. This scenario will be probable even in case of high penetration of PHEVs since not many vehicle owners will allow PHEVs incorporation in frequency regulation. Further, the new idea of using the inverter of vehicle's electric motor as a charger [141], and the relatively small energy (in short time) demanded by the virtual inertia controller may result in sufficient incorporation of small portion of PHEVs in virtual inertia. However, these factors increase the risk of asymmetrical active power injection.

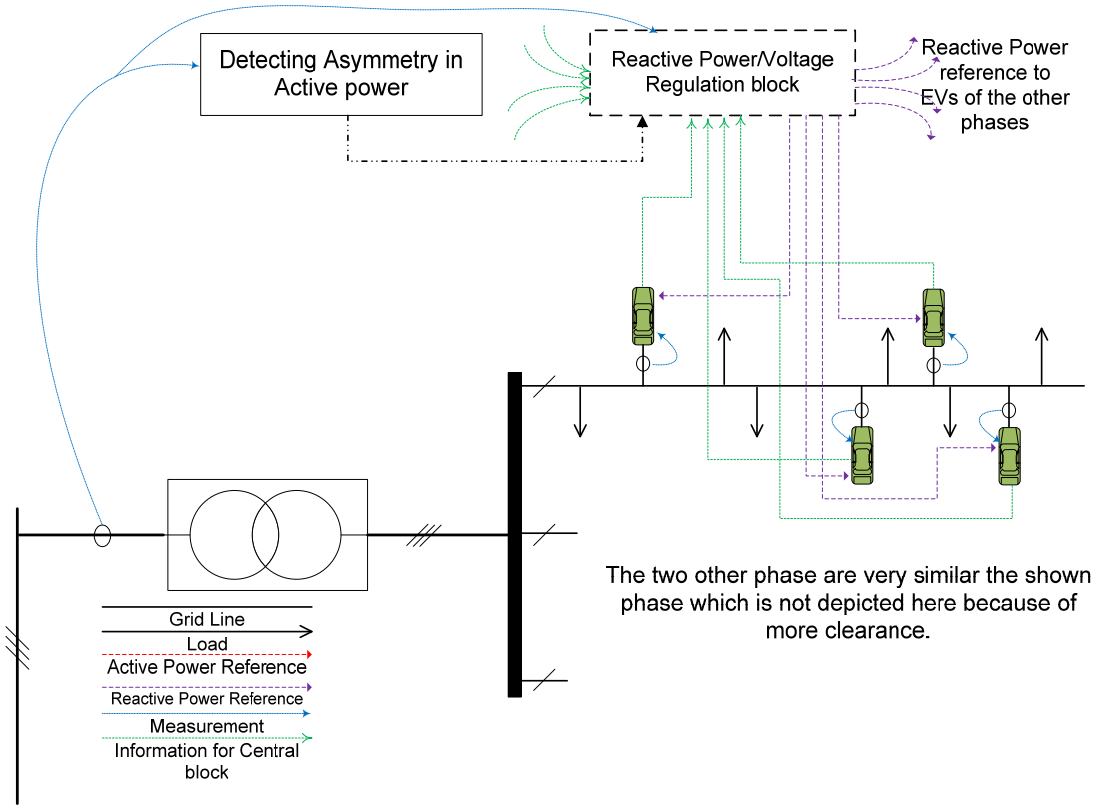

Figure 6-8 Remedy control method. Since virtual inertia injection is local no central active power regulation or active power reference is shown here. Distributed method diagram is very similar expect that "detecting asymmetry" block is absent there.

To clarify this scenario, let us assume that the voltage at the single-phase converters bus is balanced and each converter is only used to inject virtual inertia power at unity power factor. Therefore, voltages can be given by

$$v_a = \sqrt{2}V\sin(\omega t), v_b = \sqrt{2}V\sin(\omega t - 2\pi/3), v_c = \sqrt{2}V\sin(\omega t + 2\pi/3). \quad (6\text{-}8)$$

and currents can be defined as

$$i_a = \sqrt{2}I_a\sin(\omega t), i_b = \sqrt{2}I_b\sin(\omega t - 2\pi/3), i_c = \sqrt{2}I_c\sin(\omega t + 2\pi/3). \quad (6\text{-}9)$$

so that the power components are given by

$$P_a = VI_a, P_b = VI_b, P_c = VI_c. \quad (6\text{-}10)$$

and

$$P_{ev-ref} = P_a + P_b + P_c. \quad (6\text{-}11)$$

By definition, the three-phase power is:

$$P_{3-phase} = v_a i_a + v_b i_b + v_c i_c. \quad (6\text{-}12)$$

By using (6-8) and (6-9) in (6-12) and after mathematical manipulation, (6-13) could be derived

$$P_{3-phase} = VI_a + VI_b + VI_c + (-VI_a - \frac{1}{2}VI_b - \frac{1}{2}VI_c)\cos(2\omega t) + (\frac{\sqrt{3}}{2}VI_b - \frac{\sqrt{3}}{2}VI_c)\sin(2\omega t). \quad (6\text{-}13)$$

Now, without loss of generality it could be assumed that

$$P_a = aP_{ev-ref}, P_b = bP_{ev-ref}, P_c = cP_{ev-ref}. \quad (6\text{-}14)$$

so that

$$0 \le a, b, c \le 1. \quad (6\text{-}15)$$

and

$$a + b + c = 1. \quad (6\text{-}16)$$

While (6-16) seems obvious, the reason for greater or equal to zero constraint in (6-15) may need clarification. Without this constraint, some of these single-phase converters may be allowed to inject power against the virtual inertia objective. Although mathematically it is possible, in power systems, it means that some of the converters, supposed to support the system, try to destabilize the system which is not reasonable. It should be considered that since every PHEV works autonomously and without coordination, each of them tries to

stabilize the frequency. In this situation, using negative *a*, *b* or *c* opposes the virtual inertia objective by yielding a positive feedback and worsens the system stability.

By considering (6-10), (6-11) and (6-12), (6-13) could be rewritten as

$$P_{3-phase} = P_{ev-ref} + (-a + \frac{b}{2} + \frac{c}{2})P_{ev-ref}\cos(2\omega t) + (\frac{b\sqrt{3}}{2} - \frac{c\sqrt{3}}{2})P_{ev-ref}\sin(2\omega t). \quad (6\text{-}17)$$

Because of the asymmetric active power injection, the second harmonic terms appear in (6-17) and may impact not only the voltage quality but also system stability.

The impacts of this asymmetry do not remain limited to active power. For more illustration, exactly the same situation in which each single-phase converter is supposed to just inject virtual inertia and works at unity power factor could be used. It is expected that 3-phase reactive power is zero. By definition it is

$$Q_{3-phase} = \frac{1}{\sqrt{3}}(v_{bc}i_a + v_{ca}i_b + v_{ab}i_c). \quad (6\text{-}18)$$

By replacing (6-8)-(6-9) in (6-18) and using (6-10), (6-19) could be reached

$$Q_{3-phase} = (-P_a + \frac{1}{2}P_b + \frac{1}{2}P_c)\sin(2\omega t) + (-\frac{\sqrt{3}}{2}P_b + \frac{\sqrt{3}}{2}P_c)\cos(2\omega t). \quad (6\text{-}19)$$

and it could be rewritten as follows:

$$Q_{3-phase} = (-a + \frac{b}{2} + \frac{c}{2})P_{ev-ref}\sin(2\omega t) + (-\frac{\sqrt{3}b}{2} + \frac{\sqrt{3}c}{2})P_{ev-ref}\cos(2\omega t). \quad (6\text{-}20)$$

While reactive power is expected to be zero, it is oscillating and its extent depends on active power and asymmetry extent. It could be easily proved that the oscillating part of active power in (6-17) has the same amplitude as the reactive power described in (6-20). In other words, the greater asymmetrical active power injection results not only in higher active power fluctuations but also larger reactive power oscillation. It could also result in degrading both voltage quality and stability.

6.2.2.2 Asymmetric Reactive Power Injection

One of the main potential applications of PHEVs is reactive power generation especially that it does not involve PHEV's battery. Findings in the previous part bring out the question about any possible impact of reactive power asymmetry on active power. To investigate this

situation, a simple scenario is considered. Single-phase converters are adjusted to inject only reactive power and the bus voltage is assumed to be balanced, as defined by (6-8). The current of each phase under these assumptions could be described by

$$i_a = \sqrt{2} I_a \sin(\omega t - \pi/2), i_b = \sqrt{2} I_b \sin(\omega t - 7\pi/6), i_c = \sqrt{2} I_c \sin(\omega t + \pi/6). \quad (6\text{-}21)$$

Similar to (6-5), (6-6) and (6-8), the following equations could be defined:

$$Q_a = VI_a, Q_b = VI_b, Q_c = VI_c. \quad (6\text{-}22)$$

and

$$Q_{ev-ref} = Q_a + Q_b + Q_c. \quad (6\text{-}23)$$

$$Q_a = aQ_{ev-ref}, Q_b = bQ_{ev-ref}, Q_c = cQ_{ev-ref}. \quad (6\text{-}24)$$

The same constraints in (6-15) and (6-16) for the same reasoning are expected here. Now by considering (6-18) and replacing (6-8), (6-21)-(6-24) wherever they are applicable, (6-25) could be reached. Obviously it is very similar to (6-17). The reactive power asymmetry could be harmful for the system by threatening the voltage stability.

$$Q_{3-phase} = Q_{ev-ref} + (a - \frac{b}{2} - \frac{c}{2})Q_{ev-ref} \cos(2\omega t) + (-\frac{\sqrt{3}b}{2} + \frac{\sqrt{3}c}{2})Q_{ev-ref} \sin(2\omega t). \quad (6\text{-}25)$$

In a similar way, impact on active power can be quantified by replacing (6-8) and (6-21) in (6-12) and considering (6-22) to (6-24). Therefore,

$$P_{3-phase} = (-a + \frac{b}{2} + \frac{c}{2})Q_{ev-ref} \sin(2\omega t) + (-\frac{\sqrt{3}b}{2} + \frac{\sqrt{3}c}{2})Q_{ev-ref} \cos(2\omega t). \quad (6\text{-}26)$$

Similarity between (6-26) and (6-20), (6-25) and (6-17) could results in another question. Whether simultaneous asymmetric active power and reactive power could impact each other? If positive, do they amplify or attenuate each other? These questions will be answered in the following section.

6.2.2.3 Remedy

To find out any possible mutual impact between active and reactive power asymmetry, a more general case should be considered. A single-phase converter could be allowed to inject both active and reactive power. With the assumption that bus voltage is balanced and (6-8) is still valid, the currents should be described as below:

$$i_a = \sqrt{2} I_a \sin(\omega t - \varphi_a), i_b = \sqrt{2} I_b \sin(\omega t - \varphi_b - 2\pi/3), i_c = \sqrt{2} I_c \sin(\omega t - \varphi_c + 2\pi/3). \quad (6\text{-}27)$$

Based on this new definition, (6-7) and (6-19) should be modified while (6-8) and (6-20) are still valid.

$$P_a = VI_a \cos(\varphi_a), P_b = VI_b \cos(\varphi_b), P_c = VI_c \cos(\varphi_c). \quad (6\text{-}28)$$

$$Q_a = VI_a \sin(\varphi_a), Q_b = VI_b \sin(\varphi_b), Q_c = VI_c \sin(\varphi_c). \quad (6\text{-}29)$$

Then, by replacing (6-8) and (6-27) in (6-12), and considering (6-11), (6-23), (6-28) and (6-29), the following equation could be concluded.

$$\begin{aligned} P_{3-phase} = P_{ev-ref} + (-P_a + \frac{1}{2}P_b + \frac{1}{2}P_c - \frac{\sqrt{3}}{2}Q_b + \frac{\sqrt{3}}{2}Q_c)\cos(2\omega t) + \\ (\frac{\sqrt{3}}{2}P_b - \frac{\sqrt{3}}{2}P_c - Q_a + \frac{1}{2}Q_b + \frac{1}{2}Q_c)\sin(2\omega t). \end{aligned} \quad (6\text{-}30)$$

Firstly this equation shows that in case of asymmetric active-power/frequency regulation, the classical power stability analysis is not valid any more. The reason of this invalidity is the essential assumption of decoupled active-power/frequency and reactive-power/voltage in large power systems. Equation (6-30) reveals clearly that in asymmetric power regulation, active and reactive powers are not decoupled anymore. To cancel out the fluctuation in active power caused by asymmetry, the coefficients of cosine and sine in (6-30) should be equal to zero.

$$-\frac{\sqrt{3}}{2}Q_b + \frac{\sqrt{3}}{2}Q_c - P_a + \frac{1}{2}P_b + \frac{1}{2}P_c = 0. \quad (6\text{-}31)$$

$$-Q_a + \frac{1}{2}Q_b + \frac{1}{2}Q_c + \frac{\sqrt{3}}{2}P_b - \frac{\sqrt{3}}{2}P_c = 0. \quad (6\text{-}32)$$

In fact, if asymmetric active power is given (measured), the reactive power of each single-phase converter could be assigned to mitigate the fluctuations on active power. Equations (6-23), (6-31) and (6-32) can be solved simultaneously to obtain a unique solution for the required reactive power injection to cancel out active power fluctuation. In other words, the question could be represented as how $Q_{ev\text{-}ref}$ could be divided between these three single-phase converters to mitigate active power fluctuations.

$$\begin{bmatrix} Q_a \\ Q_b \\ Q_c \end{bmatrix} = \begin{bmatrix} \frac{1}{3} & 0 & \frac{\sqrt{3}}{3} & -\frac{\sqrt{3}}{3} \\ \frac{1}{3} & -\frac{\sqrt{3}}{3} & 0 & \frac{\sqrt{3}}{3} \\ \frac{1}{3} & \frac{\sqrt{3}}{3} & -\frac{\sqrt{3}}{3} & 0 \end{bmatrix} \begin{bmatrix} Q_{ev-ref} \\ P_a \\ P_b \\ P_c \end{bmatrix}. \tag{6-33}$$

Solving this 3-equation, 3-unknown problem gives a unique solution which is shown in (6-33). Obviously, in a symmetric active power case, P_a=P_b=P_c, the reactive power injection is also symmetric. The impact of such reactive power assignment on the total 3-phase reactive power has not been investigated yet. For this purpose, firstly, the total reactive power in general and similar to (6-30) should be calculated. Obviously, the coefficients of cosine and sine in (6-34) are respectively equal to sine and negative of cosine coefficients in (6-30). This means that elimination of fluctuations in active power does not result in any fluctuation in reactive power, however both of them are asymmetric.

$$\begin{aligned} Q_{3-phase} = Q_{ev-ref} + (Q_a - \frac{1}{2}Q_b - \frac{1}{2}Q_c - \frac{\sqrt{3}}{2}P_b + \frac{\sqrt{3}}{2}P_c)\cos(2\omega t) + \\ (-\frac{\sqrt{3}}{2}Q_b + \frac{\sqrt{3}}{2}Q_c - P_a + \frac{1}{2}P_b + \frac{1}{2}P_c)\sin(2\omega t). \end{aligned} \tag{6-34}$$

Now, a similar procedure could be used to find out how active power could be assigned to three single-phase converters to mitigate fluctuations caused by asymmetric reactive power. Equation (6-11) in addition to (6-31) and (6-32) are three equations, while this time active powers, P_a, P_b and P_c, are unknown and reactive power, Q_a, Q_b and Q_c are known. The result is shown in (6-35). Similarly, it is easy to prove that no fluctuations on active power will be observed, while both active and reactive power may be asymmetric.

$$\begin{bmatrix} P_a \\ P_b \\ P_c \end{bmatrix} = \begin{bmatrix} \frac{1}{3} & 0 & -\frac{\sqrt{3}}{3} & \frac{\sqrt{3}}{3} \\ \frac{1}{3} & \frac{\sqrt{3}}{3} & 0 & -\frac{\sqrt{3}}{3} \\ \frac{1}{3} & -\frac{\sqrt{3}}{3} & \frac{\sqrt{3}}{3} & 0 \end{bmatrix} \begin{bmatrix} P_{ev-ref} \\ Q_a \\ Q_b \\ Q_c \end{bmatrix}. \tag{6-35}$$

In the proposed hybrid control method, distributed control is used for active power whereas centralized control is used for reactive power regulation. The measurements occur at both PHEVs and also at the main substation bus by the computation center. Each PHEV should transmit its available capability for injecting reactive power to the computation center, and it measures the grid frequency at its coupling point and its internal indexes such as energy sources availability. PHEVs measure the frequency locally and respond to frequency disturbances autonomously (i.e. without centralized control actions). The computation center measures the active power of each phase and voltage at the substation bus and based on the proposed method and subject to voltage regulation limits, decides how much reactive power should be generated in each phase to compensate for active power asymmetry. Then based on the information sent by each PHEVs and its available capability to incorporate in reactive power injection, the desired total reactive power is shared among participating PHEVs. The share of each PHEV is communicated to each unit via the communication network.

Another important question that should be answered here is why and when the proposed remedy could be useful. Actually the answer is related to one of the main challenges of vehicle-to-grid mode of PHEVs. As mentioned, using PHEVs to inject active power is not preferred for many owners since even if does not discharge the battery significantly, it affects the battery life time. In other words, not all the customers will allow the utility to use their PHEVs as active power source and if there are not so many plug-in electric vehicles in a microgrid or weak grid, it results in higher possibility of asymmetric virtual inertia. Even with super-capacitor-based PHEVs, different charge levels and converter in-use rating may lead to this asymmetry. To stay in the safe side, the least capability among three phases could be chosen and two others should be forced to inject this amount of active power. While this method does not allow using all the available potential of the network, communication delays might still destabilize the system. On the other hand, most of PHEVs have no problem in injecting reactive power within permissible converter rating. The interesting feature of this remedy is that it allows all the available potential for active power, whatever asymmetric, be used while this asymmetry is mitigated by reactive power injection. In other words, those PHEVs which are not allowed to inject active power could be used to eliminate the impact of

asymmetric virtual inertia just by injecting reactive power. In fact, these PHEVs have incorporated in active power regulation indirectly.

6.3 Cooperating with a Wind Generator

The PHEVs are fast power sources; however, their available energy for frequency regulation is limited [63, 145, 146, 151]. On the other hand, wind generators are rich sources of energy, but fast interactions can result in their fatigue [153]. These characteristics make these two sources great choices to complement each other. Therefore, the droop or the virtual inertia can be used by a centralized controller to decide how much power is needed to regulate the power system frequency, and then, the same control center can divide the power between these two sources based on their individual characteristics.

6.3.1 Centralized Cooperative Control

The structure of the centralized controller is depicted in Figure 6-9. The controller gathers information from the microgrid, PHEVs and wind generator and sends back commands to the sources. As discussed in Chapter 4, a low-pass filter (LPF) can be employed to share the power, but the coordination in practice is not straightforward because the energy storages units of the PHEVs are distributed and dispersed.

For a meaningful analysis, a detailed model is needed. The system depicted in Figure 6-10 is adopted in this part. The system is basically the system shown in Figure 3-7 with EVs added. The system parameters are given in the Appendices. The stability analysis can be extended to larger microgrids or weak grids.

A small-signal model of a wind generator for frequency regulation dynamics is developed in Chapter 4. To avoid repetition, the procedure of linearizing around an operating point, which is a function of the wind speed, is omitted here. The final results are presented in (6-36)-(6-37) where Δx_w represents the doubly-mass wind generator and its controller states. Δv_w is the change in the wind speed, and ΔP_f is the change in the power needed for frequency regulation; both are the inputs to this state-space representation. ΔP_w, the output of the model, is the active power of the wind generator injected into the power system. H_{wf} and H_{wv}, given

by (6-38) and (6-39), are two transfer functions derived from (6-36)-(6-37), and relate the inputs and output of the wind generator.

$$\Delta \dot{x}_w = A_w \Delta x_w + B_{wv} \Delta v_w + B_{wf} \Delta P_f . \tag{6-36}$$

$$\Delta P_w = C_w \Delta x_w + D_{wv} \Delta v_w + D_{wf} \Delta P_f . \tag{6-37}$$

$$\Delta H_{wv} = C_w (sI - A_w)^{-1} B_{wv} + D_{wv} . \tag{6-38}$$

$$\Delta H_{wf} = C_w (sI - A_w)^{-1} B_{wf} + D_{wf} . \tag{6-39}$$

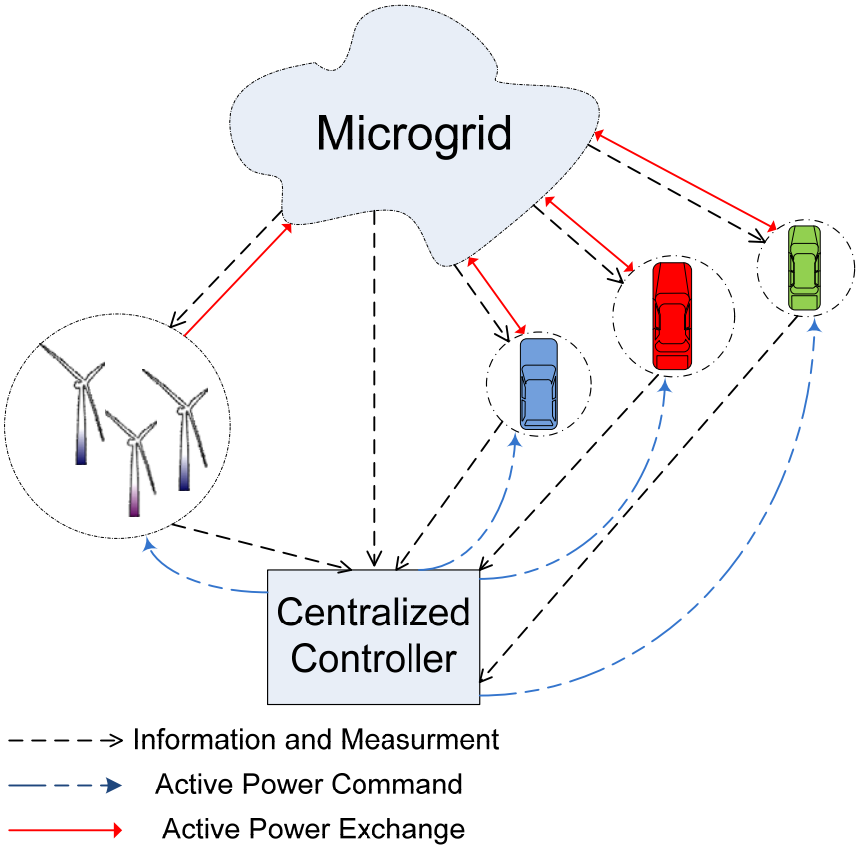

Figure 6-9 Schematic view of the centralized controller.

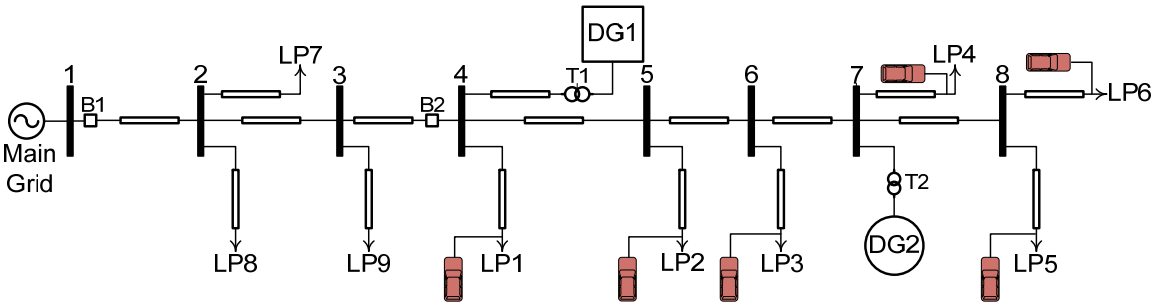

Figure 6-10 System under study.

Based on the discussions in [162] on primary frequency regulation dynamics, the frequency dynamics of the microgrid system can be presented by the block diagram shown in Figure 6-11. The traditional parts of the model, the turbine, the governor and the diesel rotating-mass, are described in detail in the literature. The wind generator and the PHEV and the proposed centralized controller are added here to the classical model to incorporate these modern components of power systems. As indicated in Figure 6-11, the centralized controller decides how to respond to the frequency fluctuation. The command power is denoted as ΔP_{reg}. It can be either the virtual inertia or the droop, formulated in (6-40) and (6-41), respectively. M_v, the virtual inertia gain, and m_p, the droop gain, are the main levers used to control the contribution of the centralized controller to the frequency regulation dynamics. τ_c is the time constant of the centralized controller. In fact, it represents the time constant of PHEVs' inverters and the grid-side converter of the PMSG. As discussed in the literature, this time constant is expected to be small [50, 149, 168]. Then, an LPF extracts the low-frequency content, which will be communicated to the wind generator, ΔP_f. The high-frequency regulation command is communicated to PHEVs parking lots and aggregators. Electric vehicles are aggregated in one block in Figure 6-11; however, the model can be easily modified to accommodate each parking lot or aggregator as one separate block. The H_{ev} block is implemented to represent the communication impacts.

$$P_{reg} = P_{vi} = -\frac{M_{vi}s}{\tau_c s + 1}\omega_m. \tag{6-40}$$

$$P_{reg} = P_{drp} = \frac{m_p}{\tau_c s + 1}(\omega_{ref} - \omega_m). \tag{6-41}$$

6.3.1.1 Ideal Case

A perfect communication system is immune against any delay. Although such a system does not exist in reality, studying this situation is very enlightening. Figure 6-12 shows the maximum frequency deviation when the droop or the virtual inertia is employed. Obviously, the filter cutoff frequency has no impact and only the frequency regulation gains, m_p or M_{vi}, are determining. On the other hand, both the frequency regulation method and the filter can impact the stress on the wind generator shaft. To better understand the situation, see

Figure 6-13 and Figure 6-14 where the maximum torque and the maximum rate of change of torque (ROCOT) of the wind generator shaft are depicted. Reference [103] discussed in detail that the shaft fatigue is a function of the torque shaft and its derivative. In fact, the cutoff frequency of the LPF used in the centralized controller can play a vital role in relieving the mechanical tension of wind generators.

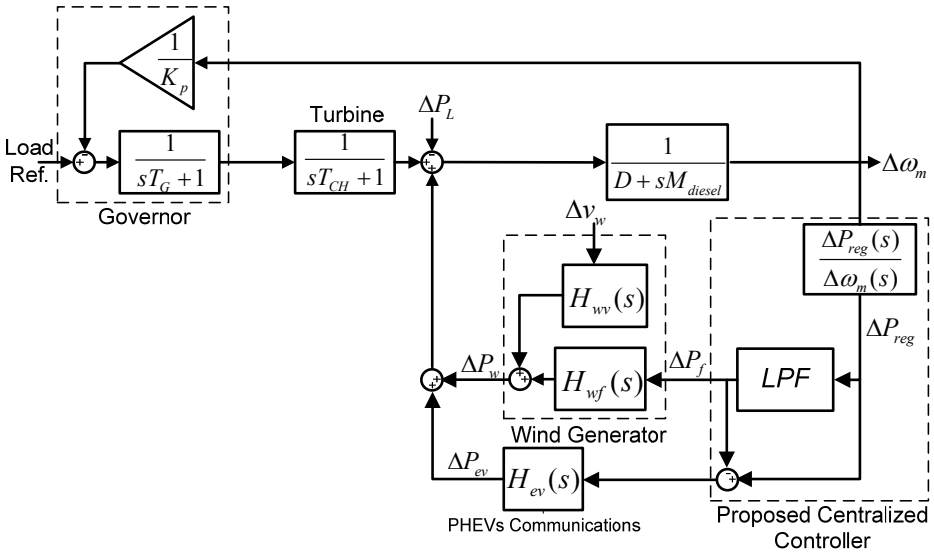

Figure 6-11 Block diagram representation of the microgrid frequency dynamics with a centralized controller.

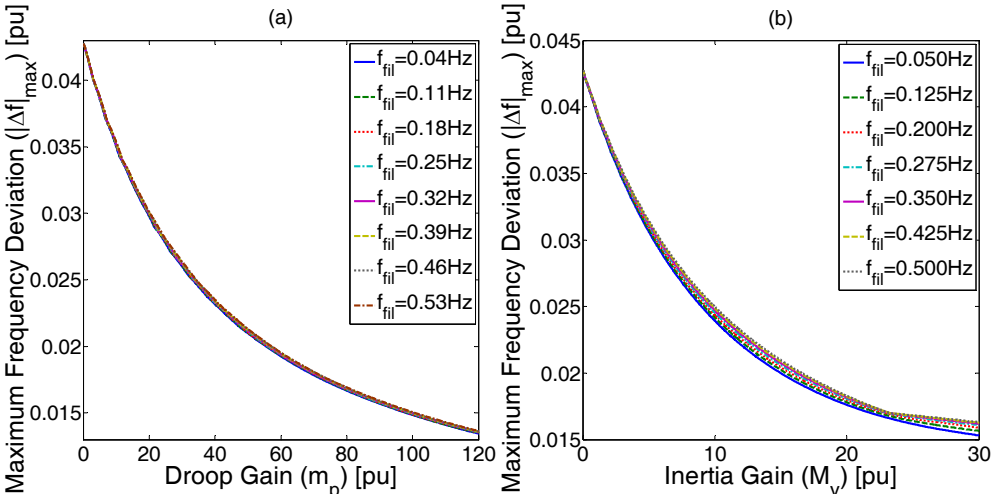

Figure 6-12 Maximum frequency deviation vs. (a) the droop gain, (b) the virtual inertia gain when different LPF frequencies are used.

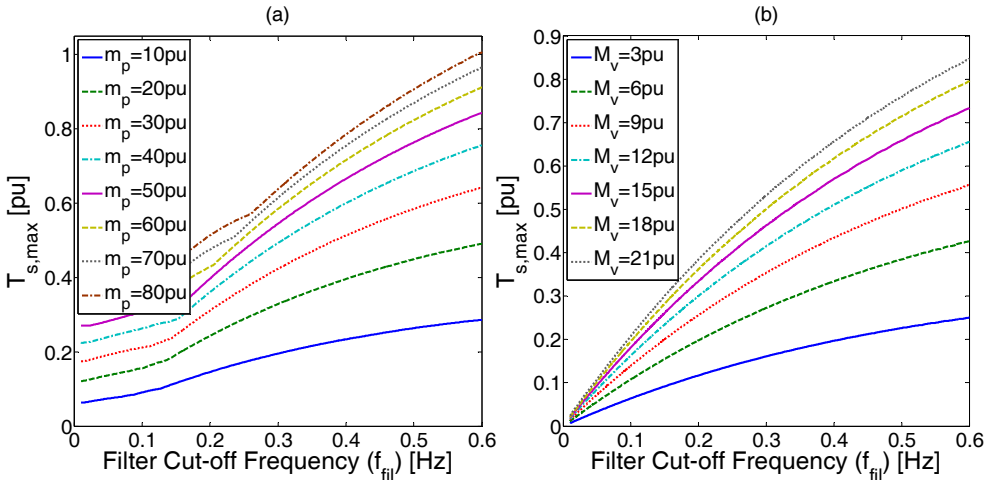

Figure 6-13 Impact of the centralized controller LPF cutoff frequency on the maximum torque of the wind generator shaft; (a) the droop method, (b) the virtual inertia method.

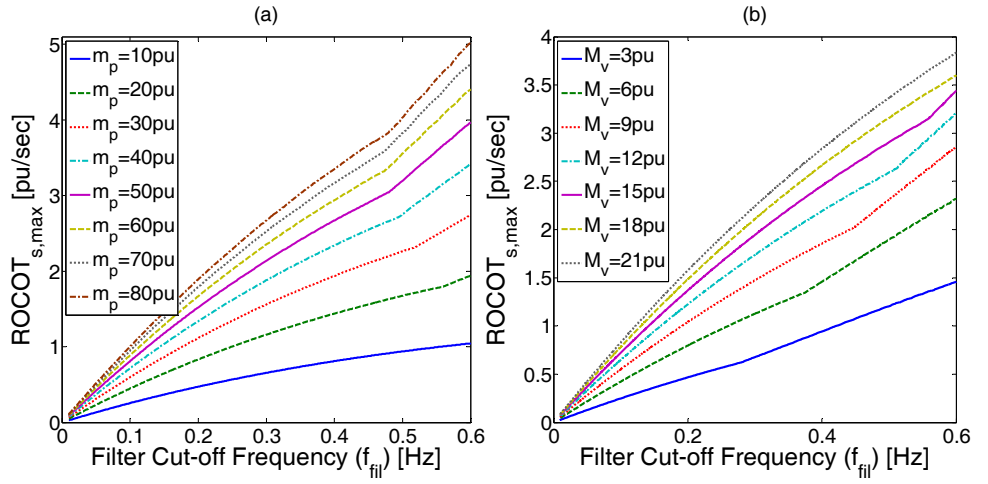

Figure 6-14 Impact of the centralized controller LPF cutoff frequency on the maximum rate of change of torque of the wind generator shaft; (a) the droop method, (b) the virtual inertia method.

The mechanical tension on the turbine shaft will be reduced by lowering the filter cutoff frequency because a larger portion of energy is provided by the PHEVs energy storages. This fact can be understood by observing the blue solid curves in Figure 6-15 and Figure 6-16. Thus, the main tradeoff is between using more energy from the PHEVs batteries and putting more tension on the turbine shaft. PHEVs energy has a close relation with their state of charge, as discussed by [186, 187]. The less the energy fed by PHEVs, the less their SOCs will change.

However, the behavior patterns of the droop and virtual inertia methods are not the same. The red dashed curves in Figure 6-15 and Figure 6-16 represent the maximum energy and power extracted from the combined hybrid source (wind generator and PHEVs together). As can be expected, they do not change significantly by changing the filter cutoff frequency. In other words, the LPF does not influence the external behavior of the combination but manages the behavior of the wind generator and PHEVs. Both the virtual inertia and the droop provide almost all the needed energy and power from PHEVs as the filter cutoff frequency converges to zero. However, in the case of the droop method, the share of the PHEVs drops very rapidly by deviating from zero and then saturates. This fast deviation provides the chance to choose a cutoff frequency that mitigates mechanical tensions on the wind turbine shaft significantly, whereas the largest share of energy still comes from the wind generator, not the vehicles storages. The situation becomes clearer when the droop case (Figure 6-15(a)) is compared to the virtual inertia one (Figure 6-16(a)). In fact, the difference is even more severe than what these figures show because the time frame used in them is just the first ten seconds right after the disturbance. While the virtual inertia usually settles to zero in this time frame, the droop method continues to provide power and energy for the power system until the secondary regulation restores the system frequency to its nominal value. The secondary control is usually activated 30 s to one minute after the disturbance and may take several minutes to regulate the system frequency. More information on the secondary frequency regulation can be found in Ref. [168]. This difference leads to questioning the benefits of the coordinated virtual inertia for the PHEVs, even though it reduces the wind generator fatigue. The burden of communication and coordination is also added to the system. For this reason, the droop will be used as the main tool for the frequency regulation by the coordinated sources in the rest of this section.

From the power extraction perspective, both the virtual inertia and the droop method act similarly. No fast fall, similar to the droop energy extraction, can be observed here. However, the PHEVs are fast sources and have no difficulty injecting active power unless it changes their SOC significantly or exceeds their inverter rating. In fact, Figure 6-15(b) can be used to find out the number of vehicles needed for cooperative frequency regulation. One per unit

power in this study is equal to the nominal rating of the synchronous generator, DG2, and is equivalent to 313 to 380 vehicles. The curves in Figure 6-15 and Figure 6-16 are obtained when the system is responding to a disturbance of 1.0 pu. Due to the linear nature of the analyses, the response to any other amount of disturbance can be calculated by using a simple scaling.

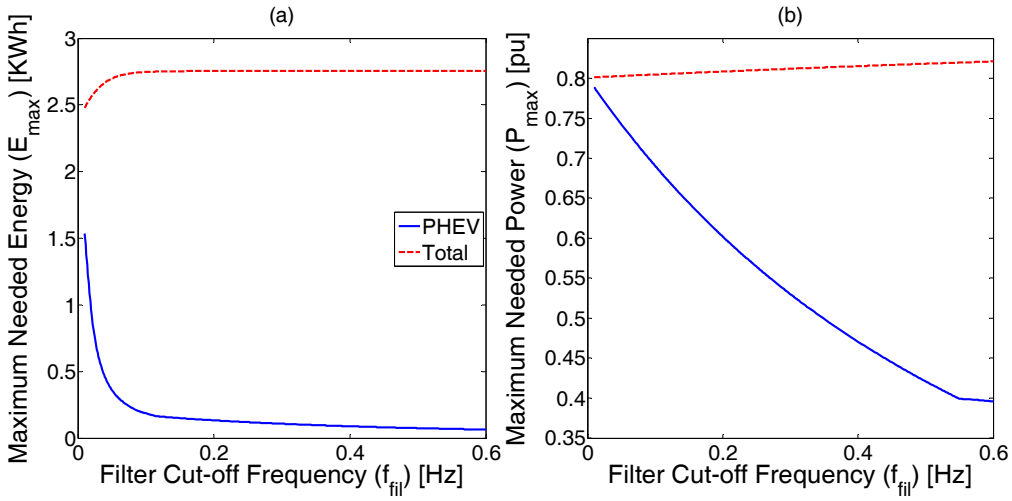

Figure 6-15 (a) Energy and (b) power provided for frequency regulation when the droop is implemented, m_p=40 pu, and 1 pu disturbance is applied to the system. Blue solid curves represent the PHEVs source whereas the red dashed curves depict the total combination of the wind and the PHEVs.

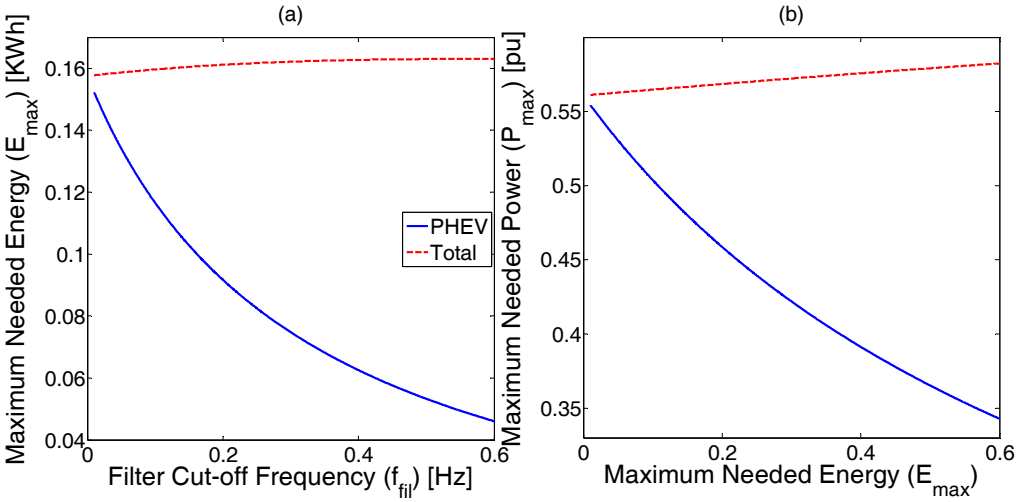

Figure 6-16 (a) Energy and (b) power provided for frequency regulation when the virtual inertia is implemented, M_{vi}=12 pu, and 1 pu disturbance is applied to the system. Blue solid curves represent the PHEVs source whereas the red dashed curves depict the total combination of the wind and the PHEVs.

By choosing the filter cutoff frequency 0.1 Hz, less than 245 vehicles are needed to respond to 1.0 pu disturbance. These vehicles in total inject less than 0.2 kWh maximally. This amount of energy is less than two percent of one battery capacity in common vehicles [138]. Considering the number of involved vehicles, the SOC of their batteries will not be significantly changed. This result is desirable for the PHEVs owners. However, the vehicles will provide a large amount of power for the system. In other words, the PHEVs in the proposed coordination are used as the power sources rather than the energy sources. In this categorization of sources, power sources provide a high amount of power in a relatively short period so that the total supplied energy is not significant. In contrast, energy sources do not inject a high amount of power in a short period, but the amount of energy supplied in longer periods is significant.

6.3.1.2 Delay

Assuming an ideal communication system is helpful for understanding some major characteristics of the proposed coordinated control; however, practical communication systems are not ideal. Therefore, the impact of the communication delay is considered in this study.

In terms of the power system dynamic analysis, the aggregated communication delay can be modeled in the complex frequency domain as shown in (6-42) [188], where τ_d is the delay time in seconds, similar to (6-4).

$$H_{ev}(s) = e^{-\tau_d s} \approx \frac{1-\tau_d s/2}{1+\tau_d s/2}. \tag{6-42}$$

This new model is used to find out the impact of the communication delay on the system stability. The maximum delay which does not destabilize the power system is shown in Figure 6-17. The calculations of the maximum delay are based on the very popular concepts of small-signal analyses and root locus. In short, in the system shown in Figure 6-11, the delay is increased in very small steps, and each time, the poles of the system are calculated. As long as whole poles are in the left-half plane, the system is stable, and consequently, the corresponding delay is allowed. However, by increasing the delay, some poles start to move

toward the right-half plane. The maximum allowable delay occurs when all the poles are still in the left-half plane, and a slight increase of the delay leads to instability. This figure reveals that in low contributions of the PHEVs to the frequency regulation, i.e., relatively small m_p or M_{vi}, the system is very robust against delays. However, it does not perform similarly when these sources play larger roles in the system frequency regulation. The situation is very similar for both the virtual inertia and droop methods. The model may be criticized for using one single delay for all PHEVs after they have been clustered by several parking lots and aggregators. To check this point, the PHEVs block was split into several blocks with unequal delays. It was found that if the average delay of these units exceeds the maximum allowable delay shown in Figure 6-17, the system becomes unstable. This point is discussed in more detail in 6.4.2.2.

This study showed that to ensure stability, the contribution of the centrally coordinated sources should be kept low; otherwise, fast and expensive communication is needed. This conclusion means that the centralized coordination scheme might have a very limited application.

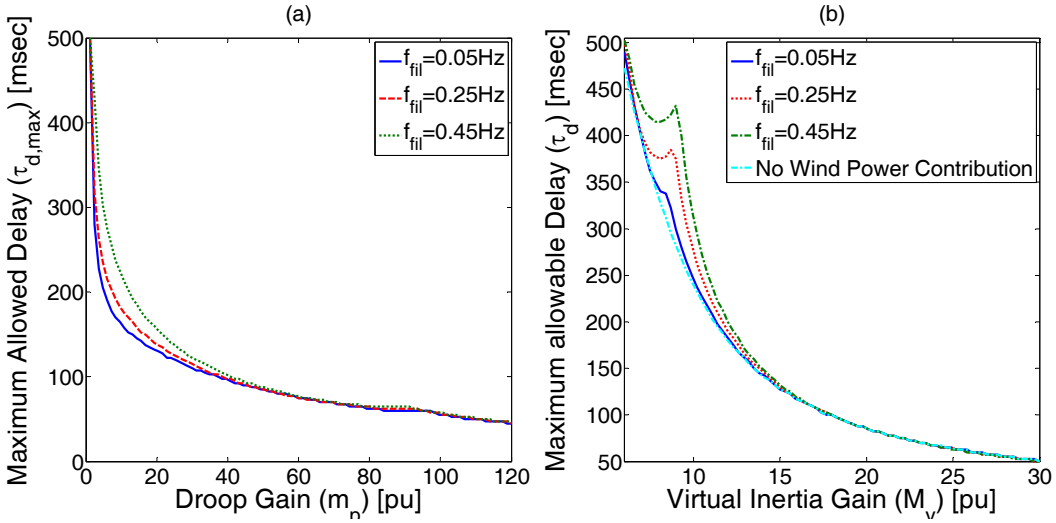

Figure 6-17 Maximum delay which does not destabilize the power system in the centralized coordination vs. (a) the droop gain, (b) the virtual inertia gain.

6.3.2 Distributed Cooperative Control

To overcome the drawbacks of the centrally coordinated control scheme, a distributed control is examined in this section. The schematic structure of such a system is depicted in Figure 6-18, and its block diagram model is shown in Figure 6-19. Unlike the systems in Figure 6-9 and Figure 6-11, no central unit is employed in the system in Figure 6-19. The frequency is measured locally and fed into the local droop blocks. The generated reference power needed for the frequency regulation goes through an LPF or a high-pass filter (HPF) before reaching the wind and the PHEVs parking lots, respectively. Ideally, the system acts exactly like the perfect centralized controller. However, achieving such an ideal situation in reality is, if not impossible, rare.

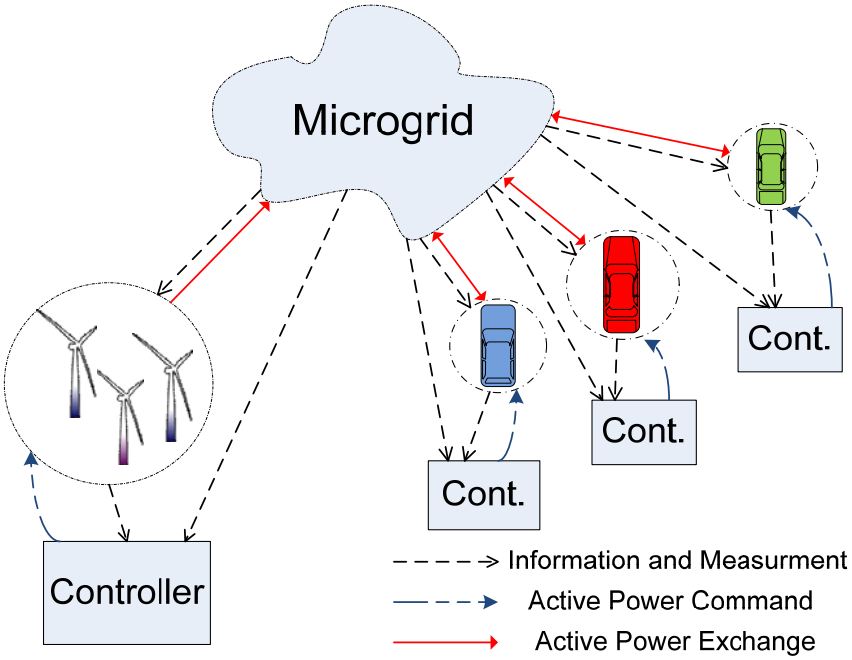

Figure 6-18 Schematic view of the distributed controller.

First of all, a delay could still exist. However, thanks to the distributed controller, the delays can be reduced dramatically with local measurements. Our studies showed that delays of less than 20 ms had no significant impact even in the case of high contributions from the wind generator and PHEVs. Smart parking lots or aggregators in dense areas can easily communicate with their vehicles with such small delays via low-cost local networks, which already exist for billing and monitoring. However, as discussed in the following subsection,

the distributed coordination scheme is subject to some other unique threats and opportunities. Because the power system is subject to continuous changes and no immediate direct communication occurs between the PHEVs and the wind generator, the proposed controller must be robust against miscoordination and provide accessible control leverages. These concerns are discussed in the following subsections.

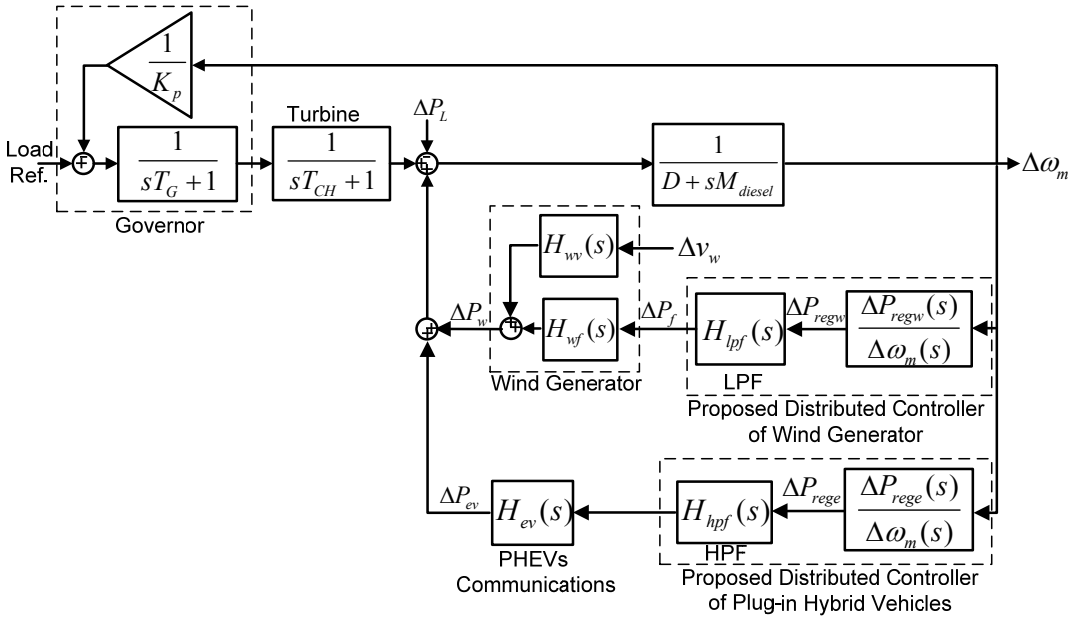

Figure 6-19 Block diagram representation of the microgrid frequency dynamics with a distributed cooperative controller.

6.3.2.1 Unmatched Sources

Because the PHEVs and the wind generator act almost independently, miscoordination is possible. In other words, each of the aggregators and the wind generator, without direct and perpetual communication with each other, might select its droop gains based only on its available resources. In other words, if one of the sources has more power/energy than the other source and no communication occurs between these sources, there is a risk of miscoordinated action. In this case, the wind droop gain, $m_{p,wind}$, will probably not be equal to the PHEVs accumulated droop gain, $m_{p,phev}$. Two crucial questions should be asked. (1) How will unequal droop gains impact the system performance? (2) Is there any chance of instability? Figure 6-20(a) and (b), respectively, help in answering these questions. If the contribution of the wind generator is not very small, instability is possible. A minimum

allowable proportion of PHEVs to wind droop gain is needed to guarantee the system stability, and this minimum proportion is highly dependent on the filter cutoff frequency. However, a huge difference between the wind generator and the PHEVs gains is needed to destabilize the power system. When the LPF cutoff frequency, f_{lpf}, is set to 0.25 Hz, the PHEVs gain should be less than one-fourth of the wind droop gain. On the other hand, when the vehicles droop gain is higher, the instability threat is removed, and the system performance is enhanced. In other words, a rough estimation of PHEVs and wind generator can be used to design the distributed cooperative control. A stable, acceptable performance is guaranteed if the model deviates reasonably from the estimation.

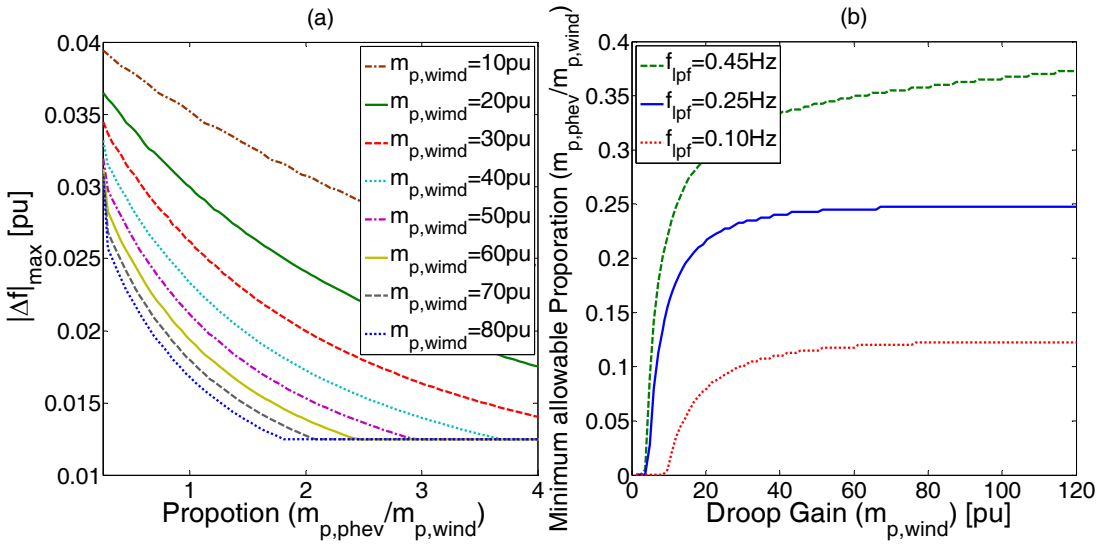

Figure 6-20 (a) Impact of unequal droop gains on the maximum frequency deviation, (b) the minimum proportion of droop gains which does not destabilize the power system at different wind droop gain.

Figure 6-21 and Figure 6-22 reveal the impact of different PHEVs droop gain on the energy provided by vehicles storages and the mechanical stress on the wind turbine shaft. As can be expected, by increasing $m_{p,phev}$, more stress on the wind mechanical system is relieved at the expense of a higher contribution from the PHEVs.

6.3.2.2 Different Cutoff Frequencies

Because the PHEVs and the wind generator use different filters, a possible scenario is a case in which HPF and LPF have different cutoff frequencies. Unless a huge difference exists between the cutoff frequencies of both filters, no instability threatens the system.

Figure 6-23(a) shows that as long as the HPF cutoff frequency, f_{hpf}, is not more than twice that of f_{lpf}, there is no risk to the system stability. This large range allows using the LPF cutoff frequency as a control lever in the distributed coordination. Figure 6-23(b) shows that changing f_{lpf}, while the cutoff frequency of the dispersed PHEVs HPF is kept constant has no significant impact on the maximum frequency deviation. Similar to the centralized coordination, the cutoff frequency still has a significant influence on the wind generator fatigue by controlling the shaft torque and its derivative (see Figure 6-24).

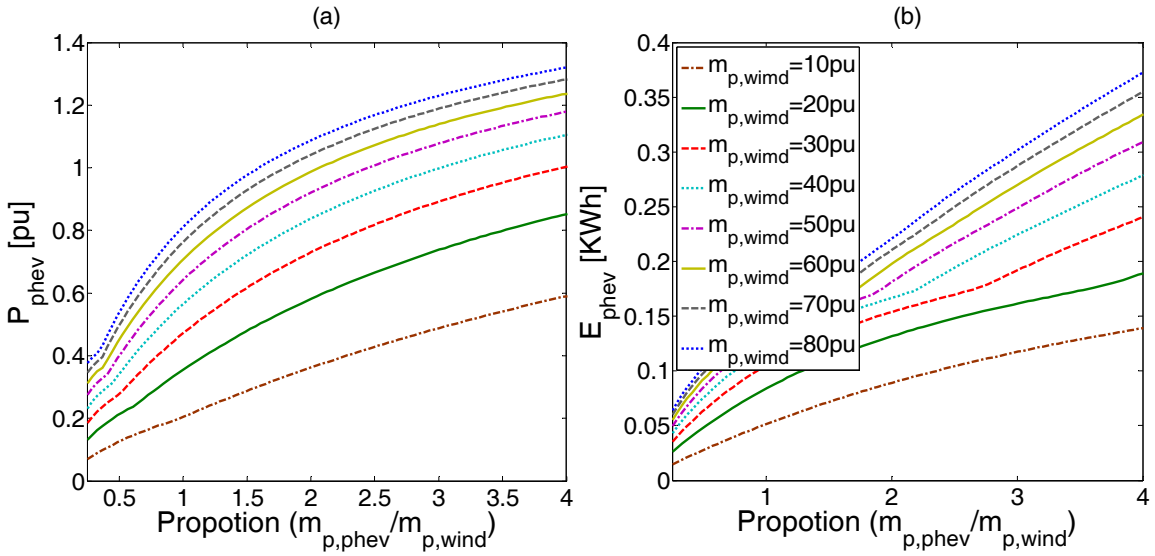

Figure 6-21 Impact of unequal droop gains on (a) the maximum power, (b) the maximum energy injected by PHEVs.

The interesting point about employing f_{lpf} is its impact on the PHEVs power and energy injection, especially in comparison to that of the centralized coordination scheme. Although the energy injected by PHEVs may be increased by reducing the LPF cutoff frequency in some cases, f_{lpf} has no significant influence on the PHEVs power injection, as shown in Figure 6-25. Because the PHEVs are used as the power sources, not energy, this almost constant power contribution means that the same number of the PHEVs is needed. In fact, separating the HPF and LPF in distributed coordination has resulted in this desired feature. In the centralized droop, the power injection of the PHEVs is highly dependent on the LPF cutoff frequency. In addition, the wind generator, and consequently the LPF, is more accessible to the system operator than the dispersed PHEVs HPF parameters. Without any

need to change the control parameters of the dispersed vehicles, the mechanical tensions of the wind generator can be controlled without either significant changing in the system frequency behavior or involving more PHEVs in frequency regulation.

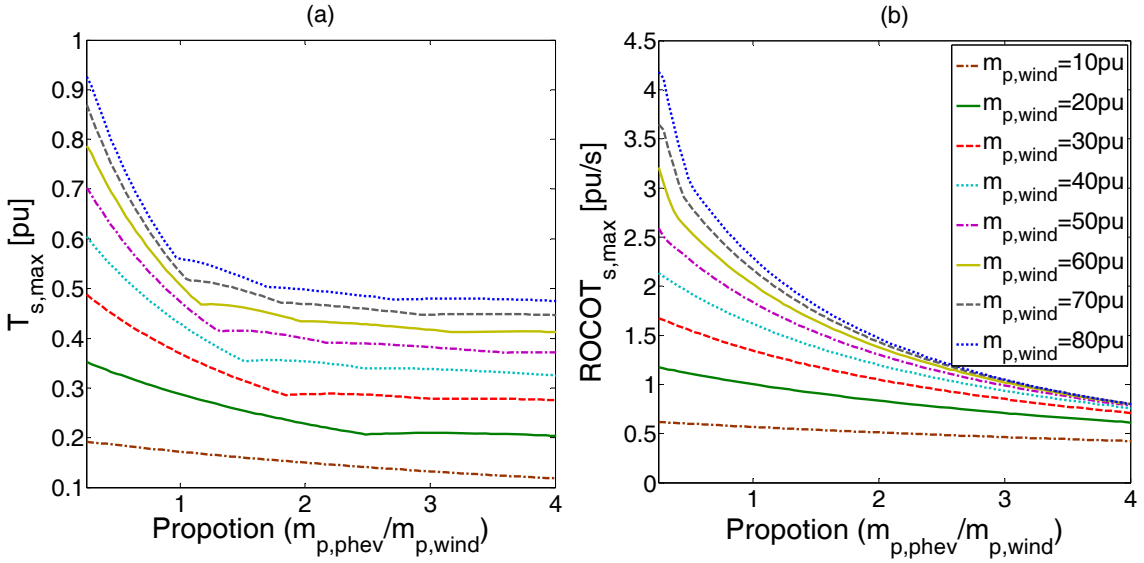

Figure 6-22 Impact of unequal droop gains on (a) the maximum shaft torque, (b) the maximum rate of changes of the shaft torque of the wind generator.

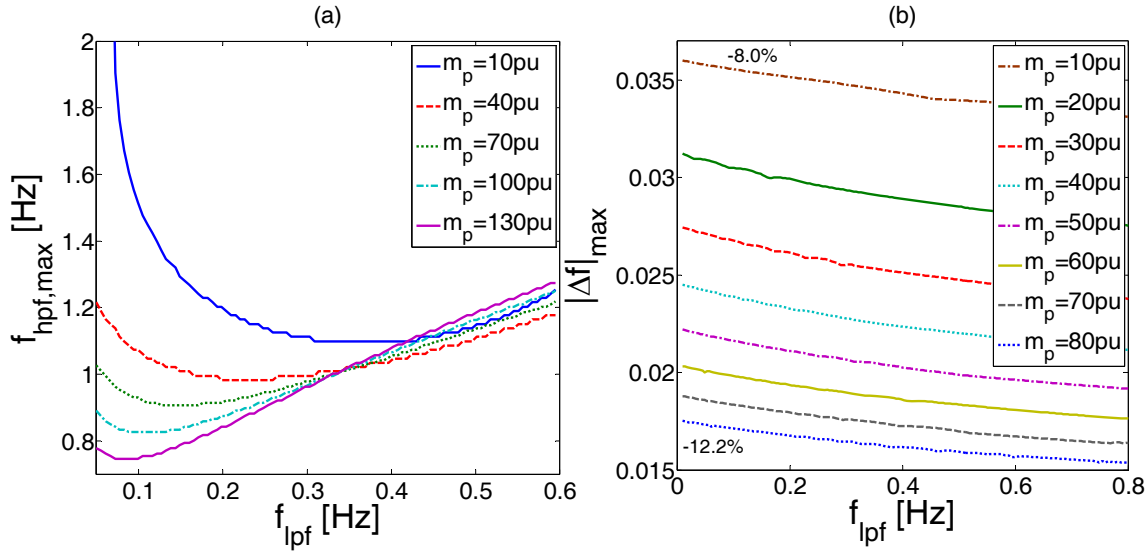

Figure 6-23 (a) Maximum allowable HPF cutoff frequency, (b) Maximum frequency deviation at different LPF cutoff frequency.

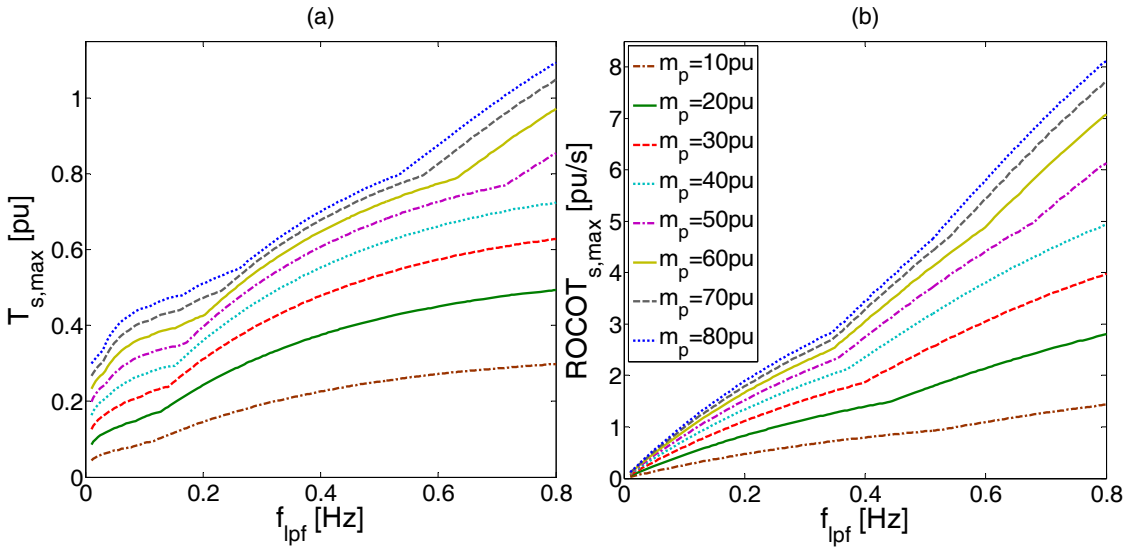

Figure 6-24 Impact of LPF cutoff frequency on (a) the maximum torque, (b) the maximum derivative of the torque of the shaft of the wind generator.

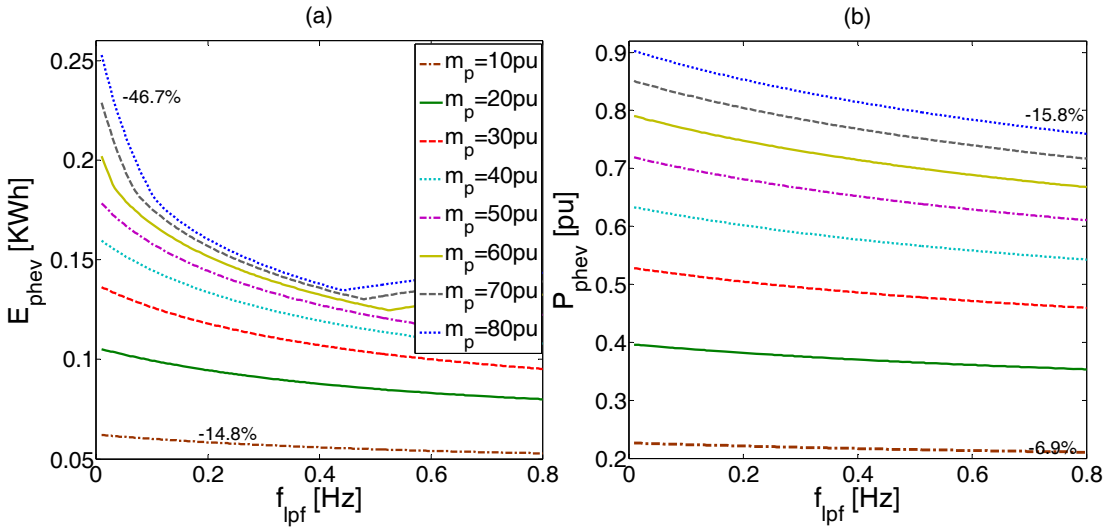

Figure 6-25 Impact of LPF cutoff frequency on (a) the maximum energy, (b) the maximum power injected by PHEVs for the frequency regulation.

6.3.2.3 Wind Speed

Some references, such as [76], proposed that some other variations of the droop mechanism are more compatible with wind generators. The torque-droop is one of them. Without vehicles contributing to frequency regulation, this method makes the frequency regulation more dependent on the wind speed as shown by the dashed curves in Figure 6-26(a). The performance of the coordinated control when the torque-droop is implemented in the wind

generator and the PHEVs are using conventional droop requires more attention. The solid curves in Figure 6-26(a) show that the maximum frequency deviation is not a function of the wind speed anymore. Whereas the PHEVs contribution guarantees much better performance at low wind speeds, no significant difference in the maximum power injection of the PHEVs exists between low and high wind speeds, as depicted in Figure 6-26(b). The results shown in Figure 6-27 assure that the mechanical tensions are well-controlled in the whole wind speed range.

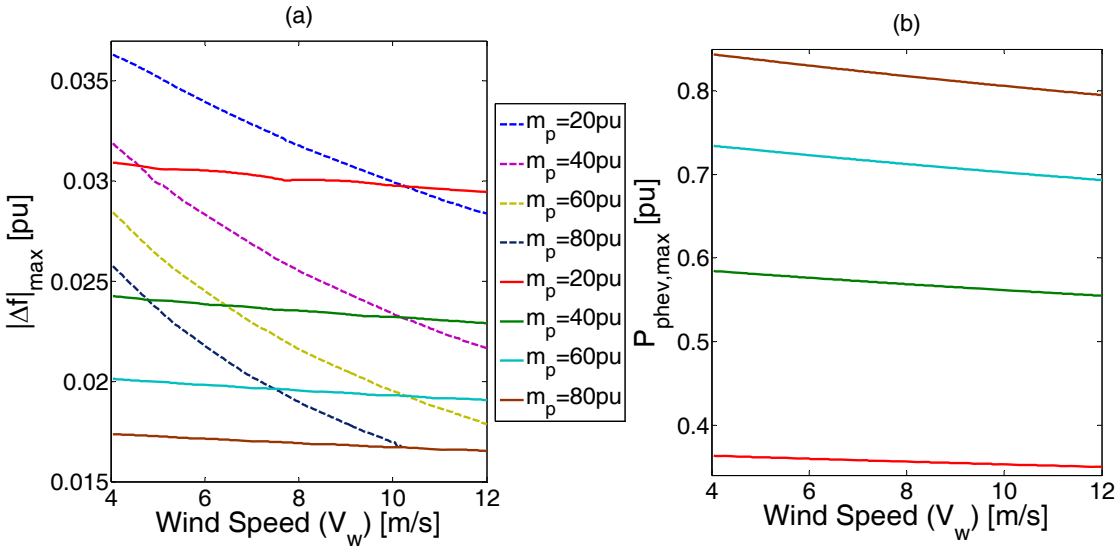

Figure 6-26 Impact of wind speed on (a) the system frequency, (b) the power injected by PHEVs. The dashed curves represent the cases where the PHEVs are not used for frequency regulation.

6.4 Time-Domain Simulation Results

Time-domain simulation is used to verify the discussions and analyses in the previous sections. Two different systems are adopted in this section. In both models, the lines are modeled as lumped RL and the load as parallel RL load. Matlab/Simulink® package is used for this study.

6.4.1 EVs as a sole source

The system shown in Figure 6-2 is used for this part. The synchronous generator is equipped with a governor and an automatic voltage regulator (AVR) [162]. The nonlinear load is

present merely at the last part of the simulation study. System parameters are given in Appendices.

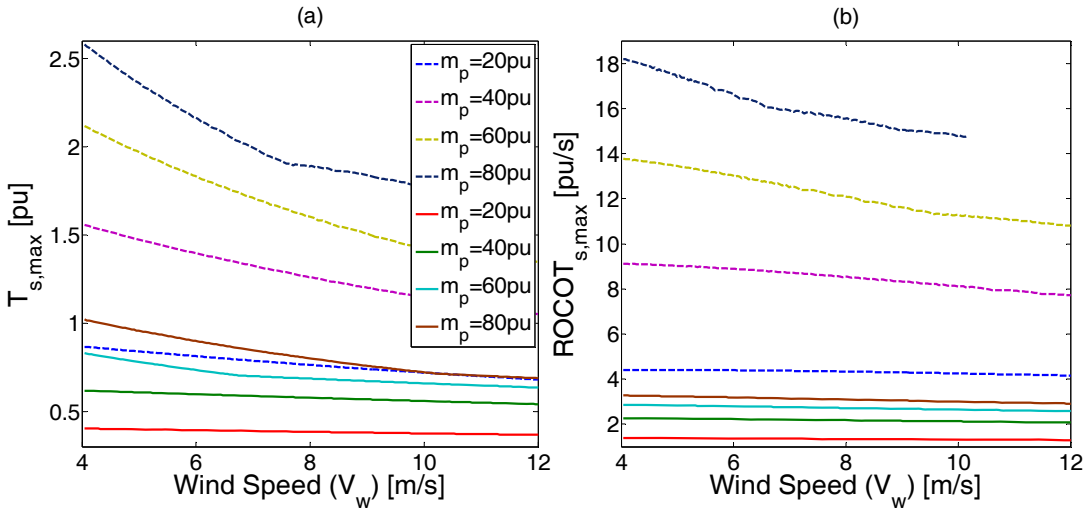

Figure 6-27 Impact of wind speed on (a) the torque, (b) the rate of the changes of torque of the wind generator shaft. The dashed curves represent the cases when the PHEVs are not used for frequency regulation.

Single-phase converters are controlled to inject the desired current which is calculated from desired active and reactive power. It could be analytically proved that these single-phase converters could be simplified as current source [189, 190]. Figure 6-28 compares the simplified and detailed model active power and they are very close to each other. Because of such similarity, in the rest of the section the simplified converter model is used. Each single-phase converter is set to consume 100 kW at unity power factor before disturbance. Considering all PHEVs to be level-2 chargers, as primary and the most preferred charger, with a rating between 8.8 kW to 3.3 kW, in each phase, 11 to 30 EVs can be connected [37]. The disturbance is an intentional islanding which in all the cases happens at t=15s. The synchronous generator operates at 1.0 MW at 0.98 leading power factor before islanding.

6.4.1.1 Non-delayed Symmetric Virtual Inertia

The virtual inertia is implemented according to [50]. It uses the already available phase-locked loop (PLL) in the control structure of single-phase converters to generate the derivative of frequency. This method could be easily generalized for single-phase PLL. For this part of the study, the nonlinear load is disconnected. Figure 6-29 shows the system

frequency in presence and absence of symmetric virtual inertia. As it was expected from analyses, introducing the symmetric virtual inertia enhances the system performance. The figure also verifies the presented analyses, where the greater the symmetric virtual inertia is, the better the system performance is.

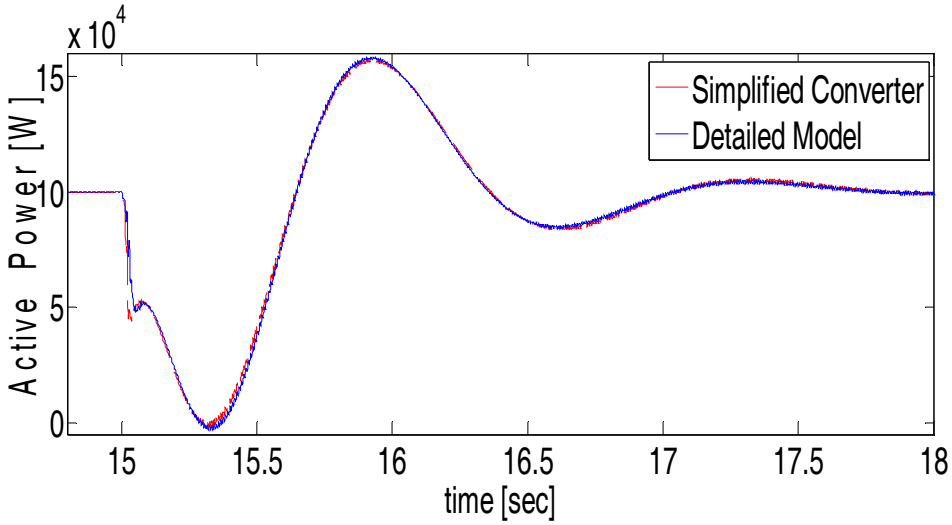

Figure 6-28 Active power output of single-phase converter.

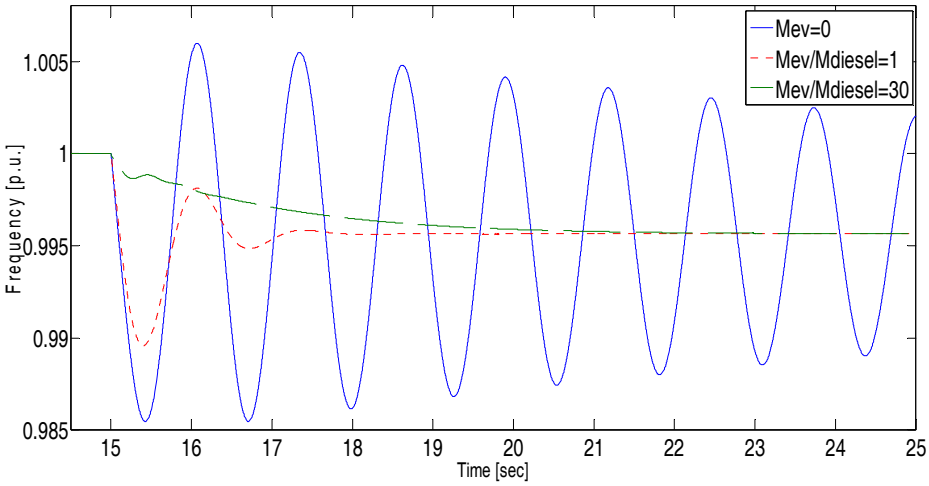

Figure 6-29 System frequency when virtual inertia experiences no delay or asymmetry.

6.4.1.2 Centralized Control

Here, the impact of communication delay on the control performance is examined. As Figure 6-30 depicts, with a relatively low contribution of virtual inertia, the system is much more robust against delay. Simulation results also verify the discussion on delay impacts on

droop method. Figure 6-31 shows the system frequency with PHEVs-droop-based control under different values of delay.

Another possible scenario is when each-phase may have different delay due asymmetrical delays in the communication network. As it was mentioned in Section 6.2.1.1, the most severe case is when all the delays are equal as it yields more delay in the equivalent 3-phase power injected to the system. Figure 6-32 verifies this finding.

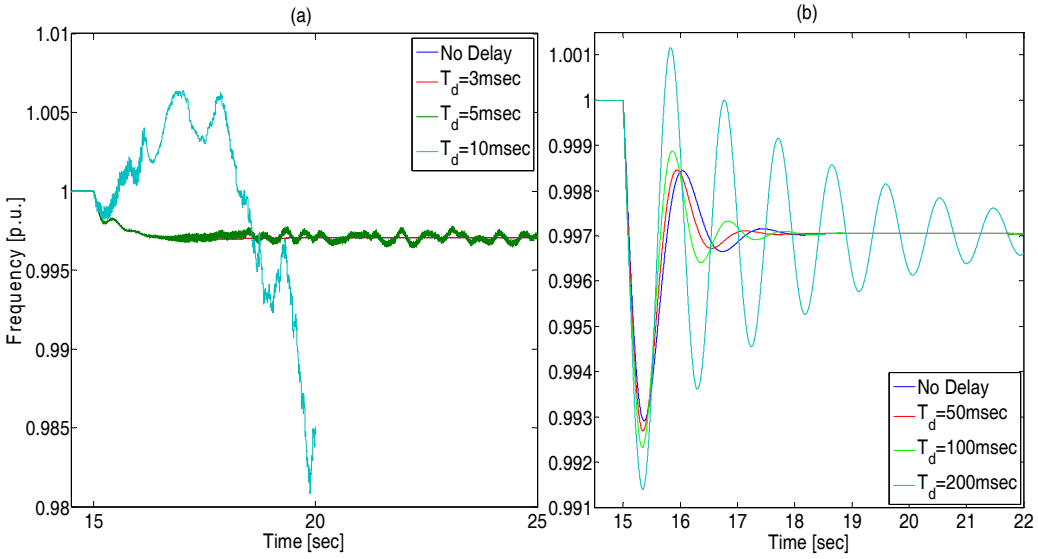

Figure 6-30 Impact of delay on virtual inertia when (a) $M_{ev}/M_{diesel}\approx 10$ and (b) $M_{ev}/M_{diesel}\approx 1$.

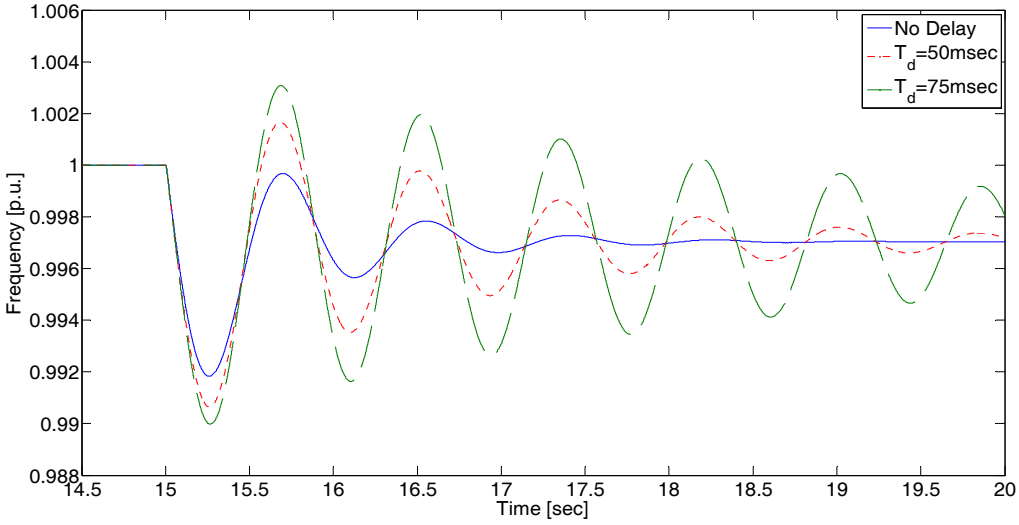

Figure 6-31 Impact of delay on droop when $K_{ev}/K_p=2$.

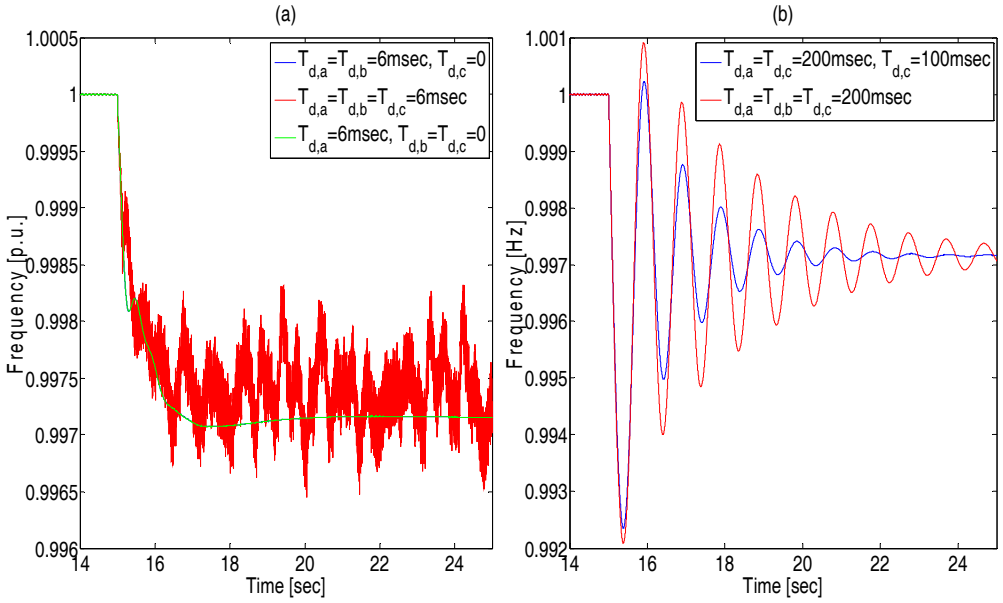

Figure 6-32 Impact of Unequal delay on virtual inertia when (a) $M_{ev}/M_{diesel}\approx10$ and (b) $M_{ev}/M_{diesel}\approx1$.

6.4.1.3 Asymmetric Virtual Inertia

A relatively low M_{ev}/M_{diesel} situation is chosen here and different possible asymmetry patterns are studied. In other words, the amount of total virtual inertia injection is kept constant and each phase contribution is changed. Figure 6-33(a) shows the total 3-phase active power injection of single-phase converters. Obviously, the greater extent of asymmetry results in higher fluctuation in 3-phase total active power, whereas the frequency behavior has not changed. Although frequency remains unchanged, the asymmetric active power injection impacts the reactive power. Figure 6-33(b) depicts the total 3-phase reactive powers. As expected, the higher fluctuations in active power lead to higher oscillations in reactive power.

Frequency could be impacted by higher virtual inertia contribution. Time-domain simulations verify that in high M_{ev}/M_{diesel} situations, asymmetrical virtual inertia injection may results in instability, although the symmetric case improves the system performance significantly. One of these unstable cases is shown in Figure 6-34, in which M_{ev}/M_{diesel}=10, the asymmetry pattern a=1, b=c=0 results in instability, whereas Figure 6-29 shows how the symmetric virtual inertia enhances the system performance. The simulations also show that, in presence of higher virtual inertia, even more moderate patterns such as a=b=0.4, c=0.2

may make the system unstable where symmetric inertia, on the contrary, improves the stability. It proves that higher dependency on this type of virtual inertia increases the risks of asymmetry influence.

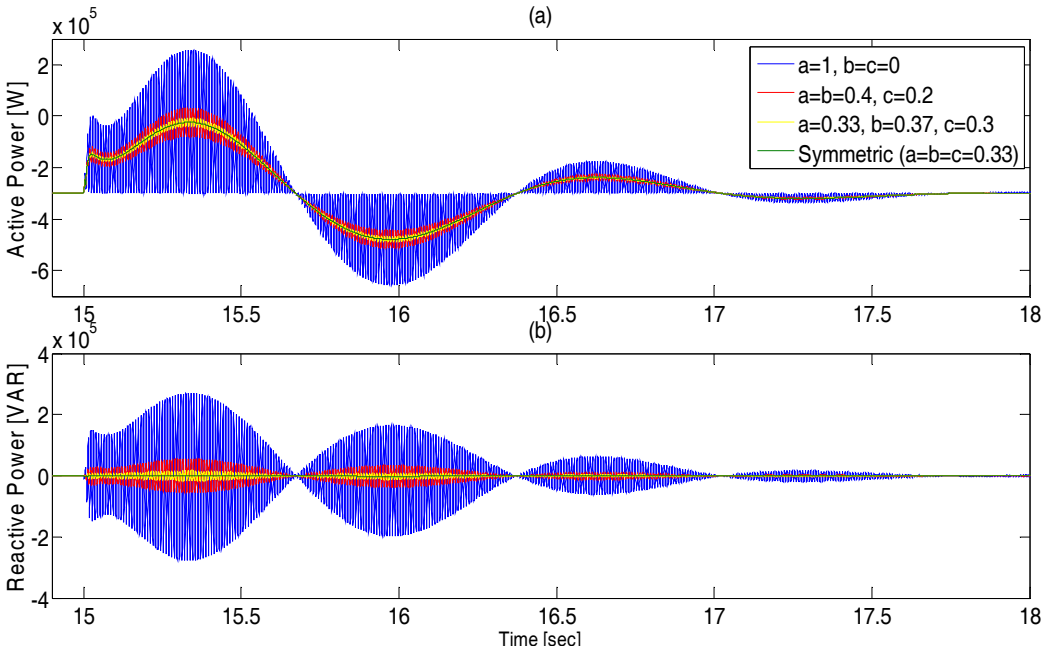

Figure 6-33 Asymmetric virtual inertia impacts on total 3-phase (a) Active power ($P_{3\text{-phase}}$), (b) Reactive power ($Q_{3\text{-phase}}$), while $M_{ev}/M_{diesel} = 1$.

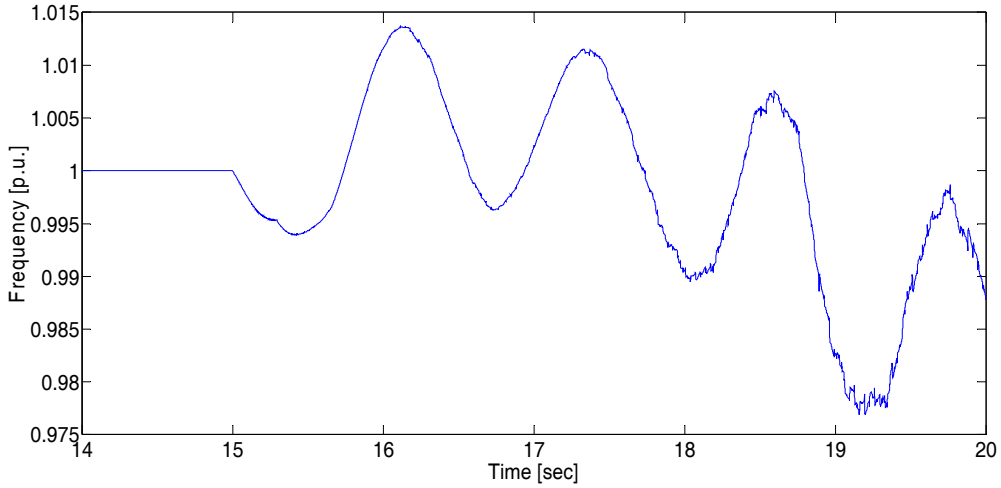

Figure 6-34 Asymmetric virtual inertia impacts on Frequency, Mev/Mdiesel≈10 and virtual inertia is highly asymmetric (a=1, b=c=0).

6.4.1.4 Asymmetric Voltage Regulation

Reactive power asymmetry could also impact the active power. In this part, a simple PI-controller is employed to regulate the converters output voltages. While in symmetric mode, each phase produces one third of the required reactive power, asymmetric patterns could be any other possible combination. Here in Figure 6-35, three different asymmetric patterns and symmetric one are chosen to produce exactly the same amount of reactive power. No virtual inertia is employed in this part. While the frequency will be exactly the same for all cases, a more asymmetric combination results in higher fluctuations in both reactive and active powers. Consequently bus voltage will also be degraded. Simulation results showed that extreme cases such as single-phase reactive power injection, a=1, b=c=0, will destabilize the system.

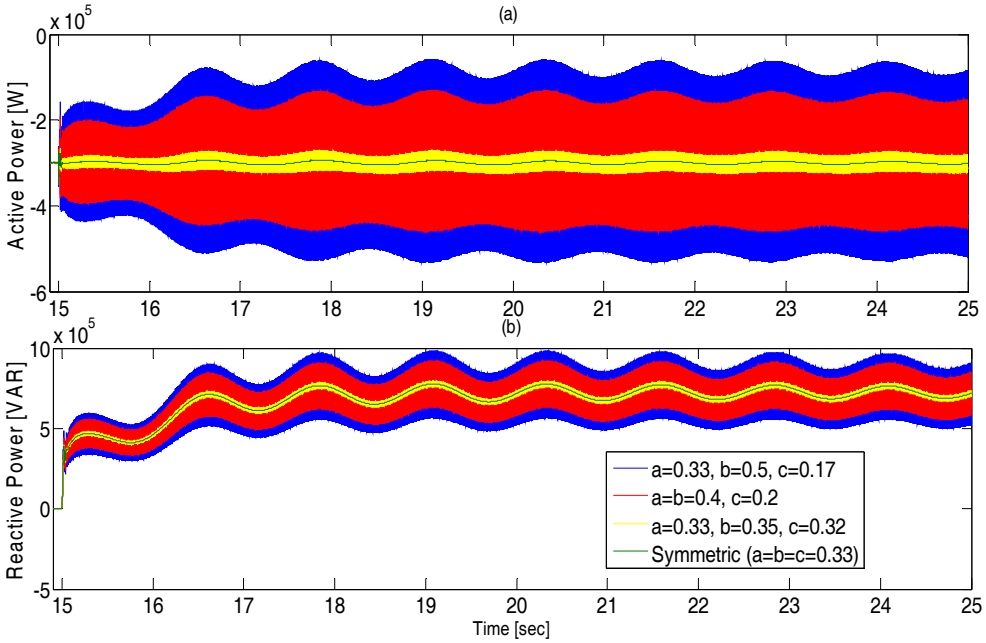

Figure 6-35 Asymmetric voltage regulation impacts on total 3-phase a) Active power ($P_{3\text{-phase}}$), b) Reactive power ($Q_{3\text{-phase}}$), while exactly the same voltage controller is applied to all the cases.

6.4.1.5 Remedy

In this part, the remedy suggested before will be examined. Firstly, it will be tried to suppress the fluctuations made by active power asymmetry via redistributing reactive power among

three single-phase converters. Later, active power will be employed to mitigate the oscillations caused by reactive power asymmetry.

The worst case scenario for virtual inertia is considered here, i.e. single-phase injection (a=1, b=c=0). Equation (6-33) is used to distribute reactive power among converters. Voltage regulation is also employed and obviously the proposed remedy has not made any interference in generating desired total 3-phase reactive power generation. Figure 6-36 shows that the fluctuations on active power disappear completely and the reactive power oscillation is much lower than before. Figure 6-37 reveals that active and reactive powers are divided completely unequally between the phases. It proves the discussion in the previous section. This remedy may also help to stabilize the situations which were previously unstable due to asymmetry. Simulations confirm that the frequency when M_{ev}/M_{diesel} is relatively high and only one of the single-phase converters is responsible for providing virtual inertia could become stable with the proposed remedy while it was previously unstable; one of such cases is shown later.

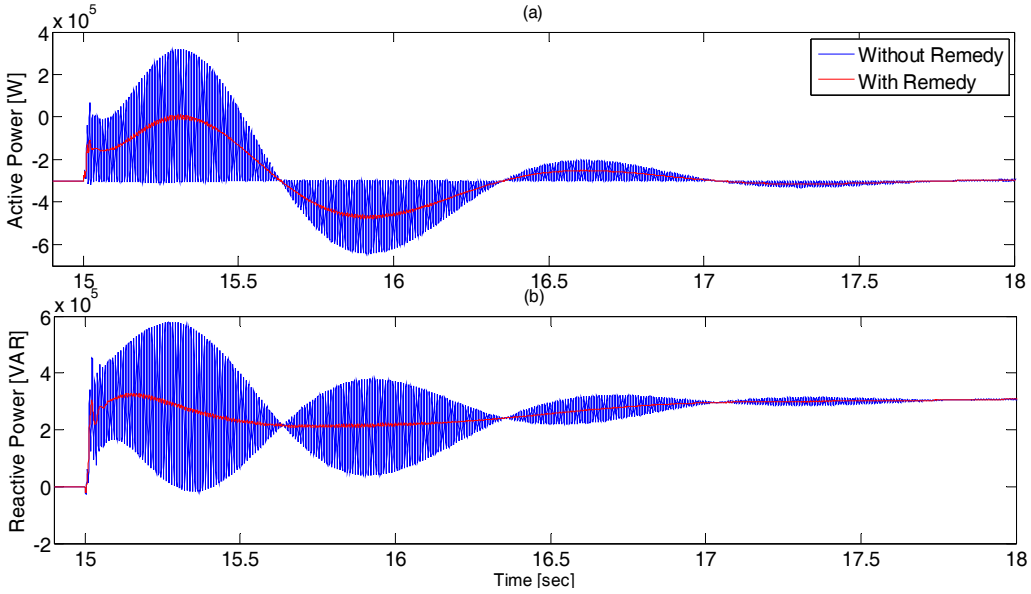

Figure 6-36 The total 3-phase (a) Active power ($P_{3\text{-phase}}$), (b) Reactive power ($Q_{3\text{-phase}}$) output of 3 single-phase converter bus, while virtual inertia is highly asymmetric (a=1, b=c=0) and $M_{ev}/M_{diesel}\approx$1.

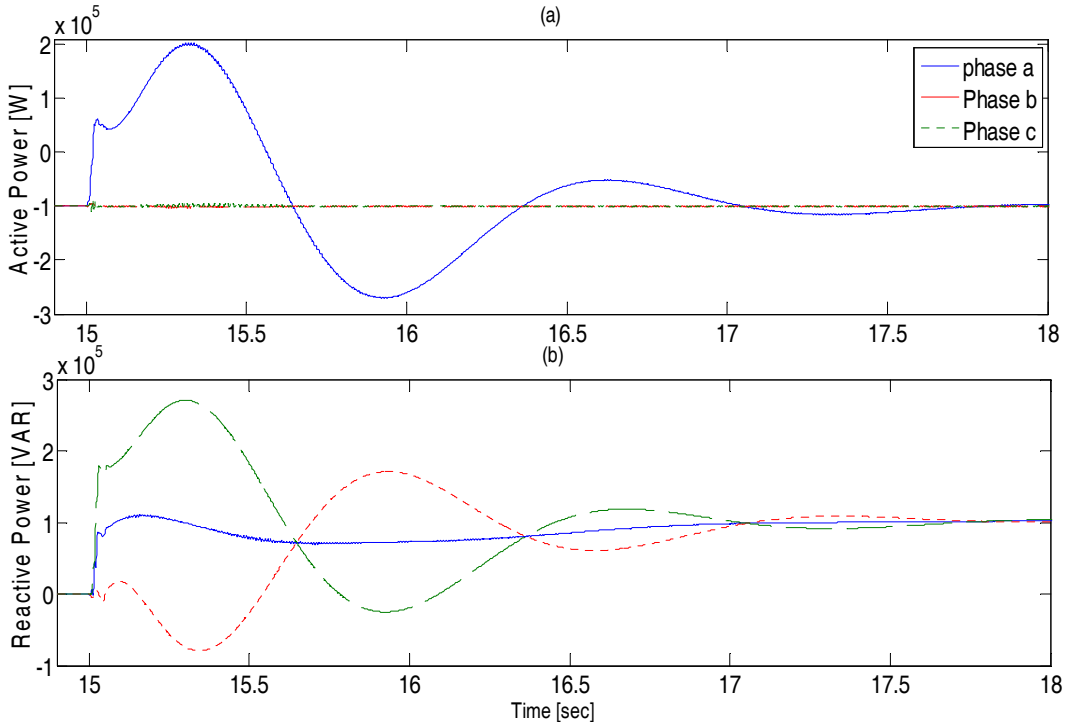

Figure 6-37 Each single-phase converter a) Active power and b) Reactive power generation, while virtual inertia is highly asymmetric (a=1, b=c=0) and remedy is applied.

Although the fluctuations on active and reactive power are eliminated with the proposed remedy, the active and reactive powers are not symmetric and it will influence the voltage balance. Figure 6-38 illustrates the unbalance factor of voltage at the load bus. The unbalance factor is defined by (6-43). As the figure depicts, the unbalance factor is much higher than symmetric virtual inertia case, though the total 3-phase active and reactive power outputs of the converters bus is very similar to symmetric situation.

$$UnbalanceFactor = \frac{\max\limits_{i=a,b,c}\{V_{rms,i}\} - \min\limits_{i=a,b,c}\{V_{rms,i}\}}{\max\limits_{i=a,b,c}\{V_{rms,i}\}} \tag{6-43}$$

Similar to the pervious part and based on (6-35), the active power of each single-phase converter can be assigned so that the oscillations due to reactive power asymmetry will be mitigated. Figure 6-39 and Figure 6-40 show that the goal is achieved successfully while the reactive power and, because of the proposed method, the active power are not symmetrical. The situation shown in Figure 6-39 and Figure 6-40 was unstable before applying the proposed method. In other words, the proposed method prevents destabilizing the system due

to possible asymmetric reactive power. This is achieved without any limiting or changing the reactive power (in previous case active power) sharing patterns. Here, the unbalance factor is also measured (Figure 6-41). Not only it is higher but also stands longer. This point reveals an important difference between using reactive power to suppress virtual inertia asymmetry and using active power to mitigate the fluctuations due to asymmetric voltage regulation. The former does not remain in steady-state, even if makes a larger unbalance factor. The reason is simply related to the nature of inertia which only incorporates in transients. Therefore, the unbalance factor due to the latter method remains permanently and it is not desired.

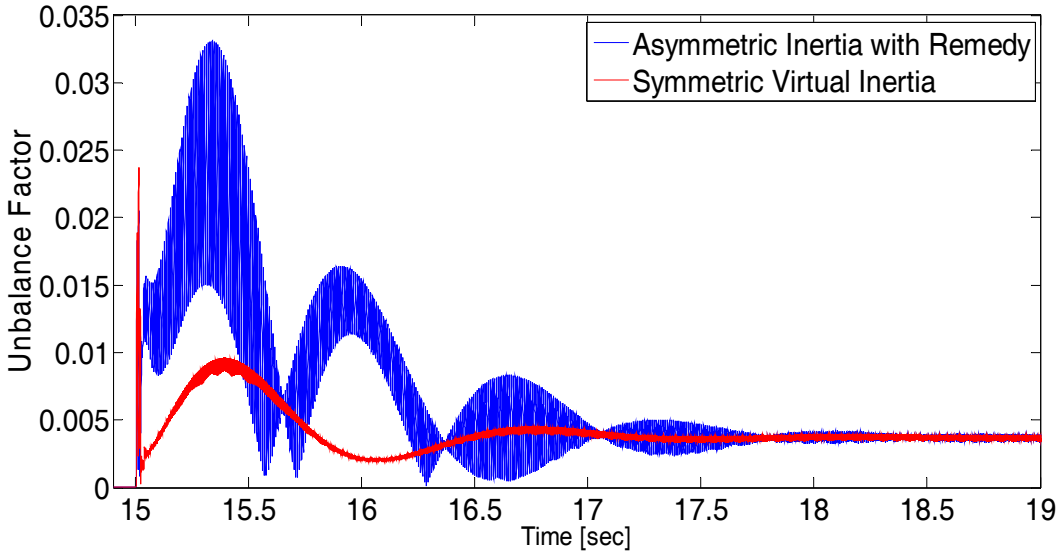

Figure 6-38 Unbalance Factor while virtual inertia is highly asymmetric (a=1, b=c=0), before and after remedy is applied.

In addition, suppressing voltage regulation asymmetry by active power means that active power consumption/injection of single-phase converters should change and these changes are permanent. Previously it was explained that active power management of PHEVs in long term is not desired. On the other hand, in suppressing virtual inertia asymmetry, single-phase converters need to change their reactive power which is not as important as active power. Beside, this situation does not last more than several seconds. All these reasons can illustrate why the virtual inertia asymmetry suppression by reactive power is more practical than voltage regulation asymmetry suppression by active power.

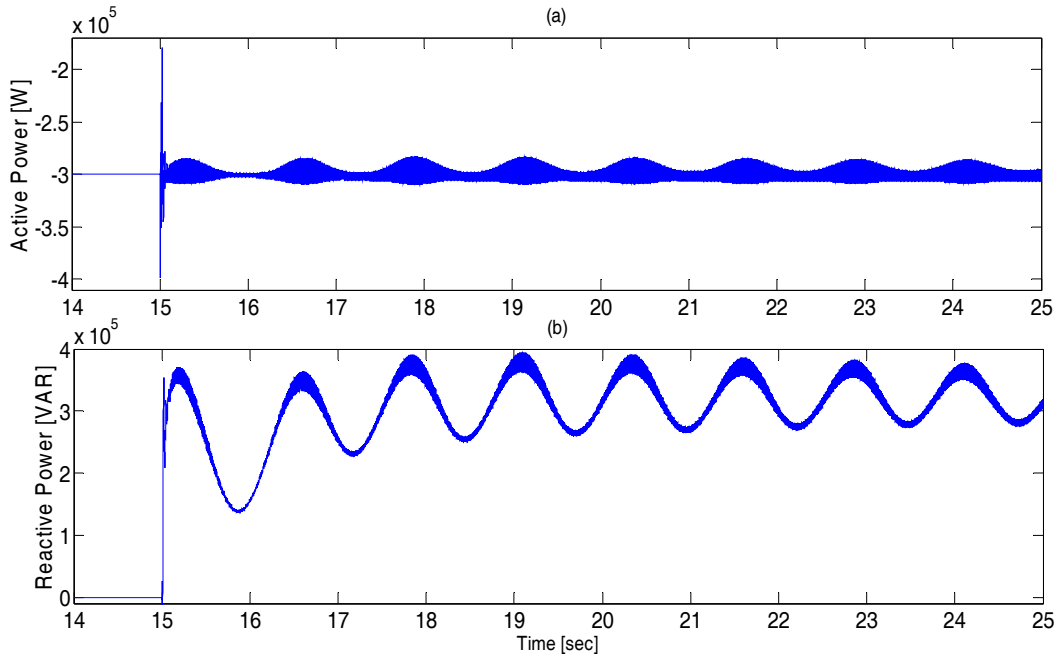

Figure 6-39 Total 3-phase a) Active power ($P_{3\text{-phase}}$), b) Reactive power ($Q_{3\text{-phase}}$) output of 3 single-phase converter bus, while voltage regulation is highly asymmetric (a=1, b=c=0).

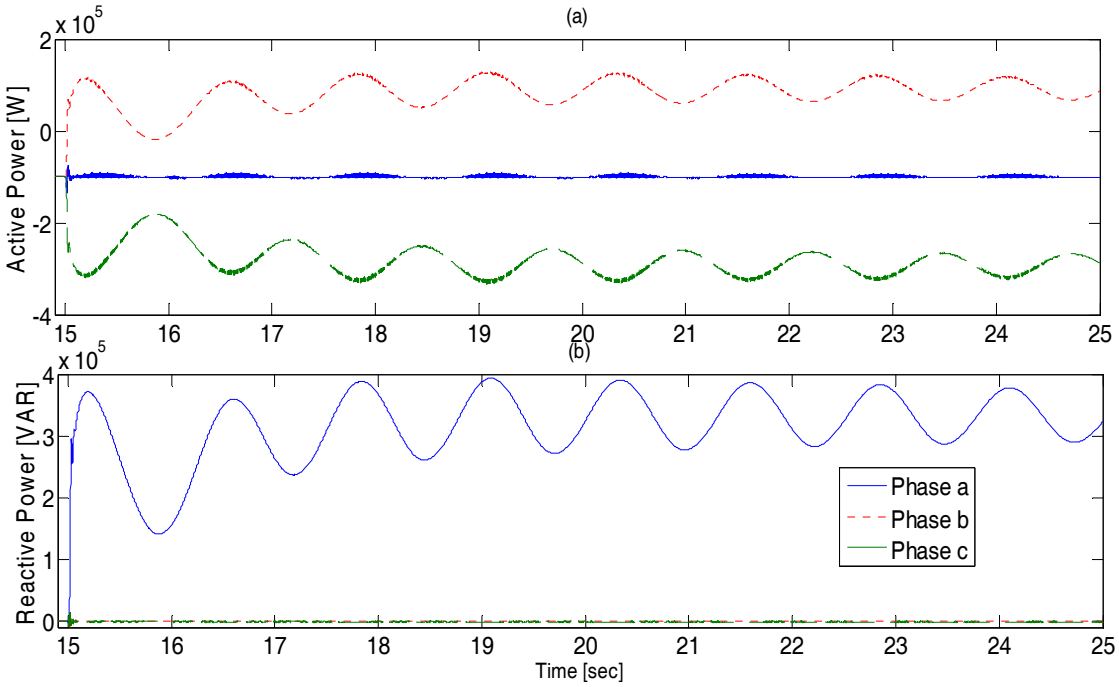

Figure 6-40 Each single-phase converter a) Active power and b) Reactive power generation, while voltage regulation is highly asymmetric (a=1, b=c=0) and the remedy is applied.

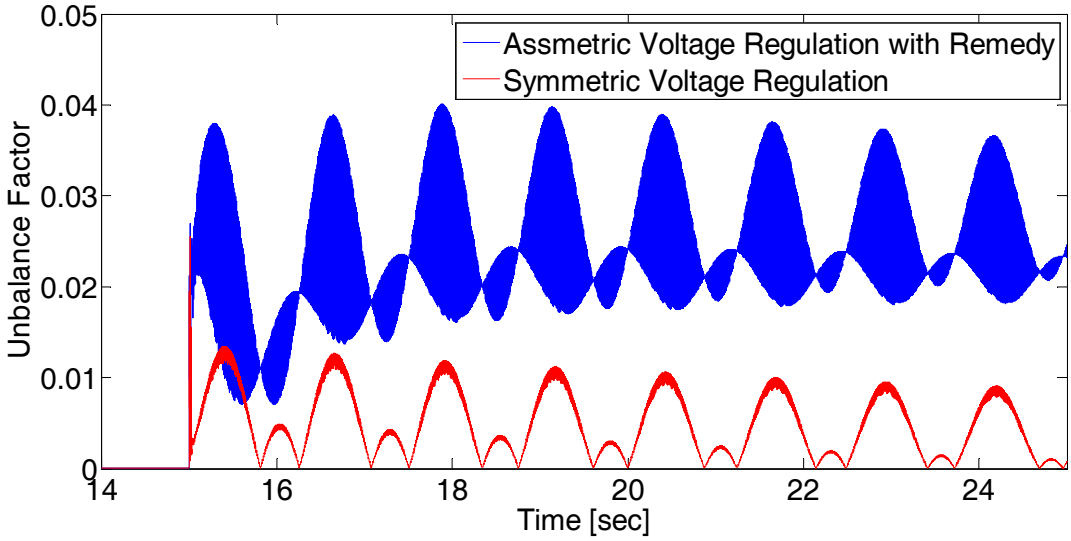

Figure 6-41 Unbalance Factor while virtual inertia is highly asymmetric (a=1, b=c=0) with remedy is applied vs. symmetric one.

6.4.1.6 Delay Impacts

The proposed remedy also needs communication lines; therefore, it may also be impacted by delays. Figure 6-42 shows a very severe case in which only one of the phases participate in frequency regulation with virtual inertia. Without the proposed remedy, this scenario will result in instability. To model the delay effect, it is assumed that every phase injects desired reactive power calculated by the proposed controller with a time delay equal to 200 ms while there is no delay in virtual inertia injection as shown by (6-35).

$$\begin{bmatrix} Q_a(t) \\ Q_b(t) \\ Q_c(t) \end{bmatrix} = \begin{bmatrix} \frac{1}{3} & 0 & \frac{\sqrt{3}}{3} & -\frac{\sqrt{3}}{3} \\ \frac{1}{3} & -\frac{\sqrt{3}}{3} & 0 & \frac{\sqrt{3}}{3} \\ \frac{1}{3} & \frac{\sqrt{3}}{3} & -\frac{\sqrt{3}}{3} & 0 \end{bmatrix} \begin{bmatrix} Q_{ev-ref} \\ P_a(t-\tau_d) \\ P_b(t-\tau_d) \\ P_c(t-\tau_d) \end{bmatrix}. \tag{6-44}$$

Although the performance is not as in the ideal case, stability is still maintained. It should be noted that a time delay as low as 10ms could destabilize centralized virtual inertia. In other words, the proposed control method makes the system much less vulnerable to time delays as compared to the centralized virtual inertia method.

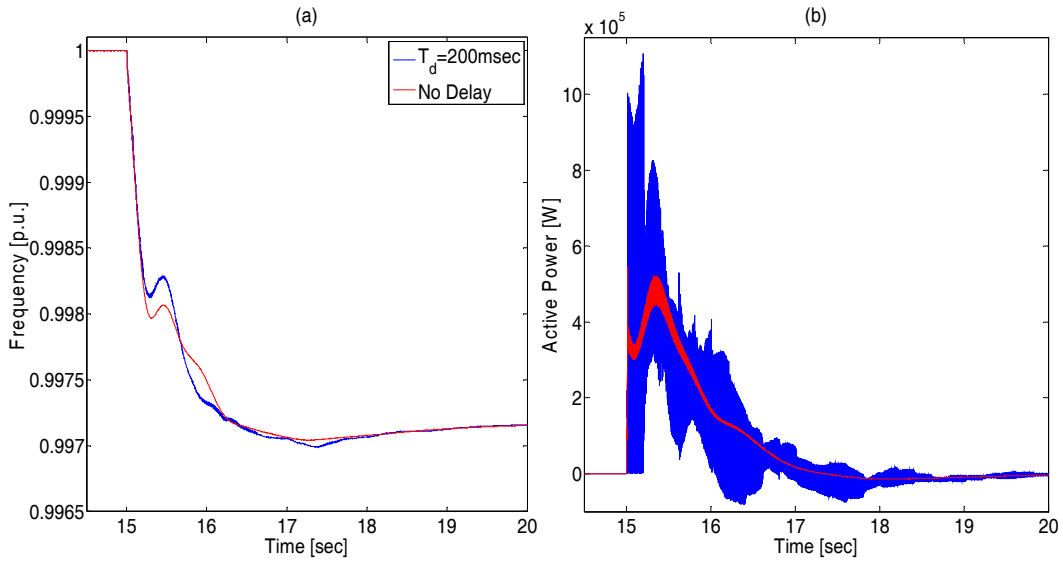

Figure 6-42 Utilization of remedy when virtual inertia is extremely asymmetric and communication delay is 200ms. (a) System Frequency (b) PHEVs total 3-phase active power.

6.4.1.7 Background Harmonic and Unbalance

To gauge the impact of background harmonic and unbalance, all the simulations were repeated in presence of the nonlinear Load 2 shown in Figure 6-2. Due to the increased load, and to avoid violating the generator limits, a similar generator is added in parallel to the first generator. Figure 6-43 shows the active power and unbalance factor when virtual inertia is highly asymmetric with reactive power remedy implemented. The transient responses are very similar in both cases with and without the nonlinear load. Indeed, the impact of background distortion can be observed more clearly in steady-state. Results show that ignoring the background distortion in the previous section does not lead to any oversimplification.

6.4.2 Cooperating with a wind generator

Detailed nonlinear time-domain simulations, using the microgrid system shown in Figure 6-10, are used to verify the results of the pervious sections and investigate the nonlinear dynamics of the microgrid system. The system parameters are given in the Appendices, and the details can be found in [161]. An intentional islanding event at t=30 s is used as the disturbance for the system. This disturbance leads to a mismatch between the

demand and the generation. In Figure 6-11 and Figure 6-19, this mismatch was modeled as the load change, represented by ΔP_L.

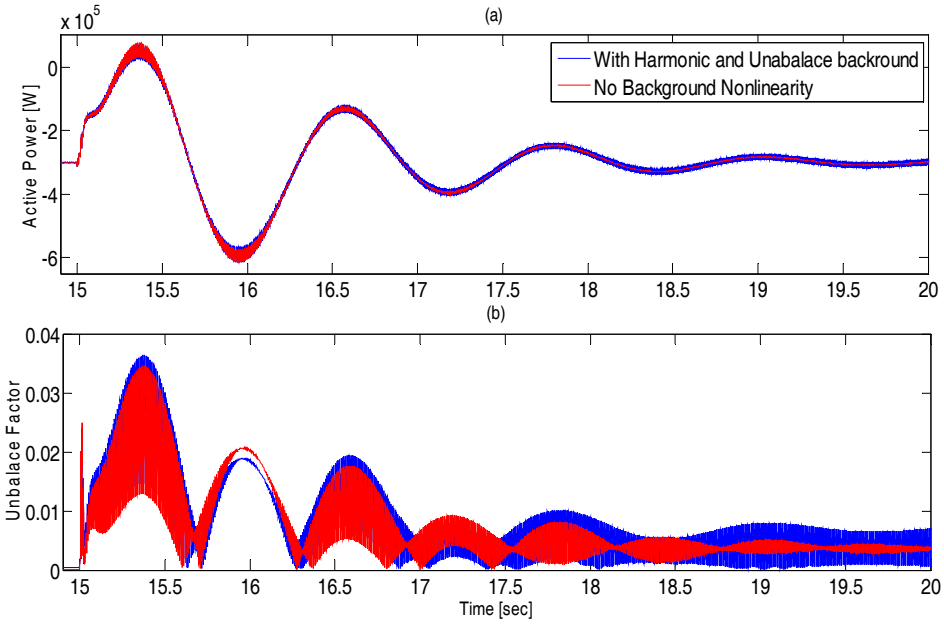

Figure 6-43 Impact of Background harmonic and unbalanced load on (a) The total 3-phase active power ($P_{3\text{-}phase}$) and (b) Unbalance factor at Load1 bus, while virtual inertia is highly asymmetric (a=1, b=c=0) and reactive power remedy is implemented.

6.4.2.1 Centralized Coordination

Figure 6-44 shows the system performance when a centralized coordination is used. The ideal and no compensation cases refer to perfect communication and wind-only frequency-regulating situations, respectively. Figure 6-44(b) and (c) verify that the coordinated control is successful in mitigating the mechanical tensions on the turbine shaft and figures (d) and (e), supporting the argument of the previous section that the PHEVs are used as power sources, not energy ones. The energy restored in PHEVs restores to its ideal amount very fast. This fast restoration shows that the SOC of the battery restores to its desired amount in a few seconds. To provide the power needed from PHEVs, 31 to 38 vehicles are needed to operate at their rating power. On the other hand, the maximum deviation from the energy stored in the wind-only case is less than 0.02 kWh in total. In other words, on average, each vehicle's battery should supply less than 0.004% of its nominal capacity to frequency regulation. This small energy consumption means that the change in the charge state of the

vehicles is negligible even though they have provided a significant amount of vital power for the power system stabilization.

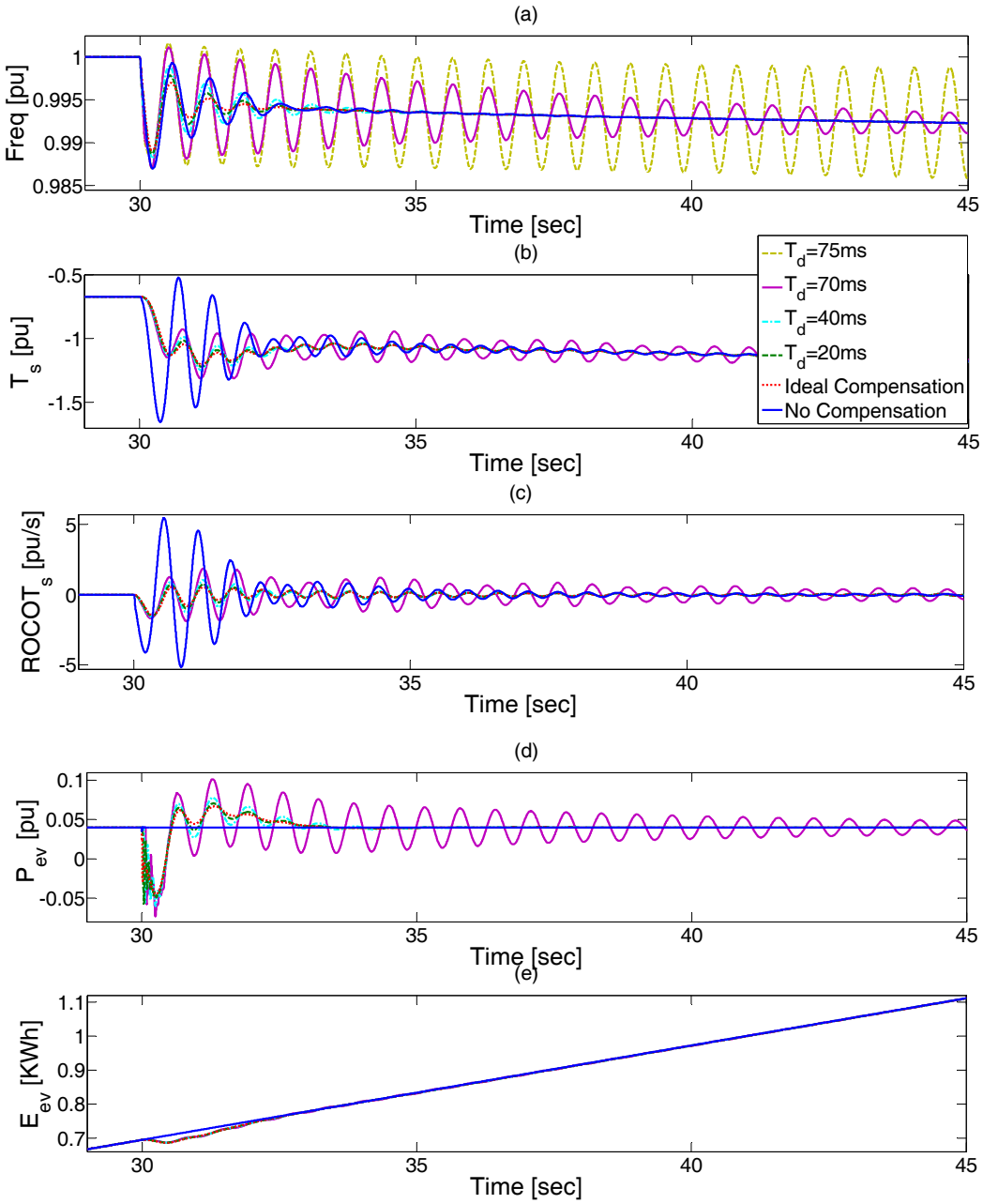

Figure 6-44 Centralized control performance with m_p=80 pu and f_{lpf}=0.25 Hz.

The impact of communication delays is also shown in this figure. The yellow dashed curve in Figure 6-44(a) shows that a delay as small as 75ms will put the whole system at the verge of instability.

The unequal delay phenomenon is shown in Figure 6-45. In Figure (a), all PHEVs have the same droop gain. The average delay is 80ms in all the cases, and, as Figure 6-45(a) reveals, the three systems are unstable. Figure (b) goes a step further when different droop gains are also applied for the different PHEVs with unequal delays. The accumulated droop gain, Σm_{pi}, and the delays, τ_{di}, are kept constant, but the average delay, $\Sigma(\tau_{di}.m_{pi})/\Sigma m_{pi}$, is changing. Interestingly, when the average delay is higher than 75ms (82.5 and 78.75 ms for the blue and red curves, respectively), the system becomes unstable, whereas with an average delay of 75 ms the system is only at the verge of instability, very similar to the case of Figure 6-44(a) with the equal delays and vehicles droop gains. These results are in compliance with the argument in the analyses section: in the cooperative droop control, the average delay will determine the stability of the system.

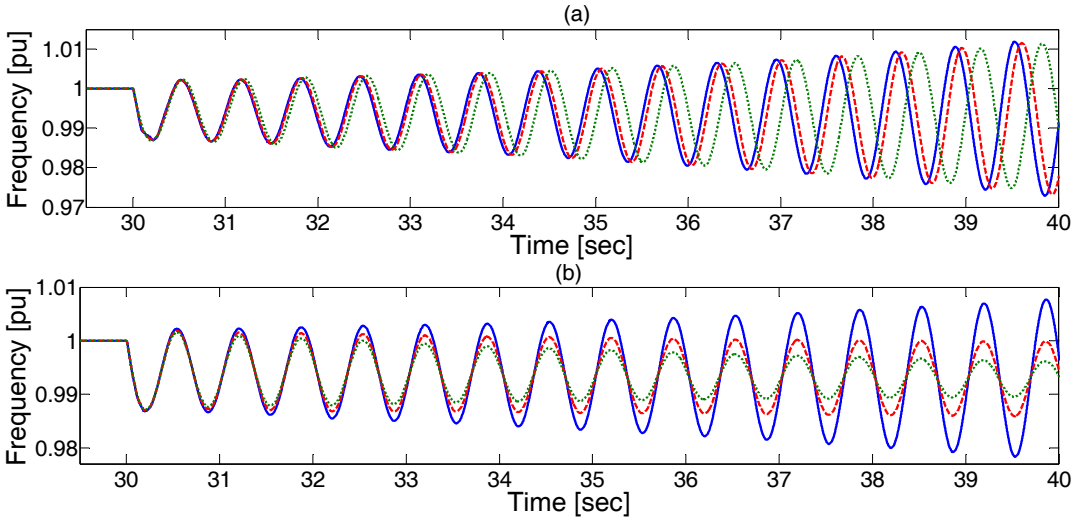

Figure 6-45 Unequal Delays; (a)m_{pi}=13.33, blue: τ_{di} =80 ms; red: τ_{d1} =120, τ_{d2} =100, τ_{d3} = τ_{d4} =80, τ_{d5} =60, τ_{d6} =40 ms; green: τ_{d1} =160, τ_{d2} =120, τ_{d3} = τ_{d4} =80, τ_{d5} =40, τ_{d6} =0 ms, (b) τ_{d1} =180, τ_{d2} =135, τ_{d3} = τ_{d4} =90, τ_{d5} =45, τ_{d6} =0 ms, blue: m_{p1}=10.67, m_{p2}=12, m_{p3}=m_{p4}=13.33, m_{p5}=14.67, m_{p6}=16 pu; red: m_{p1}=9.33, m_{p2}=11.33, m_{p3}=m_{p4}=13.33, m_{p5}=15.33, m_{p6}=17.33 pu; green: m_{p1}=8, m_{p2}=10.67, m_{p3}=m_{p4}=13.33, m_{p5}=16, m_{p6}=18.67 pu.

6.4.2.2 Distributed Coordination

Using the LPF cutoff frequency as a coordination tool is also examined in this section, and the results are shown in Figure 6-46. The maximum frequency deviation and the maximum power injected by the PHEVs, shown in Figure 6-46(a) and (d), respectively, remain unchanged, as predicted in the previous section. The wind generator shaft torque and its

derivative are depicted in Figure 6-46(b) and (c), respectively. The results confirm that f_{lpf} can be used to control the mechanical tensions on the wind turbine shaft.

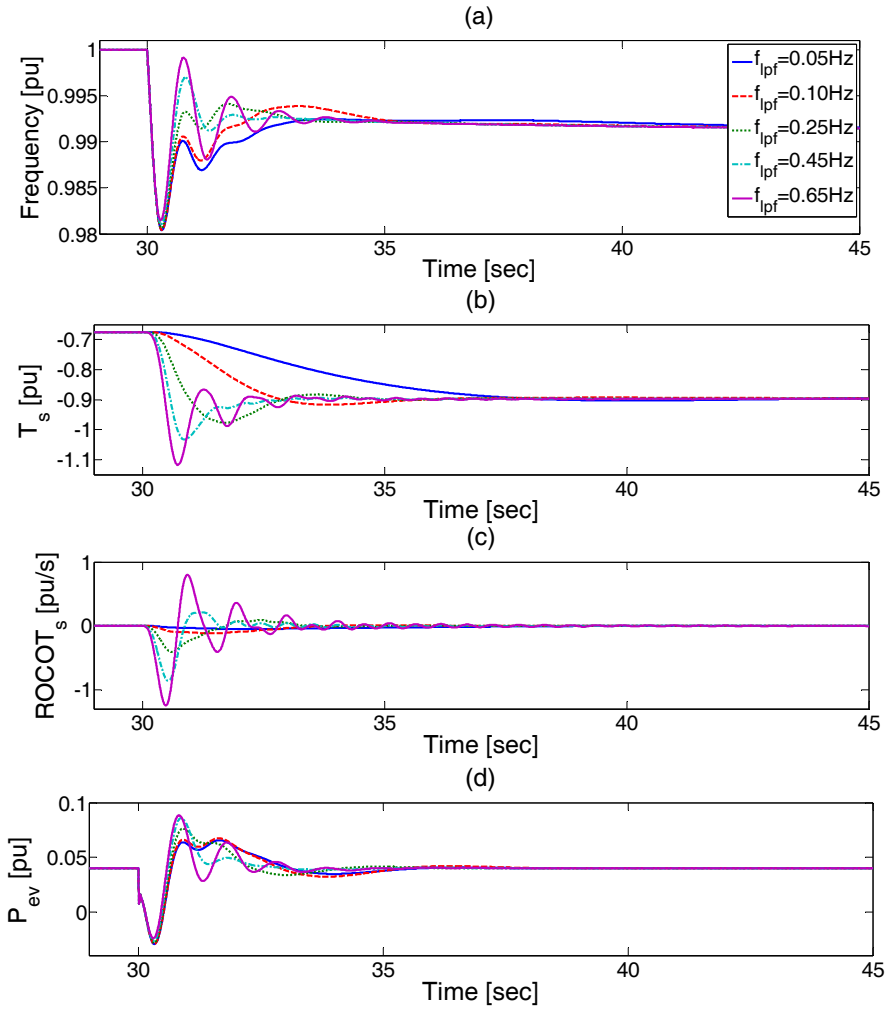

Figure 6-46 Impact of the LPF cutoff frequency in distributed coordination.

Figure 6-47 shows the case of unequal droop gains of the wind generator and the PHEVs. As predicted by the small-signal analysis, a much smaller PHEVs droop gain can make the system unstable. These results also confirm that instability happens only when $m_{p,phev}$ is a small fraction of the wind droop gain (less than one-fourth in the system under study). As shown in Figure 6-22, in the stable cases, a smaller PHEVs droop gain can amplify the mechanical tensions particularly by affecting the rate of change of the shaft torque. On the other hand, when $m_{p,phev}/\ m_{p,wind}$ is higher than one, represented by the purple curves in Figure 6-47, the system frequency dynamics and the ROCOT of the wind turbine shaft can be

improved at the expense of higher power injection by the PHEVs. These results verify the arguments in the previous section: the distributed cooperative droop is robust against miscoordinations. In other words, it is not necessary to retune the control gains by any changes in PHEVs or wind available energy for frequency regulation. The proposed method can work effectively for a relatively large range of changes.

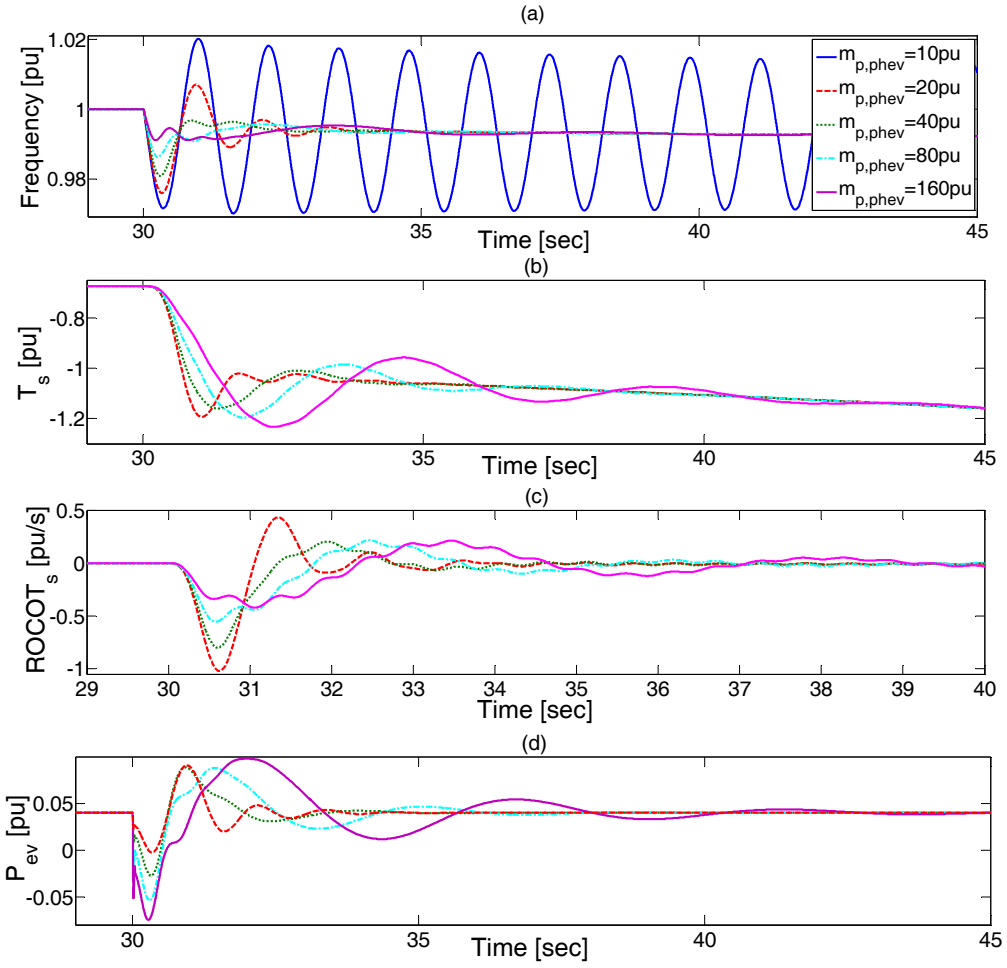

Figure 6-47 Impact of unequal droop gains when $m_{p,wind}$=40pu, f_{lpf}=0.25Hz.

6.5 Summary

This chapter addressed the use PHEVs to stabilize the frequency in microgrids and/or weak grids which lack enough inertia considering the single-phase nature and communication delays. Small-signal analysis was used to evaluate the performance of both droop and virtual inertia control methods, and show how time delay of a centralized control could impact

system stability. Advantages and disadvantages of distributed control were studied, and a new method based on a combination of both centralized and distributed control, was proposed to mitigate the impact of asymmetrical virtual inertia while it allows the utilization of all available PHEVs for active power however asymmetric they are.

Despite all merits of wind generators and plug-in hybrid electric vehicles, these two classes of sources are limited by some practical constraints which disqualify each of them from effectively contributing separately to the primary frequency regulation in power grids with reduced inertia, such as microgrids. However, when combined with proper control and coordination, wind generators and PHEVs can compensate for the individual drawbacks of each source and effectively participate in the frequency regulation. A cooperative control strategy that considers the practical limits of both sources is not available in the literature. To fill this gap, in this chapter, small-signal analysis was employed to investigate which frequency regulation method, droop or virtual inertia, is more suitable for such cooperation. The centralized and distributed control structures were examined as two possible coordination methods to ensure that the wind generator and PHEVs constraints are not violated and also that the communication system delay is considered. Based on a detailed analysis, the advantages, disadvantages and appropriate applications of the centralized and distributed structures were discussed. Time-domain simulation results validated the analytical results of the chapter.

Chapter 7
Improved VSC Control for Very Weak Grid Connections

7.1 Introduction

Voltage source converter (VSC)-based high-voltage direct current (HVDC) transmission systems have been employed widely in recent years. However, connecting of a VSC-HVDC link to a very weak grid (a high-impedance grid) is challenging. A vector-controlled VSC is incapable of injecting/absorbing its maximum theoretical active power in such grids. A simple yet effective control system for a standard vector-controlled VSC in a very weak grid condition has not been reported in the literature.

The contributions of this chapter to the research field are:

1) A thorough analysis of the dynamics of a VSC with either active power or dc-voltage regulating controllers, and connected to a very weak grid, and the impacts of the controller parameters on the overall system stability.

2) A detailed analysis of the maximum capabilities and limitations of conventional vector control.

3) The development of the artificial bus method to stabilize the performance of a vector-controlled VSC and maximize its power injection/absorption capability in a very weak grid condition.

4) An investigation of the robustness of the proposed method and a comparison with a retuned conventional vector controller.

This chapter is organized as follows. In Section 7.2, a complete model for a VSC is introduced and used for the analysis of a very weak grid in Section 7.3. Section 7.4 presents the proposed solutions and investigates them in detail. The next section presents the time domain simulation results to validate the analytical results. Finally, Section 7.6 reports the conclusions.

7.2 Modeling

The conventional VSC system, shown in Figure 7-1(a), is connected to the point of common coupling (PCC) via the passive inductive filter Z_f, and the grid line impedance Z_g is intermediating between the PCC and the grid. The capacitance C_f connected to the PCC is ignored in some studies [126]. It is argued that this capacitance is usually small and does not play a significant role in the stability of a very weak grid. However, for the sake of evaluating the complete system dynamics, it is not ignored in the models in this chapter. The parameters of the VSC system in Figure 7-1(a) are given in the Appendix B and are used in the analysis and simulation studies.

The modeling of a VSC has been discussed by many researchers such as [115, 116, 128, 129, 130, 191, 192]. Most of their models were based on linear small-signal modeling using different methods. For example, [121] utilized input/output admittance, whereas [125] and [126] employed a Jacobin matrix. A complete state-space model consisting of all controllers dynamics as well as line current and voltage equations was used in [127, 168, 175]. All of these methods are equivalent; however, for particular studies, some offer better features. In this chapter the complete state-space model is adopted.

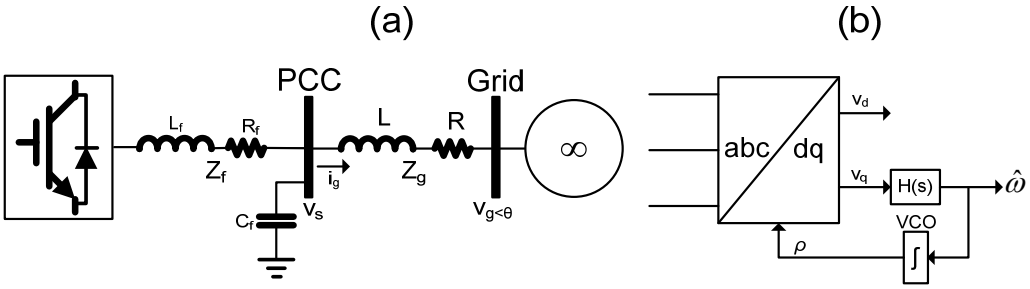

Figure 7-1 (a) Schematic diagram of a grid-connected VSC (b) Block diagram of PLL.

The model with active power and dc-voltage regulating, respectively, is shown in (7-1) and (7-2), where the states are introduced as a vector x, which contains 13 or 14 states representing all controllers (current controllers, PLL, ac-bus voltage controller, and active power controller) and power circuit dynamics in the dq-frame. Whereas the grid voltage magnitude $|V_g|$ and dc-link voltage fluctuations v_{dc} (in a dc-voltage regulating VSC, the external power P_{ext} plays the role of the disturbance) can be considered as disturbances, the

reference active power P^* (or reference dc-link voltage, V_{dc}^*) and reference PCC voltage magnitude $|V_s|^*$ are the desired inputs. Reference [126] proved that a VSC connected to weak grids works much better as a PV bus (regulating active power and PCC voltage) rather than a PQ bus (regulating active and reactive output powers of a VSC). The modeling details of a conventional VSC are available in the literature [168] and, therefore, will not be repeated here. However, some key points in the modeling are worth discussing. As reported in [130], the active power and dc-regulating controllers show similar behaviors, thus the analyses are focused mainly on the former, whereas the results of the dc-voltage regulating controller are also shown wherever doing so is necessary.

$$\Delta\dot{x}_p = A_p\Delta x_p + B_{1p}\Delta|V_s|^* + B_{2p}\Delta P^* + B_{3p}\Delta|V_g| + B_{4p}\Delta v_{dc}. \tag{7-1}$$

$$\Delta\dot{x}_v = A_v\Delta x_v + B_{1v}\Delta|V_s|^* + B_{2v}\Delta V_{dc}^* + B_{3v}\Delta|V_g| + B_{4v}\Delta P_{ext}. \tag{7-2}$$

The standard vector control structure is based on cascaded proportional-integral (PI) regulators. The active and reactive power PI regulators generate the desired current components, whereas the ac-bus voltage PI regulator generates the reactive power reference. Two PI current controllers are used to generate the converter modulating signals in the *dq*-reference frame. A standard three-phase *dq* PLL is used to generate the synchronization angle needed to transform the control variables between the stationary and rotating reference frames [175]. A PLL utilizes the voltage of the PCC to determine the system frequency and synchronization angle ρ as shown in Figure 7-1(b).

In strong grids, a PLL is usually considered to be ideal and is neglected. However, it plays a vital role in weak grids. Figure 7-2 shows the block diagram of the small-signal model in which the impact of the PLL is shown by the "*Trans.*" and "*Conv.*" blocks. Equation (7-3) introduces their function before linearization. They essentially map the voltage and current vectors, which are represented by u, from one frame whose d-axis coincides with v_g to the other whose d-axis is synchronized with v_s (or vice versa). The PLL output ρ deviates from the exact angle of the grid voltage v_s in transient and dynamic conditions. If the system remains stable and the PLL is perfectly locked, the angle ρ converges to the grid voltage angle θ.

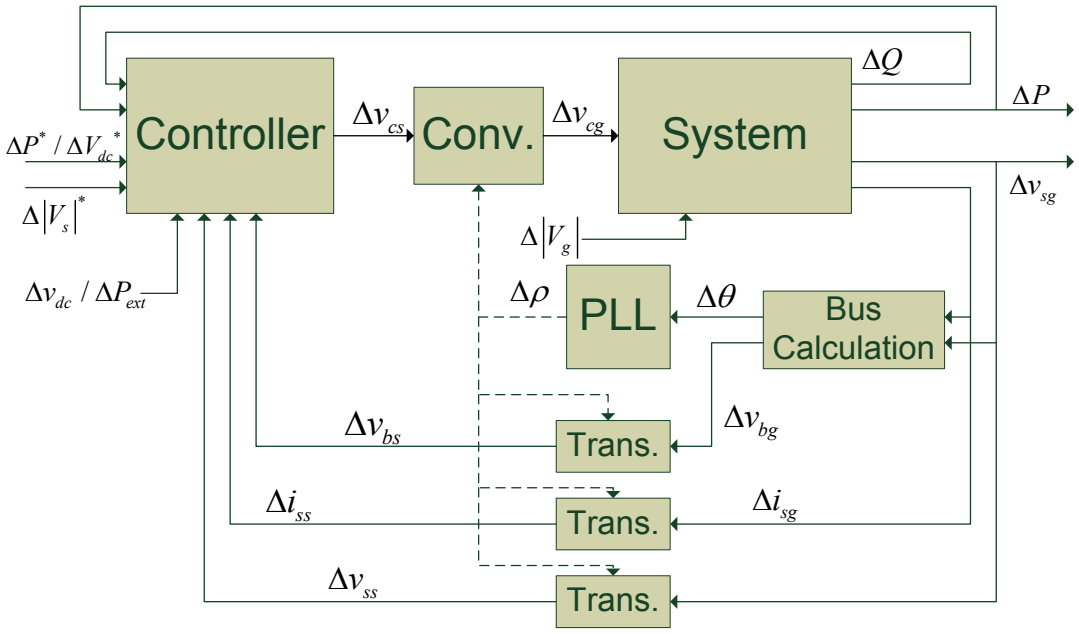

Figure 7-2 Block diagram of the small-signal modeling of a grid-connected VSC.

$$\begin{bmatrix} u_{sd} \\ u_{sq} \end{bmatrix} = \begin{bmatrix} \cos\rho & \sin\rho \\ -\sin\rho & \cos\rho \end{bmatrix} \begin{bmatrix} u_{gd} \\ u_{gq} \end{bmatrix}. \tag{7-3}$$

The impact of the PLL can now be reflected in the complete model. Although the analysis will be verified in detail in the time-domain simulation section, Figure 7-3 is included here to show the accuracy of the small-signal model used in the analysis. Obviously, the linearized model exhibits a very high level of coincidence. In light of such a model, detailed analysis of the system is possible.

7.3 Analysis

Equation (7-4) indicates the boundaries of the active power, which could be injected by a VSC into the PCC in the steady state. The negative sign indicates absorption.

$$\frac{R|V_s|^2 - |Z_g||V_s||V_g|}{|Z_g|^2} \le P \le \frac{R|V_s|^2 + |Z_g||V_s||V_g|}{|Z_g|^2}. \tag{7-4}$$

In a grid with SCR = 1, the magnitude of the grid impedance will be 1.0 pu. Without the loss of generality, if the grid and PCC voltages are assumed and controlled to be 1.0 pu, the maximum power injection and absorption will be limited to 1.1 pu and 0.9 pu, respectively.

In other words, the maximum active power that can be injected into a very weak grid is close to 1.0 pu according to static analysis. However, in reality, this amount is even less. Eigenvalue analysis can reflect these differences as shown in Figure 7-4. In fact, many researchers discussed this point; however, they usually omit the other challenges of a VSC connected to a very weak grid.

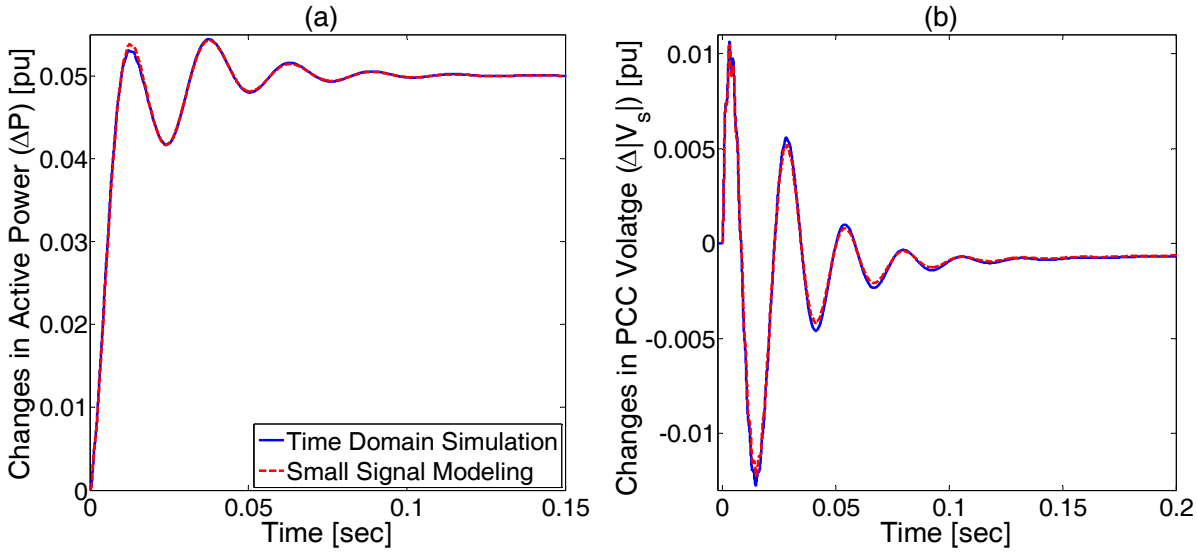

Figure 7-3 Response of the VSC to a 0.05 pu change in the reference active power. (a) Changes in VSC active power output (b) Changes in PCC voltage. SCR = 1, P_0=0.5 pu.

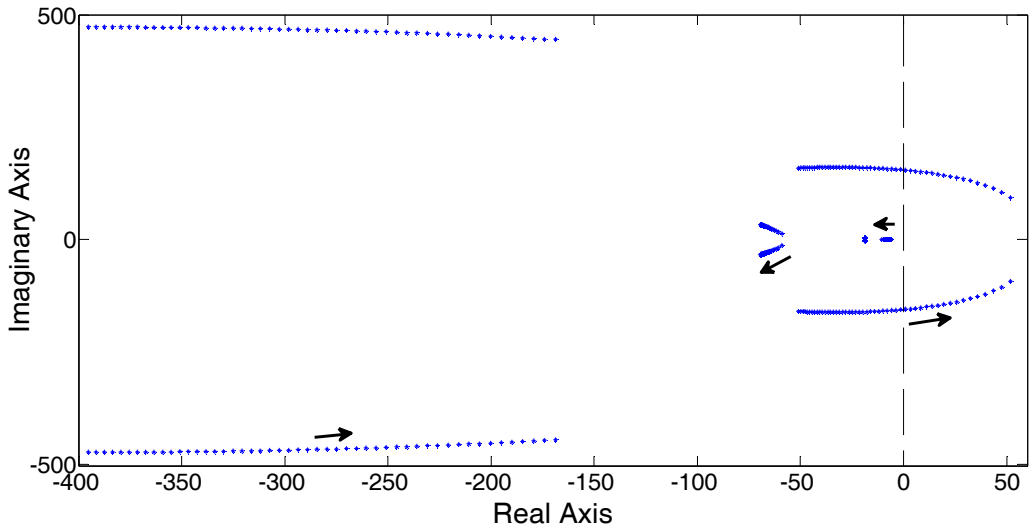

Figure 7-4 Dominant eigenvalues of the system when SCR decreases to 1.

Before proposing any solution, a better understanding of the dynamics of a VSC connected to a very weak grid is necessary. The model allows a thorough investigation of the system dynamics. However, many factors may play significant roles.

One of the most important challenges when connecting a VSC to a very weak grid is the loss of controller independence. Figure 7-5 shows the response of the PLL to the changes in the voltage magnitudes (reference ac-bus voltage V_{ref} and ac system internal voltage V_g). Here, the system frequency is kept constant while the voltage magnitude is changed. Obviously, by increasing the SCR, the changes in the reference value of the PCC voltage have less impact on the PLL output frequency in terms of the settling time and maximum deviation index. In other words, the interference of the voltage regulator on PLL performance has decreased significantly. On the other hand, in the stronger grid, the grid voltage disturbance leads to higher fluctuations in the PLL output. Although the magnitude of this deviation has increased, its settling time has decreased severely. This result means that the deviation will decay very quickly. Further, this result could also be explained by the voltage regulator. Lower SCRs allow tighter control of PCC voltage, which bypasses the disturbances from the grid voltage. Therefore, the input of PLL, PCC voltage, is less influenced by the grid voltage.

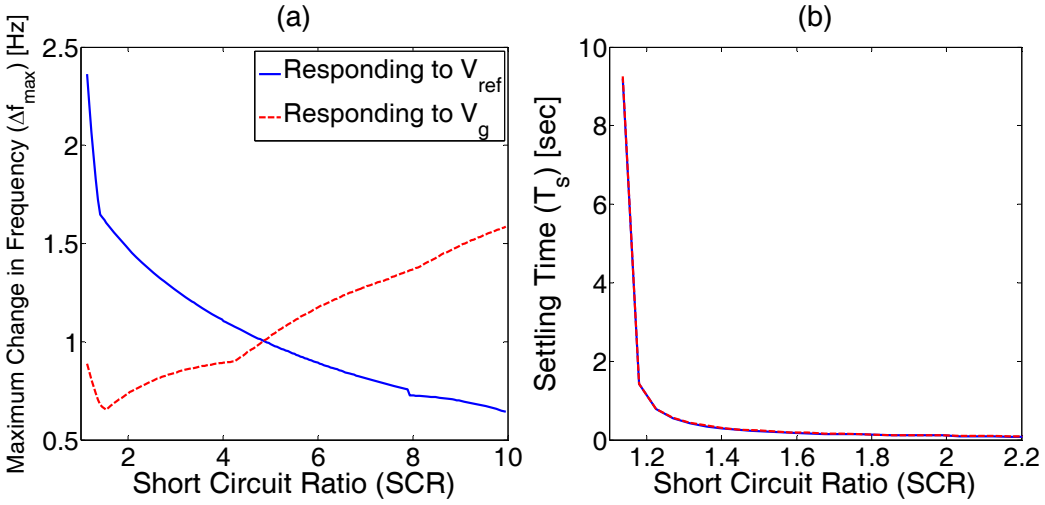

Figure 7-5 Impact of voltage magnitude disturbance on the PLL performance in different SCRs. A 10% changes in the voltage magnitude is applied in all the cases whereas the active power operating point is set to zero.

The voltage regulator also interferes with the active power regulation. Conventionally, independence of these two regulators is desired and expected. However, as Figure 7-6 reveals, a very weak grid behaves differently. The resonance, distinguished as a spike in the frequency response, was expected from Figure 7-4, in which the conjugate poles are moving toward the right half-plane. Their impact will appear as fluctuations on the VSC active power output whenever the PCC voltage magnitude reference input $|V_s|^*$ is changed.

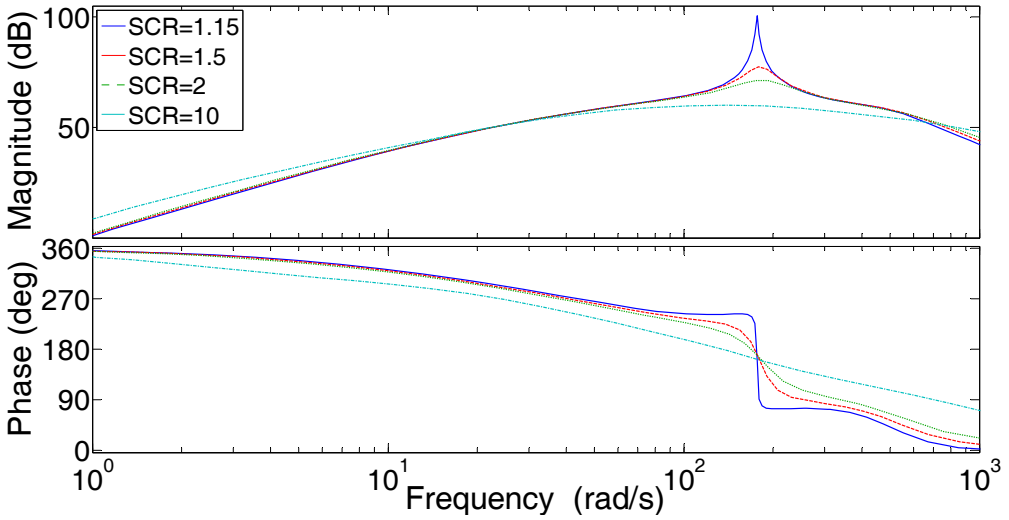

Figure 7-6 Frequency response of the output active power of a VSC responding to changes in the reference voltage of PCC.

On the other hand, the parameters of the active power regulator also affect the ac-bus voltage regulation. Figure 7-7 reveals this impact more clearly. The integral gain of the active power regulator is changed here to gain different bandwidths for the closed-loop power control dynamics. In a strong system with SCR = 10 (red dashed line), this gain has almost no impact on the voltage regulator bandwidth; however, it results in huge changes to voltage regulator performance in a very weak grid.

The situation becomes more complicated when the operating point of the system is also considered as a factor. In a weak grid with SCR = 2, changes of initial power injection from zero to almost one per unit lead to a change of less than 7% in the active power regulator bandwidth. This change is negligible; however, in a very weak grid with SCR = 1, the same changes in the operating point lead to changes of more than 24% in the controller bandwidth

(see Figure 7-8). In other words, the operating point cannot be excluded in studies of very weak grids.

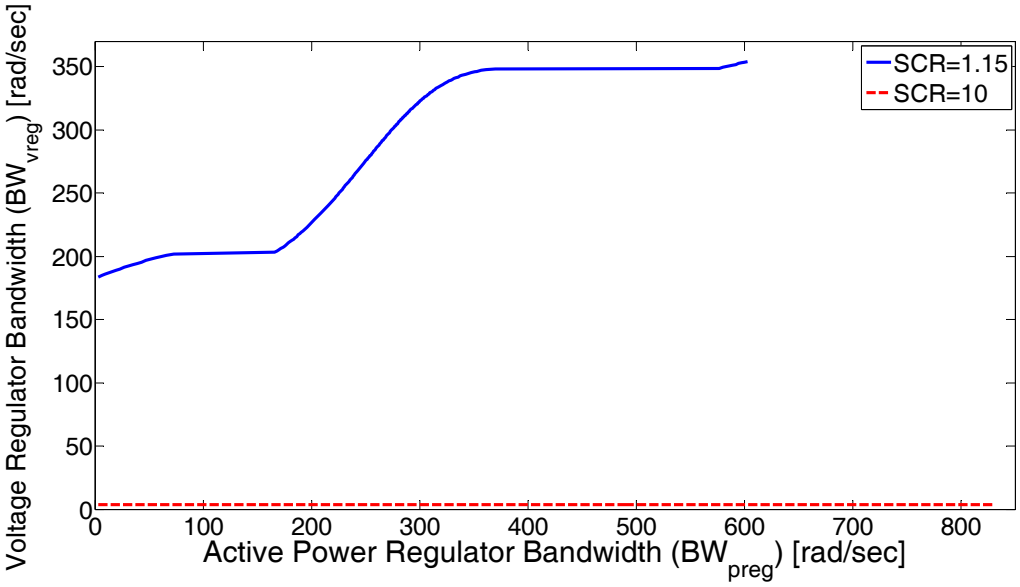

Figure 7-7 Impact of active power control bandwidth on the ac-bus voltage control bandwidth.

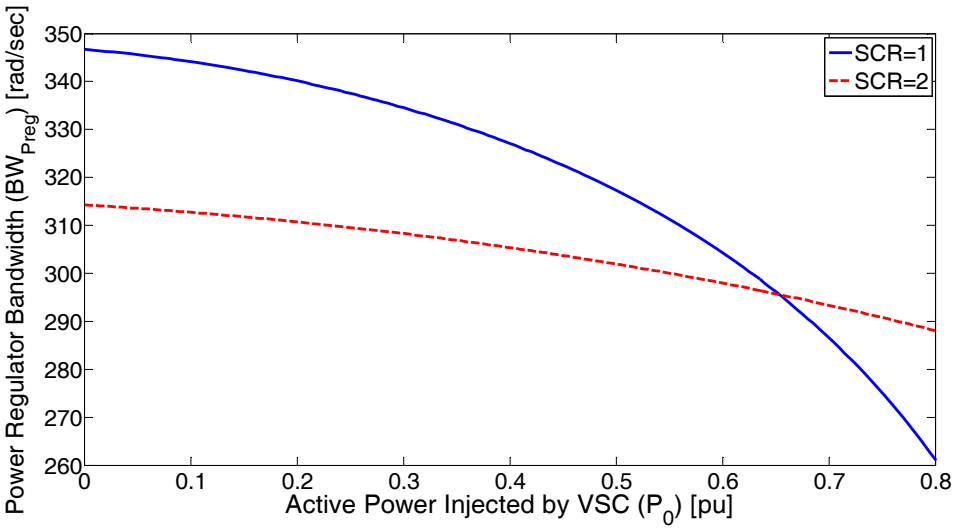

Figure 7-8 Impact of operating point on the VSC active power regulation.

Although all these facts are not explicitly mentioned in [127], they forced its authors to undertake the complicated process of designing 35 H_∞ controllers for a single converter.

7.4 Solutions

The main aim of any solution is to enable 1.0 pu power injection in a very weak power system. A solution must be robust and should be the least complicated alternative.

7.4.1 Retuning

One of the first solutions to be examined is the retuning of the controller parameters. The previous attempts in the litreature failed to reach the main goal of this present chapter. In [116], the authors focused only on the PLL bandwidth; however, the analysis in Section 7.3 showed that the independence of different regulators, observed in strong grids, no longer functioned in very weak grids.

By benefiting from the experiences reported in [115] and [116]—which emphasize the speeding up of the voltage regulator and the slowing down of the PLL, respectively—the desired goal becomes reachable, as Figure 7-9 indicates.

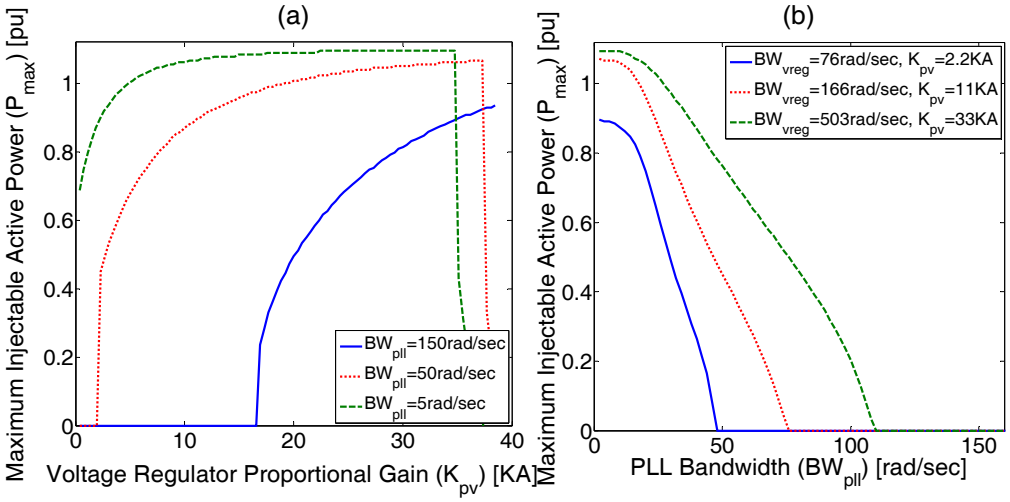

Figure 7-9 Maximum injectable active power at SCR=1 with retuning the parameters of voltage controller and PLL.

Huge changes in the voltage angle result in problems for the PLL. A slow tracking can prevent these angular stability problems but will result in a poor PCC voltage profile. Fast voltage regulation is necessary to guarantee acceptable voltage magnitude in the presence of such a slow PLL.

However, to achieve the main goal, the decoupled design of controllers, one of the main assumptions in the strong grid is neglected. In fact, such a strategy responds to the lack of decoupling between the voltage and frequency stabilities experienced in strong grids. In other words, the PLL and voltage regulator parameters are designed together, not separately. Although this strategy enables 1.0 pu power injection, it also necessitates the complete modeling of the system. This requirement is much more complicated than the requirements of the standard strong grid design.

The robustness of the controller is another important concern. Figure 7-10 reveals the active power and voltage regulator bandwidths at different operating points. Although some changes can be observed in the power controller speed, it always remains reasonable.

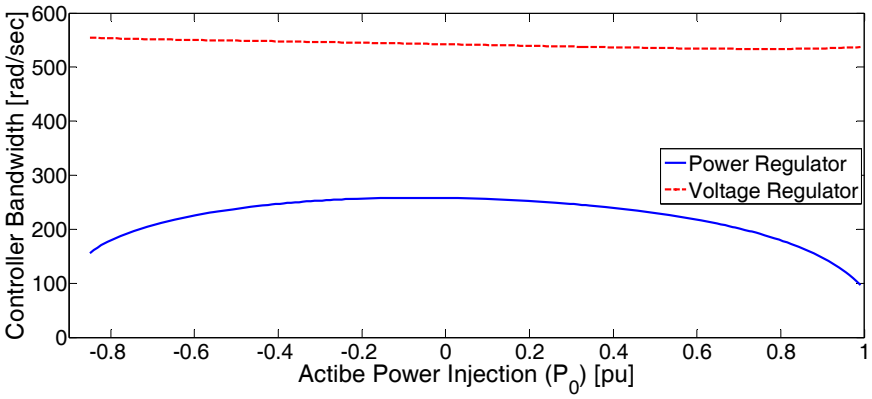

Figure 7-10 Impact of the system operating point on the retuned VSC performance.

Figure 7-11 focuses on another aspect, the impact of the voltage regulator on PLL performance. Not surprisingly, with decreasing PLL bandwidth, smaller deviations in the PLL output frequency occur. However, these results are obtained by slowing down the PLL. Such slow behavior is also reflected in the prolonged settling time of the fluctuations shown in Figure 7-11(b). In other words, PLL performance is now very slow, and the voltage regulator is very fast so that their interactions no longer destabilize the system.

Despite these advantages, some issues challenge the capabilities of the retuned controller. Figure 7-12 illustrates the situation more clearly. Part (a) shows how the proposed method is sensitive to the strength of the grid. Indeed, by decreasing the impedance of the grid, tight control of the PCC voltage will not be possible, so that the system will become unstable. On

the other hand, systems that remain stable (like the red dashed curve in the figure) utilize very small bandwidths. Such slow phase tracking is not desired, especially if the output frequency of the PLL is needed for other applications such as frequency regulation. In fact, adopting such a small bandwidth is very similar to the idea of removing the PLL, with all its advantages and disadvantages [125]. This figure also depicts the dc-voltage regulating VSC behavior to show how similarly it behaves to the active power regulating controller it behaves.

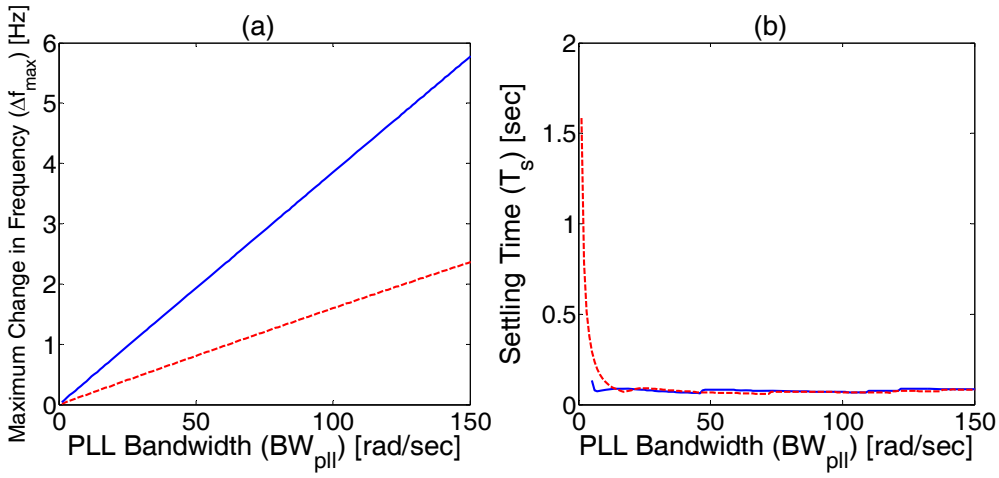

Figure 7-11 PLL output frequency responding to a 10% change in the grid voltage, $|V_g|$, (red dashed line) and the input reference voltage for PCC, $|V_s|^*$, (blue solid line).

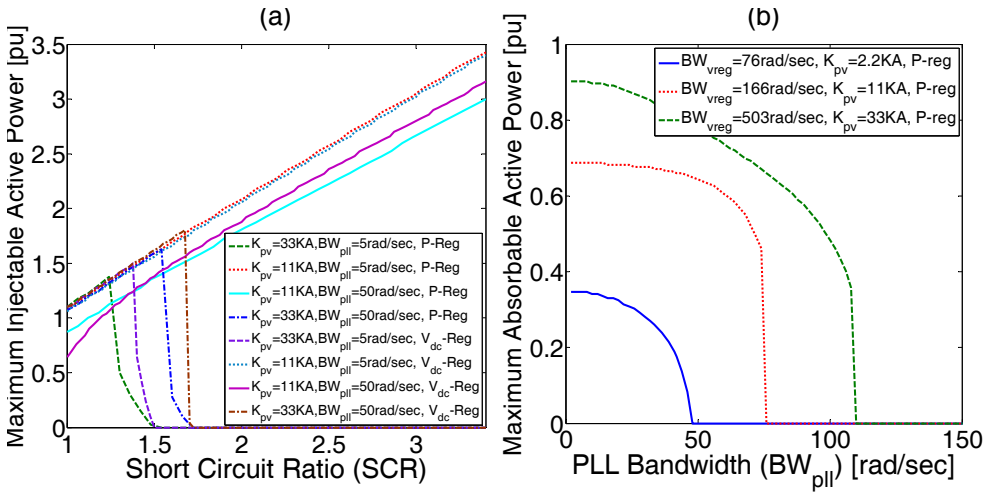

Figure 7-12 Impact of the strength of the grid on the retuned controller (b) Maximum absorbable active power by VSC in very weak grid utilizing the retuned controller.

The other notable observation is related to the absorption rather than injection of power. Sinking active power is not usually needed for HVDCs interfacing with wind generators; otherwise, such power is very practical and possible. As Figure 7-12(b) shows, very low PLL bandwidths and very fast voltage regulation are needed to enable maximum static absorption. A comparison to Figure 7-9(b) reveals that the lower ac-voltage regulation bandwidths were also able to use the entire available capability of the converter for injection. In other words, designing a retuned controller for a VSC with both injection and absorption of active power is even more complicated and also is restricted to smaller ranges of parameters.

7.4.2 Artificial Bus

The conflicts discussed regarding the retuned controller motivate the search for a new solution that attempts to address the problem's main source, which is the high impedance between the reference bus of the PLL and the grid voltage. As depicted in Figure 7-13(a), if the reference bus can be moved to some artificial point between the PCC and the grid, a VSC with high filter impedance but lower grid impedance will be attained. Consequently, the converter no longer faces a very weak grid, whereas the higher Z_f does not cause any problem owing to the high degree of current control.

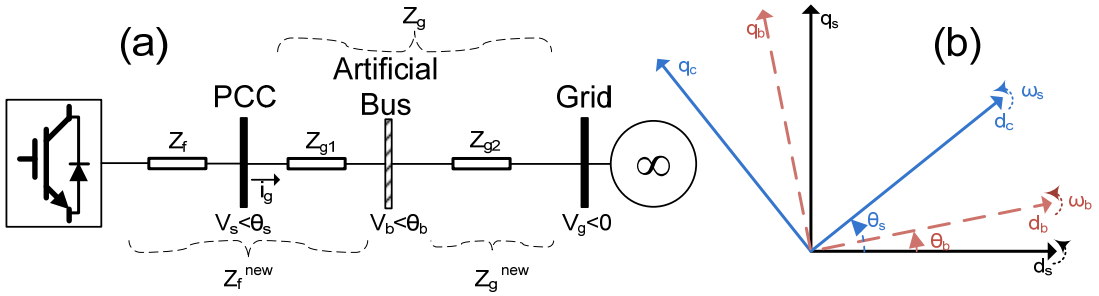

Figure 7-13 (a) Schematic view of the concept of the artificial bus method (b) dq-reference frames.

The remaining concerns are voltage and power regulation. Choosing the hypothetical impedance Z_{gl} between the PCC and artificial bus to be purely inductive solves the problem of power regulation. This solution means that the active power injections (absorptions) at the PCC and the new artificial bus are identical.

Because the voltage of this new bus has no significant meaning for grid operators, the controller can still be set to control the PCC voltage. Conventional synchronous generators inspired this idea. Sometimes, in conventional generators, instead of the voltage magnitude of the real generator bus, the voltage of some artificial bus inside the generator is fed into the exciter of the generator [168]. This method is known as "*reactive-current compensator.*"

Whereas the same voltage and power can be controlled by the HVDC, nothing has changed but the reference frame used for the controller, shown in Figure 7-13(b). Thus, the only needed modification is the input voltage of the PLL, distinguished in Figure 7-2 by the block named "*Bus Calculation.*"

Equation (7-5) formulates the artificial bus voltage, v_b. The parameters here are in vector space representing all three phases. Because the implementation of a pure derivate is not possible, a high-pass filter with a relatively small time constant τ_c is utilized. Further, Z_{gl} is chosen to have no active power consumption, so it is represented by an inductance equal to aL', where L' is equal to the inductance L between the grid and the PCC at SCR = 1, and a is the compensation factor restricted between 0 and 1. v_b is then fed into the PLL to track its phase.

$$\vec{v}_b = \vec{v}_s - aL' \frac{s}{\tau_c s + 1} \vec{i}_s. \tag{7-5}$$

The only modified part of the controller is the current controller, which is changed to consider the new filter impedance. This procedure can be accomplished simply by changing its proportional gain as formulated in (7-6) and (7-7). K_{pc}, K_{ic}, and τ_i are the proportional and integral gains and time constant of the current controller, respectively. L_f and R_f are the inductance and resistance of the AC filter Z_f, respectively. By assigning zero to a, the controller will be simply restored to the conventional VSC controller.

$$K_{pc} = \frac{L_f + aL'}{\tau_i}. \tag{7-6}$$

$$K_{ic} = \frac{R_f}{\tau_i}. \tag{7-7}$$

Obviously, the implementation of the method is easy and straightforward; the rest of this section is devoted to analyzing its performance. Figure 7-14 shows the impact of the proposed solution on the maximum injectable active power. Obviously, not only is the converter capable of injecting the maximum static active power, calculated in (7-4), but the high-speed voltage regulator is not needed; this advantage prevents problems for the proposed method at higher SCRs. The interesting point about this figure is that the bandwidth of the PLL is set to be as high as 150 rad/s, which is much higher than the bandwidths used in the retuned method. In other words, by the proper selection of the compensation factor, which Figure 7-14 reveals to be a relatively large range, the rest of control parameters can be designed as if the converter is connected to a strong grid. Similar to strong grids, very fast voltage regulators can degrade the overall converter performance as shown by the solid blue curves in Figure 7-14.

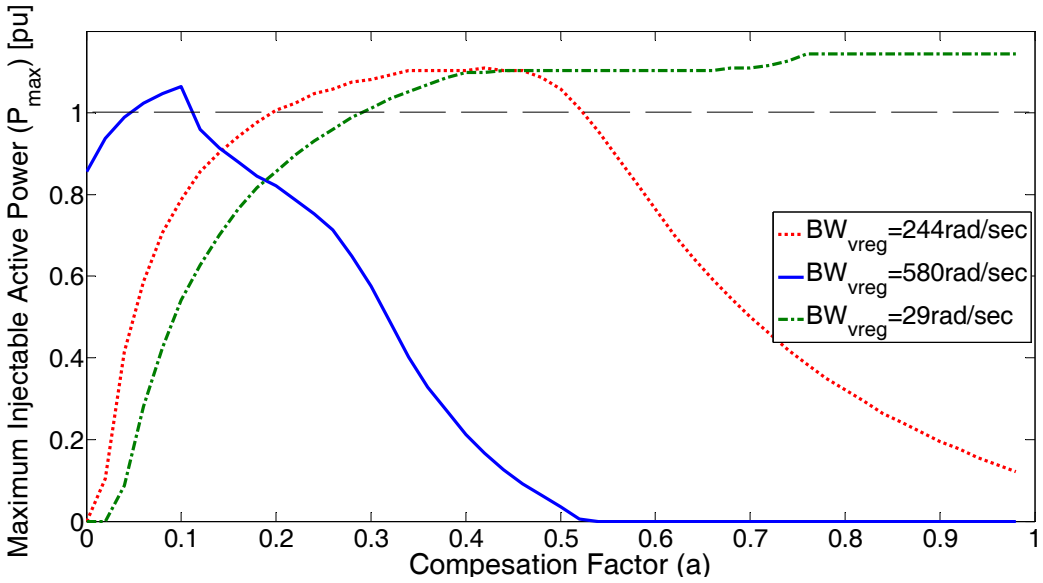

Figure 7-14 Impact of applying the artificial bus method on the maximum power injection of the converter. Bandwidth of PLL is set to at 150 rad/s.

Figure 7-15 measures the abilities of the artificial method, which eliminates the previous method's serious weaknesses. Here, all controller parameters, including a and L', are kept constant, whereas the SCR of Z_g and, consequently, L and R are changing. Obviously, the system remains stable. Thus, a sudden change in the line SCR, caused by switching, does not impact the stability of the converter. In addition, the controllers that can maximize the

injection of the VSC are capable of maximizing the power absorption, leading to a simpler design. The results for the dc-regulating VSC are shown in order to verify their resemblance to those for the active power regulating case.

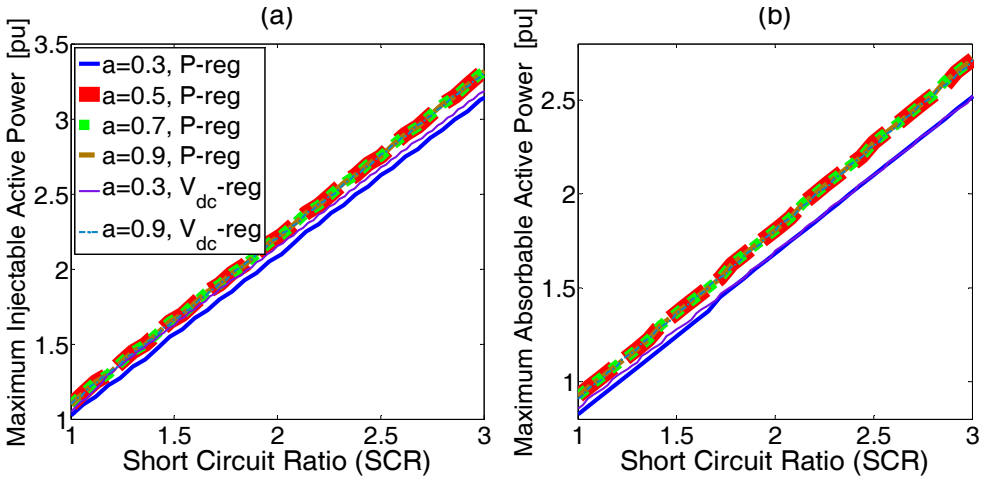

Figure 7-15 Impact of the grid strength on the performance of VSC (a) Injecting, (b) Absorbing active power. PLL and voltage regulator bandwidths are 150 rad/s and 29 rad/s, respectively.

Figure 7-14 and Figure 7-15 address another concern about the controller, which is the inaccurate measurement of *L'*. The high ranges of the compensation factor and SCRs, which allow the maximum injection and absorption of active power, imply that by proper selection of *a*, the practical inaccuracies in *L'* do not cause a serious problem for the converter.

The interference of the regulators was discussed as a characteristic of the performance of a VSC connected to a very weak grid. The impact of adopting the artificial bus for this feature is presented in Figure 7-16. This impact is especially important because it is claimed that this method is similar to reducing the weakness of the grid. As was expected, by increasing *a* equivalent to the increase in the strength of the system, the interferences decrease so that the regulators take back their independence.

These interferences are also functions of the operating point of the converter; however, in a constant operating point, increasing the compensation factor will lead to greater independence of the regulators, but in comparison to the differences in Figure 7-5, a considerable difference can be observed. An increase of the compensation factor decreases

the impact of the grid voltage, whereas in a stronger system, a higher influence of the grid voltage is expected.

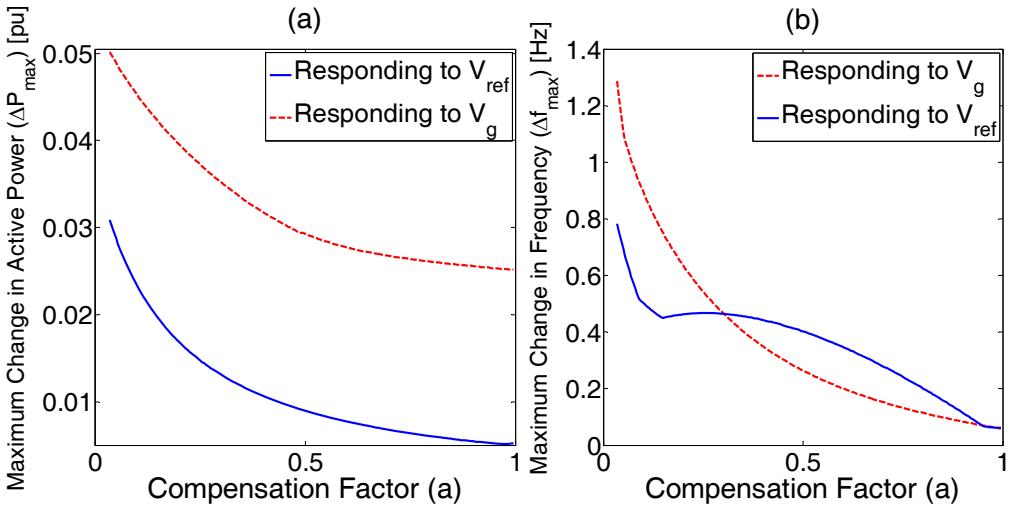

Figure 7-16 Impact of the compensation factor on interference of voltage regulator with the (a) power regulator (b) PLL.

In fact, the artificial bus method should not be considered as the exact equivalent of decreasing the SCR. Figure 7-17 is used here to discuss this point in more detail. The blue solid curves show the performance of the VSC responding to changes in the reference active power and voltage when SCR = 2, and the red dashed curves represent the same when SCR = 1 and a = 0.5. Hypothetically, similar responses are expected, but obviously they do not greatly resemble each other. Much more important than their different AC filter impedance, one of these converters directly controls the input voltage of its PLL whereas the artificial bus method does not. Therefore, although the artificial bus method can be conceptualized as a decrease of the grid weakness, the use of this method does not necessarily decrease the impedance.

7.5 Time-domain Simulation Results

Whereas small-signal analysis allowed detailed evaluation, time-domain simulation is used in this chapter to verify the discussions. The system shown in Figure 7-1(a) is modeled here, and the parameters used are listed in the Appendix B. The Matlab/Simulink® package is utilized for the simulation studies.

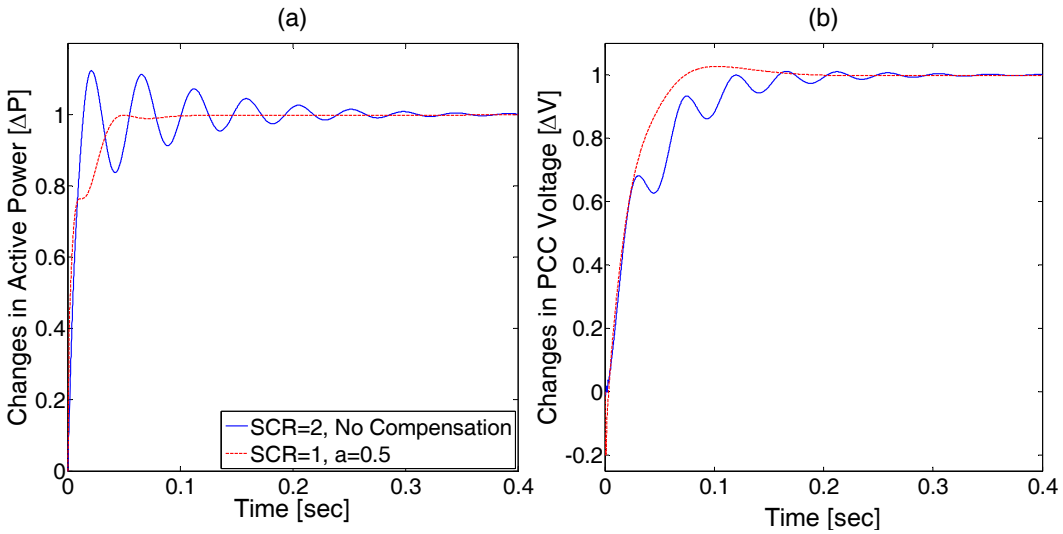

Figure 7-17 Comparing the response of conventional converter at SCR=2 with a VSC with artificial bus working at SCR=1 with a compensation factor = 0.5.

7.5.1 Injection and Absorption of Active Power

Figure 7-18 shows the situation when the reference active power changes from 1.0 pu to 1.05 pu by a step. This figure reveals that the active power tracking of the system with the proposed solutions in the very weak grid is even better than the system with SCR = 2. Even the performance of the artificial bus method is comparable to that of a relatively strong grid. However, the voltage and PLL output frequency do not act similarly. The retuned method shows less deviation in these variables; however, it takes much longer to settle. The artificial bus has almost the same deviations as the system with SCR = 2, but much faster settling can be observed. The PLL frequency returns to 0.05% vicinity of the nominal frequency in less than 3 cycles.

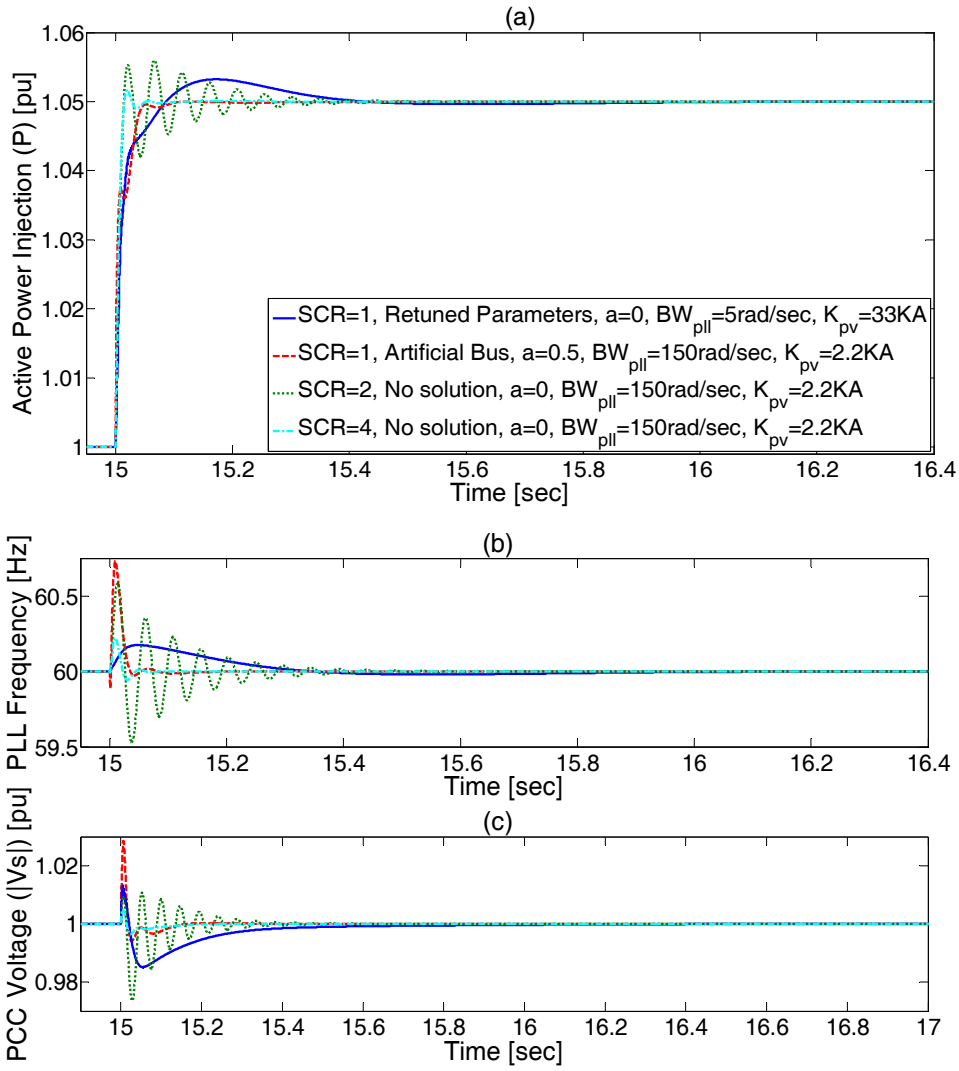

Figure 7-18 VSC performance when the reference injected power is changed from 1.0 pu to 1.05 pu by a step.

Figure 7-19 explores the absorption case where the converter is pushed to increase the sinking power from 0.8 pu to 0.85 pu by a step again. The maximum theoretical power absorption is restricted to 0.9 pu. Obviously, near the boundaries of system stability, both proposed methods still perform reliably. Moreover, in this case, the performance of the conventional controller at SCR = 2 is comparable to the performances of the proposed methods at SCR = 1. The conventional controller has a faster settling time, and its peak deviation is less than or at least comparable to that of the proposed controller. The comparing between Figure 7-18 and Figure 7-19 shows how the proposed solutions act asymmetrically

in injection and absorption. In other words, the performance of the VSC is dependent on its initial operating point in very weak grids even with the proposed solutions.

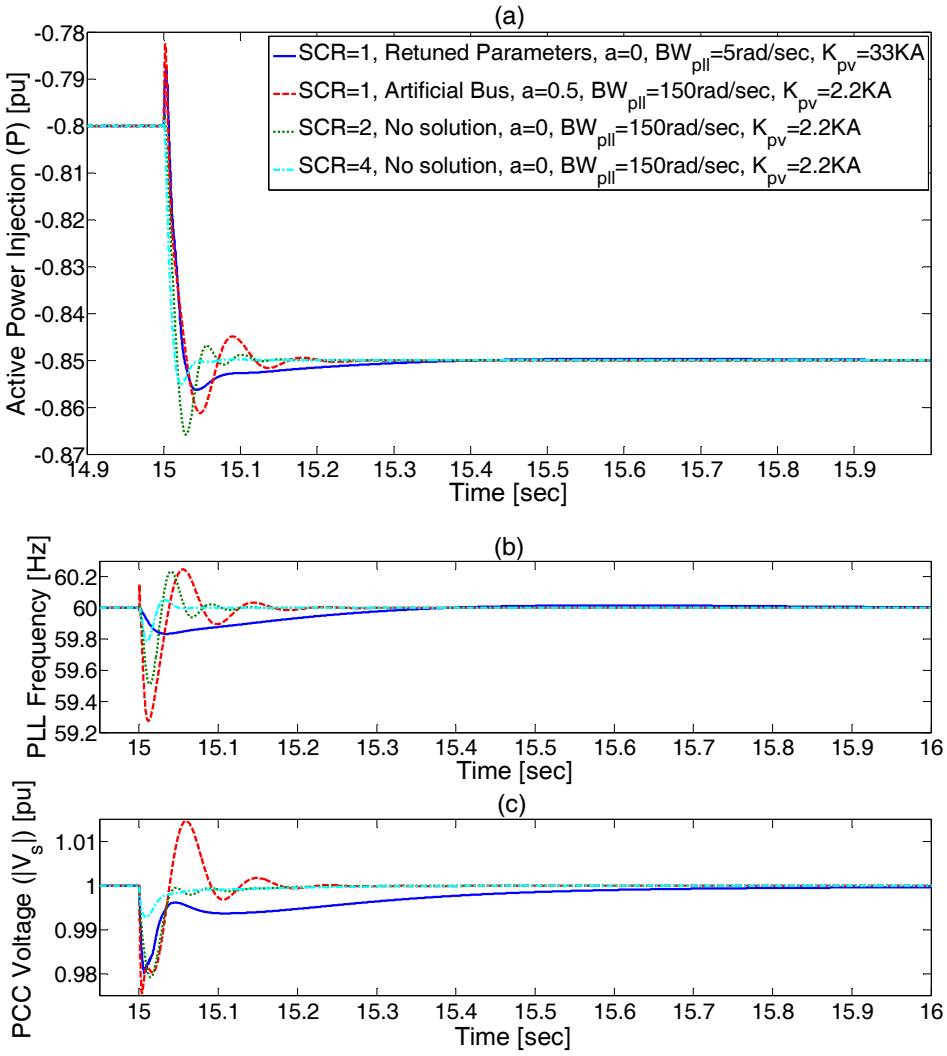

Figure 7-19 VSC performance when the reference absorbed power is changed from 0.8 pu to 0.85 pu by a step.

7.5.2 SCR Changing

In this case, a line in parallel with Z_g is considered with exactly the same impedance connected through a normally open breaker between the PCC and the grid. At t = 15 s, the breaker closes; consequently, the grid short-circuit ratio changes from 1 to 2.

As predicted by the analysis, the retuned method with a very high-speed ac-voltage regulator cannot bear the new strength of the system and becomes unstable (see the blue solid

curve in Figure 7-20(a)). For the sake of clarity, the changes of the voltage magnitude and the PLL frequency of the unstable case are omitted in parts (b) and (c).

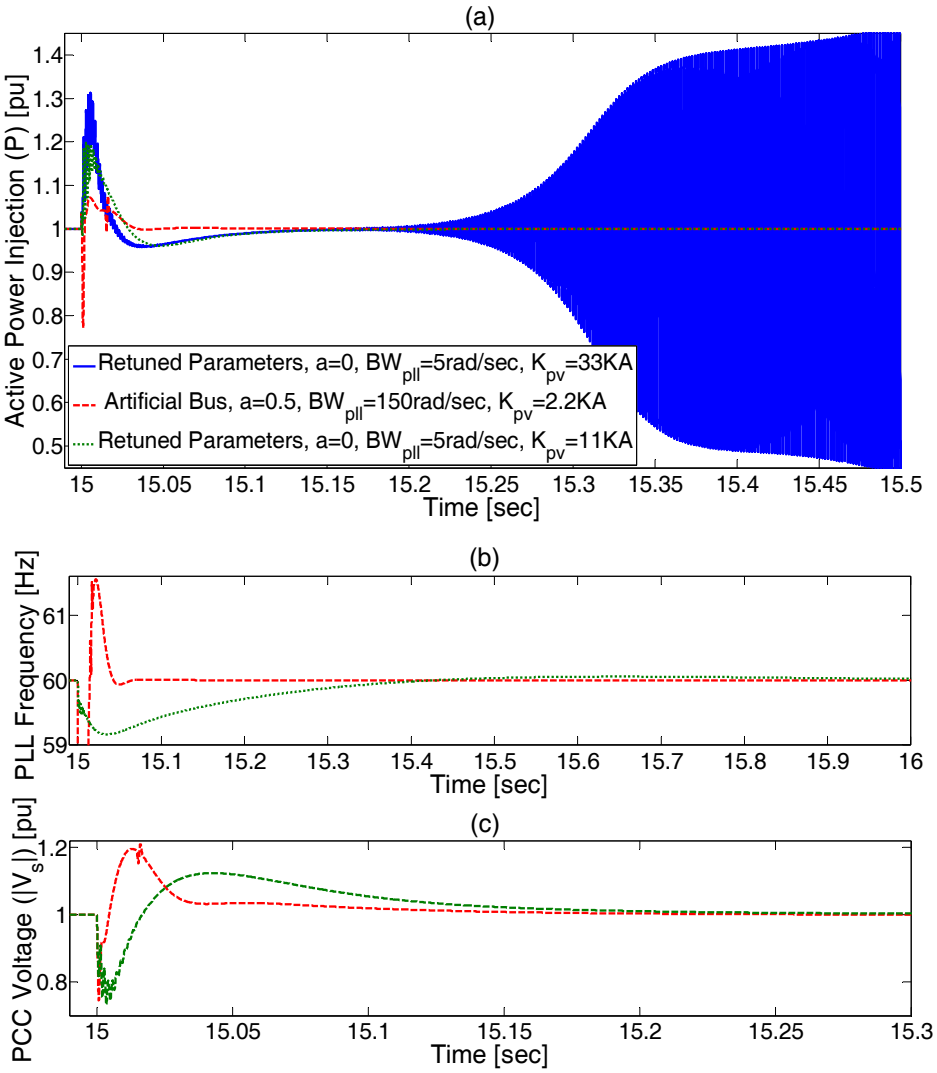

Figure 7-20 VSC performance responding to the change of SCR = 1 to SCR = 2.

The artificial bus method demonstrates its superiority in active power regulation in terms of both maximum deviation and settling time indices, even when the retuned method is stable. In the case of PLL frequency, the situation is trickier where the fast PLL of the artificial bus shows a much higher deviation. However, it returns to ±0.03 Hz of the nominal frequency in just 50 ms. The slow PLL of the retuned method takes much longer to settle in a similar vicinity to the final frequency.

The most interesting observation, however, is the PCC voltage. The much faster voltage regulator of the retuned method takes much longer to restore the voltage. Here, the impact of the slow PLL in the voltage regulator can be observed. As mentioned in the last section, in the retuned method, the PLL and ac-voltage regulator impact each other, but their response times are very different in order to minimize undesirable interactions.

7.5.3 Disturbances

The case examined here is a step change of the grid voltage magnitude from 1.0 pu to 0.9 pu. Based on the standards [91], the VSC should continue to work uninterrupted, although the grid voltage remains at this level. Figure 7-21 represents the results. The operating point is selected to be 0.9 pu instead of 1.0 pu because, based on (7-4), the maximum injectable active power decreases with a decrease in the grid voltage.

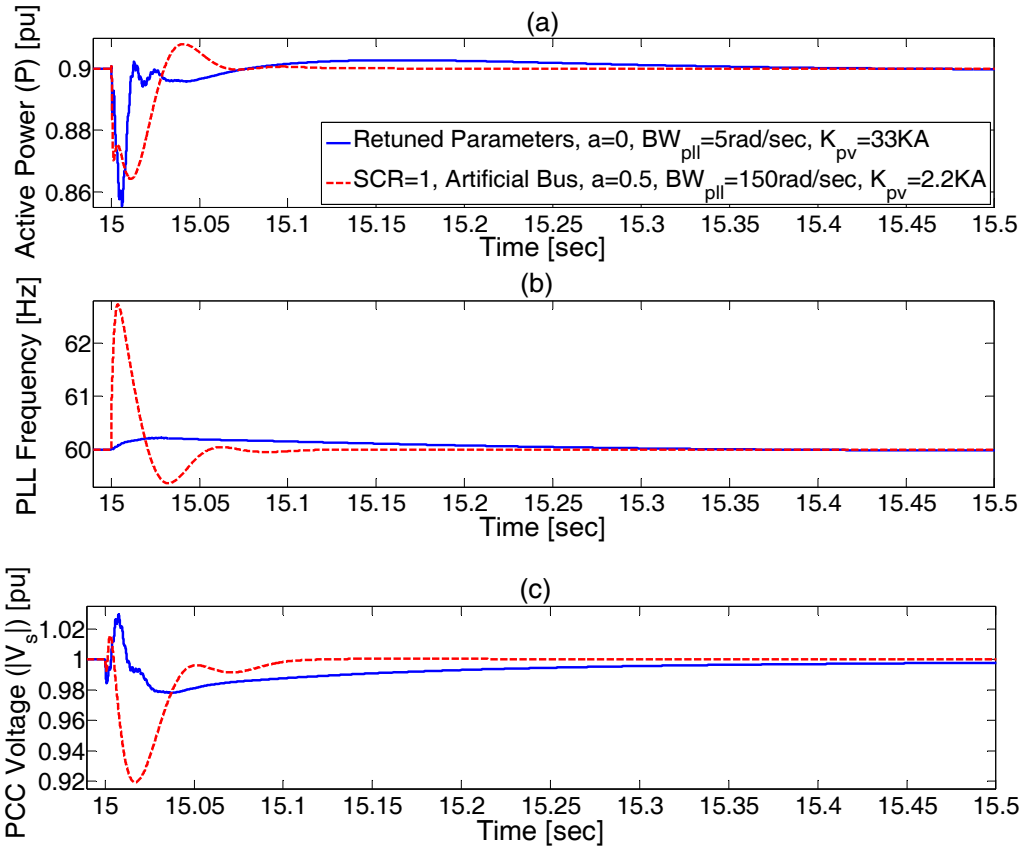

Figure 7-21 VSC responds to the sudden changes of grid voltage magnitude from 1.0 pu to 0.9 pu when SCR = 1.

Both methods show a relatively robust performance against the grid voltage. However, their performances are not similar. In active power regulation, the artificial bus experiences less deviation and settles faster, but in the cases of frequency and voltage tracking, the situation is different. Whereas the PLL of the artificial bus method deviates much more from the nominal frequency, it returns to 0.095% vicinity in less than 3.5 cycles. The same damping takes more than 39 cycles in the retuned method with its ultraslow PLL. A very similar situation can be observed in the voltage regulation, even though the ac-voltage controller of the retuned method is set to be much faster than that of the other solution.

Another possible disturbance which may threaten the VSC stability is a sudden jump in the grid phase. The phase jump should be taken seriously in this study since the PLL and tracking the voltage angle are the main sources of instability for the converters connected to very weak grids.

Figure 7-22 shows the performance of the artificial bus method when the grid voltage angle, θ_g, jumps suddenly from 0 to 10° at t=15s. Obviously, the system is very capable of rejecting the disturbance effectively. The active power injection returns to its pre-disturbance amount, 1.01 pu, in less than 100ms. A clearer picture is provided in Figure 2-1(a) where the PCC voltage angle, θ_s, with different compensation factors is compared. Increasing the compensation factor, from 0.4 to 0.8 has enhanced the VSC response; however, further increasing deteriorates the converter behavior. For a higher than or equal to 1.2 the system cannot track the phase changes properly and become unstable. This observation is important, since from the small signal analyses and without any phase jump, compensation factors as high as 1.6 do not destabilize the system.

In the rectifying mode, when the converter receives active power, the situation is similar. Figure 7-23 shows the converter responding to the same phase jump but VSC absorbs 0.89pu active power. Similarly, with proper compensation factor, such a severe disturbance is easily rejected by the converter. Like the inverter mode, high compensation factors can also destabilize the converter. However, the rectifying mode seems to be more sensitive to high values of a.

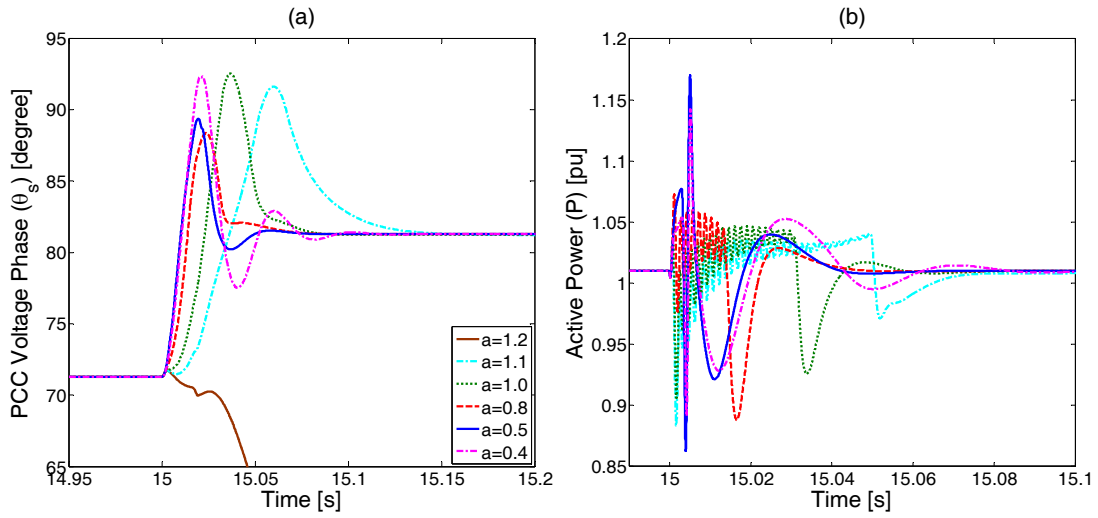

Figure 7-22 (a) The PCC voltage angle, (b) the converter output active power when a 10° phase jump at grid voltage occurs at t=15s and VSC injects 1.01 pu active power.

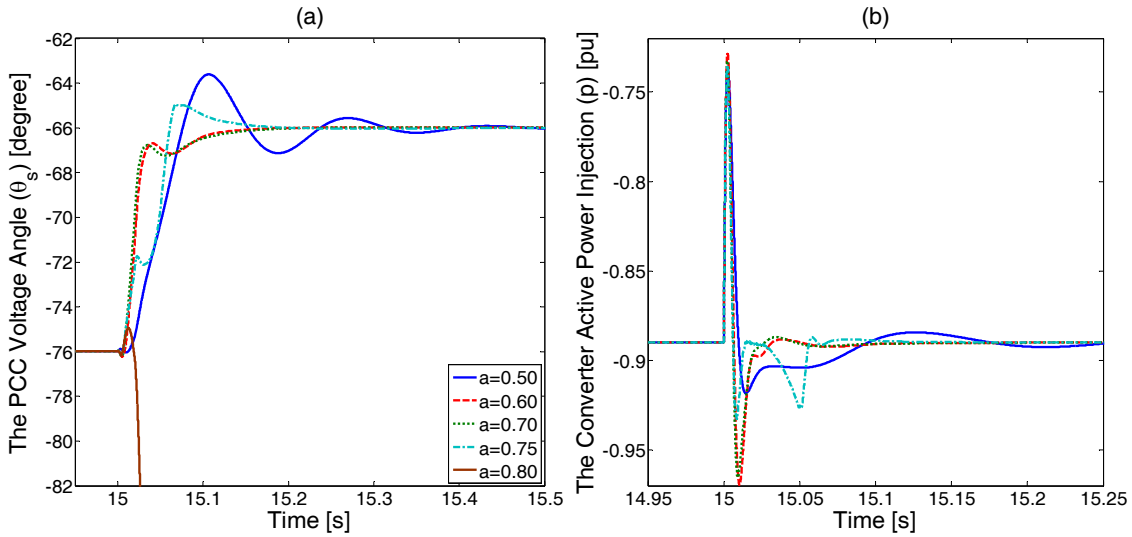

Figure 7-23 (a) The PCC voltage angle, (b) the converter output active power when a 10° phase jump at grid voltage occurs at t=15s and VSC obsorbs 0.89 pu active power.

The converter is supposed to tolerate a voltage drop to zero for 150msec. The code requires the converter to devote all its current capacity to the reactive current for a voltage drop larger than 50 percent. After the fault clearance, the active power should be restored to its pervious value with a minimum rate of 10% of its rated power.

To comply with the regulation, a fault ride through strategy is also needed. After fault detection, the ac-voltage and active power regulations should be disabled. The references for

the currents of d- and q-axes, output of those regulation units, will set to be zero and 1pu as the code dictates. However, the artificial bus method needs no enhancement and can be used with no alteration despite the method proposed by [131].

Figure 7-24 depicts the PCC voltage and the converter current when a 3-phase to ground fault happens almost at PCC bus and remains for 200ms. Despite the severity of the fault, the VSC successfully rides through it. The voltage has restored rapidly and the current never exceeds its pre-fault values.

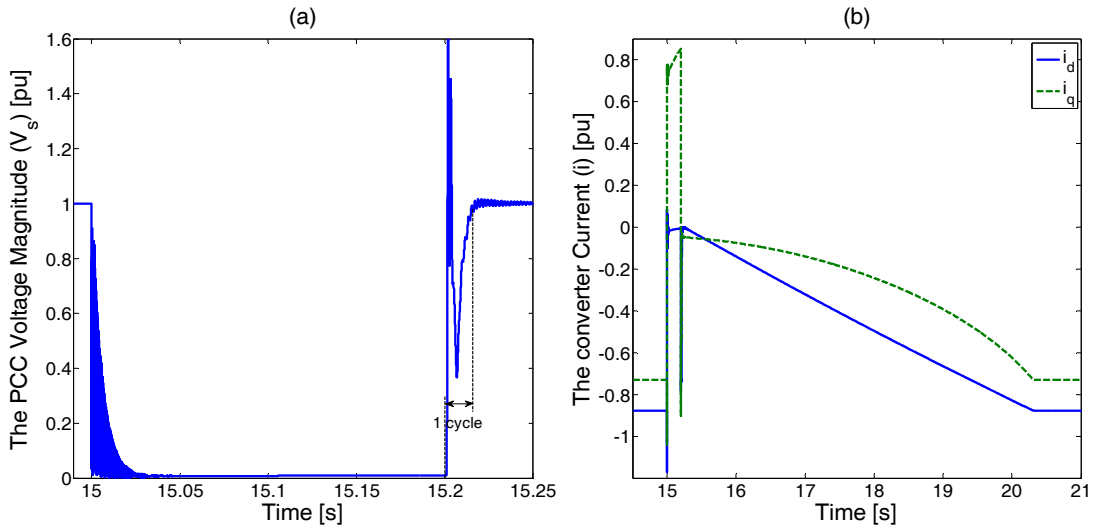

Figure 7-24 (a) PCC bus Voltage magnitude, (b) the converter output current when the 3-phase to ground fault happens almost PCC bus at t=15s and VSC injects 1.01 pu active power and utilizes the artificial bus method, a=1. Fault detection time is 1ms.

Although the PCC bus voltage and the converter current are the most important parameters to be studied in a fault, the PLL measured frequency and output power clarify the picture. Figure 7-25 reveals that the PLL rejects the disturbance in less than 6 cycles during the fault and in 3 cycles after the fault clearance. Figure 7-25(b) shows the active power whose performance is in compliance with the codes. Ignoring the unavoidable fast disappearing oscillations at the instants of fault occurrence and clearance, the active power goes to zero during the fault and restores with a 0.2pu/s rate.

Another serious scenario requiring investigation is unbalanced fault. Although references such as [100] proposed specific methods for tackling the asymmetric faults, this section only studies the robustness of the present control, with no modification, against unbalanced faults.

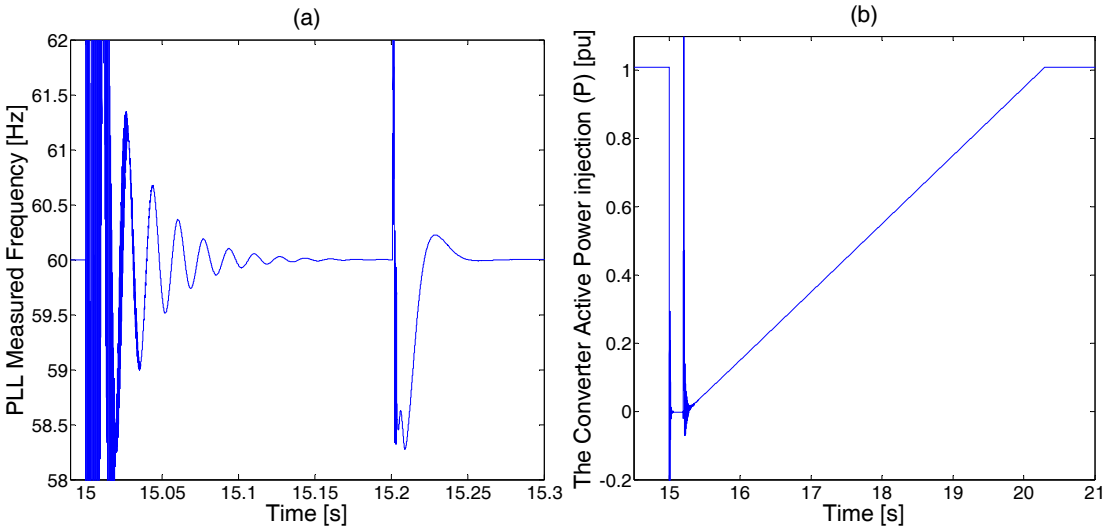

Figure 7-25 (a) PLL measured Frequency, (b) the converter output active power when the 3-phase to ground fault happens almost PCC bus at t=15s and VSC injects 1.01 pu active power and utilizes the artificial bus method, a=1. Fault detection time is 1ms.

Figure 7-26 represents the currents and the active power of the VSC when a line to line to ground fault occurs at the middle of the transmission line at t=15s. After fault detection, despite the balanced method, here the active power and ac-voltage regulation units continue to function. However, the reference active power is reduced from 1.010 to 0.337pu during fault. Since two lines are grounded, the maximum injectable active power has reduced by two-third. Not only, the converter successfully rides through the fault, but it also continues to inject the maximum possible active power during the fault. The oscillation on the currents and active power is second harmonic caused by the asymmetry of the fault.

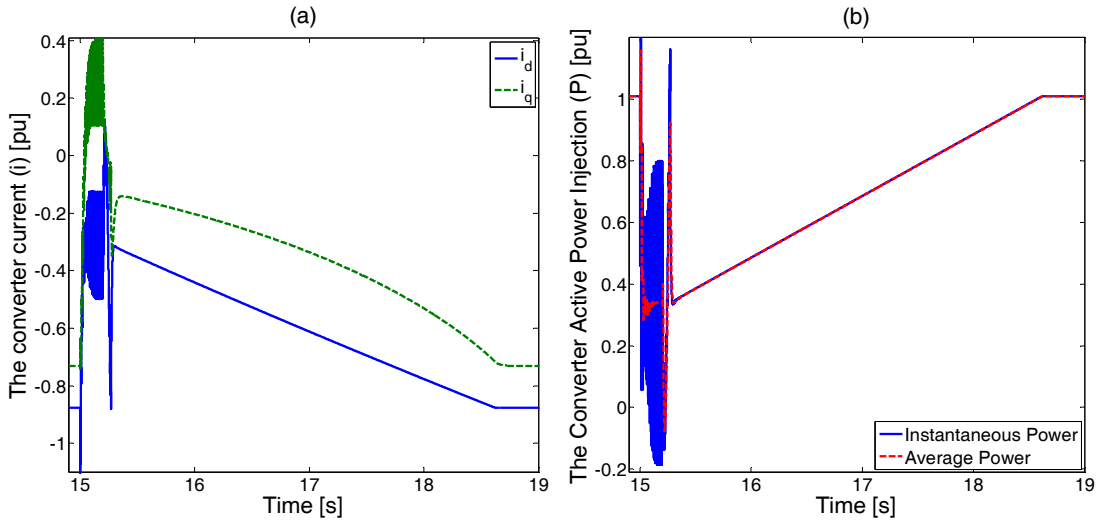

Figure 7-26 The converter (a) currents, (b) output active power when the line to line to ground fault happens at the middle of line at t=15s and VSC injects 1.01 pu active power and utilizes the artificial bus method, a=1. Fault detection time is half a cycle.

7.6 Summary

This chapter, benefiting from a comprehensive small-signal model, presented a detailed analysis of the VSC dynamics and showed how the assumptions made for designing VSC regulators in strong grids are no longer valid in very weak grids. The chapter then proposed and compared two straightforward solutions: retuning the control parameters and using an artificial bus for converter-grid synchronization. Both methods enable the VSC to operate at the maximum theoretical active power at a very weak grid condition (i.e., at unity short-circuit ratio) by minimal modification in the widely accepted vector control method. The advantages and disadvantages of each method were discussed. The analytical results were verified by detailed nonlinear time-domain simulation results. This chapter also studied the impact of severe faults and phase jump and discussed the inherent robustness of the method to fill a serious gap in the literature.

Chapter 8
Conclusions and Future Works

8.1 Research Summary and Contribution

This research focuses mainly on studying and analyzing voltage and frequency dynamics in weak grids, grids dominated by power-electronic interfaced generation or high transmission line impedances, with distributed and asymmetrical resources contributing to frequency and/or voltage stabilization. The following presents the highlights of its contributions:

In Chapter 3, the torque- and power-droop, as two conventional methods to implement droop-control in DFIG-based wind power generation units, were analyzed and compared. Small-signal analysis showed why under-speeding should be avoided and how variance of effective torque-droop could yield higher stability margins as compared to the power-droop method. Eigen-values studies (1) proved the positive impact of wind-droop on system frequency-stability; (2) showed that wind droop could compensate for the lack of inertia in microgrid in the medium-frequency range; and (3) showed the positive influence of wind-droop on turbine governor and inverter droop functions. Pitch-angle controller impact on wind-droop was also investigated; and it was found that this impact is not significant. Time-domain simulations verified all analytical results and discussions; and showed that wind power generation with autonomous frequency regulation has the ability to stabilize the frequency in an isolated microgrid. Load sharing and coordination of two wind power generation in presence of real wind speed patterns and different wind-droop method were examined.

Moreover, it was shown that the variable unpredictable reserve wind power, obtained by deloading, creates problems for implementing the present droop-based methods in wind power generators. This problem has been discussed and analyzed thoroughly in this chapter. The efficiency droop, as a new solution, was proposed to solve the problem. It was shown that (1) the proposed method can be tuned regardless of the unpredictable wind speed, similar to conventional dispatchable generators; (2) whereas changes in wind speed threaten the stability of the present droop methods, the stability of the propose method is immune; and (3)

the solution is capable of improving both transient and steady state frequency behavior as much as the present methods like power- and torque-droop can do, but this optimum behavior is independent of the wind speed and much easier to be tuned. Benefiting from small-signal analyses, analytical methods for tuning the efficiency droop were suggested, and time-domain simulations were used to verify the analyses.

A detailed model of a wind power generator considering the double-mass nature of the mechanical system, active damping controller, and frequency regulation mechanisms (droop and virtual inertia) was developed in Chapter 4. This model allowed the small-signal analysis of the frequency regulation dynamics in wind power generators as well as the characterization of the associated mechanical stresses imposed on the generator. It was shown why conventional wind generators do not suffer from these stresses and consequently have never been deeply studied. In contrast, droop and virtual inertia, as two viable frequency regulation methods, expose the mechanical system to high rates of change of torque and power, which speed up the aging process. As a conventional solution in the literature, if the ramp-rate limiter does not destabilize the system, it neutralizes the desired and expected impacts of frequency regulation. Thus, this chapter has investigated the utilization of the dc-link capacitance to respond to the fast transient part of frequency regulation dynamics, whereas the kinetic energy stored in the rotating masses is still involved in the slower yet high-energy consuming part. The management of these two sources was studied in detail. Time-domain simulation results, based on detailed nonlinear models, verified all analytical results.

The model of a wind power generator was also used to characterize the impacts of the droop and the virtual inertia on the generator mechanical resonance and the system stability, to study the mutual interactions among different wind power generators with the different frequency support controllers, and to develop stabilizing methods and compare their performance. The study showed the following. (1) Both the droop and virtual inertia methods can expose the shaft of a wind generator to forces capable of stimulating its natural resonance frequencies. (2) The mechanical resonance in a frequency-regulating wind generator should be studied as a part of the integrated power system dynamics. (3) In a system with several

wind power generators, there is a risk of amplifying the negative interactions among different generators and destabilizing the power system. (4) The dc-link bandwidth re-tuning, the active damping, and the filter methods successfully stabilize the system; however, they have different impacts on the turbine conventional performance (i.e., MPPT), the reduction in the mechanical tensions of the shaft, and the dc-link voltage regulation. (5) The filter method has the least impact on the conventional performance of MPPT and reduces the mechanical tension caused by the frequency regulation implementation. The time-domain simulation results verified the analytical results and discussions.

The modeling and analysis of a direct-drive PMSG-based wind power generator during fault and post-fault conditions were presented in Chapter 5. An analytical multi-mode model, considering the double-mass nature of the turbine/generator and typical LVRT requirements was developed and validated against the detailed nonlinear time-domain simulation results. The model was successfully used to conduct a detailed analysis to characterize the generator performance under LVRT control, and to tune the control system parameters. The analysis showed the following. (1) Using the rotating masses for storing the excessive energy during the fault can lead to over-speeding the generator. (2) An LVRT-capable PMSG can be subjected to mechanical stresses and, accordingly, faster aging, due to electrical system faults. (3) The use of the active damping method reduces the mechanical tensions at the cost of increasing the electrical stress on the dc-link capacitor. (4) The use of the dc-link voltage control bandwidth retuning reduces the mechanical stresses; however, it yields a higher electrical stress on the dc-link capacitor as compared to the active damping methods. The detailed time-domain simulation results validated the analytical results and discussions.

Chapter 6 has addressed the contribution of PHEVs in frequency regulation considering the single-phase nature of such distributed energy resources. This chapter showed why droop method could not be used instead of virtual inertia in a system which suffers from reduced inertia. It also showed analytically the disadvantages of centralized control and showed that without a dedicated communication line with negligible delay, centralized control could not be used for virtual inertia implementation. The main disadvantages of distributed control and

asymmetric power injection were discussed. It has been shown that only under low penetration levels of PHEVs, these problems could be tolerated. Then, a mitigation strategy based on a combination of centralized and distributed control, was proposed. The method allows the use of all of available sources for active and reactive power injection, and yields a solution that is much more robust to communication delay. Time-domain simulations confirm analytical results.

Chapter 6 also pertained to the proper control and coordination of wind generators and PHEVs. It was discussed that these sources can compensate for each other's drawbacks and effectively participates in the primary frequency regulation of microgrids. The coordination mechanisms of these sources were investigated in this chapter by using small-signal analysis and nonlinear time-domain simulations. The study showed the following. (1) The virtual inertia is not a suitable frequency regulation tool for the coordinated control. PHEVs do not benefit significantly from a coordinated virtual inertia, whereas the burden of the coordination is added to the system. (2) A centralized coordinated control for a droop is suitable either for a low contribution of wind-PHEVs combination to the frequency regulation or in the presence of a very fast communication system. On the other hand, the distributed coordination does not perform very effectively when uncertainties about the wind and the PHEVs are very high. (3) A distributed control can guarantee the coordination and the LPF cutoff frequency can be used as the lever to manage the wind turbine mechanical tension while the PHEVs are regulated locally without needing a fast communication infrastructure.

By employing detailed small-signal analysis, the concerns about connecting a VSC to a very weak grid were described, and straightforward solutions were proposed and compared in Chapter 7. This chapter showed the following. (1) In a very weak grid, the active power, voltage regulators, and PLL interfere with one another's functions much more than they do in the strong grid cases, so that their independent tuning does not lead to the desired results. (2) By retuning the VSC controllers, parameters reaching the maximum theoretical active power injection/absorption are possible, as opposed to claims in the present literature. (3) The retuned method uses very fast voltage regulation and a very slow PLL, which can make it

sensitive, or even unstable, to a change of SCR in the system. In addition, this method's utilization necessitates the complete modeling of the VSC. (4) By selecting an artificial bus between the real PCC and the grid as a reference point of the PLL, the VSC controller can operate as if it is facing a strong enough system. (5) The proposed method achieves the goal of maximum active power injection and absorption and is robust against changes of the system SCR. This advantage allows the regulators of the VSC to be designed independently. Detailed nonlinear time-domain simulations verified the analytical results and the effectiveness of the proposed solutions. This chapter also investigated the behavior of the method when a phase jump happens at the grid source. It was shown that by proper tuning of the compensation factor the VSC remains stable. This study proved that the proposed method is capable of riding through severe balanced faults. Such a robust performance of the artificial bus method, in addition to its straight forward idea and simplicity, makes this idea superior over alternatives methods.

8.2 Directions for Future Work

In continuation of this work, the following subjects are suggested for future studies:

- *Cyber-Physical Control and Security for Smart Microgrids*: Web-enabled communication and Internet of Things have been used to provide a new solution for smart grids: Internet of Energy. This concept can be used to effectively utilize the controllable loads and renewable energies to put an end to the stability concerns of microgrids. It is necessary to design a new control method to employ effective communication system to use all available resources in a microgrid properly. The controller should consider the practical limits of cyber system as well as physical power system to guarantee the stability, reliability and efficiency.
- *Multi-Microgrid Control and Operation*: Because the fast growth of renewable energy sources in LV networks, distribution systems are turning into active grids capable of constituting microgrids. These advances have resulted in developing the concept of the microgrid into the amazing but complex multi-microgrid. Such a system faces much more complicated operational and control issues, which have

recently gained attention in the literature. It is useful to study and design control methods incorporating the distributed nature of sources, and different levels of control to improve the stability, reliability and performance of these systems.

- *Adopting Demand-Side Management in Smart Grid Stabilization*: High penetration of distributed energy storage and controllable loads in smart grids has led researchers to use Demand Side Management (DSM) as an effective solution for future grids. However, most of their studies have focused on economy and optimizing the energy consumption and ignored the important role DSM could play in stabilizing smart grids and/or the special conditions of DSM, such as limitations of communication and different load dynamics. Another path for future studies is focusing on thoroughly analyzing and improving the stability of smart grids by using DSM.
- *Hybrid AC/DC-(Micro)Grids*: The utilization of electronic interfaces in both generation and demand in grids has increased, and power electronics has improved so much that dc-grids in both transmission and distribution have become practical assumption. These dc-microgrids will be added to the existing ac-grids. The resulting interaction needs to be studied, analyzed and, most probably, improved.

Bibliography

[1] "La aportación de la energía eólica a la red marca un nuevo récord," economica.elpais.com, 7 November 2011.

[2] "New record-breaking year for Danish wind power," ENERGINET Offical Website, 2016.

[3] "Global wind energy outlook 2016," Global Wind Energy Council, 2017.

[4] R. Iyengar, "The Netherlands Just Got One Step Closer to Eliminating Polluting Vehicles," Time, 18 April 2016.

[5] A. Neslen, "Plans for an electric car charging point in every new home in Europe," The Guardian, 11 October 2016.

[6] "Global Plug-in Sales for 2016," EVvolumes.com, 2017.

[7] M. McDiarmid, "Liberals keep most of their green election promises in 1st budget," CBC News, 22 March 2016.

[8] A. Stephenson, "Alberta wind industry praises NDP plan for renewable power procurement," Calgary Herald, 3 November 2016.

[9] "Wind Vision 2025: Powering Canada's Future," Canadian Wind Energy Association.

[10] "Eligible Electric Vehicles under the Electric Vehicle Incentive Program and Electric Vehicle Incentives," Ontario Ministry of Transportation, 2017.

[11] "Community Charging Infrastructure (CCIF) Fund Overview & Results," The Plug in BC Collaboration, 2014.

[12] "Vancouver's EV Ecosystem Strategy," City of Vancouver, Novbember 2016.

[13] "Smart Grids in Distribution Networks: Roadmap Development and Implementation," International Energy Agency, 2015.

[14] G. Prasad, "Draft National Policy on RE based Mini/Micro grids," The Ministry of New and Renewable Energy of India, 2016.

[15] "Reforming the Energy Vision," New York State Department of Public Services, 2017.

[16] J.-P. Pinard, S. Banjac, J. Maissan and S. Rahemtulla, "Potential for Wind Energy in Nunavut Communities," Prepared for Qulliq Energy Corporation, 2016.

[17] I. Baring-Gould and M. Dabo, "Technology, Performance, and Market Report of Wind-Diesel Applications for Remote and Island Communities," National Renewable Energy Laboratory, 2009.

[18] B. Muhando, K. Keith and G. Holdmann, "Evaluation of the ability of inverters to stabilize high penetration wind-diesel systems in diesel-off mode using simulated components in a test bed facility," Prepared for the Denali Commission under the Emerging Energy Technologies Grant Fund, September 2010.

[19] P. Gardner, H. Snodin, A. Higgins and S. McGoldrick, "The Impacts of Increased Levels of Wind Penetration on The Electricity Systems of The Republic of Ireland and Nortern Ireland: Final Report," Prepared for Commission for Energy Regulation/OFREG NI, 2003.

[20] G. Hutchens, "Malcolm Turnbull says South Australia blackout a wake-up call on renewables," The Gaurdian, 29 September 2016.

[21] K. Murphy, "Malcolm Turnbull was told gas plant shut down before South Australia blackout," The Guardian, 13 February 2017.

[22] P. Gilman, B. Maurer, L. Feinberg, A. Duerr, L. Peterson, W. Musial, P. Beiter, J. Golladay, J. Stromberg, I. Johnson, D. Boren and A. Moore, "National Offshore Wind Strategy," U.S. Department of Energy, 2016.

[23] "UK to Remain Top Offshore Wind Power Market by 2025, with Capacity Exceeding 23 Gigawatts, says GlobalData," GlobalData, 22 July 2015.

[24] "The European offshore wind industry: Key trends and statistics 2016," WindEurope, 2017.

[25] A. Jones, "Ontario signals moratorium on offshore wind projects will continue for years," The Globe and Mail, 13 February 2017.

[26] C. Schwägerl, "Europe's offshore wind industry booming as costs fall," The Guardian, 20 October 2016.

[27] Z. Dubinsky, "Electric car sales seem poised for big jump: Can our grid take the load?," CBC News, 10 April 2016.

[28] A. Breitenbach, "Battery Second Use Offsets Electric Vehicle Expenses, Improves Grid Stability," National Renewable Energy Laboratory, 22 June 2015.

[29] T. Eichner, "Helping Fort Carson Meet DOD Energy Goals," *Continuum,* no. 7, pp. 22-23, Fall 2014.

[30] "Nissan and Enel launch groundbreaking vehicle-to-grid project in the UK," Nissan GB, London (UK), 10 May 2016.

[31] "Reliability considerations from the integration of smart grid," North American Electric Relibility Corporation (NERC), December 2010.

[32] "Intelligrid program: 2012 annual review," Electric Power Research Institute (EPRI), 2013.

[33] P. Jones, "The role of new technologies: A power engineering equipment supply base perspective," Grid Policy Workshop, Paris, France , 2010.

[34] B. A. Hamilton, J. Miller and B. Renz, "Understanding the Benefits of the Smart Grid: Smart Grid Implementation Strategy," National Energy Technology Laboratory, 18 June 2010.

[35] T. Bhattacharya and L. Umanand, "Negative sequence compensation within fundamental positive sequence reference frame for a stiff micro-grid generation in a wind power system using slip ring induction machine," *IET Electric Power Application,* vol. 3, no. 6, pp. 520-530, 2009.

[36] "20% Wind Energy by 2030: Increasing Wind Energy's Contribution to U.S. Electricity Supply," U. S. Department of Energy, Washington, DC, July 2008.

[37] K. Morrow, D. Karner and J. Francfort, "Plug-in hybrid electric vehicle charging infrastructure review," US Deparment of Energy - Vehicle Technologies Program, 2008.

[38] P. Mitra and G. Venayagamoorthy, "Wide area control for improving stability of a power system with plug-in electric vehicles," *Generation, Transmission & Distribution,* vol. 4, no. 10, pp. 1151-1163, October 2010.

[39] G. Venayagamoorthy, P. Mitra, K. Corzine and C. Huston, "Real-time modeling of distributed plug-in vehicles for V2G transactions," in *IEEE Energy Conversion Congress and Exposition (ECCE)*, San Jose, CA, USA, 2009.

[40] P. Mitra, G. Venayagamoorthy and K. Corzine, "SmartPark as a Virtual STATCOM," *IEEE Transsctions on Smart Grid,* vol. 2, no. 3, pp. 445-455, September 2011.

[41] G. Venayagamoorthy and P. Mitra, "SmartPark Shock Absorbers for Wind Farms," *IEEE Transactions on Energy Conversion,* vol. 26, no. 3, pp. 990-992, September 2011.

[42] H. Polinder, F. F. A. van der Pijl, G. J. de Vilder and P. J. Tavner, "Comparison of direct-drive and geared generator concepts for wind turbines," *IEEE Transactions on Energy Conversion,* vol. 21, no. 3, pp. 725-733, September 2006.

[43] G. Ramtharan, J. B. Ekanayake and N. Jenkins, "Frequency support from doubly fed induction generator wind turbines," *IET Renewable Power Generation,* vol. 1, no. 1, pp. 3-9, March 2007.

[44] V. Courtecuisse, M. El-Mokadem, C. Saudemont, B. Robyns and J. Deuse, "Experiment of a wind generator participation to frequency control," in *Wind Power to the Grid - EPE Wind Energy Chapter 1st Seminar*, Delft, Netherlands, March 2008.

[45] B. H. Chowdhury and H. T. Ma, "Frequency regulation with wind power plants," in *IEEE Power and Energy Society General Meeting - Conversion and Delivery of Electrical Energy in the 21st Century*, Pittsburg, USA, July 2008.

[46] R. G. de Almeida, E. D. Castronuovo and J. A. Peas Lopes, "Optimum generation control in wind parks when carrying out system operator requests," *IEEE Transactions on Power Systems,* vol. 21, no. 2, pp. 718-725, May 2006.

[47] M. Shahabi, M. R. Haghifam, M. Mohamadian and S. A. Nabavi-Niaki, "Microgrid dynamic performance improvement using a doubly fed induction wind generator," *IEEE Transactions on Energy Conversion,* vol. 24, no. 1, pp. 137-145, March 2009.

[48] J. Morren, J. Pierik and S. W. H. de Haan, "Inertial response of variable speed wind turbines," *Electric Power Systems Research,* vol. 76, no. 11, pp. 980-987, July 2006.

[49] L. Wu and D. G. Infield, "Towards an assessment of power system frequency support from wind plant—Modeling aggregate inertial response," *IEEE Transactions on Power System,* vol. 28, no. 3, pp. 2283-2291, August 2013.

[50] M. F. M. Arani and E. El-Saadany, "Implementing Virtual Inertia in DFIG-Based Wind Power Generation," *IEEE Transactions on Power Systems,* vol. 28, no. 2, pp. 1373-1384, May 2013.

[51] A. Teninge, C. Jecu, D. Roye, S. Bacha, J. Duval and R. Belhomme, "Contribution to frequency control through wind turbine inertial energy storage," *IET Renewable Power Generation,* vol. 3, no. 3, pp. 358-370, September 2009.

[52] E. Loukarakis, I. Margaris and P. Moutis, "Frequency control support and participation methods provided by wind generation," in *IEEE Electrical Power & Energy Conference (EPEC)*, Montreal, Canada, 2009.

[53] M. Fazeli, G. M. Asher, C. Klumpner and L. Yao, "Novel integration of DFIG-based wind generators within microgrids," *IEEE Trans. on Energy Conversion, vol. 26, pp. , 2011.,* vol. 26, no. 3, pp. 840-850, September 2011.

[54] D. Boëda, A. Teninge, D. Roye, S. Bacha and R. Belhomme, "Contribution of wind farms to frequency control and network stability," in *European Wind Energy Conference and Exhibition*,

Milan, Italy, 2007.

[55] H. Ye, W. Pei and Z. Qi, "Analytical Modeling of Inertial and Droop Responses From a Wind Farm for Short-Term Frequency Regulation in Power Systems," *IEEE Transactions on Power Systems,* vol. 31, no. 5, pp. 3414-3423, September 2016.

[56] J. Van de Vyver, J. D. M. De Kooning, B. Meersman, L. Vandevelde and T. L. Vandoorn, "Droop Control as an Alternative Inertial Response Strategy for the Synthetic Inertia on Wind Turbines," *IEEE Trans. on Power Systems,* vol. 31, no. 2, pp. 1129-1138, March 2016.

[57] Y. Tan, L. Meegahapola and K. M. Muttaqi, "A Suboptimal Power-Point-Tracking-Based Primary Frequency Response Strategy for DFIGs in Hybrid Remote Area Power Supply Systems," *IEEE Transactions on Energy Conversion,* vol. 31, no. 1, pp. 93-105, March 2016.

[58] S. Ghosh, S. Kamalasadan, N. Senroy and J. Enslin, "Doubly Fed Induction Generator (DFIG)-Based Wind Farm Control Framework for Primary Frequency and Inertial Response Application," *IEEE Transactions on Power Systems,* vol. 31, no. 3, pp. 1861-1871, May 2016.

[59] S. M. Ashabani and Y. A.-R. I. Mohamed, "General Interface for Power Management of Micro-Grids Using Nonlinear Cooperative Droop Control," *IEEE Transactions on Power Systems,* vol. 28, no. 3, pp. 2929-2941, August 2013.

[60] Y. A.-R. I. Mohamed and E. F. El-Saadany, "Adaptive Decentralized Droop Controller to Preserve Power Sharing Stability of Paralleled Inverters in Distributed Generation Microgrids," *IEEE Transactions on Power Electronics,* vol. 23, no. 6, pp. 2806-2816, November 2008.

[61] J. Chen, L. Wang, L. Diao, H. Du and Z. Liu, "Distributed Auxiliary Inverter of Urban Rail Train—Load Sharing Control Strategy Under Complicated Operation Condition," *IEEE Transactions on Power Electronics,* vol. 31, no. 3, pp. 2518-2529, March 2016.

[62] C. Gavriluta, J. I. Candela, J. Rocabert and A. R. P. Luna, "Adaptive Droop for Control of Multiterminal DC Bus Integrating Energy Storage," *IEEE Transactions on Power Delivery,* vol. 30, no. 1, pp. 16-24, February 2015.

[63] H. Liu, Z. Hu, Y. Song and J. Lin, "Decentralized Vehicle-to-Grid Control for Primary Frequency Regulation Considering Charging Demands," *IEEE Transactions on Power Systems,* vol. 28, no. 3, pp. 3480-3489, August 2013.

[64] L. Y. Lu and C. C. Chu, "Consensus-based P-f /Q-V droop control in autonomous micro-grids with wind generators and energy storage systems," in *IEEE PES General Meeting*, National

Harbor, MD, 2014.

[65] A. Maknouninejad, Z. Qu, F. L. Lewis and A. Davoudi, "Optimal, Nonlinear, and Distributed Designs of Droop Controls for DC Microgrids," *IEEE Transactions on Smart Grid,* vol. 5, no. 5, pp. 2508-2516, September 2014.

[66] C. A. Hernandez-Aramburo, T. C. Green and N. Mugniot, "Fuel consumption minimization of a microgrid," *IEEE Transactions on Industry Applications,* vol. 41, no. 3, pp. 673-681, May-June 2005.

[67] A. Elrayyah, F. Cingoz and Y. Sozer, "Construction of Nonlinear Droop Relations to Optimize Islanded Microgrid Operation," *IEEE Transactions on Industry Applications,* vol. 51, no. 4, pp. 3404-3413, July-August 2015.

[68] F. Cingoz, A. Elrayyah and Y. Sozer, "Plug-and-Play Nonlinear Droop Construction Scheme to Optimize Islanded Microgrid Operations," *IEEE Transactions on Power Electronics,* vol. 32, no. 4, pp. 2743-2756, April 2017.

[69] A. M. Egwebe, M. Fazeli, P. Igic and P. M. Holland, "Implementation and Stability Study of Dynamic Droop in Islanded Microgrids," *IEEE Transactions on Energy Conversion,* vol. 31, no. 3, pp. 821-832, September 2016.

[70] F. Cingoz, A. Elrayyah and Y. Sozer, "Optimized Resource Management for PV–Fuel-Cell-Based Microgrids Using Load Characterizations," *IEEE Transactions on Industry Applications,* vol. 52, no. 2, pp. 1723-1735, March-April 2016.

[71] J. Lee, E. Muljadi, P. Srensen and Y. C. Kang, "Releasable Kinetic Energy-Based Inertial Control of a DFIG Wind Power Plant," *IEEE Transactions on Sustainable Energy,* vol. 7, no. 1, pp. 279-288, January 2016.

[72] M. Hwang, E. Muljadi, J. W. Park, P. Sørensen and Y. C. Kang, "Dynamic Droop–Based Inertial Control of a Doubly-Fed Induction Generator," *IEEE Transactions on Sustainable Energy,* vol. 7, no. 3, pp. 924-933, July 2016.

[73] O. D. Mipoung, L. A. C. Lopes and P. Pillay, "Frequency Support From a Fixed-Pitch Type-2 Wind Turbine in a Diesel Hybrid Mini-Grid," *IEEE Transactions on Sustainable Energy,* vol. 5, no. 1, pp. 110-118, January 2014.

[74] K. V. Vidyanandan and N. Senroy, "Primary frequency regulation by deloaded wind turbines using variable droop," *IEEE Transactions on Power Systems,* vol. 28, no. 2, pp. 837-846, May

2013.

[75] Y. Zhang and B. T. Ooi, "Stand-alone doubly-fed induction generators (DFIGs) with autonomous frequency control," *IEEE Transactions on Power Delivery,* vol. 28, no. 2, pp. 752-760, April 2013.

[76] M. F. M. Arani and Y. A.-R. I. Mohamed, "Analysis and Impacts of Implementing Droop Control in DFIGs on Microgrid/Weak-Grid Stability," *IEEE Transactions on Power Systems,* vol. 30, no. 1, pp. 385-396, January 2015.

[77] S. De Rijcke, P. Tielens, B. Rawn, D. Van Hertem and J. Driesen, "Trading Energy Yield for Frequency Regulation: Optimal Control of Kinetic Energy in Wind Farms," *IEEE Transactions on Power Systems,* vol. 30, no. 5, pp. 2469-2478, September 2015.

[78] I. D. Margaris, S. A. Papathanassiou and N. D. Hatziargyriou, "Frequency Control in Autonomous Power Systems With High Wind Power Penetration," *IEEE Transactions on Sustainable Energy,* vol. 3, no. 2, pp. 189-199, April 2012.

[79] N. Soni, S. Doolla and M. C. Chandorkar, "Improvement of Transient Response in Microgrids Using Virtual Inertia," *IEEE Transactions on Power Delivery,* vol. 28, no. 3, pp. 1830-1838, July 2013.

[80] M. Kayikci and J. V. Milanović, "Dynamic Contribution of DFIG-Based Wind Plants to System Frequency Disturbances," *IEEE Transactions on Power Systems,* vol. 24, no. 2, pp. 859-867, May 2009.

[81] Y. Wang, G. Delille, H. Bayem, X. Guillaud and B. Francois, "High Wind Power Penetration in Isolated Power Systems—Assessment of Wind Inertial and Primary Frequency Responses," *IEEE Transactions on Power Systems,* vol. 28, no. 3, pp. 2412-2420, August 2013.

[82] F. D. Kanellos and N. D. Hatziargyriou, "Optimal control of variable speed wind turbines in islanded mode of operation," *IEEE Transactions on Energy Conversion,* vol. 25, no. 4, pp. 1142-1151, December 2010.

[83] G. Hughes, "The performance of wind farms in the United Kingdom and Denmark," Renewable Energy Foundation, London, UK, 2012.

[84] F. D. Kanellos and N. D. Hatziargyriou, "Control of Variable Speed Wind Turbines in Islanded Mode of Operation," *IEEE Transactions on Energy Conversion,* vol. 23, no. 2, pp. 535-543, June 2008.

[85] F. D. Kanellos and N. D. Hatziargyriou, "Control of variable speed wind turbines equipped with synchronous or doubly fed induction generators supplying islanded power systems," *IET Renewable Power Generation,* vol. 3, no. 1, pp. 96-108, March 2009.

[86] K. Clark, N. W. Miller and J. J. Sanchez-Gasca, "Modeling of GE wind turbine-generators for grid studies," General Electric International, Technical Report , 2010.

[87] H. Geng, D. Xu, B. Wu and G. Yang, "Active damping for PMSG-based WECS with DC-link current estimation," *IEEE Transactions on Industrial Electronics,* vol. 58, no. 4, pp. 1110-1119, April 2011.

[88] A. D. Hansen and G. Michalke, "Modelling and control of variable-speed multi-pole permanent magnet synchronous generator wind turbine," *Wind Energy,* no. 11, p. 537–554, 2008.

[89] V. Akhmatov, "Analysis of dynamic behaviour of electric power systems with large amount of wind power," PhD Dissertation, Electric Power Engineering, Technical University of Denmark, , Ørsted-DTU, 2003.

[90] T. Ackermann, Wind power in power systems: Vol. 140., Chichester, UK: John Wiley, 2005.

[91] "Grid Code: High and Extra High Voltage," E. ON Netz GmbH, Germany, Apr. 2006.

[92] S. M. Muyeen, R. Takahashi, T. Murata and J. Tamura, "A variable speed wind turbine control strategy to meet wind farm grid code requirements," *IEEE Transactions Power Systems,* vol. 25, no. 1, pp. 331-340, February 2010.

[93] R. Cardenas, R. Pena, S. Alepuz and G. Asher, "Overview of control systems for the operation of DFIGs in wind energy applications," *IEEE Transactions Industrial Electronics,* vol. 60, no. 7, pp. 2776-2798, July 2013.

[94] L. Zhou, J. Liu and S. Zhou, "Improved Demagnetization Control of a Doubly-Fed Induction Generator Under Balanced Grid Fault," *IEEE Transactions on Power Electronics,* vol. 30, no. 10, pp. 6695-6705, December 2015.

[95] D. Xie, Z. Xu, L. Yang, J. Østergaard, Y. Xue and K. P. Wong, "A Comprehensive LVRT Control Strategy for DFIG Wind Turbines With Enhanced Reactive Power Support," *IEEE Transactions on Power Systems,* vol. 28, no. 3, pp. 3302-3310, August 2013.

[96] P. Li, Y. D. Song, D. Y. Li, W. C. Cai and K. Zhang, "Control and Monitoring for Grid-Friendly Wind Turbines: Research Overview and Suggested Approach," *IEEE Transactions on Power Electronics,* vol. 30, no. 4, pp. 1979-1986, April 2015.

[97] J. F. Conroy and R. Watson, "Low-voltage ride-through of a full converter wind turbine with permanent magnet generato," *IET Renewable Power Generation,* vol. 1, no. 3, pp. 182-189, September 2007.

[98] V. Yaramasu, B. Wu, S. Alepuz and S. Kouro, "Predictive control for low-voltage ride-through enhancement of three-level-boost and NPC-converter-based PMSG wind turbine," *IEEE Transactions on Industrial Electronics,* vol. 61, no. 12, pp. 6832-6843, December 2014.

[99] S. Alepuz, A. Calle, S. Busquets-Monge, S. Kouro and B. Wu, "use of stored energy in PMSG rotor inertia for low-voltage ride-through in back-to-back NPC converter-based wind power systems," *IEEE Transactions on Industrial Electronics,* vol. 60, no. 5, pp. 1787-1796, May 2013.

[100] K. H. Kim, Y. C. Jeung, D. C. Lee and H. G. Kim, "LVRT Scheme of PMSG Wind Power Systems Based on Feedback Linearization," *IEEE Transactions on Power Electronics,* vol. 27, no. 5, pp. 2376-2384, May 2012.

[101] H. Geng and D. Xu, "Stability analysis and improvements for variable-speed multipole PMSG-based wind energy conversion system," *IEEE Transactions on Sustainable Energy,* vol. 2, no. 4, pp. 459-467, October 2011.

[102] A. Hansen and G. Michalke, "Multi-pole PMSG wind turbines' grid support capability in uninterrupted operation during grid faults," *IET Renewable Power Generation,* vol. 3, no. 3, pp. 333-348, September 2009.

[103] J. de Jesus Barradas-Berglind, R. Wisniewski and M. Soltani, "Fatigue damage estimation and data-based control for wind turbines," *IET Control Theory & Applications,* vol. 9, no. 7, pp. 1042-1050, May 2015.

[104] M. Jackson and S. Umans, "Turbine-generator shaft torques and fatigue: part III - refinements to fatigue model and test results," *IEEE Transactions on Power Apparatus and Systems,* Vols. PAS-99, no. 3, pp. 1259-1268, May 1980.

[105] P. Pourbeik, D. Ramey, N. Abi-Samra, D. Brooks and A. Gaikwad, "Vulnerability of large steam turbine generators to torsional interactions during electrical grid disturbances,"," *IEEE Transactions on Power Systems,* vol. 22, no. 3, pp. 1250-1258, August 2007.

[106] M. Molinas, J. Suul and T. Undeland, "Extending the life of gear box in wind generators by smoothing transient torque with STATCOM," *IEEE Transactions on Industrial Electronics,*

vol. 57, no. 2, pp. 476-484, February 2010.

[107] H. Xu, H. Xu, L. Chen and J. Wenske, "Active damping control of DFIG wind turbines during fault ride through,"," in *3rd International Conference on Electric Power and Energy Conversion Systems (EPECS)*, Istanbul, Turkey, October 2013.

[108] "HVDC projects listing," IEEE Transmission and Distribution Committee, 2012.

[109] P. Bresesti, W. L. Kling, R. L. Hendriks and R. Vailati, "HVDC connection of offshore wind farms to the transmission system," *IEEE Transactions on Energy Conversion,* vol. 22, no. 1, pp. 37-43, March 2007.

[110] V. Akhmatov, M. Callavik, C. M. Franck, S. E. Rye, T. Ahndorf, M. K. Bucher, H. Muller, F. Schettler and R. Wiget, "Technical Guidelines and Prestandardization Work for First HVDC Grids," *IEEE Transactions on Power Delivery ,* vol. 29, no. 1, pp. 327 - 335, February 2014.

[111] B. Franken and G. Andersson, "Analysis of HVDC converters connected to weak AC systems,"," *IEEE Transactions on Power Systems,* vol. 5, no. 1, pp. 235-242, February 1990.

[112] Y. Li, L. Luo, C. Rehtanz, S. Ruberg and F. Liu, "Realization of reactive power compensation near the LCC-HVDC converter bridges by means of an inductive filtering method," *IEEE Transactions on Power Electronics ,* vol. 27, no. 9, pp. 3908-3923, September 2012.

[113] N. Flourentzou, V. Agelidis and G. Demetriades, "VSC-based HVDC power transmission systems: An overview," *IEEE Transactions onPower Electronics,* vol. 24, no. 3, pp. 592-602, March 2009.

[114] P. Mitra, L. Zhang and L. Harnefors, "Offshore wind integration to a weak grid by VSC-HVDC links using power-synchronization control: A Case Study," *IEEE Transactions on Power Delivery,* vol. 29, no. 1, pp. 453-461, February 2014.

[115] N. P. W. Strachan and D. Jovcic, "Stability of a Variable-speed permanent magnet wind generator with weak AC grids," *IEEE Transactions on Power Delivery,* vol. 25, no. 4, pp. 2779-2788, October 2010.

[116] J. Z. Zhou, H. Ding, S. Fan, Y. Zhang and A. M. Gole, "Impact of short-circuit ratio and phase-locked-loop parameters on the small-signal behavior of a VSC-HVDC converter," *IEEE Transactions on Power Delivery,* vol. 29, no. 5, pp. 2287-2296, Oct. 2014.

[117] S.-K. Chung, "A phase tracking system for three phase utility interface inverters," *IEEE Transactions on Power Electronics,* vol. 15, no. 3, pp. 431-438 , May 2000.

[118] L. Hadjidemetriou, E. Kyriakides and F. Blaabjerg, "A new hybrid PLL for interconnecting renewable energy systems to the grid,"," *IEEE Transactions on Industrial Applications,* vol. 49, no. 6, pp. 2709-2719, November- December 2013.

[119] S. Golestan, M. Ramezani and J. M. Guerrero, "An Analysis of the PLLs With Secondary Control Path," *IEEE Transactions on Industrial Electronics,* vol. 61, no. 9, pp. 4824-4828, September 2014.

[120] B. Wen, D. Dong, D. Boroyevich, R. Burgos, P. Mattavelli and Z. Shen, "Impedance-Based Analysis of Grid-Synchronization Stability for Three-Phase Paralleled Converters," *IEEE Transactions on Power Electronics,* vol. 31, no. 1, pp. 26-38, January 2016.

[121] L. Harnefors, M. Bongiorno and S. Lundberg, "Input-admittance calculation and shaping for controlled voltage-source converters,"," *IEEE Transactions on Industrial Electronics,* vol. 54, no. 6, pp. 3323-3334, December 2007.

[122] D. Dong, J. Li, D. Boroyevich, P. Mattavelli, I. Cvetkovic and Y. Xue, "Frequency behavior and its stability of grid-interface converter in distributed generation systems," in *Twenty-Seventh Annual IEEE Applied Power Electronics Conference and Exposition (APEC)*, Orlando, USA , February 2012.

[123] T. Midtsund, J. Suul and T. Undeland, "Evaluation of current controller performance and stability for voltage source converters connected to a weak grid," in *2nd IEEE International Symposium. on Power Electronics for Distributed Generation Systems (PEDG)*, Hefei, China, June 2010.

[124] O. Goksu, R. Teodorescu, C. Bak, F. Iov and P. Kjaer, "Instability of wind turbine converters during current injection to low voltage grid faults and PLL frequency based stability solution," *IEEE Transactions on Power Systems,* vol. 29, no. 4, pp. 1683-1691, 1683-1691 July 2014.

[125] L. Zhang, L. Harnefors and H.-P. Nee, "Interconnection of two very weak AC systems by VSC-HVDC links using power-synchronization control," *IEEE Transactions on Power Systems,* vol. 26, no. 1, pp. 344-355, February 2011.

[126] L. Zhang, H.-P. Nee and L. Harnefors, "Analysis of stability limitations of a VSC-HVDC link using power-synchronization control,"," *IEEE Transactions on Power Systems,* vol. 26, no. 3, pp. 1326-1337, August 2011.

[127] A. Egea-Alvarez, S. Fekriasl, F. Hassan and O. Gomis-Bellmunt, "Advanced vector control for

voltage source converters connected to weak grids," *IEEE Transactions on Power Systems,* vol. 30, no. 6, pp. 3072-3081, November 2015.

[128] Y. Huang, X. Yuan, J. Hu, P. Zhou and D. Wang, "DC-Bus Voltage Control Stability Affected by AC-Bus Voltage Control in VSCs Connected to Weak AC Grids," *IEEE Journal of Emerging and Selected Topics in Power Electronics,* vol. 4, no. 2, pp. 445-458, June 2016.

[129] Y. Huang, X. Yuan, J. Hu and P. Zhou, "Modeling of VSC Connected to Weak Grid for Stability Analysis of DC-Link Voltage Control," *IEEE Journal of Emerging and Selected Topics in Power Electronics,* vol. 3, no. 4, pp. 1193-1204, Dec. 2015.

[130] J. A. Suul, S. D'Arco, P. Rodríguez and M. Molinas, "Extended stability range of weak grids with voltage source converters through impedance-conditioned grid synchronization," in *11th IET International Conference on AC and DC Power Transmission*, Birmingham, UK, February 2015.

[131] C. Guo, W. Liu, C. Zhao and R. Iravani, "A Frequency-based Synchronization Approach for theVSC-HVDC Station Connected to a Weak AC Grid," *IEEE Transactions on Power Delivery,* To be published.

[132] M. F. M. Arani and Y. A.-R. I. Mohamed, "Analysis and Performance Enhancement of Vector-Controlled VSC in HVDC Links Connected to Very Weak Grids," *IEEE Transactions on Power Systems,* vol. 32, no. 1, pp. 684-693, January 2017.

[133] A. Khaligh and Z. Li, "Battery, Ultracapacitor, Fuel Cell, and Hybrid Energy Storage Systems for Electric, Hybrid Electric, Fuel Cell, and Plug-In Hybrid Electric Vehicles: State of the Art," *IEEE Transactions on Vehicular Technology,* vol. 59, no. 6, pp. 2806-2814, July 2010.

[134] W. Gao, "Performance comparison of a fuel cell-battery hybrid powertrain and a fuel cell-ultracapacitor hybrid powertrain," *IEEE Transactions on Vehicular Technology,* vol. 54, no. 3, pp. 846-855, May 2005.

[135] J. Cao and A. Emadi, "A New Battery/UltraCapacitor Hybrid Energy Storage System for Electric, Hybrid, and Plug-In Hybrid Electric Vehicles," *IEEE Transactions on Power Electronics,* vol. 27, no. 1, pp. 122-132, January 2012.

[136] A. Schneuwly, "Charge ahead (ultracapacitor technology and applications)," *Power Engineer,* vol. 19, no. 1, pp. 34-37, February-March 2005.

[137] E. G. Bakhoum, "New mega-farad ultracapacitors," *IEEE Transactions on Ultrasonics,*

Ferroelectrics and Frequency Control, vol. 56, no. 1, pp. 14-21, January 2009.

[138] M. Yilmaz and P. T. Krein, "Review of Battery Charger Topologies, Charging Power Levels, and Infrastructure for Plug-In Electric and Hybrid Vehicles," *IEEE Transactions on Power Electronics,* vol. 28, no. 5, pp. 2151-2169, May 2013.

[139] M. Yilmaz and P. T. Krein, "Review of the Impact of Vehicle-to-Grid Technologies on Distribution Systems and Utility Interfaces," *IEEE Transactions on Power Electronics,* vol. 28, no. 12, pp. 5673-5689, December 2013.

[140] A. Khaligh and S. Dusmez, "Comprehensive Topological Analysis of Conductive and Inductive Charging Solutions for Plug-In Electric Vehicles," *IEEE Transactions on Vehicular Technology,* vol. 61, no. 8, pp. 3475-3489, October 2012.

[141] S. Dusmez and A. Khaligh, "Cost effective solutions to level 3 on-board battery chargers," in *Twenty-Seventh Annual IEEE Applied Power Electronics Conference and Exposition (APEC)*, Orlando, USA, February 2012.

[142] X. Zhou, J. Fan and A. Q. Huang, "High-Frequency Resonance Mitigation for Plug-In Hybrid Electric Vehicles' Integration with a Wide Range of Grid Conditions," *IEEE Transactions on Power Electronics,* vol. 27, no. 11, pp. 4459-4471, November 2012.

[143] Y. Ota, H. Taniguchi, T. Nakajima, K. M. Liyanage, J. Baba and A. Yokoyama, "Autonomous Distributed V2G (Vehicle-to-Grid) Satisfying Scheduled Charging," *IEEE Transactions on Smart Grid,* vol. 3, no. 1, pp. 559-564, March 2012.

[144] S. Vachirasricirikul and I. Ngamroo, "Robust LFC in a Smart Grid With Wind Power Penetration by Coordinated V2G Control and Frequency Controller," *IEEE Transactions on Smart Grid,* vol. 5, no. 1, pp. 371-380, January 2014.

[145] H. Yang, C. Y. Chung and J. Zhao, "Application of plug-in electric vehicles to frequency regulation based on distributed signal acquisition via limited communication," *IEEE Transactions on Power Systems,* vol. 28, no. 2, pp. 1017-1026, May 2013.

[146] T. Liu, D. J. Hill and C. Zhang, "Non-Disruptive Load-Side Control for Frequency Regulation in Power Systems," *IEEE Transactions on Smart Grid,* vol. 7, no. 4, pp. 2142-2153, July 2016.

[147] H. Liu, Z. Hu, Y. Song, J. Wang and X. Xie, "Vehicle-to-Grid Control for Supplementary Frequency Regulation Considering Charging Demands," *IEEE Transactions on Power Systems,* vol. 30, no. 6, pp. 3110-3119, November 2015.

[148] T. Masuta and A. Yokoyama, "Supplementary Load Frequency Control by Use of a Number of Both Electric Vehicles and Heat Pump Water Heaters," *IEEE Transactions on Smart Grid,* vol. 3, no. 3, pp. 1253-1262, September 2012.

[149] M. F. M. Arani, Y. A.-R. I. Mohamed and E. El-Saadany, "Analysis and Mitigation of the Impacts of Asymmetrical Virtual Inertia," *IEEE Transactions on Power Systems,* vol. 29, no. 6, pp. 2862-2874, November 2014.

[150] C. Gouveia, J. Moreira, C. L. Moreira and J. A. Peças Lopes, "Coordinating Storage and Demand Response for Microgrid Emergency Operation," *IEEE Transactions on Smart Grid,* vol. 4, no. 4, pp. 1898-1908, December 2013.

[151] S. Gao, K. T. Chau, C. Liu, D. Wu and J. Li, "SMES Control for Power Grid Integrating Renewable Generation and Electric Vehicles," *IEEE Transactions on Applied Superconductivity,* vol. 22, no. 3, pp. 5701804-5701804, June 2012.

[152] M. Datta and T. Senjyu, "Fuzzy Control of Distributed PV Inverters/Energy Storage Systems/Electric Vehicles for Frequency Regulation in a Large Power System," *IEEE Transactions on Smart Grid,* vol. 4, no. 1, pp. 479-488, March 2013.

[153] M. F. M. Arani and Y. A.-R. I. Mohamed, "Analysis and Mitigation of Undesirable Impacts of Implementing Frequency Support Controllers in Wind Power Generation," *IEEE Transactions on Energy Conversion,* vol. 31, no. 1, pp. 174-186, March 2016.

[154] C. A. Baone and C. L. DeMarco, "From Each According to its Ability: Distributed Grid Regulation With Bandwidth and Saturation Limits in Wind Generation and Battery Storage," *IEEE Trans. on Control Systems Technology,* vol. 21, no. 2, pp. 384-394, March 2013.

[155] M. F. M. Arani and Y. A.-R. I. Mohamed, "Analysis and Damping of Mechanical Resonance of Wind Power Generators Contributing to Frequency Regulation," *IEEE Transactions on Power Systems,* To be published.

[156] J. W. Choi, S. Y. Heo and M. K. Kim, "Hybrid operation strategy of wind energy storage system for power grid frequency regulation," *IET Generation, Transmission & Distribution,* vol. 10, no. 3, pp. 736-749, February 2016.

[157] J. Dang, J. Seuss, L. Suneja and R. G. Harley, "SoC Feedback Control for Wind and ESS Hybrid Power System Frequency Regulation," *IEEE Journal of Emerging and Selected Topics in Power Electronics,* vol. 2, no. 1, pp. 79-86, March 2014.

[158] K. V. Vidyanandan and N. Senroy, "Frequency regulation in a wind–diesel powered microgrid using flywheels and fuel cells," *IET Generation, Transmission & Distribution,* vol. 10, no. 3, pp. 780-788, February 2016.

[159] L. Miao, J. Wen, H. Xie, C. Yue and W. J. Lee, "Coordinated Control Strategy of Wind Turbine Generator and Energy Storage Equipment for Frequency Support," *IEEE Transactions on Industry Applications,* vol. 51, no. 4, pp. 2732-2742, July-August 2015.

[160] J. Tan and L. Wang, "A Game-Theoretic Framework for Vehicle-to-Grid Frequency Regulation Considering Smart Charging Mechanism," *IEEE Transactions on Smart Grid,* To be published.

[161] M. F. M. Arani, "Incorporating DFIG-nased wind power generator in microgird frequency stabilization," M.A.Sc. Dissertation, University of Waterloo, Waterloo, ON, Canada, 2012.

[162] P. C. Kundur, Power System Stability and Control, New York; Toronto: McGraw-Hill, 1994.

[163] S. Heier, Grid integration of wind energy: onshore and offshore conversion systems, John Wiley & Sons , 2014.

[164] B. Wu, Y. Lang, N. Zargari and S. Kouro, Power conversion and control of wind energy systems, John Wiley & Sons, 2011.

[165] F. Mei and B. Pal, "Modal Analysis of Grid-Connected Doubly Fed Induction Generators," *IEEE Transactions on Energy Conversion,* vol. 22, no. 3, pp. 728-736, September 2007.

[166] S. Ghosh and N. Senroy, "Electromechanical Dynamics of Controlled Variable-Speed Wind Turbines," *IEEE Systems Journal,* vol. 9, no. 2, pp. 639-646, June 2015.

[167] J. Zhao, X. Lyu, Y. Fu, X. Hu and F. Li, "Coordinated Microgrid Frequency Regulation Based on DFIG Variable Coefficient Using Virtual Inertia and Primary Frequency Control," *IEEE Transactions on Energy Conversion,* vol. 31, no. 3, pp. 833-845, September 2016.

[168] N. Pogaku, M. Prodanovic and T. C. Green, "Modeling, Analysis and testing of autonomous operation of an inverter-based microgrid," *IEEE Transactions on Power Electronics,* vol. 22, no. 2, pp. 613-625, March 2007.

[169] F. Katiraei, M. R. Iravani and P. W. Lehn, "Small-signal dynamic model of a micro-grid including conventional and electronically interfaced distributed resources," *IET Generation, Transmission & Distribution,* vol. 1, no. 3, pp. 369-378, May 2007.

[170] "Database of wind characteristics located at DTU, Denmark," WindData.

[171] R. Datta and R. V. T. Ranganathan, "Variable-speed wind power generation using doubly fed wound rotor induction machine-a comparison with alternative schemes," *IEEE Transactions on Energy Conversion,* vol. 17, no. 3, pp. 414-421, September 2002.

[172] W. Freitas, W. Xu, C. M. Affonso and Z. Huang, "Comparative analysis between ROCOF and vector surge relays for distributed generation applications," *IEEE Transactions on Power Delivery,* vol. 20, no. 2, pp. 1315-1324, April 2005.

[173] C. M. Affonso, W. Freitas, W. Xu and L. C. P. Da Silva, "Performance of ROCOF relays for embedded generation applications," *IEE Proceedings- GTD,* vol. 152, no. 1, pp. 109-114, 10 January 2005.

[174] M. F. M. Arani and Y. A.-R. I. Mohamed, "Assessment and Enhancement of a Full-Scale PMSG-Based Wind Power Generator Performance Under Faults," *IEEE Transactions on Energy Conversion,* vol. 31, no. 2, pp. 728-739, June 2016.

[175] A. Yazdani and R. Iravani, Voltage-sourced converters in power systems: modeling, control, and applications, John Wiley & Sons, 2010.

[176] H. Wang and F. Blaabjerg, "Reliability of capacitors for DC-link applications in power electronic converters—an overview,"," *IEEE Transactions on Industrial Applications,* vol. 50, no. 5, pp. 3569-3578, September-October 2014.

[177] G. Chen, R. Burgos, Z. Liang, F. Lacaux, F. Wang, J. v. Wyk, W. Odendaal and D. Boroyevich, "Reliability-oriented design considerations for high-power converter modules," in *IEEE 35th Annual Power Electronics Specialists Conference*, Aachen, Germany, 2004.

[178] P. Rodriguez, A. V. Timbus, R. Teodorescu, M. Liserre and F. Blaabjerg, "Flexible active power control of distributed power generation systems during grid faults,"," *IEEE Transactions Industrial Electronics,* vol. 54, no. 5, pp. 2583-2592, October 2007.

[179] M. Torres and L. A. C. Lopes, "Virtual synchronous generator control in autonomous wind-diesel power systems," in *IEEE Electrical Power & Energy Conference (EPEC)*, Montreal, Canada, 2009.

[180] A. Kahrobaeian and Y.-R. I. Mohamed, "Analysis and mitigation of low-frequency instabilities in autonomous medium-voltage converter-based microgrids with dynamic loads," *IEEE Transactions on Industrial Electronics,* vol. 61, no. 4, pp. 1643-1658, April 2014.

[181] J. Nilson, "Real-Time Control Systems with Delays," Ph.D. dissertation, Lund Institute of

Technology, Lund, Sweden, 1998.

[182] B. A. Hamilton, "Route Diversity Project (RDP): AT&T Wireless Broadband Service Evaluation Results Report," National Communications System, Atlanta, GA, February 2007.

[183] C. A. Macana, E. Mojica-Nava and N. Quijano, "Time-delay effect on load frequency control for microgrids," in *10th IEEE International Conference on Networking, Sensing and Control (ICNSC)*, Evry, France, April 2013.

[184] L. Jiang, W. Yao, Q. H. Wu, J. Y. Wen and S. J. Cheng, "Delay-Dependent Stability for Load Frequency Control With Constant and Time-Varying Delays," *IEEE Transactions on Power Systems,* vol. 27, no. 2, pp. 932-941, May 2012.

[185] Q.-C. Zhong, Robust control of time-delay systems, Berlin: Springer, 2006.

[186] D. Linden and T. B. Reddy, Handbook of Batteries, Third Edition, McGraw-Hill , 2002.

[187] S. Pang, J. Farrell, J. Du and M. Barth, "Battery state-of-charge estimation," in *American Control Conference* , Arlington, VA, USA, 2001.

[188] F. Milano, "Small-Signal Stability Analysis of Large Power Systems With Inclusion of Multiple Delays," *IEEE Transactions on Power Systems,* vol. 31, no. 4, pp. 3257-3266, July 2016.

[189] X. Zhong, "A Single Phase Grid Connected DC/AC Inverter with Reactive Power Control for Residential PV Application," M.A.Sc. Dissertation, University of Toronto, Toronto, Ontario, Canada, 2011.

[190] V. Khadkikar, A. Chandra and B. N. Singh, "Generalised single-phase p-q theory for active power filtering: simulation and DSP-based experimental investigation," *IET Power Electronics,* vol. 2, no. 1, pp. 67-78, January 2009.

[191] L. Zhang, "Modeling and control of VSC-HVDC links connected to weak AC systems," PhD thesis, Royal Institute of Technology, Stockholm, Sweden, 2010.

[192] M. Durrant, H. Werner and K. Abbott, "Model of a VSC HVDC terminal attached to a weak AC system," in *IEEE Conference on Control Applications*, Istanbul, Turkey, June 2003.

[193] I. C. Report, "Dynamic models for steam and hydro turbines in power system Studies," *IEEE Transactions on Power Apparatus and Systems,* Vols. PAS-92, no. 6, pp. 1904-1973, November 1973.

Appendix A

Generators

Table 2 DG1 (Wind Generator) Parameters [161], [89]

		DFIG	PMSG
Specifications	Rating	2.5 MVA	2 MVA
	Pole pairs	2	32
Mechanical System	H_G	0.6 s	0.53 s
	H_T	2.4 s	4.27 s
	K_s	0.6 pu/elec. rad	1.6 pu/elec. rad
	D_G	0.01pu	0
	D_T	0	0
DC-link	C_{dc}	160mF	24 mF
	V_{dc}	1500V	5.4 kV
Controller	Regulator Parameters (SI units)	K_{p1}=114, K_{i1}=76, K_{p2}=3, K_{i2}=30, T_p=0.01 s	K_p=0.02 K_i=100 τ_i=0.3 ms

Table 3 Wind turbine parameters

K_{OPT}	0.628
c_1	0.5176
c_2	116
c_3	0.4
c_4	5
c_5	21
c_6	0.0068

Table 4 DG2 (Synchronous Generator) Parameters

Rating	2.5MVA	
Mechanical System (Non-reheat Thermal Turbine [162], [193])	Droop gain	80 pu
	T_{CH}	450 ms
	T_G	0.08 s
	H	3 s
AVR Parameters	K_A	400
	T_A	0.02 s

Appendix B

The Model Details

Table 5 The loads of the model shown in Figure 3-7

Load Name	Corresponding Bus	P(KW)	Q(KVAR)
LP1	4	47.50	15.61
LP2	5	2565.0	843.06
LP3	6	289.75	95.24
LP4	7	152	49.96
LP5	8	517.75	170.18
LP6	8	194.75	64.01
LP7	2	7155.0	2566.71
LP8	2	3348.8	1100.7
LP9	3	1071.75	621.95

Table 6 The connections of the model shown in Figure 3-7

From	To	R(Ω)	X(Ω)
1	2	1.096	2.710
2	3	0.232	0.573
3	4	1.277	3.157
4	5	0.066	0.089
5	6	0. 675	0.909
6	7	0.567	0.764
7	8	0.738	0.993
4	LP1	1.500	0.680
5	LP2	1.631	2.706
6	LP3	0.853	1.148
7	LP4	0.663	0.582
8	LP5	0.884	1.190
8	LP6	0.817	0.718

Table 7 The model shown in Figure 6-2.

Lines	PCC to Grid	1.2768+j3.1575 Ω
	PCC to EVs	0.0485+j.05823 Ω
	PCC to Generator	0.0636+j0.7636 Ω
Load1		1.52MW+j0.4996MVAR
Load2	Phase a	0.6MW+j33.3kVAR
	Phase b	0.63MW+j35kVAR
	Phase c	0.57MW+j31.7kVAR

Table 8 The electric vehicle loads in the model shown in Figure 6-10

Connection Bus	EV Nominal Load
LP1	100 kW
LP2	500 kW
LP3	50kW
LP4	50kW
LP5	50kW
LP6	500 kW

Table 9 The parameter of the model shown in Figure 7-1(a)

$P_{nominal}$	350 MVA
$V_{nominal}$	195 kV
f_{nominal}	60 Hz
X/R ratio	10
R_f	1.089Ω
L_f	0.0575 H
C_f	1.22 μF
C_{dc}	166.7 μF
V_{dc}	350 kV

Table 10 The control parameters used in Chapter 7

K_{pv}	2.2 kA
K_{iv}	98.92 kA/s
K_{pp}	2.09×10^{-3}/MV
K_{ip}	789.3/(MV.s)
K_{pq}	0.419/MV
K_{iq}	209.4/(MV.s)
τ_i	0.796 ms
K_{ppll}	0.0013/(V.s)
K_{ipll}	$0.1413/(V.s^2)$
L'	0.2868 H
τ_c	0.01 ms